UNIVERSIDADE TÉCNICA DE LISBOA
INSTITUTO SUPERIOR TÉCNICO

J/ψ and ψ' Production in Pb-Pb Collisions at 158 GeV/nucleon

Helena de Fátima Nunes Casimiro dos Santos
(Licenciada)

Dissertação para obtenção do Grau de Doutor em Física

Orientador: Doutor Sérgio Eduardo Campos Costa Ramos

Júri:
Presidente: Reitor da Universidade Técnica de Lisboa
Vogais: Doutor Louis Kluberg
Doutor Rui Ferreira Marques
Doutor José Mariano Rebelo Pires Gago
Doutor Jorge Venceslau Comprido Dias de Deus
Doutor João Carlos Carvalho de Sá Seixas
Doutora Maria Paula Frazão Bordalo e Sá
Doutor Sérgio Eduardo Campos Costa Ramos

Outubro de 2004

UNIVERSIDADE TÉCNICA DE LISBOA
INSTITUTO SUPERIOR TÉCNICO

J/ψ and ψ' Production in Pb-Pb Collisions at 158 GeV/nucleon

Helena de Fátima Nunes Casimiro dos Santos
(Licenciada)

Dissertação para obtenção do Grau de Doutor em Física

Orientador: Doutor Sérgio Eduardo Campos Costa Ramos

Júri:
Presidente: Reitor da Universidade Técnica de Lisboa
Vogais: Doutor Louis Kluberg
Doutor Rui Ferreira Marques
Doutor José Mariano Rebelo Pires Gago
Doutor Jorge Venceslau Comprido Dias de Deus
Doutor João Carlos Carvalho de Sá Seixas
Doutora Maria Paula Frazão Bordalo e Sá
Doutor Sérgio Eduardo Campos Costa Ramos

Outubro de 2004

À minha Família.
Amo-vos infinitamente...

Abstract

This work presents the results on the J/ψ and ψ' production in 158 AGeV Pb-Pb interactions at the CERN SPS NA50 experiment and its dependence on the transverse energy.

The study of charmonium production in ultra-relativistic heavy ion collisions has been addressed since the mid 80s by the NA38 Collaboration, followed in the 90s by NA50. The motivation is to search for the phase transition of nuclear matter from its normal state to a deconfined quark-gluon plasma, as predicted to occur, under extreme energy densities or temperature conditions, by non-perturbative QCD. In such a deconfined matter, it is expected that J/ψ is suppressed by Debye colour screening. As the vector-meson is produced at the very early stages of the collisions, its leptonic decay provides a useful probe of these stages, since muons, are insensitive to strong interactions and, therefore, to the hadronization stage.

The ψ', a more loosely bound state than J/ψ, may also dissociate at lower energy densities. However, due to its small binding energy, its production can, as well, be suppressed by standard nuclear interactions, namely by normal absorption of the pre-resonant state in the nuclear matter and by dissociation of the final states due to hadronic interactions.

The reference to the J/ψ and ψ' suppressions is provided by Drell-Yan, one of the physical processes which contributes to the dimuon invariant mass spectrum, since these lepton pairs do not suffer from nuclear medium effects.

Three data taking are analysed, devoting a special detail to the 2000's run. This data sample is the best, not only due the significant number of J/ψ and ψ' collected, but also because the data have been taken with the target region in vacuum. Such improved conditions have allowed the study of the peripheral collisions safely.

Key-words:

Quark-Gluon Plasma, Ultra–relativistic Pb–Pb collisions, Dimuon invariant mass spectrum, Charmonia suppression, Drell-Yan, Transverse energy

Resumo

Este trabalho apresenta os resultados das medidas de produção dos estados charmonium J/ψ e ψ' em colisões Pb-Pb a 158 GeV/nucleão e a sua dependência com a energia transversa.

O estudo da supressão de charmonia em colisões de iões pesados a energias ultra-relativistas tem vindo a realizar-se desde os anos 80 pelas Colaborações NA38 e NA50. A motivação física prende-se com a previsão da Cromodinâmica Quântica não perturbativa segundo a qual, em condições extremas de densidade de energia e/ou de temperatura, uma transição de fase da matéria hadrónica para um estado desconfinado, denominado plasma de quarks e gluões, deverá ocorrer. Uma forte assinatura deste estado da matéria é a suppressão do J/ψ por efeito de blindagem de cor (*Debye colour screening*). Como este mesão-vector é produzido nos primórdios da colisão, o seu decaimento leptónico constitui uma excelente prova destes primeiros instantes, já que os muões são insensíveis à interacção forte e, portanto, à fase de hadronização.

Por seu turno, o ψ', por ser um estado ligado mais fraco que o J/ψ, pode dissociar-se a densidades de energia mais baixas, esperando-se que a sua supressão ocorra por interacções nucleares standard, tais como a absorção do estado pré-ressonante $c\bar{c}$ pela matéria nuclear e a dissociação do estado final por interacções com os hadrões produzidos nas colisões (os *comovers*).

Os pares de Drell-Yan presentes no espectro de massa invariante dos dimuões constituem uma referência segura na determinação das supressões dos estados charmonia, uma vez que este processo físico permanece insensível aos efeitos hadrónicos nucleares.

Três conjuntos de dados são analisados, com especial destaque para a tomada de dados de 2000. Estes constituem a melhor amostra estatística de sempre, não só pelo elevado número de J/ψ e ψ' recolhidos, como também pelo facto de terem sido tomados com a região do alvo colocada em vácuo, garantindo assim um estudo seguro das colisões periféricas.

Palavras-chave:

Plasma de quarks e gluões, Colisões Pb-Pb ultra-relativistas, Espectro de massa invariante de dimuões, Suppressão de Charmonia, Drell-Yan, Energia transversa

Thanks

I would like to express my deep gratitude to the people who helped me during these years, particularly to my Supervisor, Sérgio Ramos and to the NA50-LIP team leader, Paula Bordalo. I have learned a lot with you. A special thanks goes to my colleagues Catarina Quintans and Gonçalo Borges. This work have also your essential touch.

I want to thank to whole LIP people. You are great at work and friendship. Thanks a lot to the computer experts Jorge Gomes, João Martins and José Aparício for the ready solutions on my computer troubles.

I am very grateful to the NA50 Collaboration for the opportunity to work in such an exciting task. Particularly, I would like to thank deeply to Louis Kluberg and Luciano Ramello for the support in the most hard moments.

I want to express my gratitude to Bernard Chaurand and Carlos Lourenço for the useful discussions. My special thanks to Enrico Scomparin, Francesco Prino, Roberta Arnaldi, Federica Sigaudo, Carl Castanier, Pietro Cortese and Giovanna Puddu for the work interaction, always constructive, and sympathy.

I acknowledge the financial support provided by Fundação para a Ciência e a Tecnologia.

Contents

List of Figures

List of Tables

Esta terra quente em perpétuo trabalho,
possuída pela febre da gestação. [1]

Ferreira de Castro

Chapter 1

Physical motivation

1.1 The Quark-Gluon Plasma

Quantum Chromodynamics (QCD) is the theory of the strong interactions. It is developed in terms of elementary fields (quarks and gluons), which interactions obey to principles of a relativistic quantum field theory with a non-Abelian gauge invariance SU(3) [1]. Matter is formed by leptons $(e, \mu, \nu_e...)$ and hadrons, the proton and neutron being the simplest ones. Hadrons are bound states of quarks, which in turn are spin-1/2, colour-triplet fermions. These interact via the exchange of an octet of spin-1, coloured gluons. QCD, in its perturbative framework, predicts that quarks cannot exist by themselves; they are confined within hadrons by a binding potential $V(r)$ which increases linearly with the quark separation r.

We are interested in the study of the phase transition that occurs when matter is under extreme conditions, namely very high energy densities or temperatures. Within such conditions the ordinary hadronic matter undergoes a transition to a new state where quarks and gluons are no more confined, the Quark-Gluon Plasma (QGP). In order to understand the dynamics of this new state of matter, its equation of state must be known. To obtain it, a non-perturbative method, based on lattice formulation of QCD [2], should be used, because the critical behaviour occurs in a regime of strong gauge coupling. A brief description of the method is based in [3].

The thermodynamics is obtained from the partition function in form of a path integral [4]

$$\mathcal{Z}(V,T) = \int dA d\psi d\bar{\psi} \exp(-\int_V d^3x \int_0^{1/T} d\tau \mathcal{L}(A,\psi,\bar{\psi})) \ , \tag{1.1}$$

[1] *This warm land in perpetual work,*
possessed by the fever of gestation.

where $\mathcal{L}(A, \psi, \bar{\psi})$ is the QCD Lagrangian:

$$\mathcal{L}(A, \psi, \bar{\psi}) = -\frac{1}{4}(\partial_\mu A^i_\nu - \partial_\nu A^i_\mu - g f^{ijk} A^j_\mu A^k_\nu)^2 + \sum_f \bar{\psi}^f_\beta (i\gamma^\mu \partial_\mu + m_f - g\gamma^\mu A_\mu)^{\beta\alpha} \psi^f_\alpha \; . \quad (1.2)$$

The time component is rotated to become purely imaginary, $\tau = it$. The integration over τ in equation 1.1 runs over a finite slice which thickness is determined by the temperature of the system. In this way $1/T$ plays the role of time.

In a lattice, the continuum Euclidean space-time is replaced by a set of discrete points. The volume and temperature are given by $V = N_s^3 a^3$ and $1/T = N_t a$, where a is the lattice spacing. The Euclidean form of the partition function becomes:

$$\mathcal{Z}(V, T) = \int \prod_{links} dU_{ij} \prod_{sites} d\psi d\bar{\psi} \exp(-S^G(U) - S^F(U, \psi, \bar{\psi})) \; , \quad (1.3)$$

where the gauge field $A_\mu(x_i + x_j)/2$, associated to the link between two adjacent sites, i and j, is replaced by the gauge group element

$$U_{ij} = \exp[-i(x_i - x_j)^\mu A_\mu(\frac{x_i + x_j}{2})] \quad (1.4)$$

and $S^G(U)$ and $S^F(U)$ are the gluon and fermion actions in the lattice. The thermodynamical variables, pressure and energy density, are derivatives of the partition function:

$$\frac{p}{T} = \frac{\partial lnZ}{\partial V} \; , \quad (1.5)$$

$$\epsilon = -\frac{1}{V}\frac{\partial lnZ}{\partial(1/T)} \; . \quad (1.6)$$

Lattice QCD predicts a critical temperature $T_c = 173 \pm 8$ MeV, in two flavour QCD [5] and $T_c = 154 \pm 8$ MeV, in three flavours; the quoted errors are only statistical. A large systematic error is expected due to lattice discretization and still too large quark masses which are used in the Monte Carlo studies. The corresponding critical energy density is $\epsilon_c \simeq 0.7$ GeV/fm^3, for two-flavours [6]. This value is affected by a 50% error, mainly due to the uncertainty on T_c. Taking into account this large uncertainty, the critical energy density is 2-6 times the current nuclear one, $\epsilon_n \sim 0.17$ GeV/fm^3. Figure 1.1 shows the ϵ/T^4 steep change in a very narrow range of T, a typical behaviour of a system with a phase transition. The arrows show the ideal quark-gluon gas, ϵ_{SB}, values as given by

$$\frac{\epsilon_{SB}}{T^4} = (2 \times 8 + \frac{7}{8}(3 \times 2 \times 2 \times 2))\frac{\pi^2}{30} \; , \quad (1.7)$$

where the first term accounts for the two spin and (3^2-1) SU(3) colour states of the gluons and the second one for the three colour, two flavour, two spin and two (anti)particle degrees of freedom of the quarks, times 7/8 to deal with the correct Fermi-Dirac statistics.

Such a transition is expected to occur in the laboratory by means of ultra-relativistic

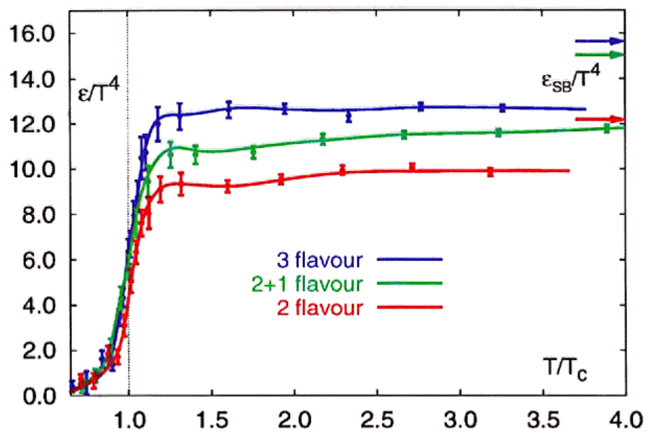

Figure 1.1: *The energy density in Lattice QCD [6]. The arrows show the ideal quark-gluon gas, ϵ_{SB}.*

heavy ion collisions. In fact, this transition would have occurred in the opposite sense, a few microseconds after the Big Bang, and it is expected that such deconfined medium is present in the core of neutron stars (figure 1.2).

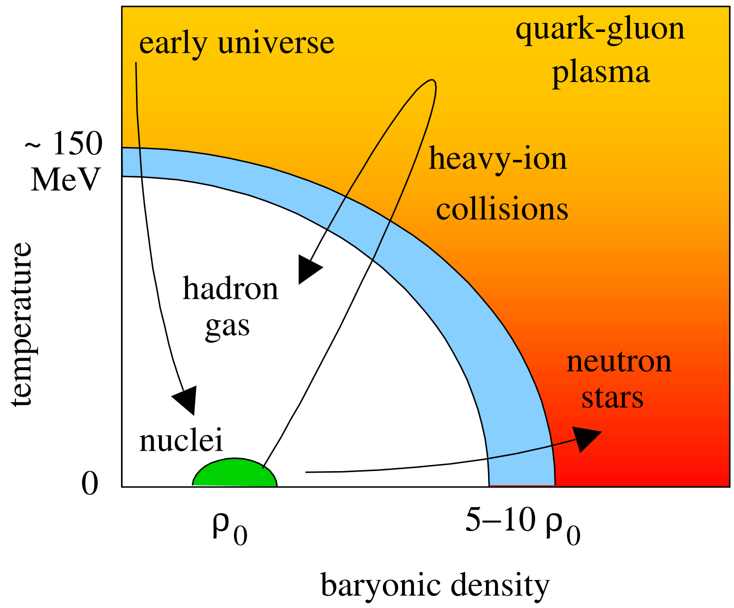

Figure 1.2: *Strongly interacting matter phase diagram as a function of temperature and barionic density.*

1.2 Phenomenology of heavy ion collisions

Several regimes take place in central ultra-relativistic heavy ion collisions. They are schematically described in the space-time diagram of the collision (figure 1.3).

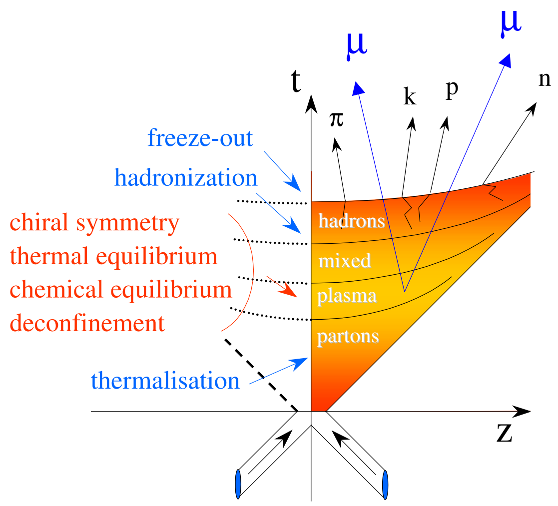

Figure 1.3: *Evolution of the matter along the collision (z axis) as a function of time: pre-equilibrium partonic system, thermalized quark-gluon plasma, hadronization and its subsequent freeze-out.*

For $t < 0$, the projectile and target nuclei travel along the light cone until they meet at the origin. At $t = 0$, the two nuclei overlap, partially if it is a peripheral collision, i.e., if the two nuclei interact with an impact parameter b, which can be as large as the sum of the two radii, or totally if a central collision ($b \simeq 0$) occurs. The nuclear matter distributes itself in two zones, the fragmentation and the central zone, a region where the initial dynamics conditions are invariant under Lorentz transformations (figure 1.4). In

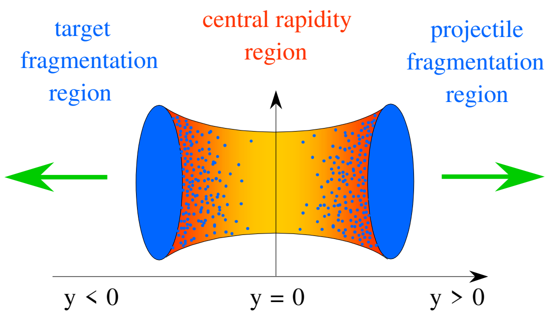

Figure 1.4: *Rapidity distribution of matter in a heavy ion collision.*

the central region, a high number of partons, during the pre-equilibrium time $\tau \leq 1$ fm (at the Super Proton Synchrotron, CERN–SPS), is expected to be formed. These partons interact and, for sufficient high energy densities, a thermalized quark-gluon plasma is formed. This plasma expands and cools undergoing an hadronization, i.e., a hadron gas, in which hadrons interact. Subsequently it freezes-out and the hadrons become free from interactions.

The length of time that a given element of matter stays in the several stages described above, measured in the local matter rest frame, is approximately the same for all elements in the central rapidity regime. The rapidity, y, is defined as

$$y = \frac{1}{2}\ln\frac{t+z}{t-z} \ . \tag{1.8}$$

The local fluid velocity is $\sim z/t$, and the local proper time, $\tau \sim (t^2 - z^2)^{1/2}$, is constant, so the proper time surfaces, which envelop the several dynamic regions, are approximately hyperbolae [7]. As the central rapidity region is boost invariant, the thermodynamic observables, such as energy density and pressure, do not depend on rapidity, but on the proper time.

The main object of this work is to probe the second stage, that is, the QGP formation. And here, three questions arise:

1. Are the initial energy densities, necessary to form the QGP, reachable in heavy ion collisions?

2. Are the relevant space and time scales sufficiently large to expect equilibrium?

3. If QGP occurs are we able to detect it?

The initial energy density in a heavy ion collision can be estimated through the hydrodynamical model proposed by Bjorken [8]: in a A–B central collision, the energy contained in a slice of the rapidity space of thickness Δy is given by:

$$E = N\frac{d < E >}{dy}\Delta y \ , \tag{1.9}$$

where N is the number of secondary particles contained in the slice and $< E >$ is the average energy of the N particles. Considering a volume V determined by the transverse area of the nuclei and the Lorentz invariant length element $\Delta z = c\tau_0 \Delta y$ in the beam direction, the energy density of matter created at the parton formation time, τ_0, becomes:

$$\epsilon_0(\tau_0) \equiv \frac{E}{V} = N\frac{d < E >}{dy}\frac{1}{c\tau_0 \pi {R_A}^2} \ . \tag{1.10}$$

The longitudinal momenta are small in the central collision region, so the following approximation holds:

$$N\frac{d < E >}{dy} = \frac{dN}{dy} < m_T > \quad \longrightarrow \quad \epsilon_0(\tau_0) = \frac{dN}{dy}\frac{< m_T >}{c\tau_0 \pi {R_A}^2} \ , \tag{1.11}$$

where $< m_T >^2 = < m^2 + {P_T}^2 >$ is the average transverse mass of the secondary hadrons. As pions dominate N and have an average transverse momentum of $\sim$0.35 GeV, the $< m_T >$ value is $\sim$0.4 GeV. Assuming $\tau_0 \sim 1$ fm/c and using the $dN/dy|_{y\simeq 0}$ results obtained in Pb–Pb collisions at the CERN–SPS [9, 10] ($\sqrt{s}$=17.3 GeV), one should expect an energy density of the order of 3 GeV/fm^3 . At the Brookhaven National Laboratory's Relativistic Heavy–Ion Collider, BNL–RHIC, the thermalization time is expected to be 3–5 times smaller than at SPS, so, assuming a τ_0= 0.3 fm/c in Au-Au collisions [11, 12] ($\sqrt{s}$=56 and 130 GeV), one gets $10 \lesssim \epsilon_0 \lesssim 15$ GeV/fm^3.

These initial energies obtained in laboratory, compared with Lattice QCD results, seem to be sufficient to reach QGP experimentally. However, a large energy density may still not be sufficient to create it; the system must thermalize. The lifetime of the expanding system should be higher than the hadronic time scale, which is assumed to be 1 fm.

* * *

Evidence of thermalized systems formed in Pb–Pb collisions is shown by the scaling of charged particle multiplicity with the number of participating nucleons in a collision [10, 13, 14]. This behaviour is expected in scenarios dominated by soft processes, when particles undergo a strong re-scattering in the final state and the memory of the exact history of multiple collisions is lost. Figure 1.5 shows the $dN/d\eta|_{max}$ distribution with the number of participants, as measured by the NA50 experiment, parametrized with the usual power law: $dN/d\eta|_{max} \propto N^{\alpha}_{part}$. The extracted α value is $1.00 \pm 0.01(stat) \pm 0.04(syst)$, with both E_T and E_{ZDC} selections [2], a value compatible with the one obtained by the WA97/NA57 experiments: $\alpha = 1.05 \pm 0.05$.

Hadron transverse momentum spectra are sensitive to the collision dynamics, because all transverse motion is generated during the interaction. Figure 1.6 displays the neutral pion p_T spectra [15] measured in the WA98 experiment. For centralities with more than 30 participating nucleons, the shape of the transverse momentum spectrum is invariant over the interval $0.5 < p_T < 3$ GeV/c. Since the amount of re-scatterings increases with centrality, the invariance of the spectral shape suggests a dominantly thermal emission process.

Hadron production cross sections as functions of the transverse mass (or transverse momentum) provide information about the reached thermalization and collective

[2] E_T is the neutral transverse energy and E_{ZDC} is the forward energy, as measured by the NA50 Electromagnetic and Zero Degree Calorimeters.

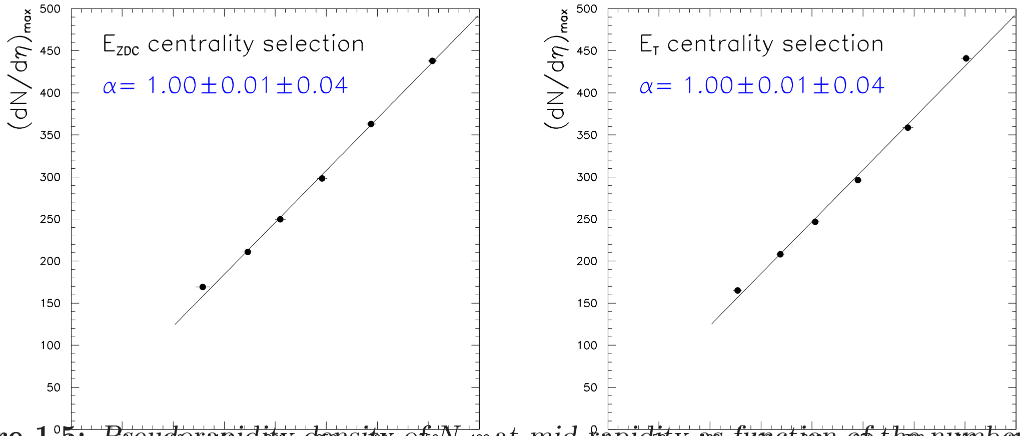

Figure 1.5: *Pseudorapidity density of N_{ch} at mid-rapidity as function of the number of participants in Pb–Pb collisions at 158 GeV/n with the two independent centrality selections [10].*

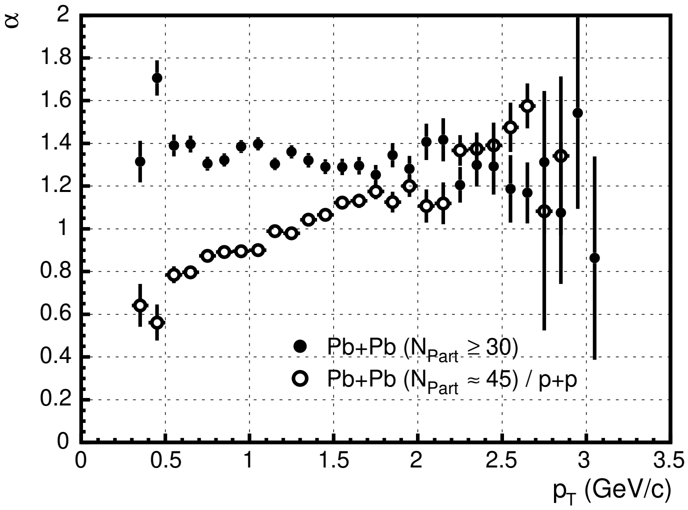

Figure 1.6: *The exponent $\alpha(p_T)$ of the π^0 yield dependence on the average number of participants N_{part} ($Ed^3N/dp^3 \propto N_{part}^{\alpha(p_T)}\sigma_0(p_t)$), plotted as a function of the transverse momentum for 158 AGeV Pb–Pb interactions [15].*

expansion. The NA57 Collaboration has made a compilation of data collected in several SPS Pb–induced experiments, relatively to the m_T inverse slopes as a function of the hadron mass (figure 1.7). The double differential distributions in m_T and y have been parametrized by the expression [3]:

$$\frac{d^2N}{dm_T dy} = m_T f(y) exp(-\frac{m_T}{T}) \ , \tag{1.12}$$

assuming a flat rapidity distribution within the acceptance region considered ($f(y) =$

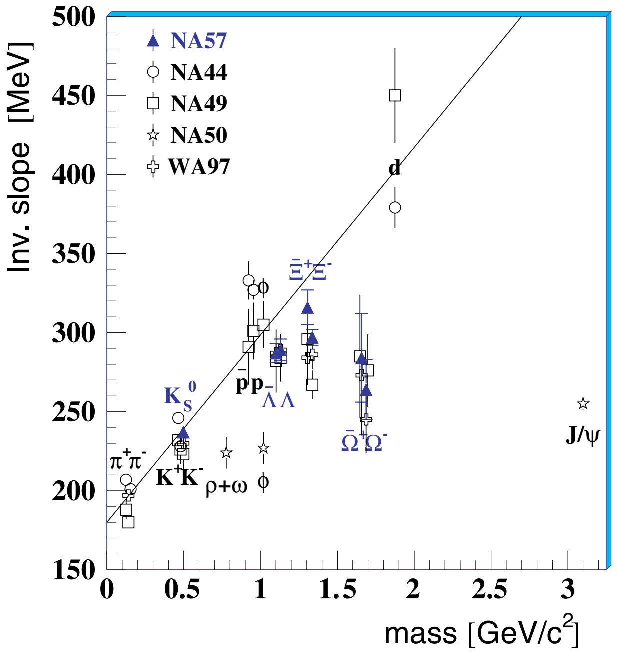

Figure 1.7: *Inverse slopes as functions of the particle rest mass in Pb–Pb interactions at 158 AGeV/c. Only statistical errors are shown. The line through π, K and proton is shown to guide the eye (see [16] and references therein).*

$const$). The temperature (T) is interpreted as due to the thermal motion coupled with a collective transverse flow of the fireball components assumed to be in thermal equilibrium. In the non-relativistic regime ($p_T << m$), T can be approximated by the expression $T_{slope} \simeq T_{fo} + m < \beta_T >^2$, while in the relativistic regime ($p_T >> m$) T is better described as $T_{slope} \simeq T_{fo}\sqrt{1+ < \beta_T > /1- < \beta_T >}$, T_{fo} and $< \beta_T >$ being the thermal freeze-out and the mean velocity of the collective transverse expansion (*flow*). Consequently, for a given species (fixed m), temperature and flow cannot be separated. The blast-wave model describes successfully the m_T spectra and is used to disentangle the two contributions [18], through the following parametrization:

$$\frac{dN}{m_T dm_T dY} \propto m_T K_1(\frac{m_T cosh\rho}{T}) I_0(\frac{p_T sinh\rho}{T}) \ , \tag{1.13}$$

[3]The J/ψ spectra were fitted using the modified Bessel function $1/T \cdot m_T^2 \cdot K1(m_T/T)$; this yields a transverse slope $T = 255 \pm 4$ MeV for the most central collisions, which is 5–10 MeV smaller than the one obtained with the exponential function [17]. See also section 1.7.3.

where $\rho = \tanh^{-1}\beta_T$.

One notices that the inverse slopes of the Ω hyperon and of Ξ fall below the line drawn through the π, K and proton points. These hyperons, while having two and three units of strangeness, have smaller interaction cross sections in the hadron gas, as compared to other hadrons. These particles should decouple earlier from the hadron gas, and therefore be less affected by the transverse collective flow, which would explain their low effective temperature [20]. Also, ϕ, $\rho + \omega$ and J/ψ inverse slopes are steeper than expected [19, 17].

Going for a while beyond the thermalization subject, the ϕ one is particularly puzzling, since the NA49 Collaboration measures T_ϕ=305$\pm$ 15 MeV [21], while the NA50 Collaboration measures T_ϕ=216$\pm$ 15 MeV , both in the same transverse mass range (1.5–2.4 GeV/c^2) [22]. Furthermore, the two experiments measure ϕ yields that differ by factors between 2 and 4 in the common m_T interval. The fact that NA49 measures the ϕ resonance in the hadronic K^+K^- decay channel, while NA50 measures it in the dilepton $\mu^+\mu^-$ one, could explain the observed discrepancy based on the same arguments used for hyperons. Also a modification in the measured branching ratios, as reflecting changes in the ϕ meson properties, is expected and may constitute a signal of the chiral symmetry restoration. However, some authors argue that this hypothetical effect is not sufficient to describe the data [23]. Hopefully CERES Collaboration (NA45), which upgraded spectrometer is also suitable to study the vector meson in its K^+K^- decay channel, will be able to solve the puzzle [25]. More details on ϕ production are given in section 1.4.

Assuming QGP formation in the initial state of heavy ion collisions one expects that the thermal nature of the partonic medium could be preserved during hadronization. Consequently, the particle yields measured in the final state should resemble a thermal equilibrium population [26, 27]. One of the most successful tests of chemical and thermal equilibrium is given by the description of particle yields by statistical thermal models. Hadron multiplicities produced in central A–B collisions at AGS [4], SPS and RHIC energies can be quantitatively described by a grand-canonical partition function assuming a system in thermal and chemical equilibrium at the point of hadro-chemical freeze-out. Figure 1.8 shows the fits results for central Pb–Pb collisions at 158 GeV per nucleon, the chemical freeze-out temperature, T_{ch} and the barionic chemical potential, μ_B, being free parameters [26, 27]. The obtained values for T_{ch} and μ_B are 170$\pm$5 MeV and 255$\pm$10 MeV, respectively. It is remarkable that the extracted chemical freeze-out temperature is consistent, within errors, with the critical temperature $T_c = 173 \pm 8$ MeV determined in the framework of lattice QCD. Such an agreement indicates that chemical equilibrium is not caused by kinetic re-scattering. Thus, the observed hadrons seem to proceed by statistical hadronization from a pre-hadronic state of deconfined quarks [28].

Thus, it seems that the necessary conditions to form the Quark-Gluon Plasma in the laboratory at SPS are met. The remaining question is: are we able to detect it?

[4] Brookhaven National Laboratory's Alternating Gradient Synchrotron

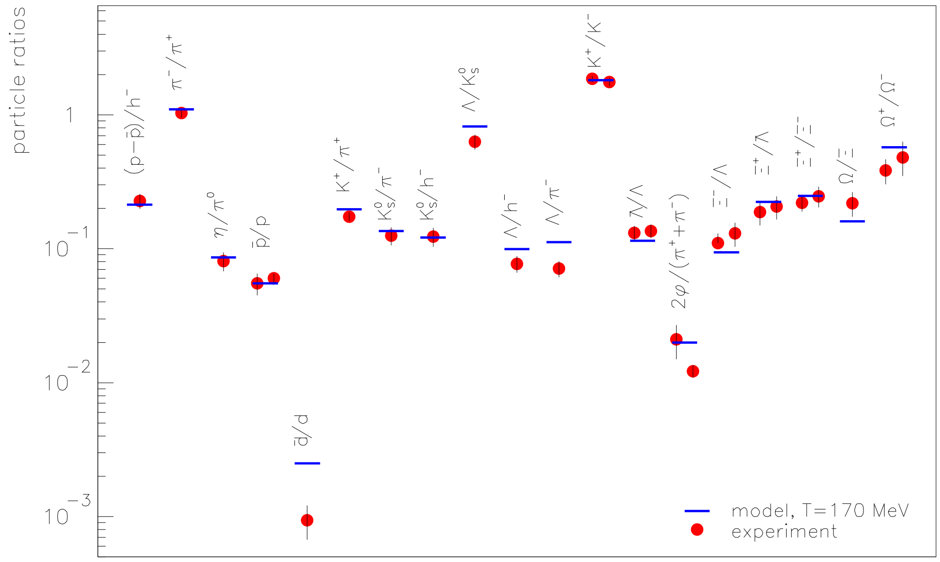

Figure 1.8: *Comparison between thermal models predictions and experimental particle ratios for Pb–Pb collisions at 158 GeV/nucleon. Thermal model calculations are obtained with T = 170 MeV and μ_B = 255 MeV (from [27]+reanalysis in 2003 with more data).*

Which signatures can we take as a probe for QGP formation? In the following sections an overview of the QGP search, particularly at the SPS, is presented.

1.3 Thermal photons and dileptons

Direct photons, as well as dileptons, are an important tool to look for QGP formation. Once produced, they interact with the surrounding matter only electromagnetically, resulting in a long mean free path. Thus, photons and dileptons can escape from the system immediately after production, storing in memory the history of the early stages of the collisions.

The measurement of prompt photons is challenging due to the huge background from π^0 and η decays. The WA98 Collaboration has reported an observation of direct photon excess production in ultra-relativistic heavy ion collisions [29] (figure 1.9). The direct photon excess for central Pb–Pb collisions is calculated as:

$$\nu_{excess} = (1 - \nu_{bkg}/\nu_{meas}) \cdot \nu_{meas} \ . \qquad (1.14)$$

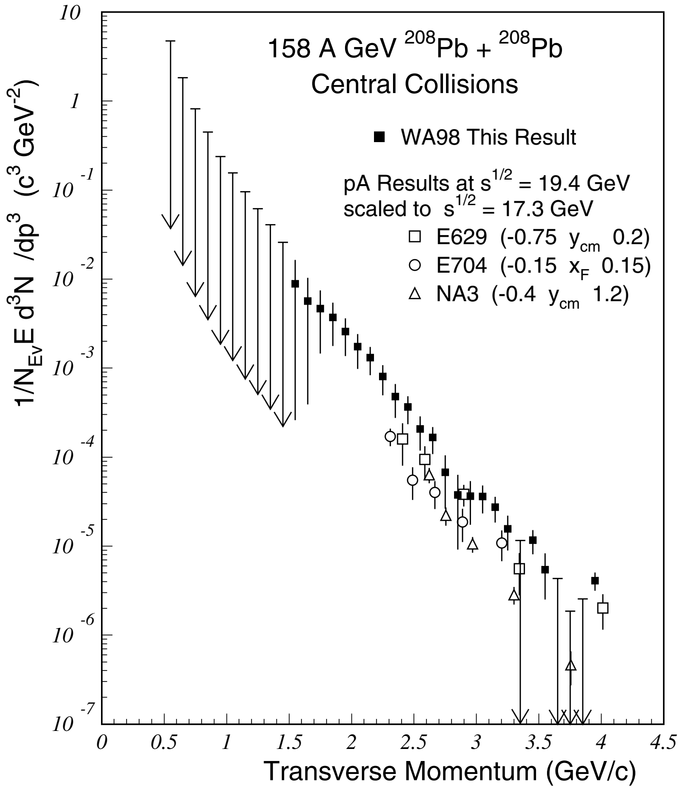

Figure 1.9: *The invariant direct photon multiplicity for central 158 AGeV Pb–Pb collisions. The error bars indicate the combined statistical and systematic errors. Data points with downward arrows indicate unbounded 90% C.L. upper limits. Results of several direct photon measurements for proton induced reactions have been rescaled to central Pb–Pb collisions for comparison (from [29]).*

While peripheral Pb–Pb collisions do not show any significant excess, the most central interactions exhibit a clear excess of prompt photons for $p_T > 1.5$ GeV/c. For comparison purposes, the p–A interactions at 200 GeV, properly rescaled to 158 GeV, are also shown. One observes that the direct photon production excess in central Pb–Pb collisions stands beyond the expected from proton-induced reactions up to very high p_T.

CERES Collaboration (NA45) has observed the enhancement of low mass e^+e^- pairs ($m_{ee} > 0.2$ GeV/c^2) relatively to the expected yield from hadron decays [24]. Particularly, the decay of the ρ meson in e^+e^- pairs is pointed as a hint of chiral symmetry restoration. Due to its short lifetime (1.3 fm/c), the e^+e^- spectrum in the intermediate ρ range is dominated by decays within the hot and dense medium, thus reflecting its properties. Once more, the study of e^+e^- pairs is very difficult due to its ρ small branching ratio into leptons and to the large background contribution to the mass spectrum in ultra-relativistic heavy ion collisions. Figure 1.10 shows the preliminary invariant mass spectrum of e^+e^- pairs emitted in 158 GeV/nucleon Pb-Au collisions, from the 2000 run. The enhancement of the experimental data compared to the hadron *cocktail* in the mass range $m_{e^+e^-} >$ 200 MeV/c^2 is 3.1 ± 0.3 (*stat*). On the right, it is shown that only the modification of ρ properties allows to reproduce the data. Two main approaches are possible. The first one invokes the decrease of the ρ mass as a precursor of chiral symmetry restoration. It transfers most of the ρ strength to the low-mass region. The second one is the broadening of the ρ meson spectral shape within the dense hadron matter, transferring the yield to both lower and higher masses [30]. Unfortunately, the errors level does not allow disentangle the two different scenarios.

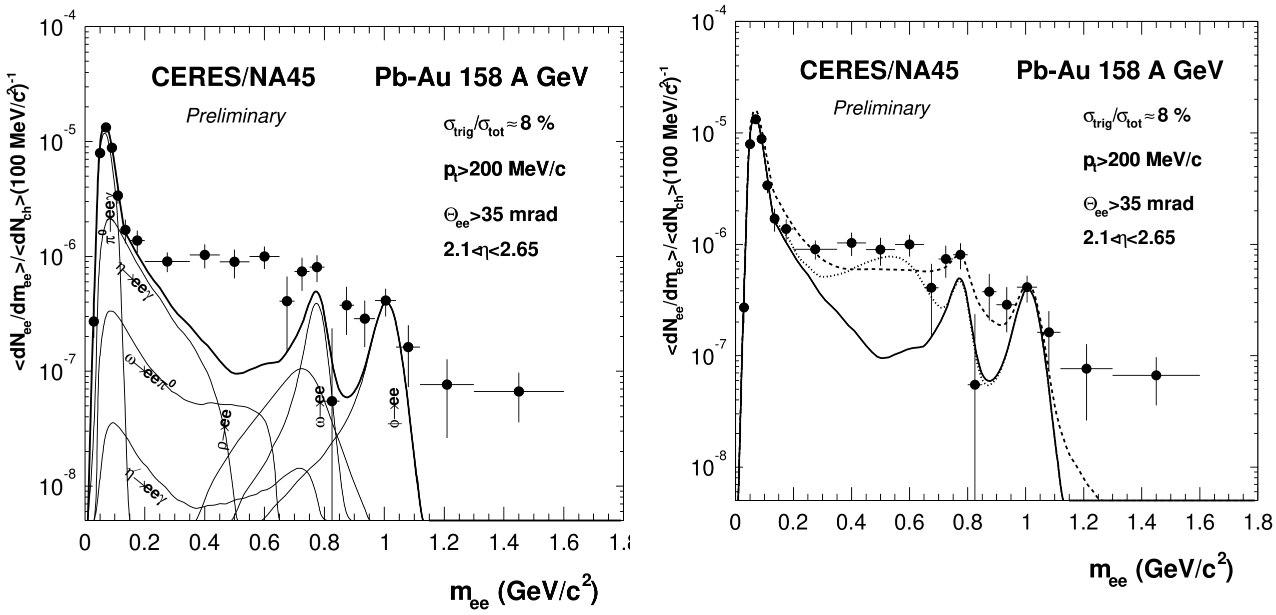

Figure 1.10: *The invariant mass spectrum of e^+e^- pair emitted in 158 GeV/nucleon Pb-Au 2000 collisions (left). Comparison of the experimental data with models invoking decrease of ρ mass (dotted line) and in-medium broadening of ρ mass (dashed line) (right) (from [30]).*

The NA38/NA50 experiments have observed an excess of the dimuon yield in the continuum mass interval between the ϕ and the J/ψ, known as the intermediate mass region, IMR [31]. While in p–A collisions the dimuon mass spectrum in the mass range 1.5≤ $M_{\mu\mu}$ ≤2.5 GeV/c^2 is well reproduced by a superposition of Drell-Yan and open charm decays into muons, a linear extrapolation from p–A yields to A–B collisions underestimates this mass region data. The nature of this excess, behaving like open charm, is not known. Figure 1.11 shows the ratio between the measured data over expected sources. The excess increases roughly linearly with N_{part}, reaching a factor of ∼2.1 for central Pb–Pb collisions [32]. Several models have been proposed to explain it. While a D-meson re-scattering model [33], described by a thermal distribution depending on a temperature parameter T, does not reproduce the experimental mass distribution, as can be verified in figure 1.12 (middle), other models seem to be more successful. One pro-

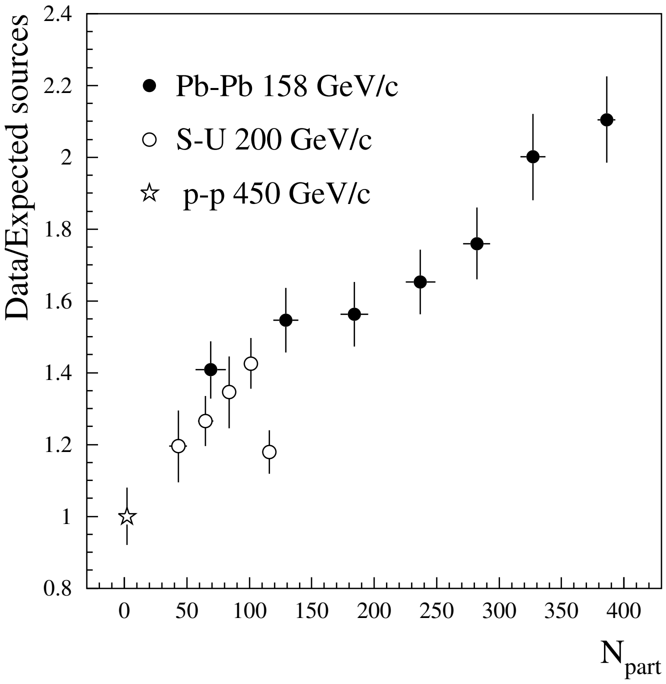

Figure 1.11: *The ratio data over expected sources as a function of the number of participants.*

poses that the observed excess is due to an enhancement of the charm component [34]. To quantify this enhancement, the IMR mass spectra have been described as a superposition of DY and $D\bar{D}$ and fitted leaving free their normalizations. Figure 1.12 (left) shows the fit result. Thermal dilepton models associate the excess to thermal dimuon production from an expanding fireball. The right panel of fig 1.12 shows the result from an analysis based on one of these models [35] for central Pb–Pb collisions. The $D\bar{D}$ normalization is deduced from the $D\bar{D}$/DY proton ratio and the thermal yield is given by the model. The IMR production can be well accounted for thermal radiation when combined with the expected DY and $D\bar{D}$ productions. A specifically devoted measurement performed by the NA60 experiment [36], successor of NA50, should be able to distinguish between these last two possible explanations.

1.4 Strangeness enhancement

Strangeness enhancement has been proposed as a signature for the QGP formation [37]. While in an hadronic scenario, the production of particles containing strange quarks is suppressed relatively to the ones composed by u and d quarks only, in a QGP environment the threshold to produce $s\bar{s}$ is low, since s-quark mass is reduced to the current m_s, predicted to be between 80 and 155 MeV [38], so the maximum energy to form an $s\bar{s}$ pair is only $2m_s \sim 300$ MeV. Besides, the strange quark pairs production is favoured in a

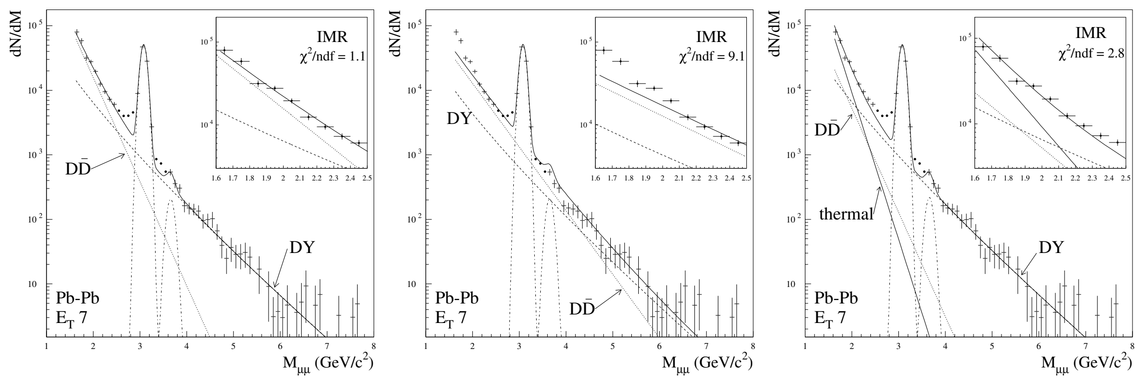

Figure 1.12: *Dimuon mass spectrum from central Pb–Pb collisions (N_{part} $\simeq$380) compared with the prediction of different models: enhancement of charm production (left), D–mesons re-scattering (middle) and thermal dimuon production (right) [32].*

gluon rich QGP environment, predominantly through gluon-gluon interactions. However, the strangeness enhancement is also expected in a hadronic scenario, where the relative abundance of strange particles may increase in a chain of re-scattering processes.

WA97 and its successor NA57 experiments have measured enhanced production of particles with S(Λ)=–1, S(Ξ)=–2 and S(Ω)=–3. The enhancement is defined by the ratio of the hyperon yields in Pb–Pb collisions to the observed yield in p-Be collisions. Both hyperon yields are normalized by the number of participating nucleons in the collision. Figure 1.13 shows the enhancement as a function of the number of participants ($N_{<wound>}$) at 158 AGeV/c. Particles having at least one valence quark in common with the nucleon (that is, particles that could take at least one quark from the projectile or the target) are shown on the left. Particles having no valence quarks in common with the nucleon, i.e., formed only by antiquarks or just by s-quarks, are shown on the right. The results show an enhancement increasing with the strangeness content of the hyperon, up to a factor of 20 for Ω. Furthermore, in Pb–Pb collisions, a significant centrality dependence of the yields per wounded nucleon for all hyperons is seen, with exception for $\bar{\Lambda}$ [39].

The NA50 experiment has measured ϕ production with respect to the yields of the non-strange resonances, ρ and ω [22]. The ϕ vector-meson is a $s\bar{s}$ bound state, produced through a 3 gluon process, (i.e., a very unlikely α_s^3 process), and its enhancement was also proposed as QGP probe [40]. In such a gluon rich medium provided by heavy ion

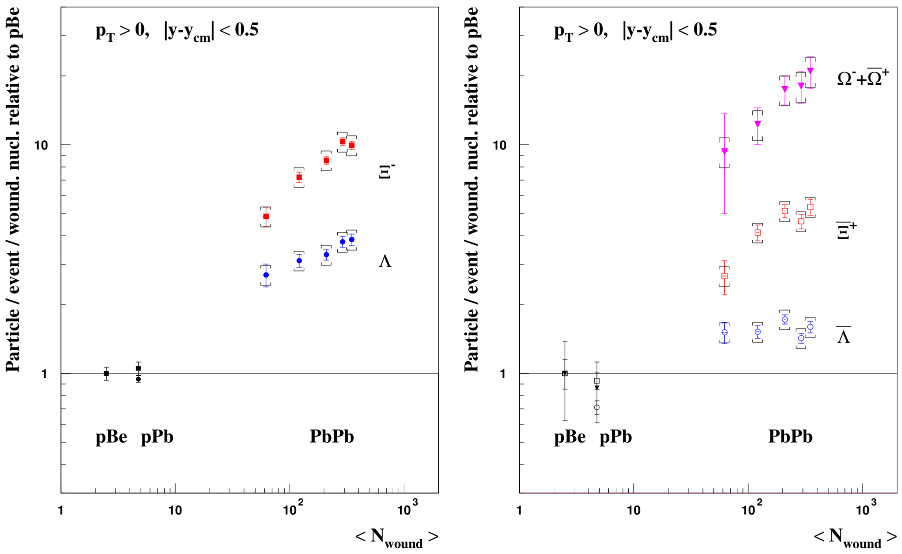

Figure 1.13: *Hyperons enhancement as functions of the number of participants at 158 AGeV/c. The symbol ⌷ stand for the systematic errors. From [39].*

collisions, the enhancement arises from the break of the OZI rule, which inhibits the ϕ production in p-p and π–p collisions. Among the most significant NA50 results on this subject stands the continuous enhancement of the ϕ with respect to $\rho+\omega$ [5] against the number of participating nucleons in the collision, N_{part}, shown in figure 1.14 (left panel). Regarding the same centrality, the cross section ratios increase is not dependent on the size of the interacting nuclei and the continuous trend observed in Pb–Pb collisions seems to saturate at N_{part} ~250. On the right panel the $\phi/(\rho+\omega)$ ratio exhibits an increase, dependent on the size of interacting nuclei, but remaining constant with the dimuon p_T.

1.5 Jet quenching

High energy partons propagating through matter are predicted to lose energy via induced gluon radiation, with the total energy loss strongly dependent on the colour charge density of the medium. The hard scattering and subsequent fragmentation of partons generates jets of correlated hadrons. Jets may be studied via observables such as high transverse momentum hadronic inclusive spectra and correlations. Figure 1.15 (left panel) shows the $< N_{binary} >$–scaled ratio of particle yields in central relative to peripheral collisions, R_{CP}. The observed suppression factor of 5 in central collisions was shown to be independent of p_T for $6 < p_T < 12$ GeV/c. The curves are theoretical model comparisons: two models based on pQCD incorporating shadowing, the Cronin effect and jet quenching in dense matter (pQCD-I, pQCD-II) and a model incorporating gluon saturation in the incoming

[5] The experimental resolution of 70 MeV does not allow disentangle of the ρ and ω resonances.

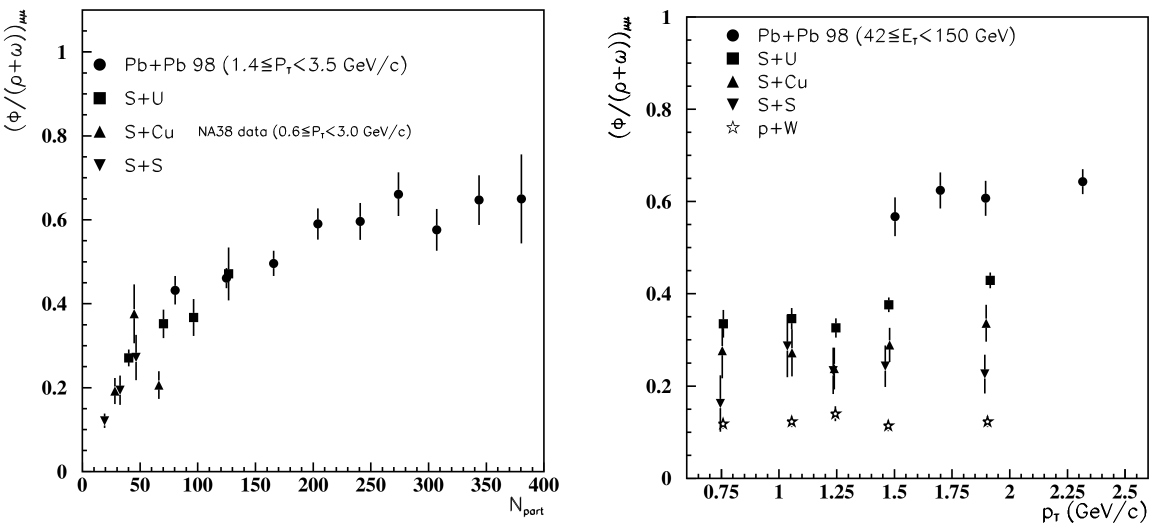

Figure 1.14: *The of $\phi/(\rho+\omega)$ as a function of N_{part} (left) and p_T (right). From [41].*

Au nuclei. Similarly, suppression of high p_T hadron production has been observed at RHIC in central Au–Au collisions relative to p–p collisions [42]. These behaviours have been interpreted as energy loss of the energetic partons crossing the produced hot and dense medium.

Besides this strong suppression, direct evidence that back-to-back dijet quenching depends on the azimuthal orientation of the jets relative to the reaction plane has been observed. Figure 1.15 (right panel) shows the azimuthal distribution of charged hadrons at 2 GeV/c $< p_T < p_T^{trig}$ relatively to a trigger particle with $4 < p_T^{trig} < 6$ GeV/c for p-p collisions at $\sqrt{s}$=200 GeV. This distribution exhibits an enhancement around $\Delta\phi \sim 0$, which is typical of jet production, and around $\Delta\phi \sim \pi$, typical of dijets events. Also azimuthal distributions from mid-central Au-Au collisions for particles within the reaction plane ($|\phi| < \pi/4$) and out-of-plane ($|\phi| > \pi/4$) are shown [6]. Au-Au results show a relative suppression in the away-side region, which is stronger in out-of-plane direction. The observed suppression is consistent with the jet quenching scenario, where fast partons or their hadronic fragments lose energy due to interactions with the medium [43].

1.6 Saturation of the gluon density The Colour Glass Condensate theory of QCD

At high energy (or small values of Bjorken x) gluons are the most abundant partons. When the saturation scale Q_s, corresponding to the gluon density per transverse unit area, becomes large ($Q_s \gg \Lambda_{QCD}$), the coupling constant α_s becomes weak ($\alpha_s \ll 1$),

[6] $\Delta\phi$ is the particle azimuthal angle with respect to the trigger particle and ϕ is the particle azimuthal angle with respect to the reaction plane.

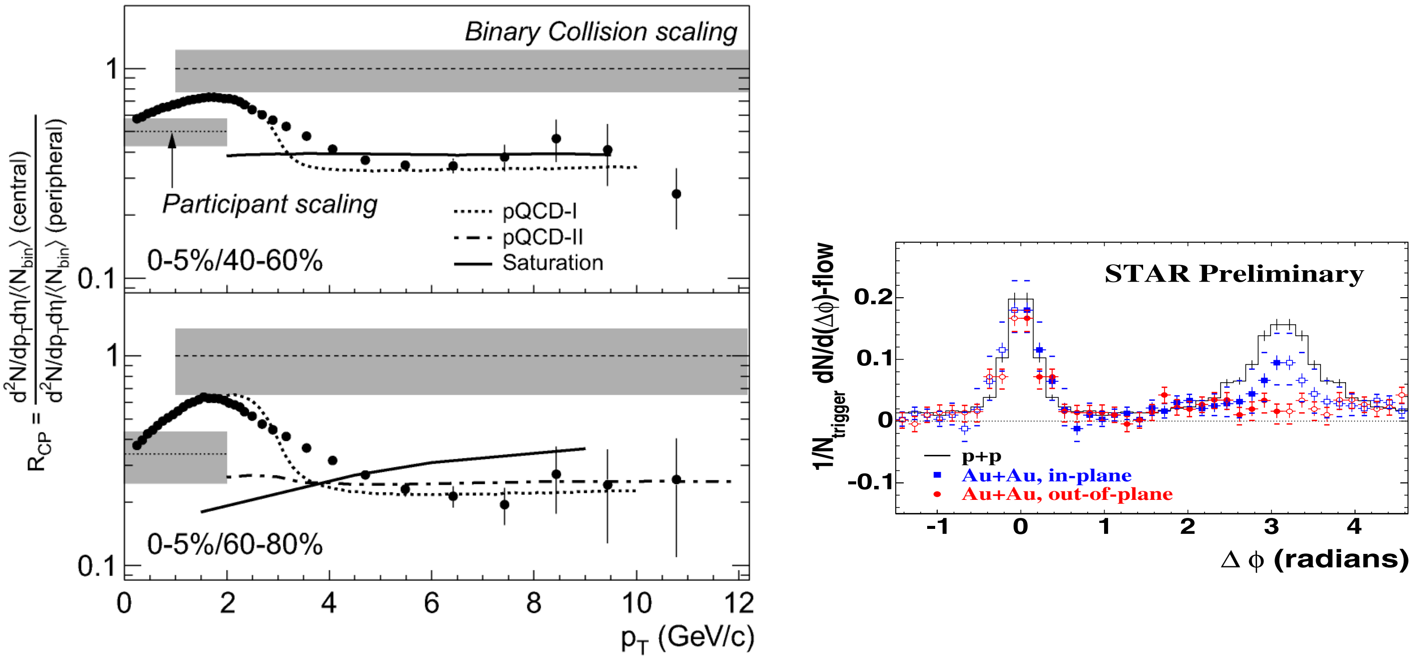

Figure 1.15: *The $< N_{bin} >$–scaled ratio of hadron yields in central Au-Au to peripheral Au-Au collisions, R_{CP}, for two centrality classes as a function of p_T. The curves are theoretical model comparisons (left). The azimuthal distributions of the associated particles, corresponding to trigger particles in-plane and out-of-plane for Au-Au collisions at centrality 20–60%, are compared with p+p reference data (right histogram).*

which suggests that the high energy limit of QCD may be studied using weak coupling methods. This feature is formalized in terms of an effective theory of QCD, the Colour Glass Condensate [44]. The CGC can be probed in deeply inelastic scattering, in photo-production in peripheral heavy ion collisions, in p–A collisions and in heavy ion collisions (see [45] and references therein).

Identified hadron transverse mass spectra measured in Au–Au collisions at $\sqrt{s}$=130 AGeV follow a scaling law, which may be interpreted as a consequence of the gluon saturation [45]. The transverse momentum spectra are well described as a function only of the transverse mass and are parametrized as

$$\frac{1}{\sigma}\frac{dN_h}{dyd^2m_T} = \frac{1}{\alpha_s(p_s)}k_h \cdot f(\frac{m_T}{p_s}) \ , \tag{1.15}$$

where σ is the transverse area of the two colliding nuclei, $m_T = \sqrt{m_h^2 + p_T^2}$ and k_h is a constant which reflects the difference in abundances of various species of particles. The function f depends on m_T and the corresponding saturation scale for hadrons, the latter being determined by the energy and centrality of the collision. If all hadrons are described by only one function of the transverse mass, their spectra should then result in one single curve. This feature is found in figure 1.16 (left plot), which shows minimum bias data of the PHENIX Collaboration for charged pions, kaons, protons and antiprotons, as well as neutral pions, as a function of m_T. Curves for kaons and protons are shifted downwards and upwards, respectively, due to the different strangeness and baryon numbers, which are not taken into account in the universal–m_T scaling relation. The production of strange particles is suppressed due to the s–quark mass, while the number of protons is enhanced due to the initial baryon number excess coming from the two colliding nuclei. The constant k_h accounts for these effects, so shifting the proton curve up by a factor of ∼2 while shifting the kaon curve down by a factor of two from the universal curve, as can be seen in the right plot.

Still in the RHIC physics framework, this theory has been also successful in the de-

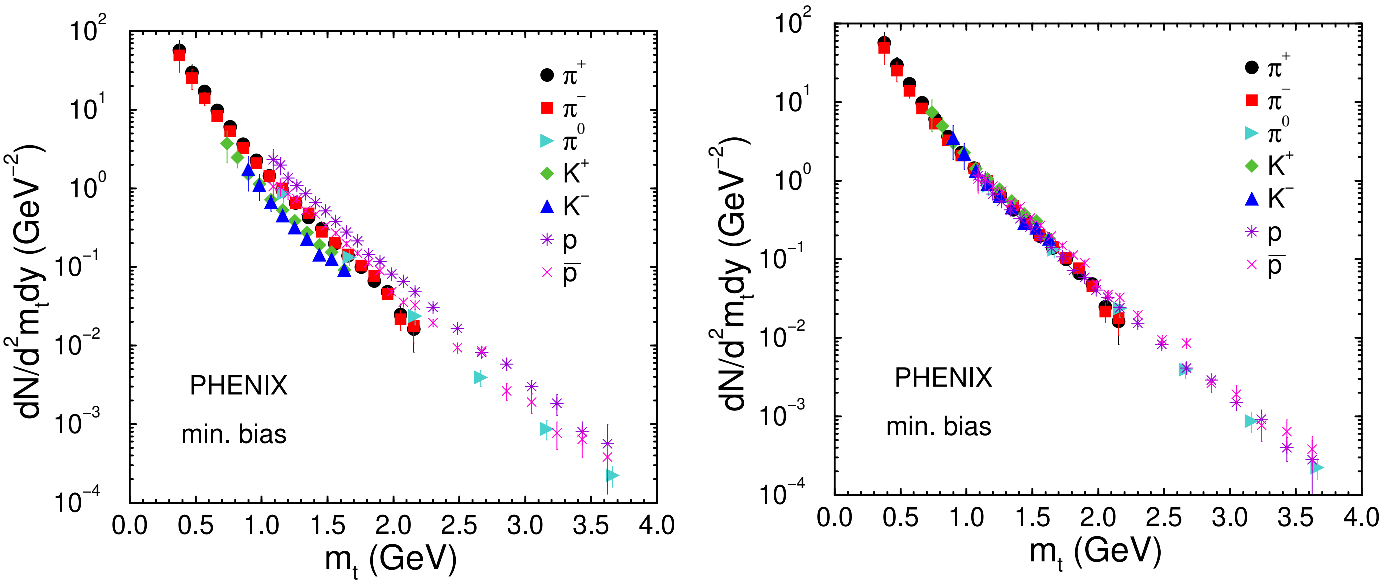

Figure 1.16: *Left plot: preliminary transverse mass spectra of identified hadrons for minimum bias Au–Au collisions as measured for $\sqrt{s}$=130 AGeV at RHIC; right plot: the same transverse mass spectra where the proton and kaon/antkaon data points are multiplied by 1/2 and 2, respectively. (From [45] and references therein).*

scription of the centrality dependence of the suppression of the negatively charged hadron spectra in the forward-rapidity region of d–Au collisions [46].

1.7 Charmonia suppression

Among the probes of QGP formation, the charmonium states play a central role. In 1986, Matsui and Satz [47] predicted the suppression of the J/ψ vector-meson via Debye screening of the quark colour potential [48]:

$$V_0(r) \simeq \sigma r \quad \longrightarrow \quad V(r) \simeq \sigma r \Big[\frac{1-\exp(-\mu r)}{\mu r}\Big] \tag{1.16}$$

where σ is the confinement string tension and μ is the colour screening mass, being the inverse of the screening radius r_D. The exponential term removes all long range effects (see figure 1.17). Due to the large mass of the c quark, charmed mesons are predominantly

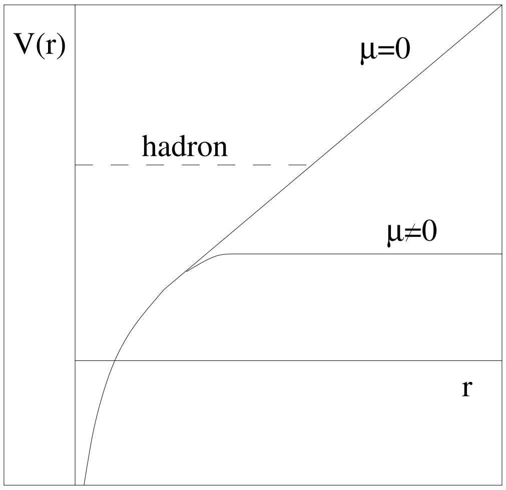

Figure 1.17: *Colour screening of the confining potential [48].*

produced in the early hard scattering processes. However, in a deconfined medium the screening radius, r_D, becomes smaller than the binding radius, r_H, of the heavy quark system, preventing quarks from being together and hence to form quarkonium states ($J/\psi, \psi', \chi_c, \Upsilon, \Upsilon'$). In this case, the two quarks fly apart and in the hadronization phase they will find a lighter partner like u or d to form open charm (beauty) mesons.

The most general model for charmonium (bottonium) production is the colour evaporation model [49]. Here the description of quarkonium yields is equivalent to the open heavy quark production except for the restriction of the heavy quark pair invariant mass in the quarkonium case. For charmonia, the upper limit on the $c\bar{c}$ pair is $2m_D$=3740 MeV. The quarkonium yield results from the annihilation of $q\bar{q}$ and the gg fusion mechanisms. The cross section is then a convolution of the $q\bar{q}$ and gg partonic cross sections with the projectile and target partonic densities. One feature of this model is the postulate that the different charmonium states cross sections are simply fractions of the total $c\bar{c}$ cross section:

$$\sigma_i(s) = c_i \sigma_{c\bar{c}}(s), \qquad i = J/\psi, \psi', \chi_c \; . \tag{1.17}$$

For each state, c_i is constant and accounts both for direct and indirect production. As an example, J/ψ includes its direct production and also its feed down through the radiative decay of χ_c and the hadronic decay of ψ'. As a consequence, the ratios of different charmonium production cross sections are energy-independent. This assumption is very well satisfied by the experimental results on J/ψ production from χ_c and ψ' decays [50]: $\sigma_{\chi_c}/\sigma_{J/\psi} \simeq 0.4$ and $\sigma_{\psi'}/\sigma_{J/\psi} \simeq 0.14$.

Lattice QCD calculations for the finite-T free energy of a heavy quark pair with dynamical quarks is shown in figure 1.18 [5]. The decrease of the asymptotic plateau value is interpreted as the reduction of $D\bar{D}$ threshold due to medium effects (increasing temperature) in the heavy quark potential. Such a decrease establishes the several temperature thresholds beyond which a charmonium (bottonium) state cannot exist [51]: for the J/ψ this value is $T \simeq 1.2\ T_c$. For higher excited states, due to their lower binding energies, $E^i_{dis} \equiv 2m_D - m_i$, the temperature is even lower than T_c: $T \simeq 0.74\ T_c$ for χ_c and $T \simeq (0.1$ or $0.2)\ T_c$ for ψ'. As a consequence, a sequential suppression pattern of the J/ψ is expected. Nevertheless, only the suppression of directly produced J/ψ requires the onset of deconfinement. The higher excited charmonium states dissociate already before T_c through their decays into open charm. Such decays become possible because the open charm threshold in a hot confined medium decreases with temperature faster than the masses of the corresponding quarkonium states.

Recent J/ψ and η spectral functions calculated with the maximum entropy method (MEM) suggest that J/ψ persist in a deconfined phase as well-defined resonance up to temperatures of $T \simeq 1.5 - 1.9\ T_c$ [52, 53] (figure 1.18, right panel).

Table 1.1 reports pertinent characteristics of the charmonium states.

state	$J/\psi(1S)$	$\chi_{c1}(1P)$	$\psi'(2S)$
mass (MeV)	3096.87 ± 0.04	3510.51± 0.12	3685.96± 0.09
full width (KeV)	87 ± 5	920 ± 130	300 ± 25
Branching ratio	$\mu^+\mu^-$ (5.88±0.10)%	J/ψ (31.6±3.2)%	J/ψ (55.7±2.6)% $\mu^+\mu^-$ $(7.0\pm0.9)\times10^{-3}$
μ_D (GeV)	0.68	0.35	0.35
$E^i_{dis} \equiv 2m_D - m_i$ (GeV)	0.64	0.20	0.05
T_D/Tc	1.2 (1.5—1.9)	0.74	0.1—0.2

Table 1.1: *Charmonia characteristics values [38, 51].*

1.7.1 Charmonia suppression studies in NA50 experiment

The study of charmonium production was started in 1986 by the NA38 experiment at CERN SPS. An extensive experimental program was pursued using 450 GeV/c proton beams colliding on different targets and beams of oxygen and sulphur ions accelerated at 200 GeV per nucleon. The charmonium states J/ψ and ψ' were identified through their dilepton decay channel, by means of a 18 meters long muon spectrometer. But not only muons from charmonia decaying were identified. The acceptance covered by the apparatus also allowed the detection of ϕ, ρ and ω mesons, as well as the continuum formed

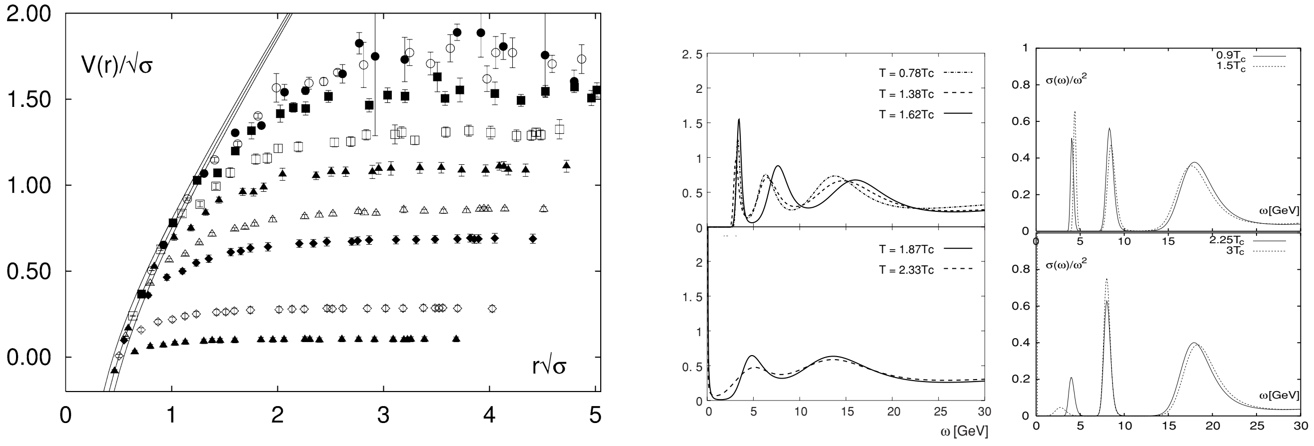

Figure 1.18: *Left: Temperature dependence of the heavy quark potential for three flavour QCD with a quark mass m_q=0.1. The band of lines gives the Cornell-potential in units $\sqrt{\sigma}$. The temperatures corresponding to the different data sets are T/T_c=0.58, 0.66, 0.74, 0.84, 0.9, 0.94, 0.97, 1.06 and 1.15 (from top to bottom) [5]. Right: Thermal vector spectral functions (J/ψ) from MEM analyses of meson correlation functions calculated in quenched QCD on anisotropic and isotropic lattices.*

by the semi-leptonic decays of charmed mesons, $D\bar{D}$, and the Drell-Yan pairs up to 7 GeV/c^2. This last contribution was particularly important to measure charmonia suppression because it constitutes a reference process with a probability depending linearly on the number of nucleons of both target and projectile.

NA50 proposed in 1994 the study the charmonia suppression in induced Pb–Pb interactions. In this new framework, conditions to form QGP are much better than with lighter ions, because of the much larger volume and number of participating nucleons involved. These features have favoured thermalization of the medium and increase the lifetime of a possible QGP. Figure 1.19 shows the ratio $B_{\mu\mu}\sigma(J/\psi)/\sigma(DY)$ as a function of the transverse energy, E_T, for the collected Pb–Pb data samples – 1995 [54, 55], 1996 [56] and 1998 [57]. The closed points are the results obtained with the standard analysis method, while the open points are the 1996 and 1998 results obtained through the Minimum Bias analysis method, as explained in [56, 57]. The continuous line is the J/ψ normal absorption in nuclear matter which fits the NA51 p-p and p-d and the NA38 p–A and S–U results. A clear departure of the $B_{\mu\mu}\sigma(J/\psi)/\sigma(DY)$ ratios from this normal absorption curve is observed at mid-centrality, suggesting the onset of an anomalous J/ψ suppression mechanism. Furthermore, no saturation of the ratio at high E_T is observed, as opposed to the absorption curve trend.

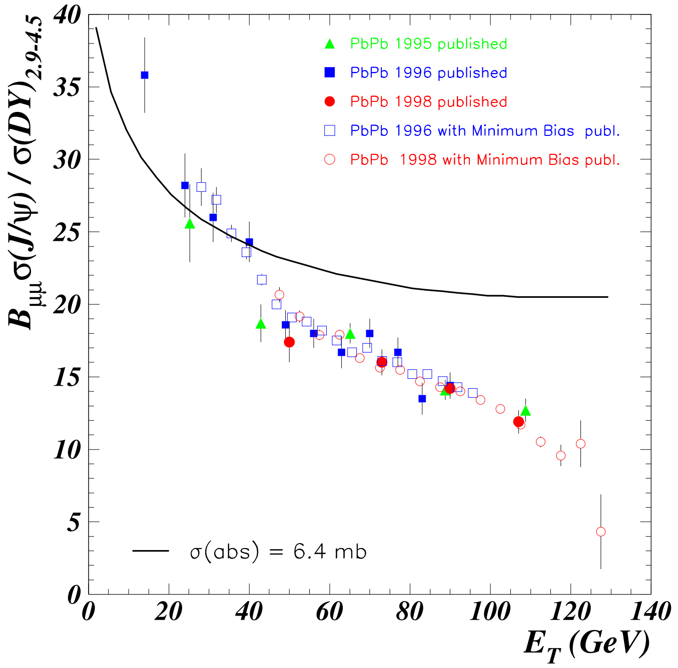

Figure 1.19: *The $J/\psi/DY$ as a function of E_T, for the 1995, 1996 and 1998 data samples. The absorption curve fits the NA38 p–A and S–U results.*

The present work aims the study of J/ψ and ψ' production in Pb–Pb collisions at 158 GeV/c per nucleon at the CERN SPS. A special detailed study will be performed using the 2000 data. These were taken under improved experimental conditions, namely the target region placed in vacuum. The 1998 and 1996 data samples will be also analysed, following the same criteria used for the 2000 one. To achieve such an enterprise, a deep understanding of the continuum is needed, namely which contributions come from the uncorrelated background from π and K decays, as well as from the $D\bar{D}$ mesons and Drell-Yan pairs. As referred, the ψ' production in Pb–Pb collisions will also be studied. This is a challenging task, because the branching ratio in the dimuon channel is much smaller than for J/ψ. On the other hand, one expects that ψ', a more loosely bound state than J/ψ, may also be dissociated at lower energy densities.

1.7.2 Charmonia absorption in p–A and S–U systems

In proton-nucleus collisions, the main purpose is to study the J/ψ production in a medium where the energy density is too low to produce a deconfined quark-gluon phase. Such a study is crucial to interpret the J/ψ yield in a heavier system as Pb–Pb.

In p–A interactions the J/ψ signal is reduced with the increasing target atomic mass number, A. The measured absorption cross section, in the framework of the Glauber model [61], is $\sigma_{abs}^{J/\psi}$=4.4±0.4 mb [62]. The typical interpretation is the following: once the $c\bar{c}$ pair is produced it may undergo inelastic collisions with target nucleons, thus preventing the formation of J/ψ and resulting, instead, in open charm production [59, 60]. Since the J/ψ absorption cross sections for p–A and S–U collisions are compatible within statistical errors, a simultaneous fit has been performed leading to a common value of $\sigma_{abs}^{J/\psi}$=4.3±0.3 mb (see figure 1.20). Thus, together with the S–U collision system, the proton-nucleus studies constitute the baseline to determine the J/ψ suppression in Pb-Pb collisions.

The ψ' also has been studied in lighter systems. A Glauber fit to ψ' absolute cross sections for p–A at 400 GeV/c leads to an absorption cross section of $\sigma_{abs}^{\psi'}$=9.6±1.6 mb [62]. The high accuracy of the NA50 p–A results allows to conclude that ψ' is more absorbed than J/ψ. This observation indicates that the charmonium formation times, relevant for the NA50 kinematic domain, are small enough so that the nuclear matter, on the way of the produced resonances, can distinguish the more loosely ψ' bound state from the J/ψ.

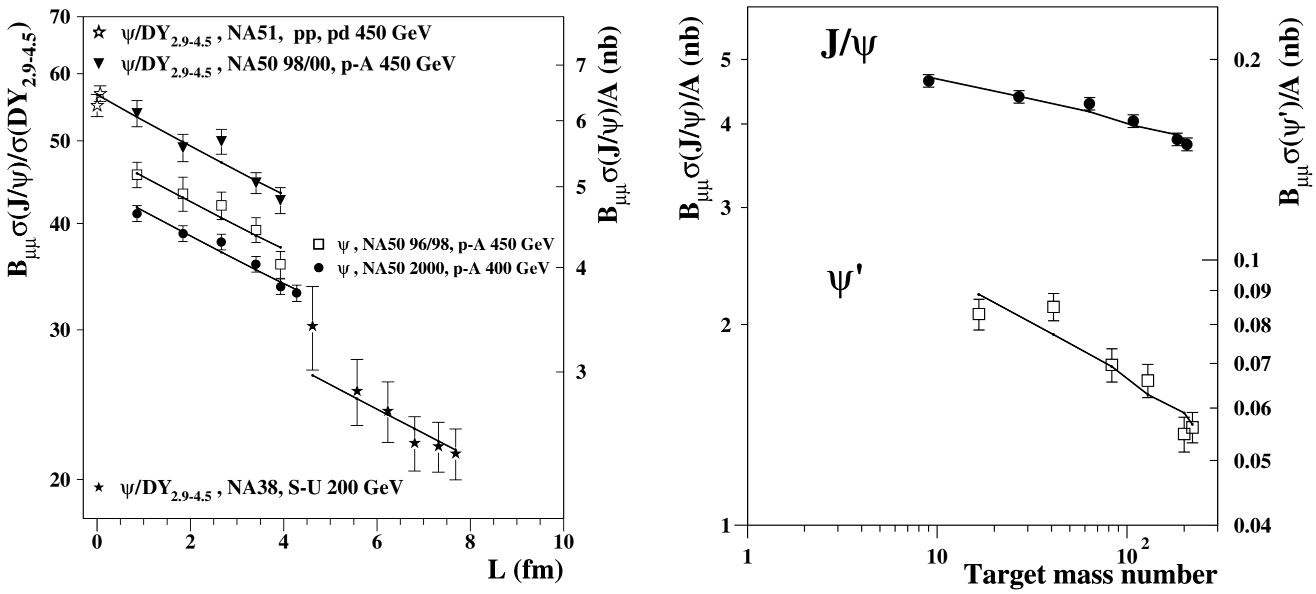

Figure 1.20: *Left panel: $B_{\mu\mu}\sigma(J/\psi)/DY$ (right scale) and $B_{\mu\mu}\sigma(J/\psi)/A$ (left scale) results for NA50 p–A and NA38 S–U data fitted with a common absorption value of $\sigma_{abs}^{J/\psi}$=4.3±0.3 mb. Right panel: Glauber fit to J/ψ and ψ' absolute cross sections for p–A at 400 GeV/c leading to $\sigma_{abs}^{J/\psi}$=4.2±0.5 mb and $\sigma_{abs}^{\psi'}$=9.6±1.6 mb (from [62]).*

1.7.3 Transverse momentum studies

The formation of QGP is expected to induce a change in the J/ψ transverse momentum distributions, increasing $< p_T^2 >$, since high–p_T J/ψ can escape without being suppressed by the plasma ([17] and references therein). Figure 1.21 shows the ratios $R(p_T)$ between the J/ψ p_T distributions for a given E_T region and the lowest E_T region, normalized to the ratio of the corresponding Drell-Yan events. The J/ψ suppression is clearly stronger at low p_T.

The J/ψ transverse mass distributions have also been studied. They were fitted with the analytical function $1/T \cdot M_T^2 \cdot K_1(M_T/T)$, where K_1 is the modified Bessel function and the inverse slope T is interpreted as being the effective temperature of the system in thermal models. The inverse slope T is plotted in figure 1.22 as a function of the energy density, calculated in the framework of the Bjorken model [8]. All data sets have been rescaled to the same beam energy, 158 GeV. For the peripheral Pb–Pb collisions, only the points from data collected in 2000, not biased by Pb–air collisions, are used. One can see that the linear increase of T against ϵ becomes flatter when approaching the most central Pb–Pb collisions, with the slopes changing their values, suggesting an onset at ~2.5 GeV/fm^3.

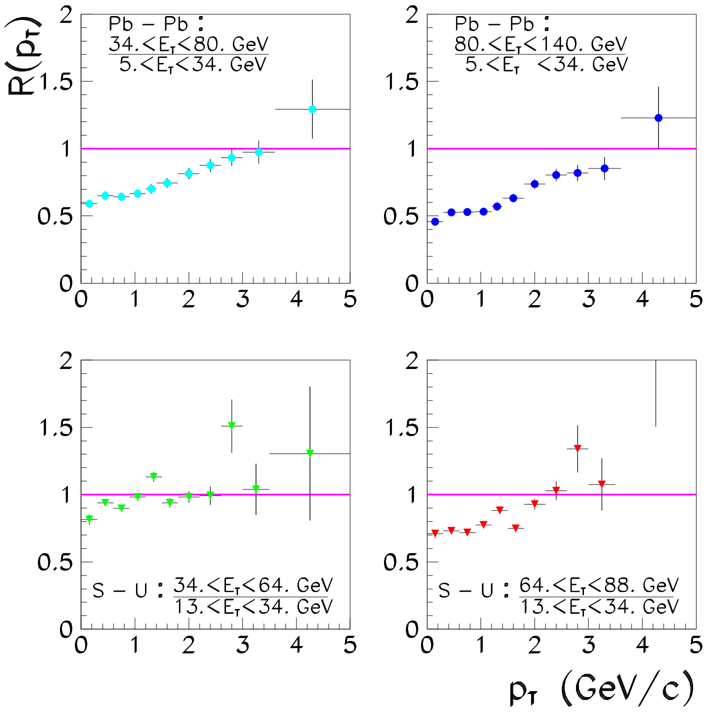

Figure 1.21: *Ratios between p_T distributions of J/ψ corresponding to different centralities for Pb–Pb and S–U [63].*

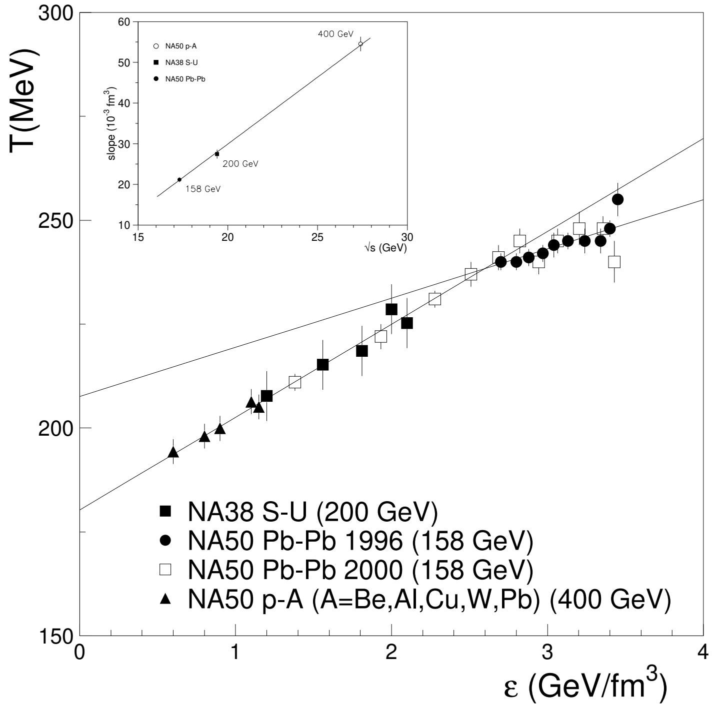

Figure 1.22: *Inverse slope parameter, T, of the J/ψ as a function of the energy density. The lines are linear fits to the data points, all data sets rescaled to 158 GeV. The inset shows the slopes of the linear fits vs $\sqrt{s}$ [64].*

1.8 The Drell-Yan process

At the Born level, the Drell-Yan process is the production of a lepton pair through the annihilation of a $q\bar{q}$ pair into a virtual photon [65]. The partonic cross section is:

$$\frac{d\sigma}{dM^2} = \frac{4\pi\alpha^2}{3M^2} e_q^2 \delta(x_1 x_2 s - M^2) \ , \tag{1.18}$$

where M is the invariant mass of the produced dilepton, α is the fine-structure constant, $\alpha = e^2/4\pi\epsilon_0\hbar c$, and x_1 and x_2 are the projectile and target nucleons momentum fractions carried by partons with charge e_q in a collision of center of mass system energy, $\sqrt{s}$. To obtain the cross section in a hadron-hadron collision as a function of the pair mass, M, and rapidity, y, we must convolute the partonic cross section with the quark and antiquark densities:

$$\frac{d^2\sigma(AB \to \mu^+\mu^-)}{dydM^2} = \frac{1}{3} \cdot \frac{4\pi\alpha^2}{3M^2} \int_0^1 dx_1 dx_2 \delta(x_1 x_2 s - M^2)\delta(y - \frac{1}{2}\ln\frac{x_1}{x_2})$$
$$\times \sum_q e_q^2 [F_q^A(x_1, M^2) F_{\bar{q}}^B(x_2, M^2) + F_{\bar{q}}^A(x_1, M^2) F_q^B(x_2, M^2)] \ , \quad (1.19)$$

where the factor 1/3 takes into account that the quark and antiquark within the pair should share the same colour. After integrating the delta functions to obtain $x_{1,2} = \frac{M}{\sqrt{s}} \cdot exp(\pm y)$, the leading order cross section, evaluated at scale $Q^2 = M^2$, and taking into account that $\sigma_{pp}^{DY} \neq \sigma_{pn}^{DY} \neq \sigma_{np}^{DY} \neq \sigma_{nn}^{DY}$ [7], becomes:

$$\frac{d^2\sigma(AB \to \mu^+\mu^-)}{dydM} = \frac{8\pi\alpha^2}{9M^3} \sum_q e_q^2 \Big[\frac{Z_A}{A} F_q^p(x_1, Q^2) + \frac{N_A}{A} F_q^n(x_1, Q^2) \times \frac{Z_B}{B} F_{\bar{q}}^p(x_2, Q^2) +$$
$$\frac{N_B}{B} F_{\bar{q}}^n(x_2, Q^2) + \frac{Z_A}{A} F_{\bar{q}}^p(x_1, Q^2) + \frac{N_A}{A} F_{\bar{q}}^n(x_1, Q^2) \times \frac{Z_B}{B} F_q^p(x_2, Q^2) + \frac{N_B}{B} F_q^n(x_2, Q^2) \Big] \ , \quad (1.20)$$

where $Z_{A,B}$ and $N_{A,B}$ are the number of protons and neutrons of the projectile and target nuclei and one assumes that $F_d^p = F_u^n$ and $F_u^p = F_d^n$.

When this first order cross section is compared to data, one founds that it fails by a constant factor ∼1.7–2.5, the so-called K_{exp} factor. The values measured by NA38, NA51 and NA50 at beam energies of 158–450 GeV/n for different collision systems, are consistent with $K_{exp} \simeq 1.8$, obtained with Leading Order (LO) calculations, using MRS 43 parton distribution functions from the PDFLIB package [66]. Since the Drell-Yan pairs only interact electromagnetically, an A dependence is not expected because no final-state interactions affect the lepton pair. This means that the Drell-Yan cross section is proportional to the number of nucleon-nucleon collisions, from pp to A–B, as shown in figure 1.23. This process constitutes, therefore, a good reference for the J/ψ and ψ' mesons production.

[7] σ_{pn}^{DY} and σ_{np}^{DY} are the same only at mid-rapidity.

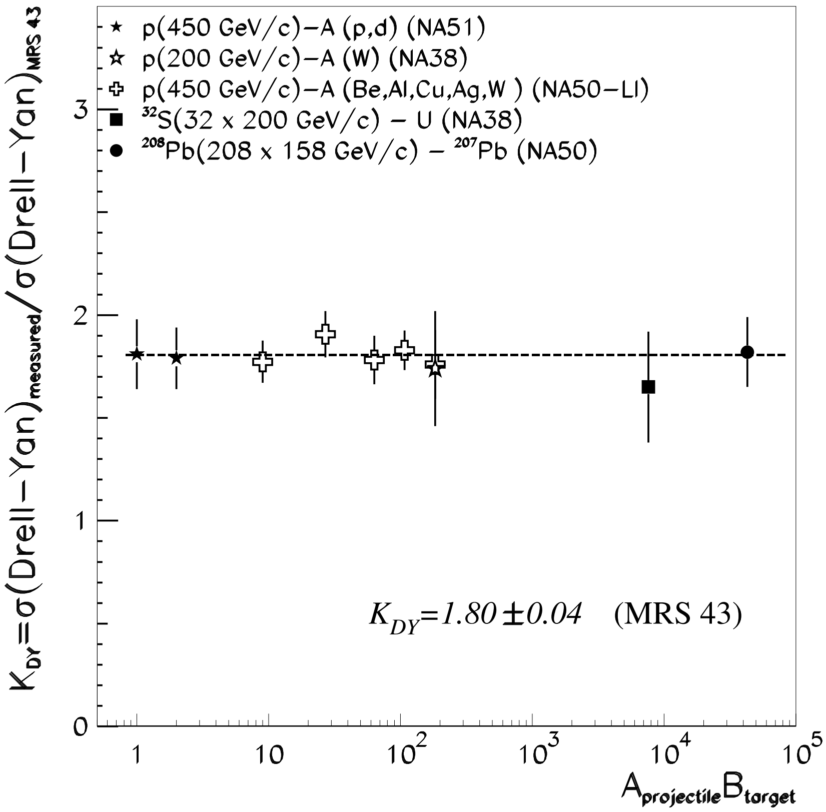

Figure 1.23: *The Drell-Yan K_{exp} factor measured at 158 - 450 GeV/c beam momenta in p–A and A–B collisions. MRS 43 PDF are used in the calculus of cross sections.*

Bibliography

[1] See, e.g., M. Mangano, Introduction to QCD, Lectures of the I CERN-CLAF School of High Energy Physics (2001)

[2] K.G. Wilson, Phys. Rev. D10 (1974) 2445

[3] H. Satz, Nuc. Phys. A400 (1983) 541c

[4] C. Bernard, Phys. Rev. D9 (1974) 3312

[5] F. Karsch, E. Laermann and A. Peikert, Nucl. Phys. B605 (2001) 579

[6] F. Karsch, Quark Matter 2001, in Nucl. Phys. A698 (2002) 199c

[7] G. Baym, Proc. of Quark Matter 1984 (Ed. Springer–Verlag, 1985)

[8] J.D. Bjorken, Phys. Rev. D27 (1983) 140

[9] H. Appelshauser et al. (NA49 Coll.), Phys. Rev. Lett. 82 (1999) 2471

[10] M.C. Abreu et al. (NA50 Coll.), Phys. Lett. B530 (2002) 43

[11] B.B. Back et al. (PHOBOS Coll.), Phys. Rev. Lett. 85 (2000) 3100

[12] K. Adcox et al. (PHENIX Coll.), Phys. Rev. Lett. 86 (2001) 3500

[13] F. Antinori et al. (WA97 Coll.), Eur. Phys. J C18 (2000) 57

[14] M.M. Aggarwal et al. (WA98 Coll.), Eur. Phys. J C18 (2001) 651

[15] M.M. Aggarwal et al. (WA98 Coll.), Phys. Rev. Lett. 81 (1998) 4087

[16] F. Antinori et al. (NA57 Coll.), J. Phys. G: Nuc. Part. Phys. 30 (2004) 823

[17] M.C. Abreu et al. (NA50 Coll.), Phys. Lett. B499 (2001) 85

[18] E. Schnedermann and U. Heinz, Phys. Rev. C50 (1994) 1675

[19] N. Willis et al. (NA50 Coll.), Quark Matter 1999, in Nucl. Phys. A661 (1999) 534c

[20] H. van Hecke, H. Sorge and N. Xu, Phys. Rev. Lett. 81 (1998) 5764

[21] S. V. Afanasiev et al. (NA49 Coll.), Phys. Lett. B491 (2000) 59

[22] B. Alessandro et al. (NA50 Coll.), Phys. Lett. B555 (2003) 147

[23] S.C Johnson, B.V. Jacak and A. Drees, Eur. Phys. J C18 (2001) 645

[24] G. Agakichiev et al. (CERES Coll.), Phys. Rev. Lett. 75 (1995) 1272, Phys. Lett. B422 (1998) 405

[25] A. Marín et al. (CERES Coll.), in J. Phys. G: Nuc. Part. Phys. 30 (2004) S709

[26] P. Braun-Munzinger, K. Redlich and J. Stachel, nuc-th/0304013

[27] J. Stachel, Phys. Lett. B465 (1999) 15

[28] U. Heinz, Quark Matter 1999, in Nucl. Phys. A661 (1999) 140c

[29] M.M. Aggarwal et al. (WA98 Coll.), Phys. Rev. Lett. 85 (2000) 3595

[30] A. Cherlin and S. Yourevich (CERES/NA45 Coll.), Quark Matter 2004, in J. Phys. G: Nuc. Part. Phys. 30 (2004) S1007

[31] M.C. Abreu et al. (NA38/NA50 Coll.), Eur. Phys. J C14 (2000) 443

[32] L. Capelli (NA50 Coll.), Quark Matter 2001, in Nucl. Phys. A698 (2002) 539c

[33] Z.Lin and X.N. Wang, Phys. Lett. B444 (1998) 147

[34] C.Y. Wong and Z.Q. Wang, Phys. Lett. B367 (1996) 50

[35] R. Rapp and E. Shuryak, Phys. Lett. B444 (2000) 13

[36] NA60 Coll., CERN/SPSC 2000-010, Proposal

[37] J. Rafelski and B. Müller, Phys. Rev. Lett. 48 (1982) 1066

[38] Particle Data Book, K. Hagiwara et al., Phys. Rev. D66 (2002)

[39] G.E. Bruno (NA57 Coll.), Quark Matter 2004, in J. Phys. G: Nuc. Part. Phys. 30 (2004) S717

[40] A. Shor, Phys. Rev. Lett. 54 (1985) 1122

[41] C. Quintans (NA50 Coll.), Strangeness in Quark Matter 2001, in J. Phys. G: Nuc. Phys. 27 (2004) 405

[42] J. Adams et al. (STAR Coll.) Phys. Rev. Lett. 91 (2003) 172302

[43] K. Schweda (STAR Coll.), Quark Matter 2004, in J. Phys. G: Nuc. Part. Phys. 30 (2004) S693

[44] L. McLarren and R. Venugopalan, Phys. Rev. D49 (1994) 2233, A. Krasnitz and R. Venugopalan, Phys. Rev. Lett. 84 (2000) 4309, D. Kharzeev, E. Levin and M. Nardi, hep-ph/0111315

[45] J. Schaffner-Bielich, D. Kharzeev, L. McLarren and R. Venugopalan, nucl-th/0108048

[46] J. Jalilian-Marian, Quark Matter 2004, in J. Phys. G: Nuc. Part. Phys. 30 (2004) S751

[47] T. Matsui and H. Satz, Phys. Lett. B178 (1986) 416

[48] H. Satz, Rep. Prog. Phys. 63 (2000) 1511

[49] M. Gluck, J.F. Owens and E. Reya, Phys. Rev. D17 (1978) 2324

[50] R. Gavai et al., hep-ph/9502270

[51] S. Digal, P. Petreczky and H. Satz, Phys. Lett. B514 (2001) 57

[52] M. Asakawa and T. Hatsuda, Phys. Rev. Lett. 92 (2004) 012001

[53] F. Karsch, Quark Matter 2004, in J. Phys. G: Nuc. Part. Phys. 30 (2004) S693

[54] M.C. Abreu et al. (NA50 Coll.), Phys. Lett. B410 (1997) 327

[55] M.C. Abreu et al. (NA50 Coll.), Phys. Lett. B410 (1997) 337

[56] M.C. Abreu et al. (NA50 Coll.), Phys. Lett. B450 (1999) 456

[57] M.C. Abreu et al. (NA50 Coll.), Phys. Lett. B477 (2000) 28

[58] M.C. Abreu et al. (NA38 Coll.), Phys. Lett. B466 (1999) 408

[59] A. Capella, J.A. Casado, C. Pajares, A.V. Ramallo and J. Tran Thanh Van, Phys. Lett. B206 (1988) 354

[60] C. Gerschel and J. Hüfner, Phys. Lett. B207 (1988) 253

[61] R.J. Glauber, Lectures in Theoretical Physics, Ed. by W.E. Brittin and L.G. Dunham (Interscience, NY, 1959) Vol. 1, 315

[62] G. Borges (NA50 Coll.), Quark Matter 2004, in J. Phys. G: Nucl.Part. Phys. 30 (2004) S1351

[63] P. Bordalo (NA50 Coll.), Quark Matter 2001, in Nucl. Phys. A698 (2002) 127c

[64] N.S. Topilskaya (NA50 Coll.), Quark Matter 2002, in Nucl. Phys. A715 (2003) 675c

[65] S.D. Drell and T.M. Yan, Phys. Rev. Lett. 25 (1970) 316

[66] H. Plothow-Besch/CERN-ETT/TT, 2000

Chapter 2

The NA50 experiment

NA50 is a Super Proton Synchrotron fixed target experiment, designed to detect muons in a event-by-event basis. Its apparatus is an upgraded version of the NA38 muon spectrometer, which in turn has been inherited from the NA10 experiment[1]. Its Pb–Pb setup version has been conceived in order to stand the high luminosity and huge background produced in reactions of an ultra-relativistic SPS Pb-ion beam impinging on a Pb target, which thickness can vary from 7% to 30% interaction length. To face such a severe environment and meet the specific experimental conditions of the NA50 program, the following considerations have been taken into account [2]:

- The total space allocated to the different detectors should be kept as short as possible, in order to minimize the combinatorial background due to meson decays;

- The vector mesons, ρ, ω, ϕ, J/ψ and ψ', are identified through their dimuon decay channel; the mass resolution should be as good as possible, in order to resolve the ψ' and J/ψ, as well as ϕ and $\rho + \omega$;

- High luminosity is demanded for dimuons with mass above 2 GeV/c^2 as their cross section is small;

- Independent detectors are required to evaluate the centrality of the collisions.

The main component of the apparatus is a muon spectrometer composed by a toroidal magnet and two sets of multi-wire proportional chambers for tracking and of trigger hodoscopes. In order to protect the spectrometer from the huge radiation and to ensure that only muons are detected, a hadron absorber is placed upstream. Three independent detectors, located downstream from the target region, measure the centrality of the reactions – the Electromagnetic Calorimeter, the Zero Degree Calorimeter and the Multiplicity Detector. The most upstream detector is the Beam Hodoscope, used for beam monitoring and counting purposes. A schematic view of the apparatus can be seen in figure 2.1.

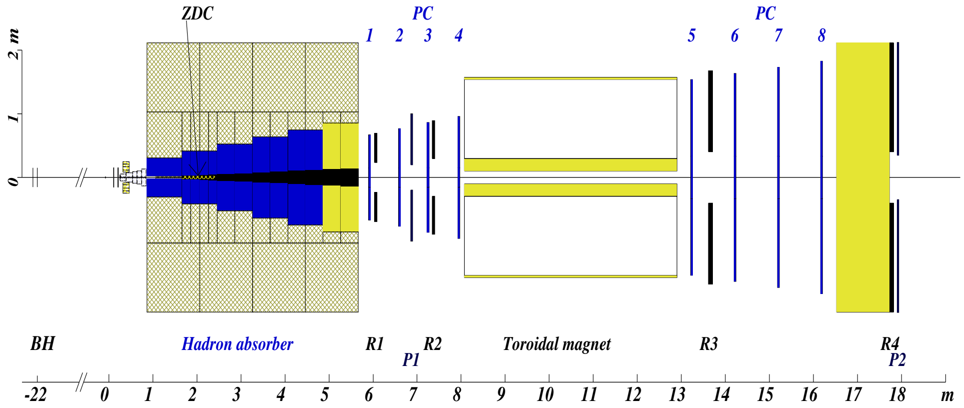

Figure 2.1: *Layout of the NA50 apparatus.*

2.1 The beam and beam monitors

The NA50 detector is located in the North Area High Intensity Facility of the SPS accelerator at CERN, ∼1 Km downstream from the beam line. It is the most remote experiment, keeping approximately 90% of the initial incoming ions, being the remnant splitted among the other NA experiments. Along the trajectory the beam is focused, both in horizontal and vertical planes.

The SPS usually operates at two energies: 450 GeV, which corresponds to the extraction of proton beams at 450 GeV/c incident momentum, and 400 GeV, allowing the extraction of protons, or fully stripped Pb ions ($^{208}Pb^{82+}$) with 400 GeV/c or 158 GeV/c per nucleon momenta, respectively [3]. For A–B collisions, the intensity is 7x10^7 ions in a beam cycle of 19.2 s, with an effective spill of 4.8 s.

The ion nominal intensity is limited by pile-up, which must be kept under control. In fact, the beam specifications described lead to a significant probability for the occurrence of two or more ions within the 20 ns time window of the Beam Hodoscope ADCs. Then, double interactions in target, too much close in time, can occur, leading to energy measurement ambiguities.

2.1.1 The beam hodoscope

The beam hodoscope, BH, is used to identify and count the incoming ions. Another important role is the definition of the dimuon trigger timing with respect to the Pb-ion time of arrival, with a precision better than 1 ns.

The BH is located 22 m upstream from the target region. It is made of a single plan of 16 quartz counters, 0.7 mm thickness each, associated with photomultipliers that detect the Čerenkov light produced in the quartz by the incident ions. The fast response of this kind of detectors allows a temporal resolution of 0.5 ns and an efficiency >98%. For each PM, both ADC and TDC informations are recorded. This allows a measure of the time interval Δt between the Pb-ion that has generated the triggered muon pair and the following, or previous, ion. In this way, pile-up events can be identified and rejected off-line. 5% of the pile-up events are not detected; however, this inefficiency is not dangerous due to the fact that only a small fraction of these pile-up ions also interacts in the target. Besides, the analysis of the signals shape in the Zero Degree Calorimeter complements the beam pile-up identification and rejection.

2.1.2 The BHI, BHInew detectors and the anti-halo counters

The beam hodoscope interaction detector, BHI, is made of two scintillating counters located 19 cm downstream from the BH, off the beam axis. The BHInew is positioned after the BHI and is made of four scintillating counters with the central hole of the same radius of the BH, in order to avoid interactions of the incoming ions in its blades. Both detectors tag interactions of a Pb-incident ion in the BH itself.

Two anti-halo quartz counters are located 51.2 and 18.7 cm upstream from the target (in the 2000 data taking there was a single anti-halo, located at 8 cm). They have an area of 40 x 40 mm^2 and have a 3 mm central hole to let the Pb beam pass through, undetected. Their role is to tag interactions upstream from the target and to identify events produced by a Pb-incoming ion 1.5 mm out of the beam axis.

2.2 The target

The NA50 experiment uses several targets, depending on the objective of the collision system study. For proton-nucleus collisions Be, Al, Cu, Ag, W and Pb targets are used. In Pb–Pb collisions, depending on the data taking period, a Pb sub-targets system is used: a single sub-target in the 1998 and 2000 runs and several ones in the 1995 and 1996 ones (figure2.2). In units of interaction lengths, they vary between 7% and 30% λ_I. The nuclear interaction length on a given medium is defined as the average distance a high energy hadron travels inside the medium before a nuclear interaction occurs:

$$\lambda_I = \frac{A_{target}}{N_A \sigma_{ine} \rho} \tag{2.1}$$

where A_{target} is the atomic mass number of the target, ρ its density and σ_{ine} is the total inelastic cross section, given by:

$$\sigma_{ine} = \sigma_o (A^{1/3}_{projectile} + A^{1/3}_{target} - \delta)^2 \tag{2.2}$$

Assuming $\sigma_o = 68.8$ mb and $\delta = 1.32$, values deduced from an interpolation between the results reported in [4, 5], we obtain for lead: $\sigma_{ine} = 7.62^{+0.54}_{-1.23}$ b, and using $\rho = 11.35$ g/cm^3, A_{target}=207.19 g/mole, we final extract, $\lambda_I^{Pb} = 3.98^{+0.21}_{-0.27}$ cm.

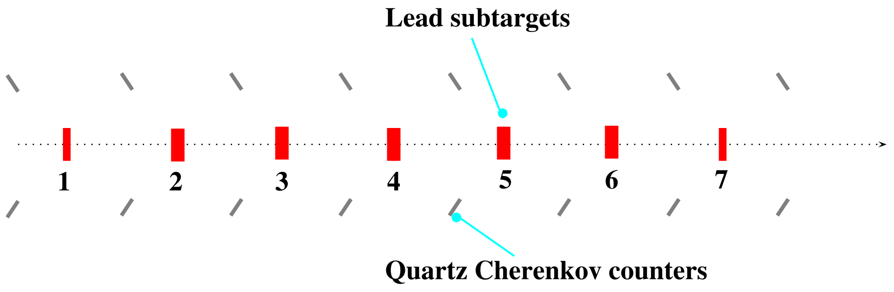

Figure 2.2: *The multi-target system*

In 1995 7 sub-targets of 1 mm each were used, corresponding to 17% λ_I. In 1996, the aim was to increase the statistics, so the target was extended to 30% λ_I. Such a thick target has originated a significant number of re-interactions of secondary fragments that could not be disentangled by the electromagnetic calorimeter leading, therefore, to biased energy measurements. In order to clarify this problem, a thin target was introduced in 1998. These 3 three data taking periods had a common drawback — the target identification algorithm was not efficient in the detection of peripheral collisions. Since these interactions led to results somewhat incompatible with the ones obtained with lighter systems (see figure 1.19), a hypothesis was raised - results from peripheral collisions could be contaminated by ones obtained from Pb-air interactions. Indeed, this total inelastic cross section is not negligible, σ_{ine}^{Pb-air} ~3.4 b. To clarify the peripheral collisions results, the target region was placed in vacuum in the year 2000. In table 2.1 the target characteristics and beam intensities of the several NA50 data takings are quoted.

2.3 The hadron absorber

The hadron absorber's composition and length is optimized to retain, as far as possible, the huge number of hadrons produced in Pb–Pb collisions, prior their decay into muons.

data sample	total target thickness L_T (mm)	Interaction length L_T/λ_I	number of sub-targets	beam intensity (ions/burst)
1995	7	17%	7 (in air)	3×10^7
1996	12	30%	7 (in air)	5×10^7
1998	3	7%	1 (in air)	5.5×10^7
2000	4	9.5%	1 (in vacuum)	7×10^7

Table 2.1: *Target characteristics and beam intensities of the NA50 Pb–Pb collisions.*

These particles constitute the resonances background and should be, obviously, reduced to the minimum. Simultaneously, the absorber materials must be appropriate to reduce the multiple scattering suffered by muons, since this instrumental effect is the main cause for the mass resolution degradation. A compromise should be found between the interaction length λ_I, which is proportional to $A^{1/3}$ of the component materials and should be small enough to absorb the hadrons, and the radiation length ($X_o \propto A/Z^2$), that should be as large as possible in order to reduce the multiple scattering, since they are anti-correlated through the scattering angle:

$$\theta_0 = \frac{13.6MeV}{\beta cp} z \sqrt{\frac{z}{X_0}}[1 + 0.038\ln(\frac{\mathrm{x}}{\mathrm{X}_0})] \ , \tag{2.3}$$

where βc, p and z are the velocity, momentum and charge number of the incident particle, and x/X_0 is the thickness of the scattering medium in units of radiation lengths [6]. Taken these demands into account, the absorber begins 25 cm downstream from the target and its first component is a pre-absorber composed by beryllium oxide with an extension of 60 cm and a conical shape. In its center stands a hole, large enough to let the non-interacting incoming ions pass towards the Zero Degree Calorimeter. The BeO is followed by a set of carbon disks, totalizing 400 cm and surrounded by iron blocs beyond the spectrometer acceptance (figure 2.3). At the end stands a 80 cm set of iron disks, which purpose is to reduce the forward telescope illumination, increasing, therefore, the first chamber efficiency. The total absorbers length is 13 interaction lengths. However, high energy hadrons survive and may give rise to fake triggers. To face it, a last iron wall, 120 cm deep, is placed before the last trigger hodoscope, R4.

In table 2.2 are quoted the characteristics of the hadron absorber materials.

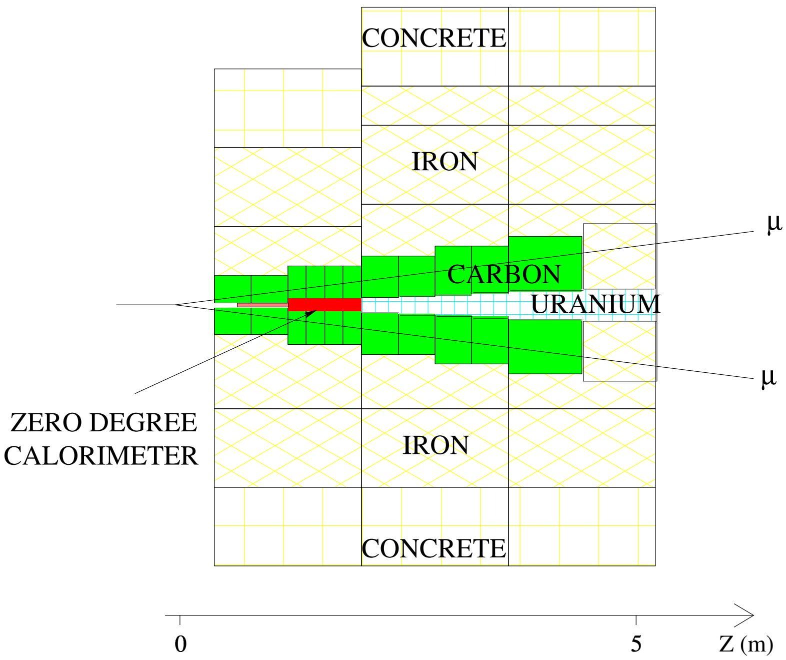

Figure 2.3: *Schematic view of the hadron absorber.*

Material	Function	Length (cm)	λ_I (g/cm^2)	ρ (g/cm^3)	X_0 (g/cm^2)
BeO	pre-absorber	61.2	86.0	2.92	40.88
C	main absorber	400	86.3	2.26	42.70
Fe	main absorber	200	131.9	7.87	13.84
air	beam axis	158.8	90.0	1.21×10^{-3}	36.66
Ta	ZDC(plug)	65	198.0	16.65	6.66
U	plug	320	199.0	18.95	6.00

Table 2.2: *Characteristics of the hadron absorber materials.*

2.4 The muon spectrometer

The NA50 spectrometer measures the muons produced in the target interactions. These muons are accepted in the pseudo-rapidity interval 2.70< η <3.90 where maximum energy densities are expected.

2.4.1 The multi-wire proportional chambers

Two MWPCs telescopes, each formed by four chambers placed upstream and downstream from the magnet, reconstruct the muon tracks. Each chamber has three independent hexagonal plans, with two graphited mylar cathodes and one anode wire plane. The spacing between the planes is 2.2 cm and each one is rotated by 0^o, 60^o and 120^o with respect to the horizontal axis (figure 2.4). The upstream chambers have 749 wires per plane, while the downstream ones have 1229, all spaced apart by 3 mm. The gold-plated tungsten wires have 20 μm of diameter and are immersed in a gas mixture of argon (80%), isobutane (19.8%) and freon (0.2%). The gap between the cathodes and the wire plane is 6 mm. The nominal applied voltage is -2.8 KeV, being lowered to -2.4 KeV during the inter-burst, in order to avoid the degeneration of the gas mixture. The readout of each chamber is made through sets of 32 wires connected to a pre-amplifier. Signals are sent to the Receiver-Memory-Hybrid (RHM) modules, located in the counting room, where they are discriminated and amplified (see section 2.7).

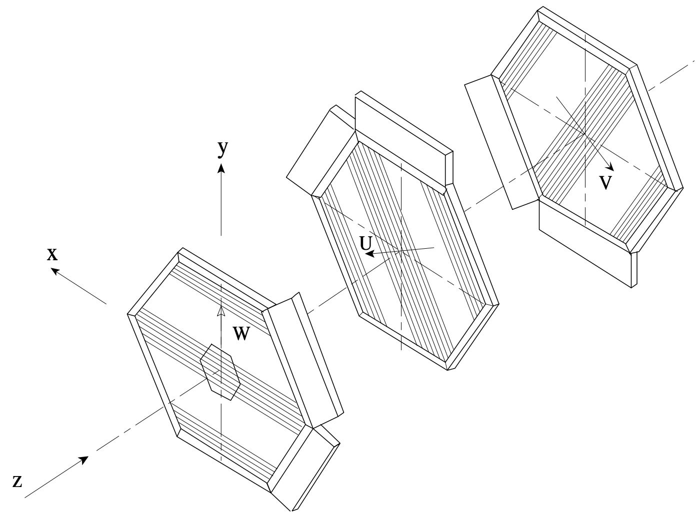

Figure 2.4: *The 3 planes of the MWPCs*

2.4.2 The trigger hodoscopes

Two sets of two hodoscopes of hexagonal symmetry (the same as the MWPCs), placed upstream and downstream from the magnet, provide a signal to trigger the data acquisition system. R_4 is placed after the last iron wall to avoid fake triggers, as explained in section 2.3. R_1 and R_2 are divided in 6 sextants, each of them containing 30 slabs. They are geometrically homothetic with respect to the target. The signal validation is done through a coincidence, $V_n = R_1^n \times (R_2^n + R_2^{n-1})$, taking into account the spatial extension of the target (figure 2.5). The light collected in each scintillating slab is read by a photomultiplier. The timing of the light reaching the PMs depends on the muon trajectory. This feature causes a fluctuation in the trigger timing, known as *jitter*. To reduce this effect, signals coming from R_1 and R_2 PMs are sent to a *mean–timer*, which gives a signal after a delay proportional to the mean time of the input signals.

R_3 and R_4 contain 24 and 32 slabs per sextant, respectively. This set, together with the coincidences V, form an association, defined by an electronic matrix, which is a pre-requisite to the *the dimuon trigger*. A dimuon is selected for off-line analysis if the hodoscopes R_3 and R_4 are in spatial and temporal coincidence with V. Furthermore, the trajectories of the two muons must follow different sextants.

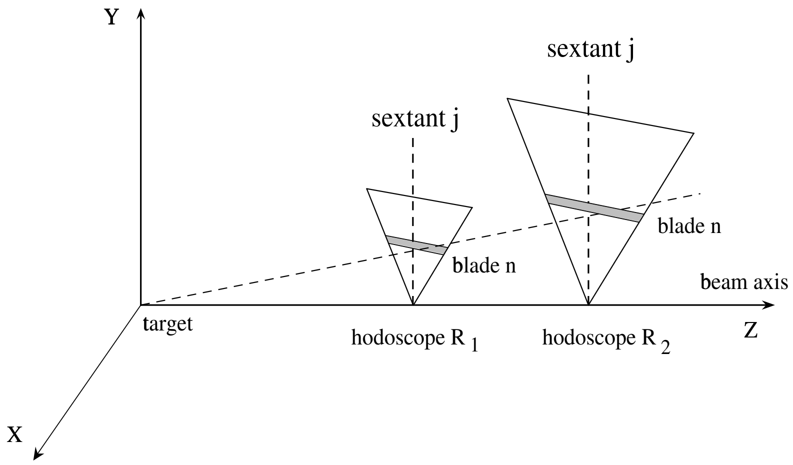

Figure 2.5: *The* $V_n = R_1^n \times (R_2^n + R_2^{n-1})$ *coincidence.*

2.4.3 The P_1 and P_2 hodoscopes

The P_1 and P_2 hodoscopes measure the trigger efficiency. P_1 is positioned between the second and third MWPCs, before the magnet, and P_2 is placed after R_4, being the most downstream NA50 detector. Each hodoscope contains 6 sextants azimuthally subdivided in 8 scintillating slabs. Each slab of P_1 is read by a single PM, while the P_2 slabs are read by 2 PMs. A *mean–timer* is used to average the signals that reach this last hodoscope.

Usually, 2 special runs are taken by data period, in order to determine the trigger efficiency, defined as the fraction of $P_1 \times P_2$ triggered events that obey to all conditions required in the section 2.6.1. Typically, the trigger efficiency for the Pb–Pb runs is on the level of 88%.

2.4.4 The magnet

The NA50 muon spectrometer has a 4.8 m air-core toroidal magnet, located 9 m downstream from the target. It has a hexagonal shape with a inner and outer radius of 29.5

and 154 cm, respectively. The magnetic field is produced by a pulsed current, synchronized with the SPC cycle, circulating in coils mounted on 6 iron supports, each of them occupying an azimuthal angle of 18^o (figure 2.6).

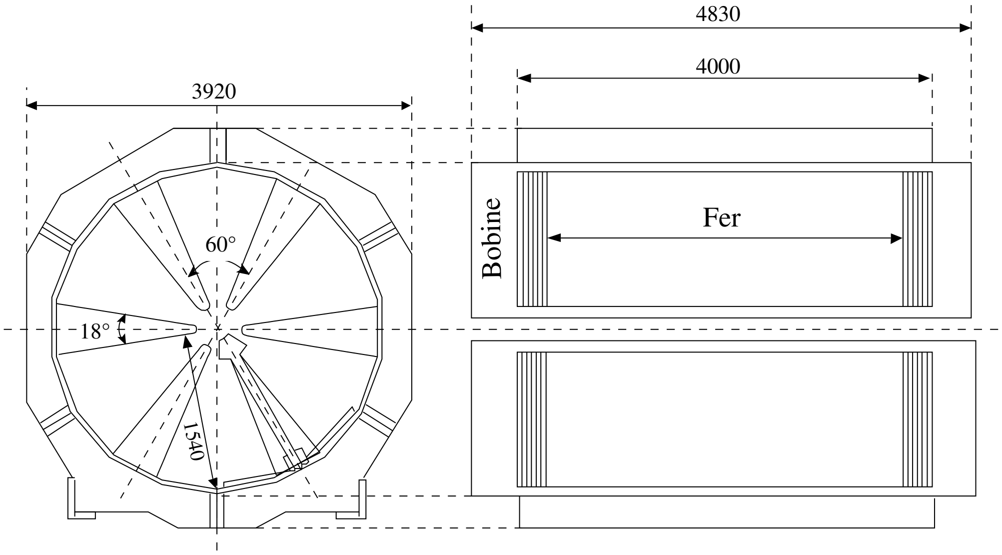

Figure 2.6: *Views of the NA50 toroidal magnet.*

The produced azimuthal field has an intensity inversely proportional to the transverse distance to the beam axis, r:

$$\overrightarrow{B}(r) = \frac{B_o}{r}\overrightarrow{u}_\phi \tag{2.4}$$

where $B_0 = 0.383$ Tm. Such design allows a muon entering this field to keep its azimuth, suffering a deflection inversely proportional to its transverse momentum. Within the spectrometer acceptance, the dimuon mass is approximately equal to the sum of both p_T, $M_{\mu\mu} \approx P_{T_1} + P_{T_2}$ [7]; thus, such magnetic field property allows the optimization detection, in terms of acceptance, of the main particles under study. Such optimization is achieved by changing the pulsed current of the magnetic field — it was 10000 A at the NA10 experiment (study of very high mass dimuons and Υ decays), 4000 A at NA38 (study of low mass dimuons and ρ, ω, ϕ and J/ψ decays) and 7000 A at NA50, since its main purpose is the study of J/ψ and ψ' productions.

The muons crossing the iron supports are off-line rejected due to their poor mass resolution, caused by the multiple scattering. In order to prevent any systematic effects related with the sign of the magnetic field, the polarity is reversed after every few runs. The field intensity continuously checked by a Hall-probe.

The characteristics of the spectrometer main components are quoted in table 2.3.

Element	z position (cm)	Characteristics
PC1	547	y, u, v plans; 448 wires per plane; 134 cm length
R1	560	6 $\times$ 30 scintillating blades of 1.05 $\rightarrow$ 3.55 cm large
PC2	643	y, u, v plans; 512 wires per plane; 153 cm length
PC3	740	y, u, v plans; 576 wires per plane; 172 cm length
R2	784	6 $\times$ 30 scintillating blades of 1.25 $\rightarrow$ 3.85 cm large
PC4	835	y, u, v plans; 640 wires per plane; 192 cm length
Magnet	850-1333	toroidal magnetic field
PC5	1356	y, u, v plans; 1024 wires per plane; 306 cm length
R3	1436	6 $\times$ 24 scintillating blades of 5.5 cm large
PC6	1486	y, u, v plans; 1088 wires per plane; 326 cm length
PC7	1607	y, u, v plans; 1152 wires per plane; 345 cm length
PC8	1725	y, u, v plans; 1216 wires per plane; 364 cm length
R3	1436	6 $\times$ 32 scintillating blades of 5.5 cm large

Table 2.3: *Characteristics of the NA50 spectrometer elements*

2.5 The centrality detectors

The energy density reached in a collision is intimately correlated with the impact parameter b, defined as the transverse distance between the geometric centers of the two nuclei in the transverse plane. An ideal zero b value corresponds to the superposition of two nuclei. On the contrary, a high b (e.g., 12 fm for Pb–Pb) corresponds to a peripheral interaction between them. Colliding ultra-relativistic ions and measuring the energy released in the reaction is the main tool to study the charmonia suppression as a function of the collision centrality.

The NA50 experiment has three independent centrality detectors: the Electromagnetic Calorimeter, the Zero Degree Calorimeter and the Multiplicity Detector.

2.5.1 The electromagnetic calorimeter

The electromagnetic calorimeter, EMC, measures the neutral transverse energy released in the collisions, mostly from $\pi^o \rightarrow \gamma\gamma$ and prompt γ. Its front face is located 32 cm downstream from the target, surrounding the BeO pre-absorber. The calorimeter is 14 cm long and is composed by four hexagonal rings containing 2 mm diameter scintillating fibers, aligned with the beam axis and embedded in a lead converter in a 1:2 volume ratio. The fibers are embedded in a stainless steel frame and are regularly spaced. This configuration allows the easy substitution of damaged fibers due to the radiation (see figure 2.7).

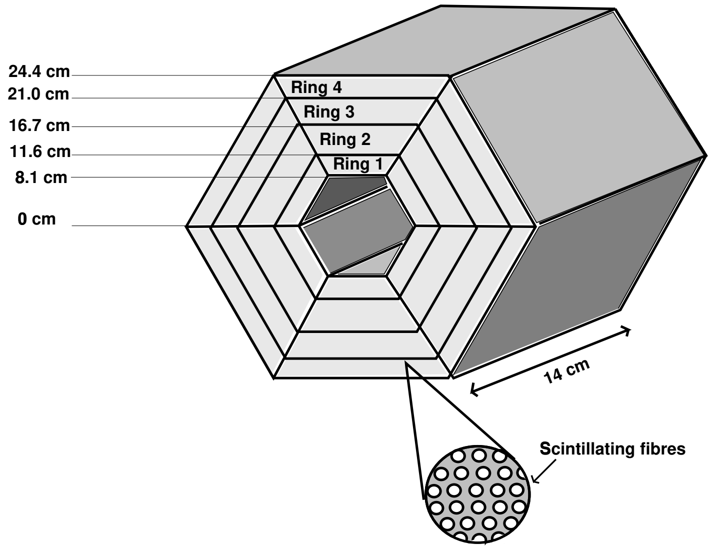

Figure 2.7: *The structure of the NA50 Electromagnetic Calorimeter.*

The hexagonal rings cover the pseudo-rapidity interval $1.1 < \eta < 2.3$. This interval is beyond the spectrometer acceptance in order to avoid the exposition to the high radiation levels produced in Pb–Pb collisions, which could degrade severely its life expectancy. On the other hand, the thickness of the lead converter is ∼14 interaction lengths ($\lambda_I^{Pb} = 194$ g/cm^2); such thickness would lead to an undesirable deterioration of the dimuons mass resolution.

About 40% of the raw measured energy in the calorimeter comes from charge particles. This contamination is estimated from a GEANT-based simulation [8] and subtracted.

The measurement of the neutral transverse energy is obtained by:

$$E_T^o = \sum_{i=1}^{4} C(i) E_i \; sin\theta_i \; , \tag{2.5}$$

where $C(i)$ is the correction factor of the ring i due to the charged particles contamination and $sin\theta_{\rm i}$ is the sinus of the angle subtended by the ring i and the target position.
The calorimeter resolution is given by:

$$\frac{\sigma(E_T^o)}{E_T^o} = \frac{0.72}{\sqrt{E_T^o(GeV)}} \; . \tag{2.6}$$

For central Pb–Pb collisions the resolution is ∼8%.

2.5.2 The zero degree calorimeter

The zero degree calorimeter [9] measures the energy emitted in the forward 35 mrad cone of aperture. It is located 165 cm downstream from the target, surrounded by the hadron absorber and its $\eta \geq 6.3$ acceptance interval is outside the muon spectrometer one, in order to minimize the multiple scattering of the detected muons. The zero-degree energy, E_{zdc}, is thus almost entirely carried by spectator nucleons and nuclear fragments not involved in the collision. In this way, by measuring E_{zdc}, it is possible to estimate the number of projectile participant nucleons:

$$N^{P}_{npart} = (A-1) - \frac{E_{zdc}}{E_{beam}} \; . \tag{2.7}$$

The high level of radiation to which the ZDC is exposed demands the use of the quartz fibers technique. In this sense, 900 silica optical fibers of 365 μm diameter collect the Čerenkov light produced by the beam spectators shower in a tantalum converter. The volume ratio of fiber/Ta is 1:17. The converter is 65 cm long and has a transverse size of 5x5 cm^2. In order to detect the beam position with good sensitivity, the fibers, of 180 cm length, are divided in four groups and read by a photomultiplier placed at rear (figure 2.8).

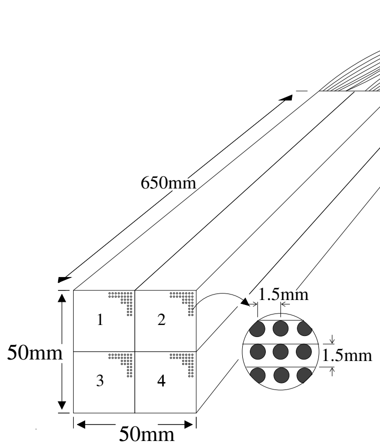

Figure 2.8: *The Zero Degree Calorimeter.*

The beam pile-up is detected comparing event-by-event the pattern of the analog sum of signals with respect to a superposition of two (or more) ions with a reference pattern, corresponding to a standard signal with no pile-up.

The resolution has been experimentally measured by means of proton, deuteron, α

and Pb beams, with the same energy per nucleon, 158 GeV. The resolution $\sigma(E_{zdc})/E_{zdc}$ is obtained by fitting a gaussian to the peak corresponding to the total energy released by the projectile. One verifies that it is linear as a function of $1/\sqrt{A}$ [10]:

$$\frac{\sigma(E_{zdc})}{E_{zdc}} = \frac{a_1}{\sqrt{A}} + a_2 \ , \tag{2.8}$$

where a_1 and a_2 are fitted to the data obtained with a 12 ns trigger gate (NA50 standard run conditions). Another fit was performed using data collected in improved conditions, namely, the use of a wider gate width of 20 ns, lower beam intensity and the fact that the calorimeter has not been exposed, previously, to an incident beam. The values are: $a_1 = 26.8\%$ and $a_2 = 6.2\%$, with respect to the 12 ns trigger gate. Considering the optimal conditions, the values obtained for a_1 and a_2 become 27.1% and 3.1%, respectively (see figure 2.9).

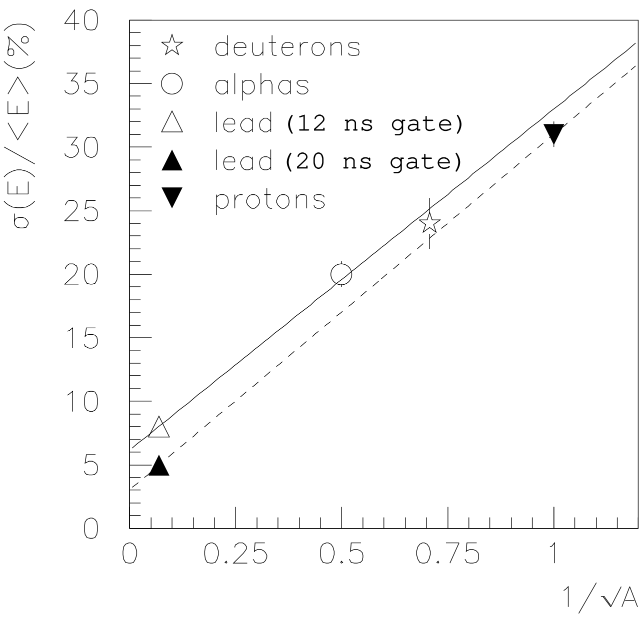

Figure 2.9: *Energy resolution of the ZDC for 158 AGeV/c incident nuclei of different A as a function of $\sqrt{A}$. The full symbols refer to a 20 ns gate (optimal conditions), the open ones to a 12 ns gate (actual conditions).*

For $< E_{zdc} > = 11$ TeV ($b = 5$ fm) the number of spectators is $A \sim 70$. From equation 2.8 the ZDC experimental resolution is then 9.4%. For peripheral collisions, e.g. $b = 11$ fm, the resolution becomes 8%.

2.5.3 The multiplicity detector

The multiplicity detector MD is a silicon micro-strip detector that measures the number of charged particles produced in the Pb–Pb collisions. Two planes, MD1 and MD2, placed 10 cm apart, compose it. This layout allows the reconstruction of "tracklets" defined by one hit in MD1 and one in MD2. In this way, the multiplicity detector can also be used as a target interaction detector. Since the experiment takes data at very high rate, and the silicon detectors operate in the high radiation area, the detector has to be very fast (double pulse resolution of the readout electronics < 50 ns), must be radiation resistant to face on the 20 Mrad of total ionizing dose and a fluency up to 10^{14} of low energy neutrons/cm^2, and should have high granularity [11]. The view of one of the two multiplicity detector planes is shown in Figure 2.10.

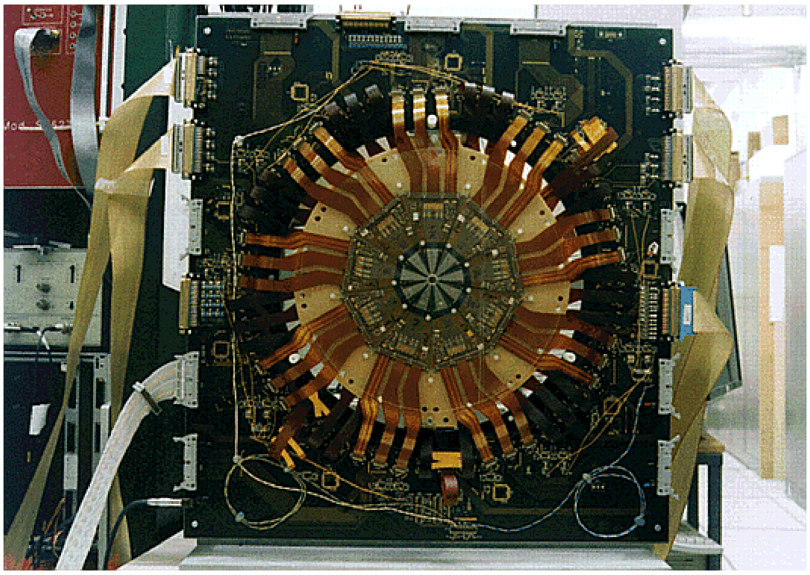

Figure 2.10: *Picture of one plane of the Multiplicity Detector.*

The first plane of the Multiplicity Detector, MD1, is located 11.65 cm downstream from the target. Both planes are centered on the beam axis with a central hole, where the primary beam fragments and the non-interacting incident ions cross through. Each detecting plane is divided into small micro-strip detectors, arranged in two circular crowns. Each sub-detector (wafer) of the inner crown covers a 20^o azimuthal angle and is segmented azimuthally in 2 sectors of $\Delta\phi$=10^o and radially in 128 strips with different dimensions. This design implies an uniform occupancy for all sensitive elements [12]. The micro-strip detectors are assembled with a segmentation in pseudo-rapidity, on average of $\Delta\eta \simeq 0.02$, in order to achieve a good angular resolution and, at the same time, a reasonable low occupancy per element. The geometrical parameters are listed in table 2.4.

plane	crown	R_{in} (mm)	R_{out} (mm)	$\Delta\eta$	azimuthal sectors	strips per sector	channels per crown
MD1	inner	6.5	36.5	1.9-3.5	36	128	4608
MD1	outer	36.5	88.5	1.1-1.9	36	64	2304
MD2	inner	6.5	36.5	2.5-4.1	36	128	4608
Md2	outer	36.5	88.5	1.6-2.5	36	64	2304

Table 2.4: *Geometrical characteristics and effective η coverages for MD1 and MD2.*

2.6 The triggers

Three kinds of triggers are used to select and record events, namely the dimuon trigger that signals the detection of a rare process, the hadronic minimum bias trigger and the monitoring laser trigger.

2.6.1 The dimuon trigger

This is the main trigger of the NA50 experiment. It selects a pair of muons obeying to the pre-requisites defined hereafter:

1 - The existence of a $V^n = R_1^n \times (R_2^n + R_2^{n-1})$ coincidence for each muon;

2 - The existence of a correlation $V^n \times R_4^m$, for which the signal from R_3^l is used to validate the association and to reduce the number of accidental coincidences (this correlation also cuts soft muons, mostly from the combinatorial background);

3 - Each muon should cross a different sextant of the spectrometer.

2.6.1.1 The matrix

The $V^n \times R_4^m$ coincidences are OR-ed in four signal classes (A, B, C and D) defined by four broad p_T bins. For each definite pair (V^n, R_4^m) the set of counters R_3^l that can be associated is determined. For each of the 12 semi-sextants, diagonal correlations between the V^n coincidences and the R_4^m signals (validated by the R_3^l signals in association) are programmed in a set of 16-channel ECL logics modules. This leads to a total of 192 correlation matrices, that take into account the fact that each V^n upstream from the magnet corresponds to hits in R_3^l and R_4^m, the more apart from a linear extrapolation, the lower the p_T. For a current of 7000 A, the muon p_T broad bins are the following:

A	$2.80 < p_T$
B	$1.40 < p_T < 2.80$
C	$0.98 < p_T < 1.40$
D	$0.42 < p_T < 0.98$

The signals width at the matrix modules inputs is 15 ns for the coincidences V and 30 ns for R_3 and R_4. At the output, the signal width is 30 ns and the transit time is 35 ns.

2.6.1.2 The "Magic Box"

A pair of p_T values is sent to a programmable unit, named *Magic Box*, that generates an output signal every time the two muons are found to be in two different sextants. For each of the 15 possible combinations of two sextants there are 16 sets for the p_T combinations (AA,AB,...,DC,DD). These combinations define 16 dimuon mass ranges, according to the expression $M_{\mu\mu} \approx P_{T_1} + P_{T_2}$. The signal from the *Magic Box* has a large *jitter* (5 to 10 ns). This signal is then put in coincidence with the overall OR of the 12 V semi-sextants, already OR-ed, resulting in a trigger signal denominated *Trigger Sans Jitter (TSJ)*, varying from 1 to 5 ns *jitter* (see section 2.6.1.3). A *Trigger Zero Jitter (T0J)* (0.5 ns) is finally obtained by synchronizing the TSJ with the BH signal. This signal opens the gates of the detectors in a very precise time; however, it is too restrictive, so in order to recover some good events it rejects, an SOS trigger, named *T0J SOS*, is used.

2.6.1.3 Timing

In order to elaborate a signal limiting the trigger *jitter*, a previous and rigorous *timing* of the hodoscopes is crucial. A brief description is made hereafter.

Electric pulses from R_1 and R_2 photomultipliers are formatted by discriminators (LeCroy 4416), which also eliminate their background, applying a minimal threshold cut. These formatted signals are sent to programmable delay modules (CAEN C211), which aim is to allow the delay adjustment in each of the 16 channels, thus compensating: different muons time of flight; delays dependent on the high voltage of photomultipliers and delays due to the electronic dispersion of the discriminators and delay modules themselves, and cables as well. The delay value attributed to each channel is obtained by measuring a *timing* in generator and/or in particles mode, the latter described as:

1. Synchronization among the reference counters (T_3), equipped with a *mean–timer*,

through their coincidence with a common and external counter coupled to a radioactive source;

2. Synchronization of R_1 and R_2 at their common *mean–timer* inputs, by measuring each delay channel with TDCs, using the T_3 reference, and programming them in order to obtain a precise timing, common to all channels, for their coincidence $V = R_1 \times R_2$;

3. Synchronization of R_3 and R_4 relatively to V at the matrix input (T_3 reference) by the previous method;

4. Synchronization of matrix outputs (p_Ts) with the OR V reference for each sextant;

5. Synchronization of the trigger (*Magic Box* output) with the OR $V \times pT$, forming the TSJ;

6. Synchronization of the TSJ by the very precise beam hodoscope signal, forming the T0J.

In parallel and with less precision, a synchronization of the RMH system is made using the TSJ and a dedicated program, which uses the acquisition.

The *timing* in the generator mode is similar, but the propagated signal does not come from the hodoscopes (so, the T_3 reference is not used) but from a generated one which enters in all test discriminators input.

2.6.2 The minimum bias triggers - ZDC and BH

A Minimum Bias trigger is generated when the ZDC signal overcomes a pre-defined threshold of 50 mV. This value is lower than the minimum signal value detectable by this calorimeter, in order to avoid any trigger bias. Most of these MB triggers are events in which a Pb-ion did not interact in the target. The number of these MB triggers is pre-scaled to 300 per burst.

In the 2000 data taking a new Minimum Bias trigger was implemented. Each ion detected by the BH has produced a trigger signal. The typical pre-scaling for these triggers number lies between 300 and 400 per burst.

2.6.3 The laser trigger

The laser trigger is obtained by means a pulse generator. A laser pulse is sent to the EMC photomultipliers, in order to monitor their gain stability. Simultaneously, this signal allows the establishment of the ZDC pedestal values, which PMs are not connected to this laser.

2.7 The data acquisition system

During the spill of 4.8 s, the data acquisition system (DAQ) reads in parallel and stores into burst memories, resident on VME crates, the following data partitions [13]:

• Receiver-memory-hybrid modules (RMH) encode the addresses of the MWPCs and hodoscopes hits and store them in burst buffers (MEMRMH);

• Signals from the EMC, ZDC and beam hodoscopes are sent to charge analogue-to-digital converters (QDCs), that digitize the pulse-height and store the result in registers. Time measurements are sent to TDCs; Pattern Units are used by the QDCs to provide them with some trigger characterization flags, in redundancy with part of the RMH produced information;

• Multiplicity Detector data are transmitted by optical links and stored in specific burst buffers (MEMOPT).

This process implies a typical dead time of 10-15%. Figure 2.11 gives a schematic overview of the hardware readout.

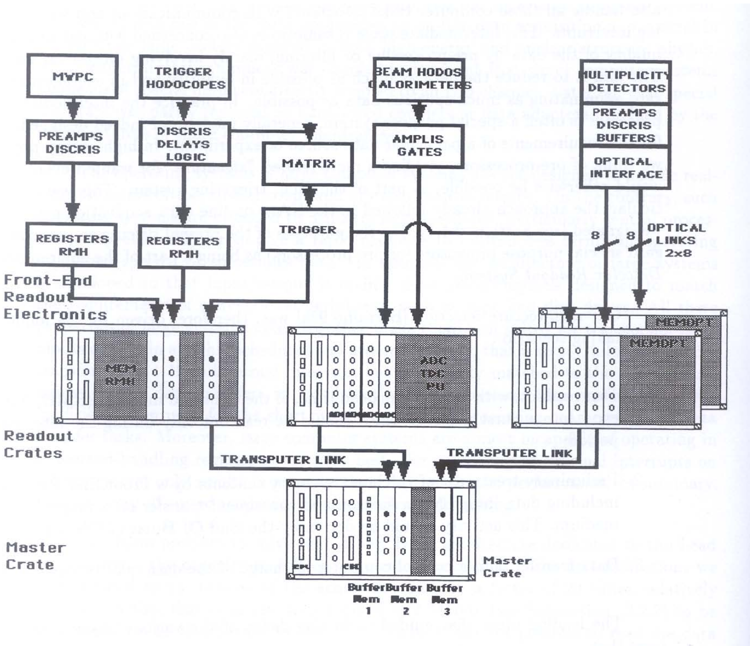

Figure 2.11: *Basic Readout Architecture*

The inter-burst is dedicated to the following tasks:

• to verify the partitions integrity, namely rejecting bad formatted ones or with wrong trigger number association;

• to the event-building, merging each event partition in a whole event;

• to record the sequence of the whole events in magnetic support.

The Front-End Processor (FEP), a FIC8243, resident in the VME master crate, performs this whole job.

The Back-End DAQ computer system is composed by a set of computers, organized in a VAX cluster; their names and functions are:

• One VAX Station, model 4000/90, serving as the main data acquisition control machine, namely for overall run control, types of runs and run dependent hardware initialization (programmable thresholds, delays, etc). This station should also guarantee the scalers display across a net of terminals, spread by the counting room;

• Another VAX Station, based on α processors, dedicated to histogram filling of all detectors, including the possibility of detector correlations and cuts;

• A VAX Station, model 4000/60, used to monitor the spectrometer, namely displaying the MWPCs and hodoscope illuminations;

• A SUN SPARC-4 which provides a on-line event display of hits in the MWPCs and hodoscopes, as well as their association and tracking reconstruction.

2.8 The performances of the NA50 apparatus

After four data taking Pb–Pb periods, one can say that, definitely, the apparatus has fully complied the objectives that the NA50 Collaboration has proposed to reach. The mass resolution of the charmonium resonances is lower than 100 MeV, sufficient to separate the ψ' from the J/ψ and to allow a systematic study of the ψ' production. The spectrometer geometry leads to an acceptance in the J/ψ mass region of 14%. The reconstruction and trigger efficiencies are on the level of 95% and 86%, respectively.

In the 2000 data taking period the target region was placed in vacuum in order to dismiss possible Pb-air contaminations. This fact, together with the new target identification algorithm, provided by the two planes of the multiplicity detector [1], has allowed the study of the peripheral interactions safely. An improved version of the reconstruction software has been developed, featuring a higher MWPCs efficiency with respect to the one used for data takings before 2000 [14]. These features, together with the high amount of statistics recorded, have produced the best quality NA50 Pb–Pb data sample.

[1] Also the data collected in the 1998 run has been analysed with this new target recognizing system.

Bibliography

[1] L. Anderson et al. (NA10 Coll.), Nucl. Instrum. Meth. in Phys. Res. 223, (1984) 26

[2] Study of muon pairs and vector mesons produced in high-energy Pb–Pb interactions, Proposal - CERN/SPSLC 91-55, SPSLC/P 265-rev, November 1991

[3] H. D. Haseroth, for the Lead Ion Accelerating Facility Collaboration, 'The CERN Heavy Ion Accelerating Facility', CERN

[4] E. Andersen et al., Phys. Lett. B220 (1989), 328

[5] H. Dekhissi et al., Nucl. Phys. A662, (2000) 207

[6] Particle Data Group, K. Hagiwara et al., Phys. Rev. D66, (2002)

[7] A. Coc, Le spectromètre à dimuons de l'expérience NA10 et son système de déclenchment, Thèse de Doctorat 3ème CYCLE, Université de Paris VII, Juin 1980

[8] M.C. Abreu et al. (NA50 Coll.), Phys. Lett. B410 (1997), 327

[9] R. Arnaldi et al., Nucl. Instrum. Meth. in Phys. Res. A411 (1998) 1

[10] R. Arnaldi, Etude de la suppréssion du ψ' dans les collisions Pb–Pb au SPS du CERN en fonction de la centralité mesurée avec le calorimètre a zero degrées, Thèse de Doctorat, Université Blaise Pascal, Clermon-Ferrand, Décembre 2000

[11] B. Alessandro et al., Nucl. Instrum. Meth. in Phys. Res. A493 (2002) 30

[12] F. Prino, Study of the phase transition to QGP at the CERN SPS with the NA50 multiplicity detector, Tesi di dottorato di ricerca, Università di Torino, January 2003

[13] S. Silva, Experience in the use of Software Engineering methodologies in the development of the Data Acquisition System of the NA38/NA50 experiment at CERN, PhD Thesis, Universidade Técnica de Lisboa, IST, March 1997

[14] B. Alessandro et al. (NA50 Coll.), Eur. Phys. J. C33 31.

Chapter 3

Data reconstruction and selection

The Data Acquisition System of the NA50 experiment has collected, during the 35 days of the 2000 run, 135 million dimuon triggers from standard runs (i.e., excluding empty target and low intensity beam runs), which led to 64 million reconstructed dimuons. The purpose of this chapter is to describe how these data are treated in order to be analysed in terms of the dimuon kinematic variables: mass, p_T, rapidity, polar angle θ_{CS} and the azimuthal angle ϕ. The data must be selected according to the fiducial spectrometer phase space and to the type of the analysis required. Run and track quality criteria are also applied.

3.1 Run selection

For the Pb–Pb 2000 data analysis, all standard runs were selected. The non-standard or the bad quality runs were excluded, namely: 39 low intensity, 32 empty target and 16 bad runs. Some non-standard runs, for specific purposes, were taken: 18 runs with a generator trigger for ADCs pedestal, 2 measurements of $P_1 \times P_2$ trigger runs, in order to determine the dimuon trigger efficiency, and 1 alignment run. In total 553 runs were used for the Pb–Pb 2000 data analyses presented in this work. In table 3.1 a summary of this data taking is shown:

3.2 The event reconstruction

During the runs, data are stored in magnetic cartridges. These data are decoded by the NA50 reconstruction program [1], DIMUREC, according to the following steps:

Magnetic Field	$\oplus$	$\ominus$	Total
Runs dimuon	284	269	553
Triggers (approx)	97733120	93551672	191284832
Dimuons	68032736	66748744	134781456
Luminosity	0.364E+13	0.314E+13	0.678E+13

Table 3.1: *Summary for 553 full target runs of the Pb–Pb 2000 data taking.*

- Trigger recognition;
- Tracks reconstruction;
- Determination of the interaction vertex;
- Calculation of the dimuon kinematic variables.

These physical variables are then registered in μDSTs (micro Data Summary Tapes), ready to be manipulated according to the analyses criteria.

3.2.1 The trigger recognition

The dimuon trigger (the main trigger of the experiment and the one used in this work) is computed offline using the RMH encoded information. It contains the addresses of the hit scintillators of hodoscopes R_1,...,R_4, as well the values of the V_n coincidences and the combined p_T of the two muon tracks. As it was explained in section 2.6.1, a trigger is selected if the two muons hit the blades according to the $R_1 \times (R_2^n + R_2^{n-1})$ condition, if the $V_n \times R_3 \times R_4$ coincidence is complied and if the "Magic Box" signs the detection of the two muons crossing the spectrometer in different sextants. The trigger efficiency for the 2000 run was 86.2 $\pm$ 0.7 %.

3.2.2 The tracks reconstruction

The RMH also encodes information relative to the hits of a MWPC plane (y, u or v). Using it, the standard procedure to reconstruct a track, which is based in the projections method, obeys to:

- In order to avoid the larger illumination of the first chambers telescope (mostly due to soft muons and "punch-through" hadrons that would be swept out, anyway, from the spectrometer acceptance by the magnetic field), the reconstruction starts by the second telescope. For each pair of hits, in MWPC 8 and MWPC 5, a root of fixed transverse length is defined; its intersection with the other two chambers should lead to the finding of two more hits (due to inefficiencies, one hit is allowed to be missing);

- For each track defined in the 2^{nd} telescope, one verifies if it fires the R_3 and R_4 slabs. If not, the track is rejected; it is also not selected if its extrapolation into the magnet crosses the iron sectors;
- The track reconstruction in the first telescope follows the same principle. Taking into account that the tracks suffers from multiple scattering while crossing the hadron absorber, the hits on these chambers must align within a root, which axis is defined by the straight line between the target mid position and the intersection point on the medium plane of the magnet;
- The reconstructed tracks in the second and first telescopes are associated to one another. This task is done finding the distance of closest approach for each extrapolated track pair within the same sextant.

The implementation of this algorithm had an inefficiency related with the storage of the tracks. Once a track was rejected for some reason, its hits could not be used anymore to combine with another hits, in order to form another possible good track. This fact had, as main consequence, the degradation of the reconstruction efficiency. For this reason the DIMUREC reconstruction algorithm has been improved [2]. The reconstruction efficiency has been improved from ~88 to ~95%.

3.2.3 The vertex determination

For each muon pair, one defines the intersection points of the tracks with the orthogonal plane to the beam axis (z=cte). The barycenter of these points is calculated taking into account their errors and the intersection point of the beam axis in the plane. The z coordinate (z_{vertex} variable) is the one that minimizes the squared sum of the distances between the intersection points and the beam axis intersection point.

3.2.4 The dimuon kinematic variables

Each reconstructed muon is represented by its 4-momentum vector:

$$\bar{P}_\mu = (E_\mu,\ \overrightarrow{p}_\mu), \quad \text{where} \quad E_\mu = \sqrt{m_\mu + \overrightarrow{p}^{\,2}_\mu}\ , \tag{3.1}$$

the dimuon 4-momentum vector being:

$$\bar{P}_{\mu_1\mu_2} = (E_{\mu_1} + E_{\mu_2},\ \overrightarrow{p}_{\mu_1} + \overrightarrow{p}_{\mu_2})\ . \tag{3.2}$$

The dimuon fundamental variables are: mass, p_T, rapidity, the azimuthal angle ϕ and the polar angle θ_{CS}. Neglecting m_μ, the dimuon mass is given by:

$$M_{\mu_1\mu_2} = \sqrt{E^2_{\mu_1\mu_2} - \overrightarrow{p}^{\,2}_{\mu_1\mu_2}} \simeq \sqrt{2p_1p_2[1 - cos\theta_1 cos\theta_2 - sin\theta_1 sin\theta_2 cos(\phi_1 - \phi_2)]}\ , \tag{3.3}$$

where p_i, θ_i and ϕ_i are the momenta, polar and azimuthal angles of each muon.

The muon p_T is calculated on the basis of the toroidal magnetic field. Let us consider a muon (in a constant azimuthal plane) trajectory making an angle α with the z axis at the entrance of a toroidal magnetic field $\vec{B}(r) = B_o/r\ \vec{u}_\phi$. In $z + \Delta z$ the correspondent elementary deflection angle is (figure 3.1):

$$d\theta = \frac{dz}{\rho} = q\frac{B(r)}{p}dz\ , \tag{3.4}$$

where q and p are the muon charge and momentum, and ρ is the curvature radius of the trajectory under the magnetic field $\vec{B}$. For high energy muons this deflection is small and we can perform the approximation [3]:

$$\frac{dr}{dz} \propto \sin\alpha\ . \tag{3.5}$$

The relation between the deflection angle and muon p_T follows:

$$\Delta\theta_0 = \int d\theta = q\frac{B_0}{p_0 \sin\alpha_0}\ln[1 + \frac{(z_{out}\ -\ z_{in})\mathrm{tg}\alpha}{r_0}]\ , \tag{3.6}$$

where α_0 and r_0 are the α and r values at the magnet entrance. A more realistic calculation, taking into account the field map, implies the division of the magnet in several slices, with thickness $\Delta z = (z_{out}\ -\ z_{in})/n$. Each deflection angle θ_i is then calculated as:

$$\Delta\theta_i = \int d\theta_i = q\frac{B_0}{p_0 \sin\alpha_i}\ln[1 + \frac{\Delta z \mathrm{tg}\alpha_i}{r_i}] \tag{3.7}$$

$$\alpha_i = \alpha_{i-1}\ -\ \Delta\theta_{i-1}, \qquad r_i = r_{i-1} + \Delta z \mathrm{tg}\alpha_{i-1}\ . \tag{3.8}$$

In general $\Delta\theta_{tot}\ =\ \sum_{i=1}^{n}\Delta\theta_i$ is different from $\Delta\theta_0$. Applying the relation:

$$\frac{\Delta\theta}{\theta} = -\frac{\Delta p}{p} \tag{3.9}$$

we get

$$\frac{\theta_0\ -\ \theta_{tot}}{\theta_{tot}} = \frac{p_{tot}\ -\ p_0}{p_0} \tag{3.10}$$

$$p_{tot} = p_0\frac{2\theta_0 - \theta_{tot}}{\theta_0}\ . \tag{3.11}$$

Through this iterative process, the muon p_T can be determined with an accuracy of less than 0.1%. In general two or three iterations are sufficient to define the muon momentum. ~1% of the events are rejected, since no momentum have been determined, either because the track has zero deflection, or it has crossed effectively the magnet coils, even after the test described in section 3.2.2. The measured p_T is corrected for the energy loss in the hadron absorber.

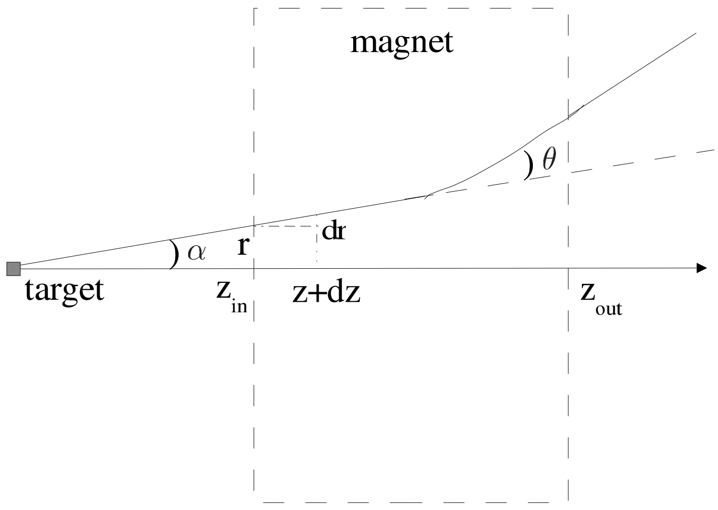

Figure 3.1: *Muon deflection in a magnetic field.*

The dimuon rapidity window in the laboratory system is $2.91 \leq y_{lab} < 3.91$. The corresponding dimuon rapidity in the hadronic center of mass frame y_{CM} is related to the dimuon rapidity in the laboratory frame through:

$$y_{lab} = y^* + y_{CM} \tag{3.12}$$

$$y^* = \frac{1}{2}\ln\frac{1+\beta_c}{1-\beta_c}, \qquad \beta_c = \frac{|\overrightarrow{P}_{lab}|}{E_{lab}} = \frac{|\overrightarrow{P}_{beam}|}{E_{beam} + m_{tgt}} \ , \tag{3.13}$$

where $\overrightarrow{P}_{beam}$ and E_{beam} are the projectile momentum and energy and m_{tgt} is the nucleus target mass (0.939×207.2 GeV/c^2). Considering Pb-incident ions at 158 GeV/c, the rapidity of the center of mass in the laboratory frame is 2.91, implying $0 \leq y_{CM} < 1$.

In order to determine the polar and azimuthal angles, θ and ϕ, in the Collins-Soper frame, let $\overrightarrow{P}_{beam}$ and $\overrightarrow{P}_{tgt}$ be the projectile and target hadrons momenta in the dimuon frame and $\overrightarrow{P}_{\mu}$ the μ^+ momentum; the $\overrightarrow{u}$ axis is chosen to be the external bisectrix of $\overrightarrow{P}_{beam}$ and $-\overrightarrow{P}_{tgt}$ and $\overrightarrow{v}$ is chosen to be parallel to $\overrightarrow{P}_{beam} \times \overrightarrow{P}_{tgt}$. Then, θ and ϕ, in the Collins-Soper frame, are defined as being the angle between $\overrightarrow{u}$ and $\overrightarrow{P}_{\mu}$ and the angle between $\overrightarrow{v}$ and $\overrightarrow{u} \times \overrightarrow{P}_{\mu}$, respectively.

For the present work the dimuons were selected having masses above 1.5 GeV/c^2, rapidity in the center of mass interval $0 \leq y_{CM} < 1$ and with a Collins-Soper angle $| cos\theta_{CS} | < 0.5$. Beyond this kinematic window of rapidity and $cos\theta_{CS}$, the acceptance is very small (<1%).

3.3 Track selection

After the reconstruction process, the tracks are selected according to geometrical and quality criteria.

- The Fiducial Cut
  This cut takes into account the active volume of the MWPCs. Only the tracks that cross entirely the three planes (u, v and y) are accepted.

- The Image Cut
  It is a cut that guarantees a spectrometer acceptance independent on the muon charge. Once a dimuon is accepted, the magnetic field is virtually reversed. Such an "image dimuon" should be equally accepted under this field, otherwise it is rejected. This cut allows a statistical treatment of the combinatorial background, as will be explained in section 4.2.1, however the price to pay is very high, since ±55% of the dimuon statistics is loss.

3.3.1 The P×Dtarget cut

The *Dtarget* variable ensures that the mostly off-target muons are excluded. This is done by means of a cut on the transverse distance, in the middle target plane, between the extrapolated muon track from the first telescope and the beam line (figure 3.2). This cut takes into account that the x and y distances to the target center of the extrapolated tracks are gaussian distributed; therefore, the transverse distance to the beam line of each track should follow a χ^2 distribution. If the probability is very small, the track is rejected. However, there is a correlation between the transverse distance dispersion and the muon momentum due to the multiple scattering suffered in the absorber:

$$\sigma_{Dtarget} \propto \frac{1}{P} \tag{3.14}$$

For this reason the $P\times Dtarget$ variable is used instead.

To establish the maximum allowed transverse distance for a reconstructed track to be considered as produced in a target interaction, the tuning of several parameters is needed. This tuning is done separately for convergent and divergent tracks [1]. Besides, only dimuons with mass above 3 GeV/c^2 are considered, a range where the statistics are still considerable and the combinatorial background formed by uncorrelated like-sign

[1] Depending on its charge and signal of the magnetic field, a muon has a convergent or divergent trajectory in the spectrometer.

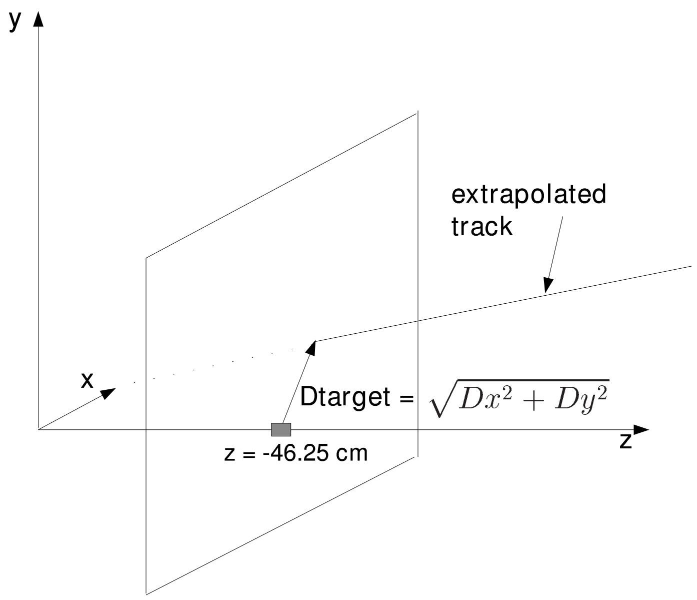

Figure 3.2: *Schematic view of the Dtarget variable.*

pairs, is no more significant. This mass cut is inevitable because signal dimuons and background have different *Dtarget* gaussian distributions, which cannot be disentangled, unless the dimuon classification of convergent and divergent tracks is lost. Then, and as the $P \times Dtarget$ variable is not mass dependent in a first order approximation, these parameters can be applied safely to all track muons to test their origin. The parameters tuning is performed in three steps:

- The first step consists in the distribution of the muons momentum, P, in 25 equidistant bins, between 0 and 75 GeV/c, and in the determination of the P mean value in each histogram bin. Therefore, there will be two sets of 25 parameters, each one for convergent and divergent tracks, which are the P mean values;

- The goal of the second step is to establish, for each momentum range, an off-set displacement of the muon tracks with respect to the target center. These offset displacements, Δx and Δy, are the mean values of the Dx and Dy gaussian distributions, fitted to the tracks, which momentum value is contained in the respective momentum range. There will be 4 sets of 25 offset parameters, with respect to the Dx and Dy projection axes, both for convergent and divergent tracks. Figure 3.3 shows a typical fit to the Dx distribution, relative to tracks which momentum ranges between 39 and 42 GeV/c.

  The tails of these gaussian distributions are composed by tracks with a small probability of belonging to an in-target produced dimuon. In fact, for the Pb–Pb 2000 data taking, the number of such tracks is very small because the target region was

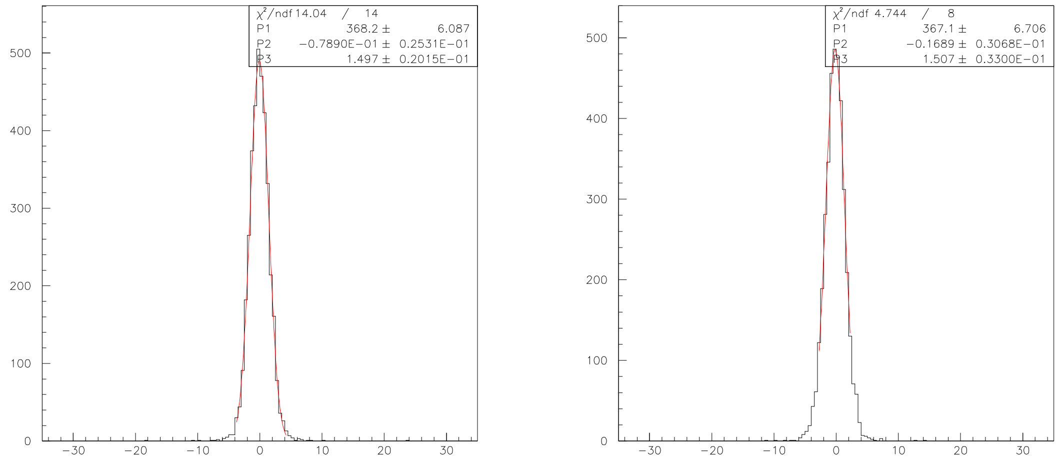

Figure 3.3: *The gaussian distributions of the distance x, w.r.t. the target center, for convergent (left) and divergent (right) muons with momentum between 39 and 42 GeV/c.*

placed under vacuum. These spurious events come, essentially, from interactions of the Pb-incident ion with the detectors surrounding the target;

- In the third step one performs the tuning of the dispersions ($\sigma_{Dtarget}$) with respect to the target center, for the transverse distance distributions within each momentum range, and taking into account the off-set displacements, Δx and Δy, tuned in the previous step. Two sets of 25 parameters, for convergent and divergent tracks, are obtained.

The variable:

$$P \times Dtarget = \frac{P \times \sqrt{Dx^2 + Dy^2}}{\sigma_{Dtarget}} \tag{3.15}$$

is characteristic of each muon track. The χ^2 probability distribution of P×Dtarget is plotted in figure 3.4 for both muons [2] in the J/ψ mass range, i.e., $2.8 < M_{\mu\mu}^{J/\psi} < 3.4$ GeV/c^2, considering opposite signs and after combinatorial background subtraction. In fact, the like sign muons contaminate slightly the J/ψ sample, imposing non-totally flat distributions, as seen on the left panel. A cut is performed in order to remove the spike. The events below this chosen value correspond to tracks which transverse distance to the target center has a very low probability to follow a χ^2 distribution, possibly because they have been originated in collisions upstream from the target, namely in a Pb-detector interaction.

The adopted cut for the Pb–Pb 2000 data is 2%, which means that, if at least one

[2] The convergent and divergent tracks are randomly distributed in muon 1 and muon 2. This classification has only to do with the track reconstruction order.

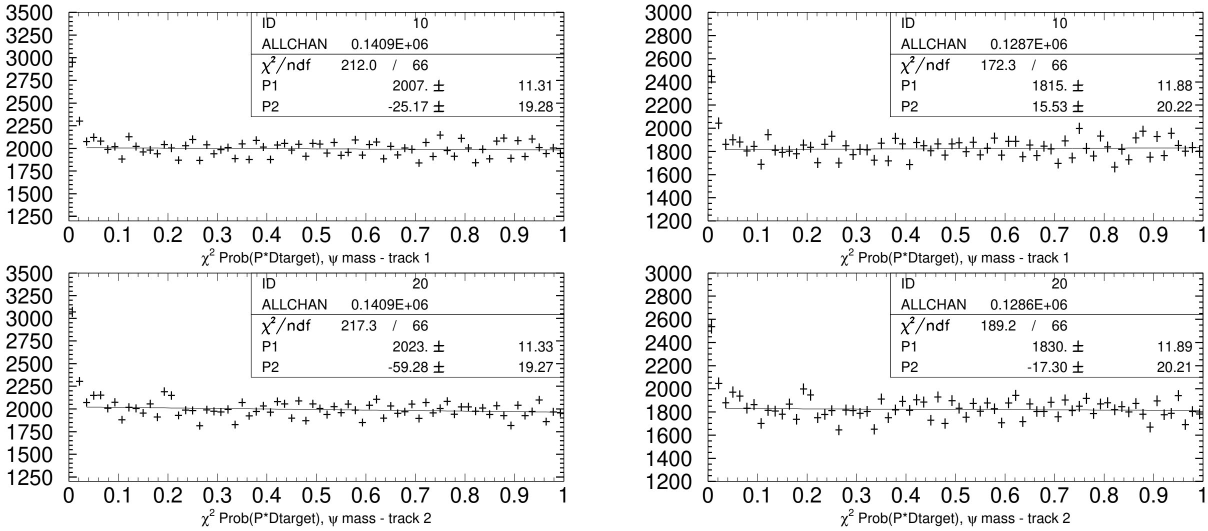

Figure 3.4: χ^2 *prob(P×Dtarget) for J/ψ mass range, before (left) and after (right) combinatorial background subtraction.*

muon track has a probability $< 2\%$ to obey to the χ^2 distribution, the dimuon is rejected.

In order to ensure track quality criteria coherence, the P×Dtarget cut is also applied to each "image track".

3.4 Data selection from detector's variables

All information concerning the kinematics of the reconstructed dimuons, as well the information from the detectors, is stored in μDSTs (Data Summary Tapes). The decoding program, called RELMIC [4], reads these cartridges and evaluates the quality of the event, based on the information from the detectors, namely the calorimeters and target region ones. The program provides ntuples storing the dimuon kinematic variables, the signal amplitudes in the calorimeters elements and detectors flags responsible for others quality cuts. In this way, a final data sample, clean and unambiguous, is obtained.

3.4.1 Pile–up rejection

There are two kinds of pile–up to be considered: the beam pile–up and the interaction pile–up.

- Beam pile–up
  It may be a problem if two or more of the pile–up events interact in the target too much closer in time, since this situation may produce a bias in the transverse energy

measurement. It may constitute a problem in the forward energy measurement, as well. One way to avoid this kind of events is to reject them directly on the incoming beam and to use only "events without pile–up". These events are those where a second incident ion is not present during the 20 ns gate of the Beam Hodoscope ADCs. However, a pile–up cut can be very penalizing as the pile–up probability is very high for our beam intensity, $7{\times}10^7$ ions per spill.
As an estimate of the beam pile–up, it is assumed that the repartition of the beam ions, within the reading gate, follows a Poisson distribution. For a beam intensity I and spill B, the probability of having pile–up, i.e., one or more ions within Δt = 20 ns window, is given by:

$$\text{pile–up} = 1 - P(0) = 1 - exp(\Delta t \times \frac{I}{B}) \; . \tag{3.16}$$

For a beam intensity of $7{\times}10^7$ ions per burst and a spill of 4.8 s, the probability of having beam pile–up within the Δt = 20 ns gate is thus 25 %.
Two flags account for the beam pile–up: one is NIBHAD (Number of Ions in the Beam Hodoscope detected by the ADcs) and the other is NIZDC (Number of Ions in the ZDC).

- Interaction pile–up
  As referred before, if two (or more) incident ions interact in the target during the 20 ns gate, the energy measurement in the electromagnetic calorimeter may be biased. Therefore, only such produced dimuons should be excluded from the final analysis data set and not all events obeying the beam pile–up condition. Those events are identified through the analysis of the analogical signal shapes in the EMC. For a given trigger, the flag NICALO=1 ensures that no interaction pile–up has occurred during a time interval of about 25 ns. This variable is also powerful in the detection of events which EMC signal is not compatible with the signal reference shape, without being necessarily pile–up events. In figure 3.5 the high E_T spectrum tail is washed out by the introduction of the NICALO=1 flag.

The number of ions interacting in target is given by:

$$I_{int} = I_{Pb}.P_{int} = I_{Pb}.[1 - exp(-L_T/\lambda_I)] \tag{3.17}$$

where I_{Pb} is the number of incoming ions, L_T is the total target thickness and λ_I is nuclear interaction length. From the information reported in table 2.1 we notice that only ~10% of the incident ions interact in the target. Since this probability is independent from the beam pile–up one, the interaction pile–up probability is only 2.5%. For this reason, one can raise the question on the necessity to activate the NIBHAD flag. Should it be used, a ~14% of dimuon statistics would be lost, a too much drastic cut. The flag NICALO should be sufficient. Indeed, fig 3.6 shows that the introduction of the NIBHAD flag does not improve the E_T spectrum.

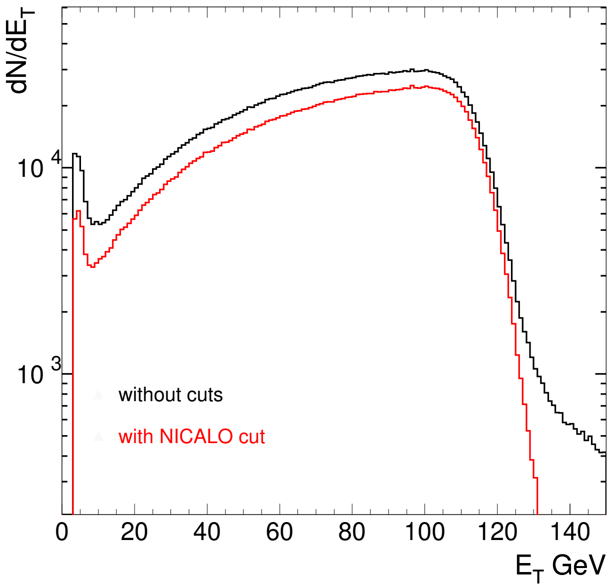

Figure 3.5: *Pb–Pb 2000 data E_T spectra (not corrected for inefficiencies): with and without NICALO cut.*

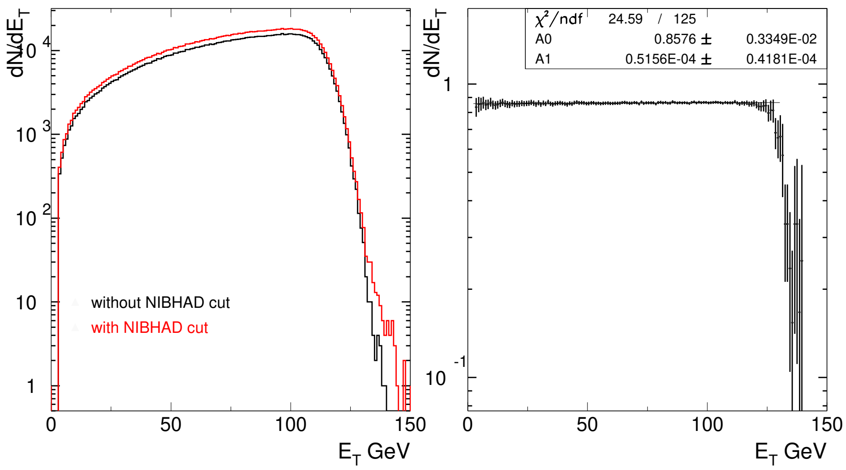

Figure 3.6: *Pb–Pb 2000 data E_T spectra (not corrected for inefficiencies): with and without NIBHAD cut (left); the ratio of the two spectra (right) is not E_T dependent.*

The NIZDC flag is used instead to reject the beam pile–up events. In fact, this variable has been tuned for analyses that use the forward energy, E_{ZDC}, as the centrality estimator. It is less restrictive than the NIBHAD flag, since its algorithm can recover pile–up events by correcting the forward energy relatively to the one of a single non–interacting Pb ion. The number of ions hitting two different BH blades in a time window of 34 ns, is set in the NIZDC flag. In order to ensure a more fiducial data sample, the NIZDC flag is required to be $\leq$2 in the present analysis. This cut implies a statistics loss less than 4%.

3.4.2 The In-target interaction identification

The target algorithm in the Pb–Pb 1996 and 1998 data analyses made use of the signals given by the two quartz blade sets, located off the beam axis on the left and right sides of each sub-target [5, 6]. Its role is to identify where the primary interaction takes place. Besides, possible re-interactions of spectator fragments downstream from the primary blade could also be tagged. The variable that accounts for the interactions is NOCIBI (meaning number of primary interaction sub-target), which attributed values are the following:

- 0 or 10 or 20 $\rightarrow$ interaction upstream from the sub-targets;
- 1-7 or 11-17 or 21-27 $\rightarrow$ number of the hit sub-target; 1-7 range means that both blades located on the left and right sides of each sub-target (7 in total) have been fired in the interaction. 11-17 and 21-27 ranges mean that only one blade has been hit, right or left, respectively;
- 8 $\rightarrow$ interaction not recognized.

This interaction algorithm is a powerful off-target rejection tool. However, its tagging efficiency for peripheral collisions ($E_T < 40$ GeV), or in the detection of re-interactions is low. These two types of events give signals which can not be disentangled from the ones generated by δ rays of the non interacting incident ions across the Pb sub-targets. This was a major problem of the Pb–Pb 1996 and 1998 setups.

For the Pb–Pb 1998 and 2000 setups, where only a sub-target was used, a new target identification was developed, based on the Multiplicity Detector features, denominated as the NOCIMD algorithm. The in-target interactions are assured requiring good correlation between the hits in the two planes, MD1 and MD2 (figure 3.7). The variable NOCIMD is set to:

- 0 or 7 if the interaction has occurred upstream or downstream from the target;
- 4 if the interaction occurs in target;
- 8 if for this triggered event no interaction has occurred.

The NOCIMD target algorithm works for $E_T > 3$ GeV, being fully efficient for $E_T > 15$ GeV, as seen in figure 3.8 [7]. The Pb–Pb 1998 and 2000 data analyses presented in this work make use of it, selecting those events for which NOCIMD flag was set to 4.

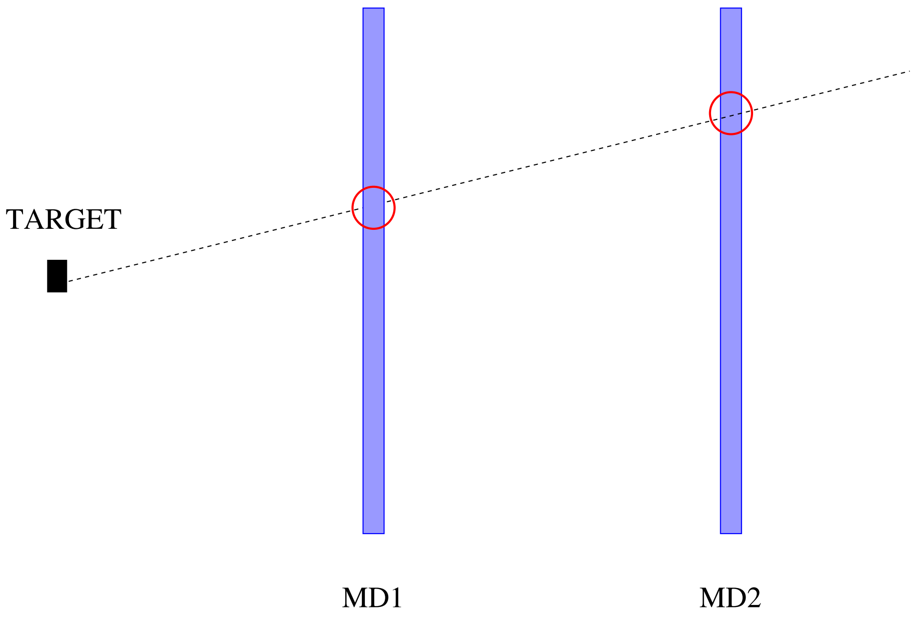

Figure 3.7: *The combining hits in the Multiplicity Detector*

3.4.3 Other beam and target cuts

- The parasitic cuts
  As referred in section 2.1.2, the interactions of a Pb-incident ion in the Beam Hodoscope are tagged by the BHI and BHInew detectors. The variable that signals such parasitic interactions, called NPARAS (Number of PARASites in BHI and BHInew detectors) is set to 1, in order to discard such events.

- The anti-halo cuts
  The two anti-halo quartz counters, located close to the target, detect ions and beam fragments that constitute the beam halo (1.5 mm apart the beam axis is tolerated). The variable NOHALO (NO particle in the anti-HALOs detectors) flags the passage of the incident ion through a hole of 1.5 mm radius with respect to the z-axis. However, this variable has not been used in the analysis of the Pb–Pb 2000 data, since the fragments produced in in-target interactions were detected by retro-diffusion, leading to the rejection of a significant number of good events. This detector was used, instead, to optimize the beam centrality.

3.4.4 The $E_T - E_{ZDC}$ correlation

In order to recover the peripheral interactions loss due to the NOCIBI target algorithm inefficiency during the Pb–Pb 1996 data run, a new selection criterium was developed, based on the correlation between the E_T and E_{ZDC} energies measured by the two NA50 calorimeters. This method rejects most of the off-target contamination without imposing

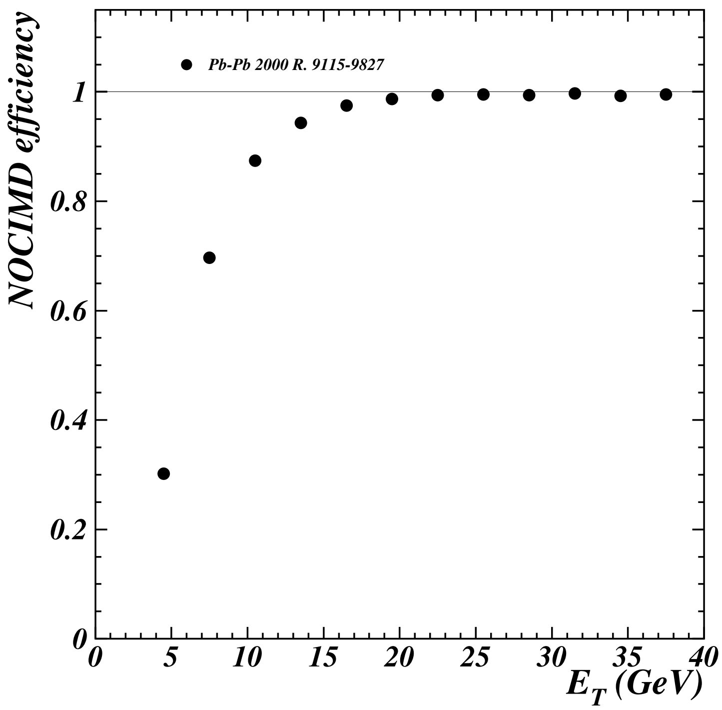

Figure 3.8: *The NOCIMD efficiency for the Pb–Pb 2000 data.*

a positive response from the target algorithm. A contour cut in the $E_T - E_{ZDC}$ correlation is applied in Pb–Pb 1996 data [5]. For the Pb–Pb 1998 analysis a new method, described hereafter, has been developed [8] and applied to Pb–Pb 2000 data. Figure 3.9 shows its $E_T - E_{ZDC}$ correlation.

As a first step, one projects the distribution in the transverse plane with respect to the $E_T - E_{ZDC}$ correlation and adjusts a gaussian function in order to obtain the dispersion, σ, as can be seen in fig 3.10. Several attempts concerning the axes rotation were done in order to minimize the dispersion. They are summarized in table 3.2.

Two straight lines forming a 2σ band around the mean (corresponding to the 3.77 mrad rotated angle) are drawn (figure 3.11). Consequently, the data selected should obey to the condition:

$$110.08 - 0.00377 \times E_{ZDC} < E_T < 148.89 - 0.00377 \times E_{ZDC} \ . \tag{3.18}$$

This 2σ level cut has the purpose to ensure a cleaner sample.

Table 3.3 shows the number of muon pairs having mass >1.5 GeV/c^2 and belonging to the NA50 kinematic domain, after each cut. The order of the cuts is somewhat arbitrary and hides some redundancy among them; i.e., an event that is rejected by some cut, could be equally rejected by another one.

Thus, after all these cuts, the final data sample has 1267736 events. This number corresponds to 55% of the data sample that has resulted from the reconstruction process

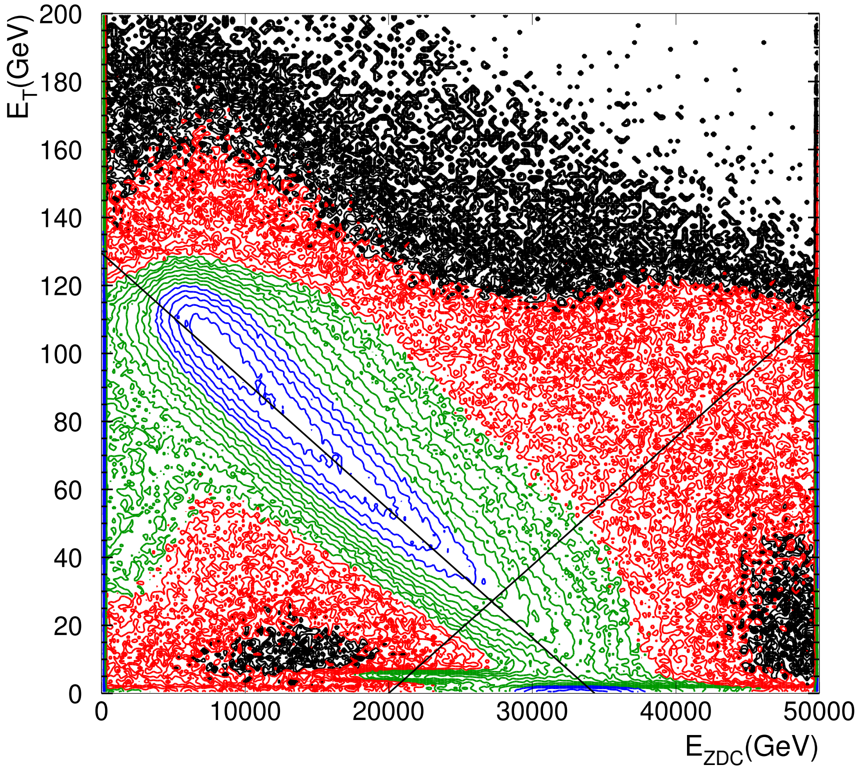

Figure 3.9: *The $E_T - E_{ZDC}$ correlation of Pb–Pb 2000 data. The plot is obtained with logarithmic scale in z.*

θ (mrad)	σ	$<\ >$	χ^2/ndf
3.57	9.873	126.7	1.81
3.67	9.757	128.1	2.04
3.77	9.704	129.5	2.33
3.87	9.708	130.9	1.95
3.97	9.765	132.3	2.06

Table 3.2: *Parameters of the gaussian fits to the $E_T - E_{ZDC}$ correlation projected in the transverse axis for Pb–Pb 2000 data.*

and the kinematic cuts application.

3.5 Data selection in the Pb–Pb 1998 sample

The event reconstruction follows the general criteria described in section 3.2, but the DIMUREC program is the standard one [1]. The main characteristics of the Pb–Pb 1998

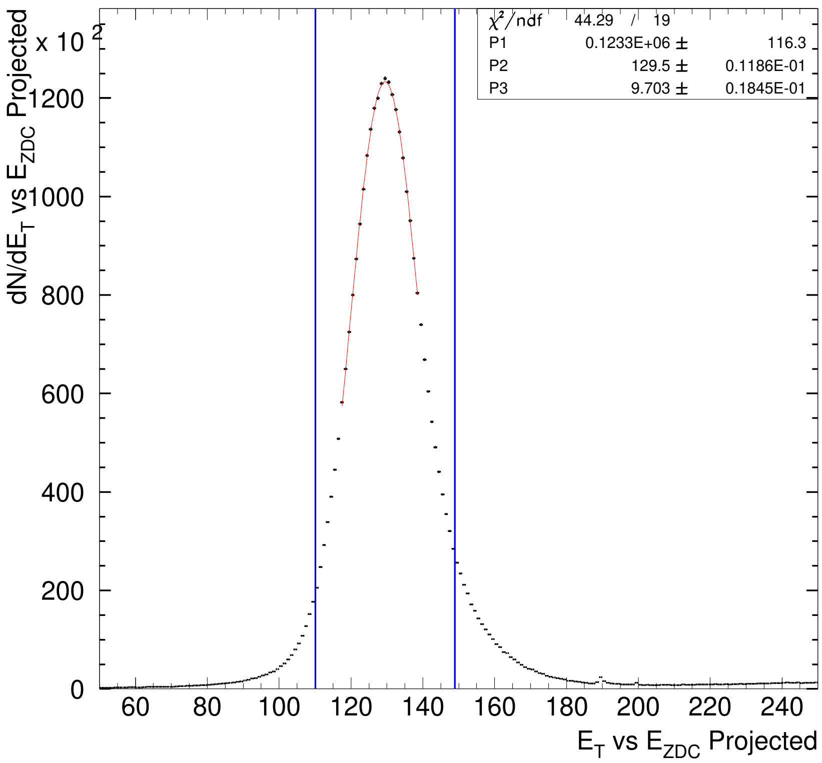

Figure 3.10: *The $E_T - E_{ZDC}$ correlation of Pb–Pb 2000 data projected in the transverse plane and adjusted with a gaussian function.*

Cut	Number of reconstructed events
After NPARAS	2285926
After NICALO	1806638
After NIZDC	1720474
After NOCIMD	1622930
After $E_T - E_{ZDC}$ band	1372288
After P×Dtarget	1267736

Table 3.3: *Number of events after each detector variables cut for the Pb–Pb 2000 data.*

run are reported in table 2.1. Table 3.4 summarizes the data selection.

One should notice the higher P×Dtarget cut (6%) relatively to the 2000 one (2%). This higher level is due to the fact that the target region was not in vacuum in the year 1998, thus providing much more off-target interactions and, therefore, demanding a higher P×Dtarget cut.

The use of NOCIMD as the target identification algorithm allows the study of peripheral collisions, while NOCIBI does not, by the reasons pointed out in section 3.4.2. Nevertheless, for the Pb–Pb 1998 data, and on contrary to the Pb–Pb 2000, this target interaction algorithm is globally less efficient than the NOCIBI one. In the Pb–Pb 2000

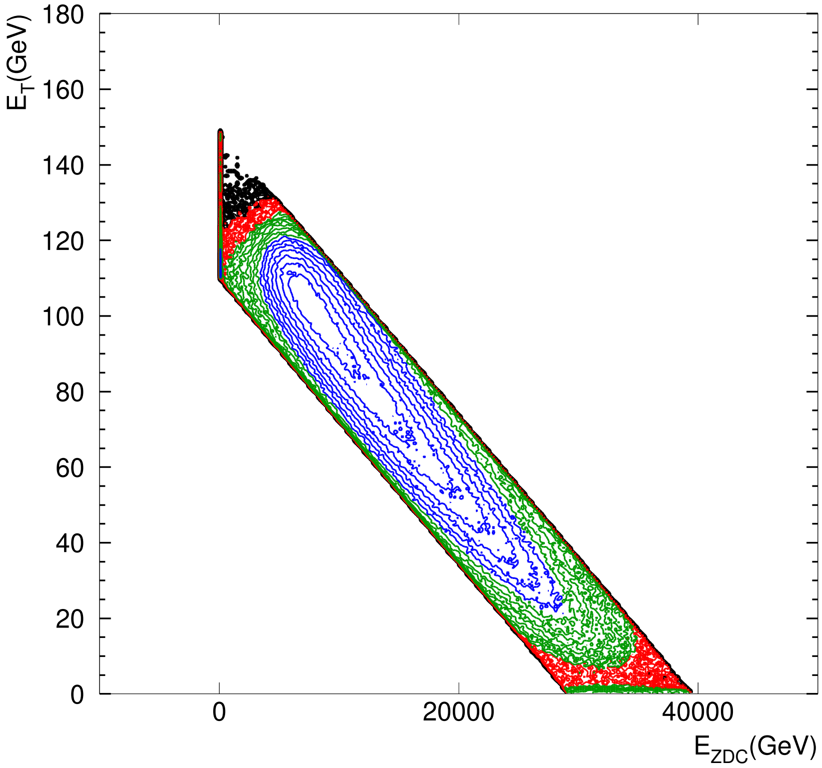

Figure 3.11: *The $E_T - E_{ZDC}$ correlation of Pb–Pb 2000 data after the 2σ cut.*

Run selection	all standard runs
P×Dtarget cut	6% at χ^2 probability level [8]
$E_T - E_{ZDC}$ correlation	diagonal projected method [8]
Parasitic cut (NPARAS)	Yes
Anti-halo cut (NOHALO)	Yes
Target Identification algorithm	NOCIMD = 4
Beam pile–up (NIBHAD)	No
Interaction pile–up (NICALO)	No

Table 3.4: *The Pb–Pb 1998 data selection.*

run, major improvements were made on the Multiplicity Detector reaching 100% efficiency of the NOCIMD algorithm for E_T>15 GeV [7]. Figure 3.12 shows the E_T spectra of Pb–Pb 1998 data with NOCIBI and NOCIMD target algorithms. One clearly observes that NOCIMD recovers a significant number of events at low E_T that has been rejected by NOCIBI.

This data selection does not include any pile–up rejection. The NICALO variable, that accounts for interaction in target pile–up, was not available for the Pb–Pb 1998 run. However, a strong redundancy between the E_T *vs* E_{ZDC} band and the NICALO cut in the

Pb–Pb 2000 data is verified, and, regarding the 1998 sample, a similar behaviour is expected. Events with signal shape problems, for instance, events with too much E_T and/or too much E_{ZDC} with respect to normal events, would be rejected either by NICALO or by the E_T *vs* E_{ZDC} band cut. In what respects the beam pile–up detection, we have verified that, on the contrary to what happens with NOCIBI, the use of NOCIMD prevents the rejection of 6% statistics the NIBHAD cut would impose, as can be seen in figure 3.13. In fact, the use of this variable has a strong effect in the E_T spectrum when the target algorithm is NOCIBI.

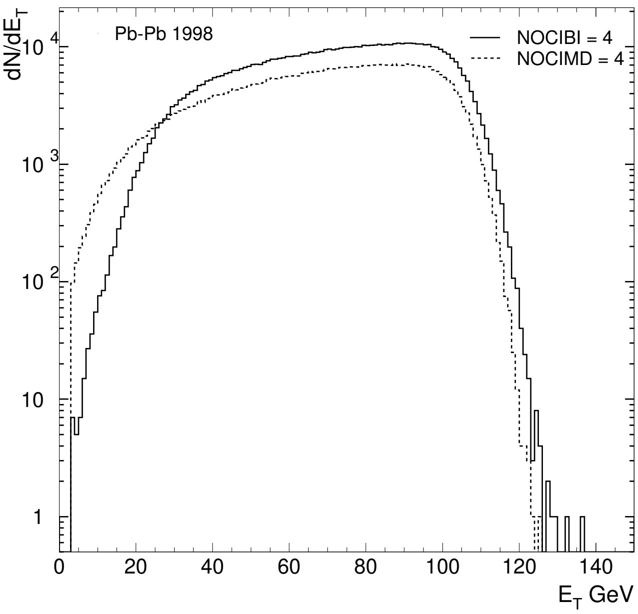

Figure 3.12: *The Pb–Pb 1998 E_T spectra with both target interaction algorithms.*

3.6 Data selection in the Pb–Pb 1996 sample.

The Pb–Pb 1996 run has provided the most significant statistical data sample. Indeed, 190000 J/ψ, ready for analysis, have been collected. Also, the amount of high mass muon pairs, in particular those produced in peripheral reactions, has been significantly increased. Several improvements, with respect the Pb–Pb 1995 run, have been implemented, namely the use of the very forward hadronic calorimeter, ZDC, and a better beam optics [5].
The main difference of the Pb–Pb 1996 setup, with respect the 2000 and 1998 ones, is the target assembly made of seven sub-targets, spaced by 25 mm and having 12 mm of total thickness. Despite the large luminosity that such thick target provides, two important

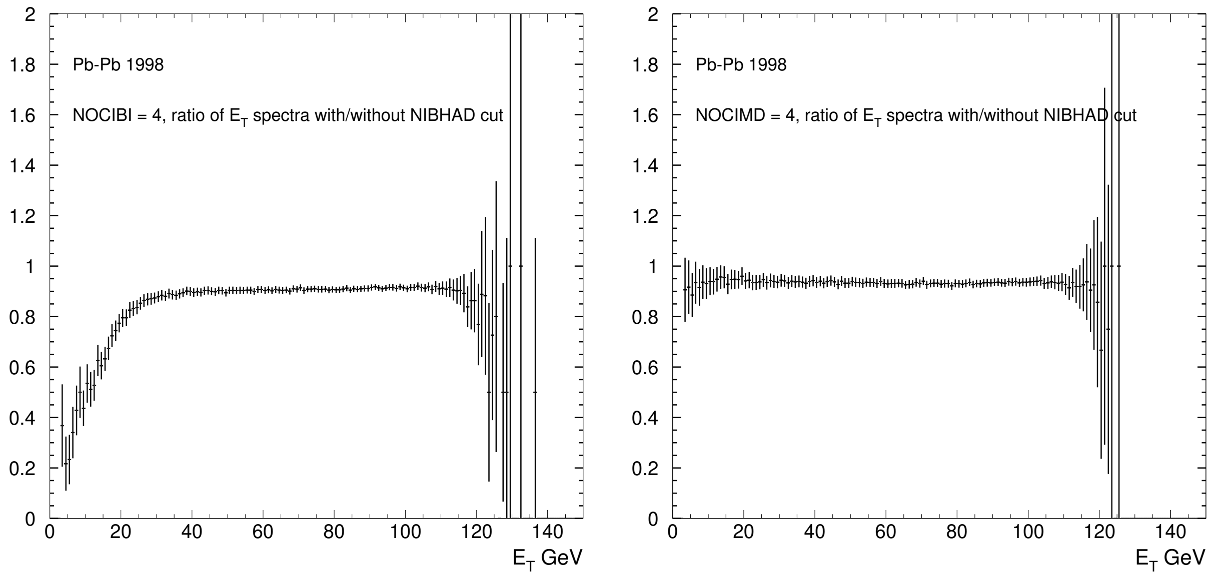

Figure 3.13: *The effect of the NIBHAD cut in the E_T spectrum when using NOCIBI or NOCIMD as the target interaction algorithm*

drawbacks were found: the sub-target identification inefficiency for events with E_T values lower than $\sim$ 40 GeV and the re-interaction problem that has affected, mainly, the high centrality domain.

The Pb–Pb 1996 data analysis presented in this work follows the criteria of the Pb–Pb 2000 (and 1998) analyses. The data selection, that takes into account the particular features of this run, is summarized in table 3.5.

Run selection	all standard runs
P×Dtarget cut	5% at χ^2 probability level
$E_T - E_{ZDC}$ correlation	2σ contour cut [5]
Parasitic cut (NPARAS)	Yes
Anti-halo cut (NOHALO)	Yes
Target Identification algorithm	NOCIBI = 1-8, 11-17, 21-27
Beam pile–up (NIBHAD)	Yes
Interaction pile–up (NICALO)	Yes

Table 3.5: *The Pb–Pb 1996 data selection.*

Bibliography

[1] A. Romana, DIMUREC User's Guide (ver 2.00/03), 1997

[2] R. Shahoyan, J/ψ and ψ' production in 450 GeV p–A interactions and its dependence on rapidity and X_F, PhD Thesis, Universidade Técnica de Lisboa, IST, April 2001

[3] P. Bordalo, Etude des distributions de l'impulsion transverse de paires de muons produits dans les intéractions π^- W à 194 et 284 GeV/c, Thèse de Doctorat, Université Paris-Sud Juin 1986

[4] A. Romana, RELMIC User's Guide (ver 2.00/06), 1997

[5] M.C. Abreu et al. (NA50 Coll.), Phys. Lett. B450 (1999) 456

[6] M.C. Abreu et al. (NA50 Coll.), Phys. Lett. B477 (2000) 28

[7] F. Prino, NA50 Internal Note, May 2004

[8] C. Quintans, Study of the Production of the $\rho + \omega$ and ϕ Vector-Mesons in Lead induced collisions at 158 GeV/nucleon, PhD Thesis, Universidade Técnica de Lisboa, IST, November 2002

Chapter 4

Data analysis

The present study on charmonia suppression is based on the dimuon invariant mass spectrum analysis in a region that stands between 1.5 and 7 GeV/c^2. The measured muon pairs have several origins. They can be true muon pairs from a resonance or virtual photon decays, or true-like muon pairs originating from the uncorrelated decays of a correlated heavy quark pair, or fake pairs from accidental combinations of muons coming from uncorrelated processes. Thus, several dilepton processes contribute to the mass spectrum: the resonances J/ψ and ψ', as well as the continuum formed by Drell-Yan, open charm semi-leptonic decays and the combinatorial background. In order to disentangle such processes and to calculate their spectrometer acceptances, each physical process is generated using the Monte Carlo method, and such events are let to go through the simulated spectrometer apparatus.

4.1 Monte Carlo simulations

The simulation package of the NA50 experiment is called DIMUJET [1]. The program generates the physical processes of interest for the NA50 program (resonances, Drell-Yan, $D\bar{D}$ mesons and like-sign pairs) and simulates the passage of the dimuons through the apparatus, evaluating the energy loss, the multiple scattering suffered by the muons while crossing the absorber, their deflection in the magnetic field and recording the hits in the telescopes (MWPCs and trigger hodoscopes). The generated dimuons are produced in the target and they are not constrained by the response of the target region detectors, as the real data (see section 3.4); but, and very important, they are reconstructed with the same NA50 DIMUREC [2] program, exactly in the same conditions as real events are. This means that the same track reconstruction and selection criteria applies, including the Image cut and P$\times$Dtarget test. It is considered that the dimuon acceptances are not dependent on the collisions centrality.

The Coulomb scattering is treated by the theory of Molière, its scattering angular distribution being independent on the radiation length, X_0, of the absorber materials [3]. The energy loss is simulated accounting for ionization, bremsstrahlung and pair creation. Straggling is modelled with a Landau distribution for ionization loss and by a $1/E$ distribution for the others. The Fermi motion of the nucleons inside the nucleus is taken into account.

The J/ψ and ψ' are generated as Dirac distributions, with masses 3.097 GeV/c^2 and 3.686 GeV/c^2, respectively, since their natural widths (87 KeV and 277 KeV) are orders of magnitude smaller than the experimental resolution. It is assumed that J/ψ is directly produced in the collision, without taking into account the fraction of events that come from decays of higher states. They are generated empirically in rapidity with a gaussian distribution with $\mu = 0$ and 0.6 units width. The transverse momentum generation follows the parametrization of a thermal distribution, $\mathrm{d}\sigma/dp_T = p_T M_T K_1(M_T/T)$, where K_1 is the modified Bessel function of the second kind and first order in the transverse mass with T=236 MeV. These parameters were tuned in order to reproduce the experimental spectra of the S–U data, taken at 200 GeV/c [4], but they account very well for Pb–Pb collisions at 158 GeV/c, as may be verified in figure 4.1. The disintegration of the

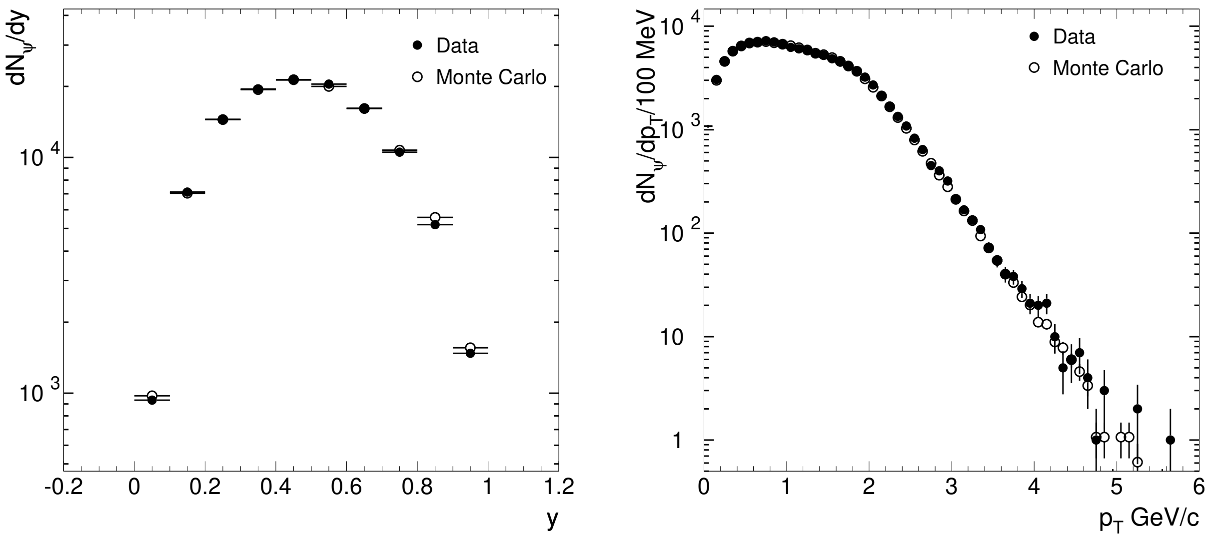

Figure 4.1: *The J/ψ (signal events of the invariant mass spectrum between 2.9 and 3.3 GeV/c^2) y and p_T experimental distributions compared to the Monte Carlo ones obtained with the physical inputs explained in the text.*

J/ψ and ψ' resonances in the Collins-Soper frame makes use of an uniform distribution, $dN/dcos\theta_{cs}$, since they are $1S$ and $2S$ states, respectively.

The Drell-Yan is evaluated at Born level with PYTHIA (ver. 6.125)[6], using GRV LO 94 [7] set of structure functions of the nucleon ($\Lambda_{QCD} = 200$ MeV, $Q^2_{min} = 0.4$ GeV^2), whose minimum 4-momentum transferred and x domain are adequate to the NA50 phase space. This parametrization describes quite well the available data on the proton structure function, F_2^p, from fixed-target NMC, BCDMS Collaborations and SLAC for $Q^2 >$ 5 GeV^2 and 0.0125$< x <$0.275 [8, 9, 10]. It reproduces also well the small–x region ($x <$0.05) and $Q^2 <$ 5 GeV^2 NMC and E665 data [8, 11]. This set of distributions has into account the asymmetry $\bar{u} \neq \bar{d}$ in the sea of partons, as measured by the NA51 experiment ($< x >$=0.18) [12]. Generations with different PDF sets are also performed in order to establish a theoretical uncertainty on the Drell-Yan differential cross section, but this subject will be discussed in the next chapter. At Born level, leptons are produced back–to–back, i.e., with zero p_T; to overcome this inadequate physical picture, a primordial K_T inside the hadrons is considered, gaussian distributed with a 0.8 GeV width. Figure 4.2 shows the comparison between data and Monte Carlo y and p_T distributions, for events with mass $>$ 4.5 GeV/c^2. To account for isospin asymmetry, pp, pn, np and nn collisions

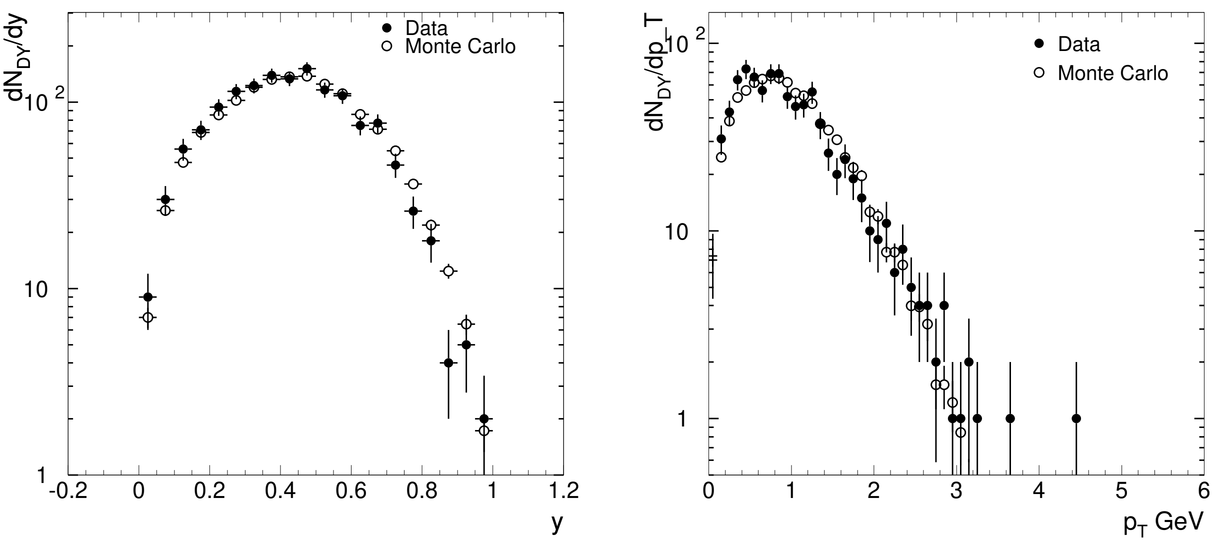

Figure 4.2: *The Drell-Yan y and p_T data distributions, compared with the ones obtained in Monte Carlo. The invariant mass is $>$ 4.5 GeV/c^2.*

are generated separately and weighted, according to the lead nuclei protons and neutrons composition, in order to match the collision system.

The $D\bar{D}$ mesons are also generated with PYTHIA, at leading order of QCD, using m_c = 1.35 GeV/c^2 and a gaussian distributed k_T with 1.0 GeV/c width. At this order only the $q\bar{q} \longrightarrow c\bar{c}$ and $gg \longrightarrow c\bar{c}$ processes are considered. The PDFs used are MRS 43 [13] (Λ_{QCD} = 230 MeV, Q^2_{min} = 0.625 GeV^2). Beyond the $D^{\pm}$ mesons, also the D^0, $\bar{D}^0$, $D_s^{\pm}$ and Λ_c ones are considered. The simulation of such mesons is heavy, in terms of CPU time, since most of the generated events do not give rise to a dimuon in the NA50 phase space domain, so, in order to reduce the time, the charmed mesons are forced to decay semi-leptonically into muons. Then, each muon pair accepted in the defined kinematic window is weighted by the branching ratio of their parents. Two more generations have been performed, in order to check the influence of the charm quark mass and the intrinsic transverse momentum of the incoming partons on the differential cross sections and acceptances. As expected, considering full phase space domain, they are very constrained by those parameters, however, in the small spectrometer kinematic domain they become very similar. Figure 4.3 shows the histograms and respective ratios of the full phase space $D\bar{D}$ generated events and the ones obtained in NA50 phase space domain, for different $c-$quark masses ($m_c = 1.35$ and 1.7 GeV/c^2). A similar comparison, displayed in figure 4.4, is obtained when the chosen σ_{k_T} is 0.8 GeV/c instead of 1.0 GeV/c. The influence of structure functions has been checked, as well. The GRV LO 98 [10] set of PDFs has been used to simulate the D mesons, but the $D\bar{D}$ shape remains unchanged as observed in figure 4.5. For this reason and as the $D\bar{D}$ generation is demanding, the one using MRS 43 is kept for analysis. Evaluating the uncertainties associated with the physical parameters used to simulate the open charm, one concludes that, in the NA50 kinematic window, the $D\bar{D}$ differential cross section is not sensitive to the chosen $c-$quark mass, intrinsic transverse momentum of partons inside the hadron and parton density functions.

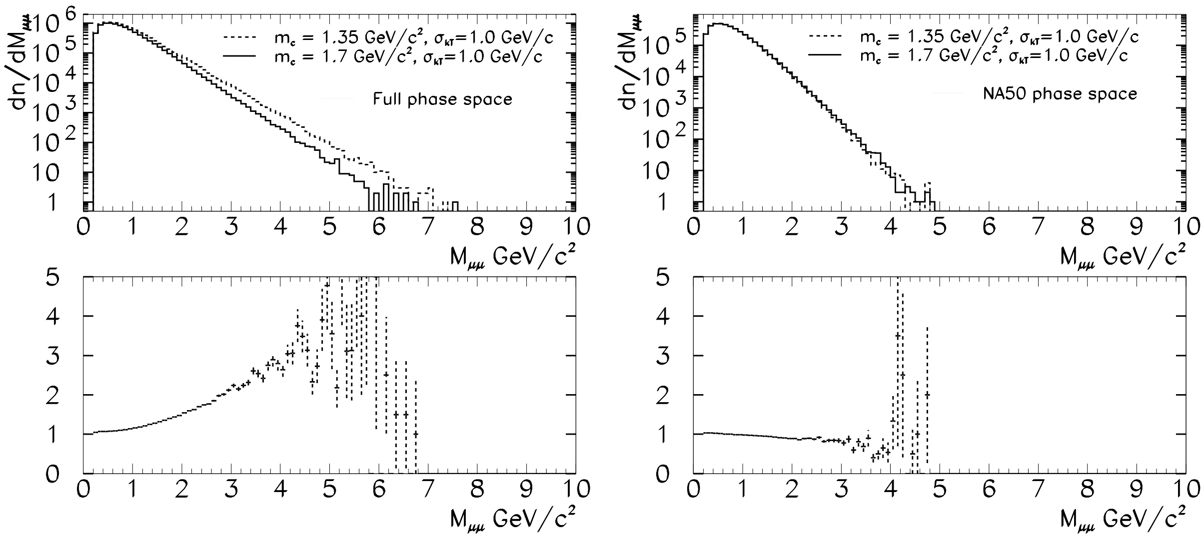

Figure 4.3: *$D\bar{D}$ PYTHIA generated events in full phase space (left) and in the NA50 spectrometer domain (right) using different values of charm quark: 1.35 GeV/c^2 or 1.7 GeV/c^2; the lower plots are the respective ratios.*

The Drell-Yan lepton pairs, as well as the semi-leptonic decays of the $D\bar{D}$ mesons, once generated, are imposed to go through the apparatus (DIMUJET-DIMUREC chain).

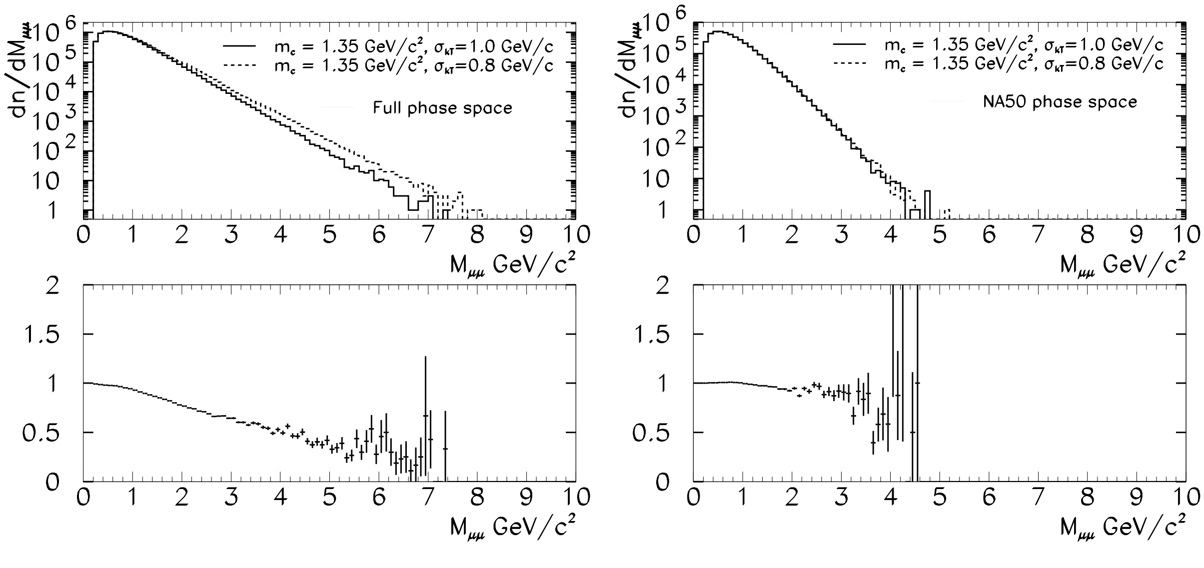

Figure 4.4: *$D\bar{D}$ PYTHIA generated events in full phase space (left) and in the NA50 spectrometer domain (right) using different values for the intrinsic transverse momentum of partons inside the hadron: 1.0 GeV/c or 0.8 GeV/c; the lower plots are the respective ratios.*

4.1.1 Mass spectra

Monte Carlo events suffer multiple scattering and energy loss in the absorber, as real muons do. This is particularly visible in the J/ψ and ψ' reconstructed shapes, whose Dirac's delta functions degenerate in gaussian distributions with increasing smearing tails. These simulated and reconstructed resonance events are smoothed by empirical functional forms, which are pure gaussians close the poles and have non symmetrical mass dependent dispersion tails:

$$\frac{dN^{J/\psi,\psi'}}{dM} = a_0 \exp\left\{-\frac{1}{2}\left(\frac{M-\mu}{\sigma(M)}\right)^2\right\} \tag{4.1}$$

with

$$\sigma(M) = \begin{cases} \sigma_0, & y_1 \leq M \leq y_2 \\ \sigma_0 + a_1(y_1 - M)^{a_2 - a_3\sqrt{y_1 - M}}, & M < y_1 \\ \sigma_0 + a_4(M - y_2)^{a_5 - a_6\sqrt{M - y_2}}, & M > y_2\ . \end{cases}$$

This parametrization accounts well for the verified discrepancy between the fitted J/ψ Monte Carlo widths and data [5, 15]. Figure 4.6 shows the J/ψ and ψ' Monte Carlo shapes after reconstruction and fit. The observed asymmetry between the right and left tails is caused by two effects: while the multiple scattering affects, in the same way, both left and right tails, the dE/dx affects more the left tail, since the muons energy whose strag-

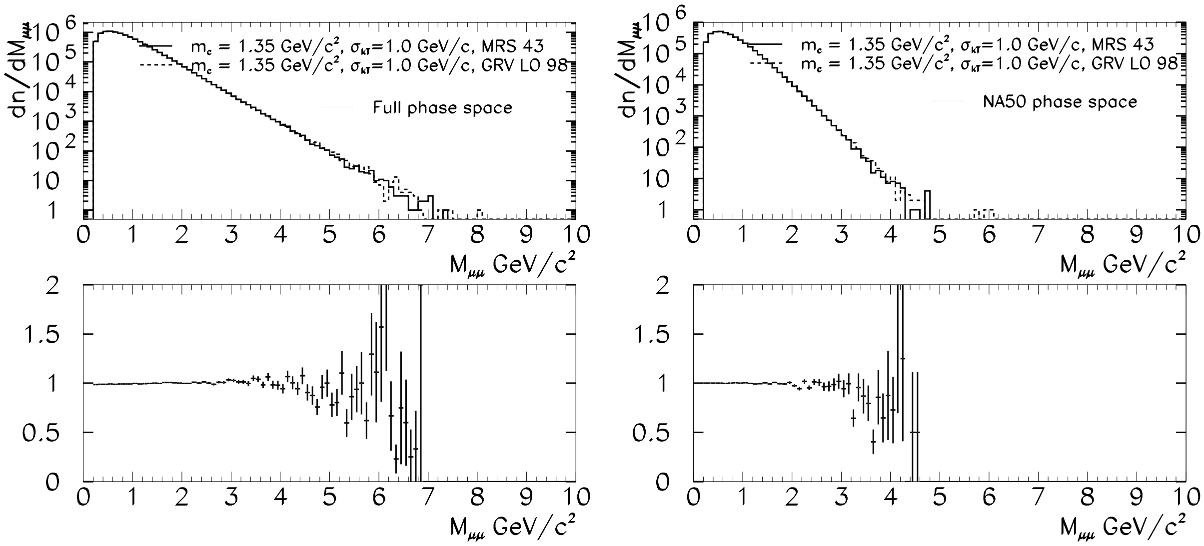

Figure 4.5: *$D\bar{D}$ PYTHIA generated events in full phase space (left) and in the NA50 spectrometer domain (right) using different parton density functions, MRS 43 or GRV LO 98; the lower plots are the respective ratios.*

gling corresponds to the Landau tail of the energy loss is not totally compensated in the reconstruction process, just a mean correction is performed.

Also Drell-Yan and open charm generated and reconstructed mass spectra are parametrized by empirical functional forms. For Drell-Yan we have:

$$\frac{dN^{DY}}{dM} = a_0 \exp\left\{-\frac{1}{2}\left(\frac{M-\mu}{\sigma(M)}\right)^2\right\} + a_1 \exp(-c_1 M) + a_2 \exp(-c_3 M) \tag{4.2}$$

and for open charm:

$$\frac{dN^{D\bar{D}}}{dM} = a_0 \exp\left\{-\frac{1}{2}\left(\frac{M-\mu}{\sigma(M)}\right)^2\right\} \tag{4.3}$$

with

$$\sigma(M) = \begin{cases} \sigma_0, & M \le c_1 \\ \sigma_0(1 + a_1 \exp(M - c_1)), & M > c_1 \ . \end{cases}$$

Figure 4.7 shows the Drell-Yan and open charm generated distributions, after reconstruction and respective fits.

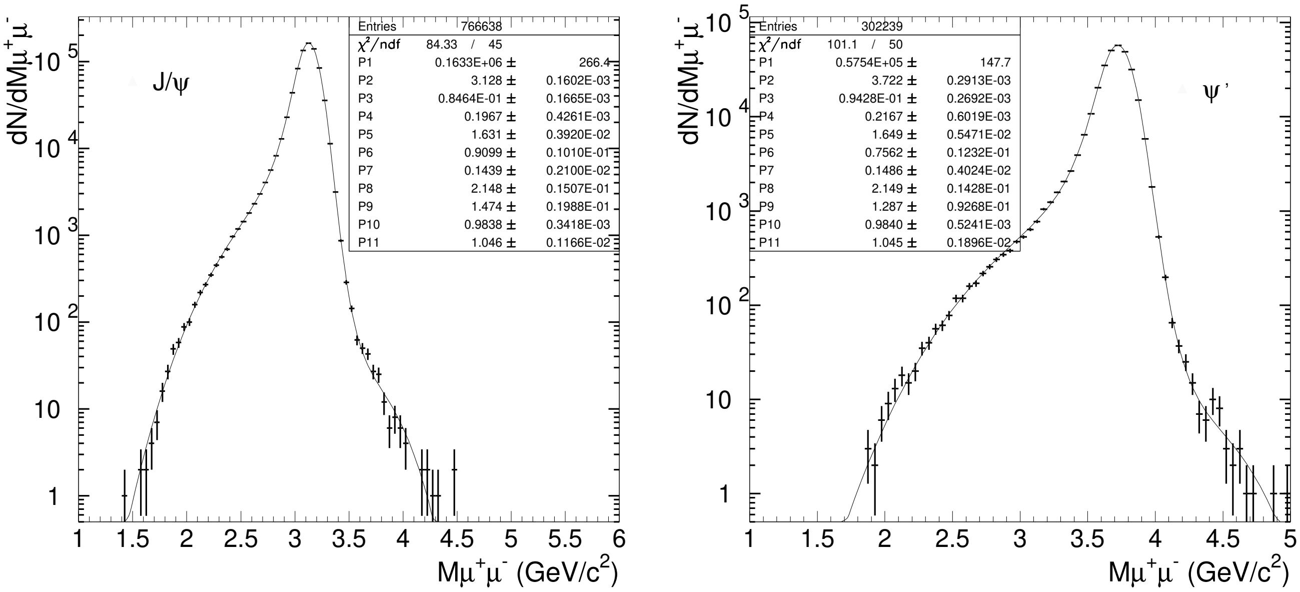

Figure 4.6: *J/ψ(left) and ψ'(right) generated and reconstructed mass spectra parametrized be equation 4.2.*

4.1.2 Acceptances

The spectrometer acceptances are calculated by means of the ratio between the number of simulated events that have been reconstructed, obeying to all selection criteria, and the number of generated events, in the same kinematic domain. The definition takes into account the smearing of the kinematic variables inherent to the finite resolution of the detector. Also due to the smearing, some events generated outside a given acceptance interval are accepted in it, while other ones, generated inside, are rejected. As a consequence, the kinematic variables have different distributions before and after reconstruction, as well as globally, within the overall apparatus kinematic window. Therefore, in order to get a correct evaluation of the acceptances, the kinematic window of the generated events is larger, being kept for the calculations those events that fall into the NA50 phase space: $0. \leq y_{CM} < 1.$ and $-0.5 \leq cos\theta_{cs} < 0.5$. Figure 4.8 shows the differential acceptances of J/ψ, ψ', Drell-Yan (in the 2.9-4.5 GeV/c^2 mass range) and $D\bar{D}$, considering the Setup 19, which corresponds to the Pb–Pb 2000 run. One can observe that the J/ψ, ψ' and Drell-Yan processes have similar differential acceptances, while the $D\bar{D}$ semi-leptonic decays are seen in a very different way by the spectrometer, namely in p_T and $cos\theta_{cs}$, thus minimizing their influence in the charmonia analyses. The integrated values are quoted in table 4.1. These values depend on the chosen P×Dtarget cut, as well on the slightly differences in the setup of each data taking, therefore they may vary from one data period to another.

The statistical error in the acceptances depends on the number of the generated events, being therefore arbitrarily small. The quoted systematic errors in the J/ψ and

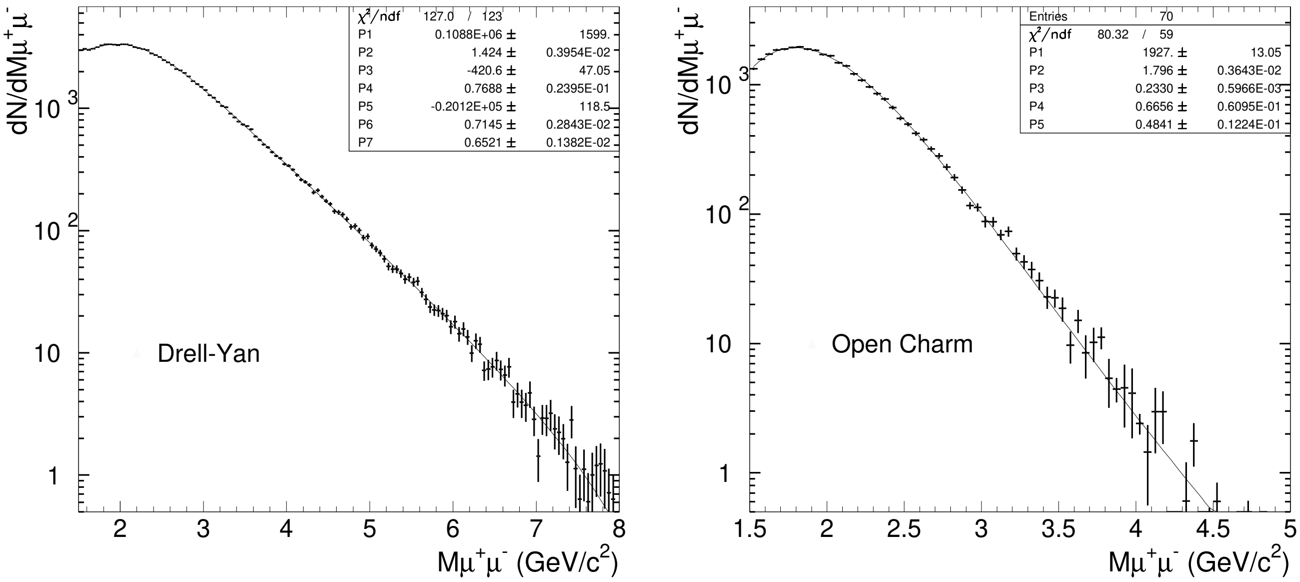

Figure 4.7: *DY(left) and $D\bar{D}$(right) generated and reconstructed mass spectra, parametrized by eqs. 4.2 and 4.3, respectively.*

	$M_{\mu\mu}$	Acceptances (Setup 19, Pb–Pb 2000)
J/ψ	> 1.5	12.52 ± 0.02(stat) $\pm$ 0.17(sys)
ψ'	> 1.5	$14.77 \pm 0.03 \pm 0.26$
DY	2.9 - 4.5	13.79 ± 0.05 – 0.16
DY	4.2 - 7.0	17.84 ± 0.17 – 0.73
$D\bar{D}$	> 1.5	$1.44 \pm 0.01\ ^{+0.14}_{-0.02}$

Table 4.1: *J/ψ, ψ', DY and $D\bar{D}$ integrated acceptances for Pb–Pb 2000 (setup 19) with statistical and systematic errors, respectively.*

ψ' acceptances come from different options in the generation, like the inclusion or not of the Fermi motion in the nucleons. Also, the $D\bar{D}$ acceptance depends on the generation parameters, namely m_c and σ_{k_T} values. The uncertainty on the Drell-Yan acceptances is the relative one among the several PDFs.

4.2 The analysis method

Figure 4.9 shows an opposite sign dimuon invariant mass spectrum for semi–central collisions. The J/ψ peak rises above a continuum formed, mainly, by the combinatorial background, Drell-Yan and open charm. On its right, the ψ' marks its presence, almost imperceptibly. Indeed, these are the main components of the mass spectrum, concerning

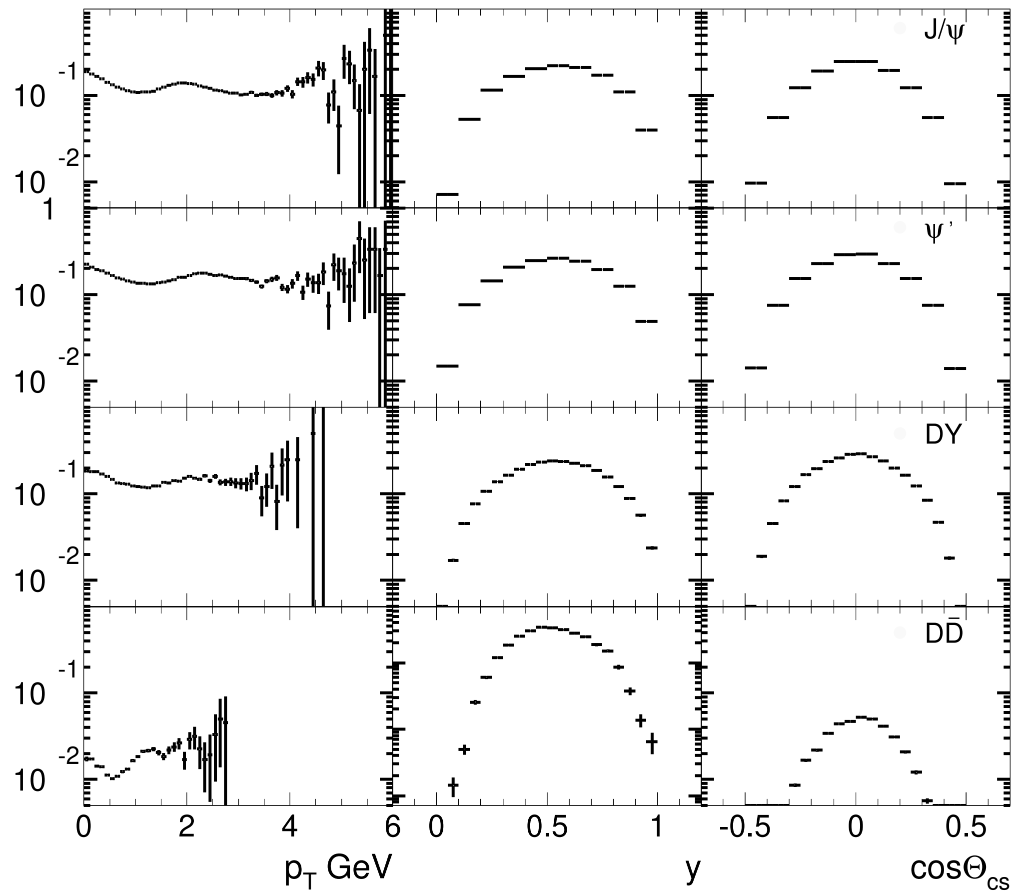

Figure 4.8: *J/ψ, ψ', Drell-Yan (events in the 2.9-4.5 GeV/c^2) and $D\bar{D}$ acceptances, concerning p_T, y and $cos\theta_{cs}$.*

the intermediate and high mass regions. To all these known processes we must add another source of contamination composed by the events produced out of target, namely J/ψ produced in the absorber or upstream from the target. However, the restricted data selection described in the previous chapter and particularly the performances of the NOCIMD target identification algorithm, ensure that our data sample is free from this kind of background [16]. The signal to combinatorial background ratio in the J/ψ mass range (2.9 – 3.3 GeV/c^2) is of the order of 20 in semi-central collisions, decreasing down to 9 for the most central ones. Therefore, a deep understanding and a correct treatment of all sources is essential to extract the resonances cross sections with high precision and to study them as a function of the collisions centrality.

In order to disentangle the different components, the treatment of the opposite sign dimuon invariant mass spectrum is performed by multi-steps. The first one consists on the evaluation of the combinatorial background. Afterward, the Monte Carlo generated processes, together with the combinatorial background, are fitted to the data. In this way, the J/ψ, ψ' Drell-Yan, and $D\bar{D}$ normalizations are extracted.

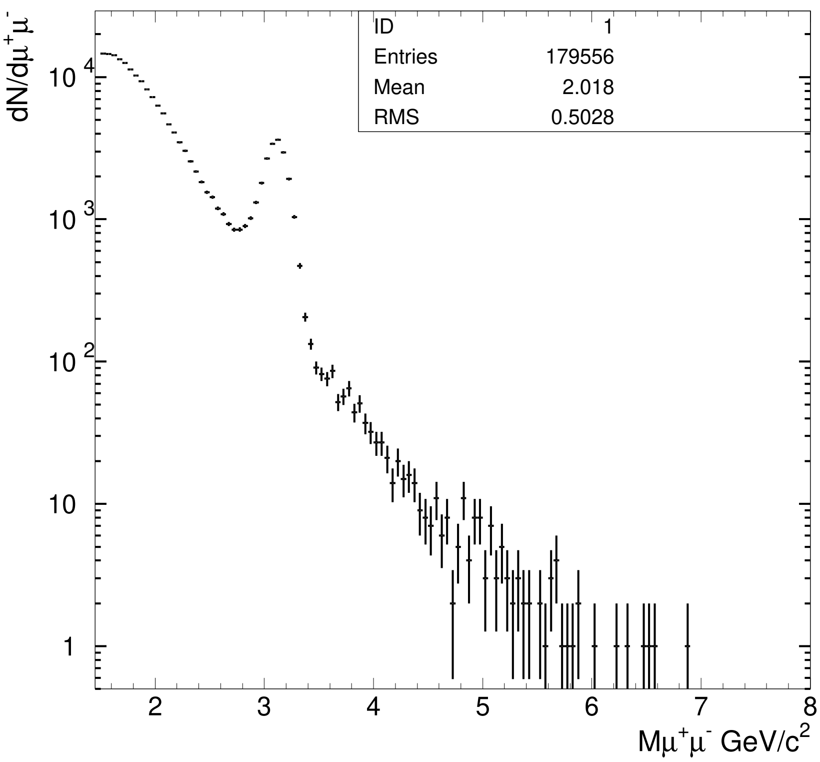

Figure 4.9: *A typical, semi–central, opposite–sign dimuon invariant mass spectrum.*

4.2.1 The treatment of the combinatorial background

In ultra-relativistic heavy ion collisions a huge amount of secondary particles, mostly pions and kaons, are produced. These particles, in turn, produce muons through the decay channels:

$$\pi^+ \longrightarrow \mu^+\nu, \qquad \pi^- \longrightarrow \mu^-\bar{\nu}\ ; \tag{4.4}$$

$$K^+ \longrightarrow \mu^+\nu, \qquad K^- \longrightarrow \mu^-\bar{\nu}\ . \tag{4.5}$$

Although most of these mesons interact hadronically with the absorber prior to their decay into muons, a large number decay before reaching it or before being absorbed, giving rise to a significant number of uncorrelated muon pairs. The treatment of this combinatorial background can be purely statistical using the measured like–sign pairs, as will be explained hereafter.

In a A–B collision the produced hadrons multiplicity follows a Poisson law. In a sample of $n^+(n^-)$ mesons, the number of different pairs that may be formed is given by:

$$^{n^+}C_2 = \frac{n^+!}{2(n^+-2)!} = \frac{n^+(n^+-1)}{2} \ . \tag{4.6}$$

If P(n$^+$(n$^-$)) is the probability to produce n$^+$ (n$^-$) charged mesons and w is the probability for a single meson to decay into $\mu + X$, the number of uncorrelated like-sign muon pairs $N^{++}(N^{--})$ produced in N collisions is given by:

$$N^{++} = NA^{++}w^2 \int P(n^+)\frac{n^+(n^+-1)}{2}dn^+ = \frac{N}{2}A^{++}w^2(< n^{+2} > - < n^+ >) \tag{4.7}$$

and

$$N^{--} = NA^{--}w^2 \int P(n^-)\frac{n^-(n^--1)}{2}dn^- = \frac{N}{2}A^{--}w^2(< n^{-2} > - < n^- >) \ , \tag{4.8}$$

where $A^{++}(A^{--})$ accounts for the like-sign dimuon acceptance in the apparatus. In the same way, the number of uncorrelated opposite–sign muon pairs is given by:

$$N^{+-} = NA^{+-}w^2 \int P(n^+)P(n^-)n^+n^-dn^+dn^- = NA^{+-}w^2(< n^+ >< n^- >) \ . \tag{4.9}$$

Since $< n >=< n^2 > - < n >^2$, we can establish the following relationship between the uncorrelated opposite–sign and the like-sign samples:

$$N^{+-} = 2\sqrt{N^{++}N^{--}}\frac{A^{+-}}{\sqrt{A^{++}A^{--}}} \ . \tag{4.10}$$

The Image cut (section 3.3) ensures that the spectrometer acceptance does not depend on the muon charge; therefore, the factor $A^{+-}/\sqrt{A^{++}A^{--}}$ is 1.

This is an exact formula in the case that both positive and negative meson distributions are poissonian distributed, i.e., when $< n^+ >$ and $< n^- >$ are high enough. This is the case of Pb–Pb collisions. However, in p–A or in lighter A–B interactions, an R_{bkg} correction factor multiplying the square root must be applied. This R_{bkg} factor may be determined by Monte Carlo simulations or, simply, extracted from a fit to the opposite–sign dimuon invariant mass spectrum.

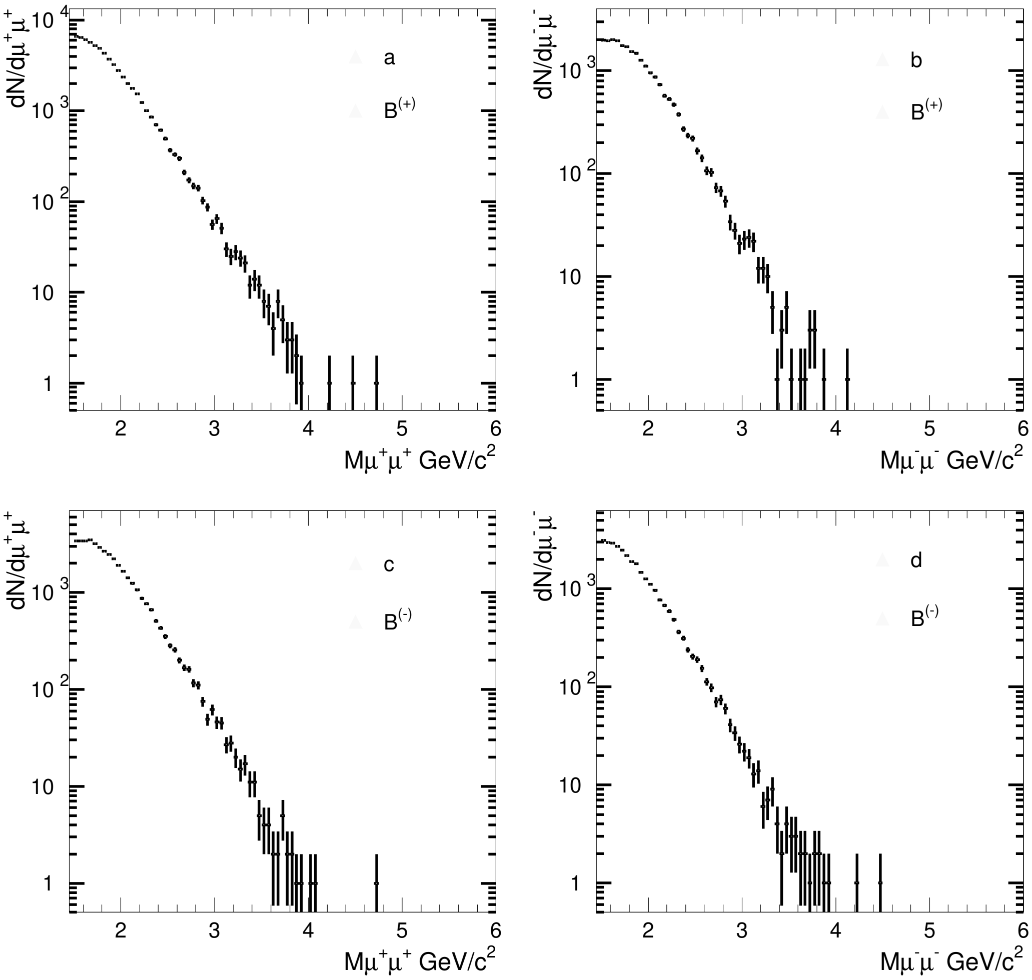

Figure 4.10: *4 like-sign mass spectra: a) positive charged muon pairs in positive magnetic field; b) negative charged muon pairs in positive magnetic field; c) positive charged muon pairs in negative magnetic field and d) negative charged muon pairs in negative magnetic field.*

Figure 4.10 shows 4 like-sign muon pairs spectra, since each like-sign sample is treated separately according to their charge and the sign of magnetic field ($\oplus$ or $\ominus$). The mass spectrum of the uncorrelated opposite–sign combinatorial background results from the like-sign ones by performing the histograms operation:

$$N^{+-} = 2 \times ([\sqrt{N^{++}N^{--}}]^{\oplus} + [\sqrt{N^{++}N^{--}}]^{\ominus}) \ . \tag{4.11}$$

This mass spectrum is then fitted with the following functional form:

$$\frac{dN^{bkg}}{dM} = a_0 \exp\left[-\frac{1}{2}\left(\frac{M-\mu_0}{\sigma_0(M)}\right)^2\right] + a_0 \cdot a_1 \exp\left[-\frac{1}{2}\left(\frac{M-\mu_1}{\sigma_1(M)}\right)^2\right] \tag{4.12}$$

with

$$\sigma_0(M) = \begin{cases} \sigma_0, & M \leq c_1 \\ \sigma_0(1 + c_2 \times (M - c_1)), & M > c_1 \ . \end{cases}$$

Figure 4.11 shows the uncorrelated opposite–sign sample that has resulted from equation 4.11, already fitted with equation 4.12.

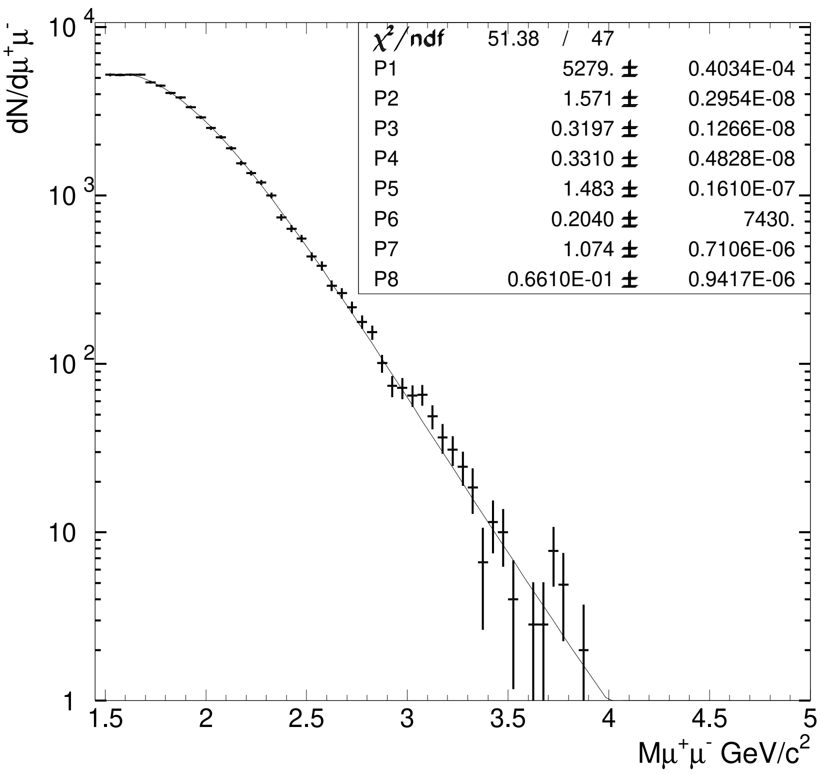

Figure 4.11: *A fitted combinatorial background mass spectrum that has resulted from equation 4.11 and fitted with equation 4.12.*

4.2.2 The fitting procedure

At this stage, we have already the Monte Carlo functional forms of the J/ψ, ψ', Drell-Yan and open charm. Also, the combinatorial background is defined. The next stage is the fit of the dimuon invariant mass spectrum. The multi–parameter function to be fitted to the data is expressed by:

$$\frac{dN^{+-}}{dM} = N_{J/\psi}\frac{dN_{J/\psi}}{dM} + N_{\psi'}\frac{dN_{\psi'}}{dM} + N_{DY}\frac{dN_{DY}}{dM} + N_{D\bar{D}}\frac{dN_{D\bar{D}}}{dM} + N_{bkg}\frac{dN_{bkg}}{dM} \tag{4.13}$$

where the different $N_{\{\}}$ are the parameters to be fitted, corresponding to each dimuon sample normalization. Taking into account that some dimuon sources are weak signals and, consequently, their contribution would not be correctly evaluated in such a global fit procedure, it is suitable to use a multi-step fit technique. In each specific step only the pertinent terms are fitted. The other contributions, that is, normalizations, are fixed according to pre-assumptions, as is the case of the combinatorial background R_{bkg} factor, or to the values extracted in a previous fit step. The set of parameters which minimize the χ^2 or –log-likelihood functions are found by the MINUIT package [18], which also evaluates the functions in the neighbourhood of the minimum, providing thus, the statistical parameter uncertainties.

Once the combinatorial background is determined, the multi-step fit to the opposite sign dimuon invariant mass spectrum is described as follows:

- 1[st] step – The aim of this step is to obtain a first shape of the J/ψ, in a region where the $D\bar{D}$ contribution is not relevant ($M_{\mu\mu}$ >3 GeV/c^2). The fit is performed with five free parameters: the J/ψ, ψ' and Drell-Yan normalizations, and M_ψ and σ_ψ. These two last parameters must be adjusted because the Monte Carlo does not reproduce well the J/ψ mass and width. The first discrepancy is due to the inefficient energy loss simulation and the second is related to the fact that the Coulomb scattering angular distribution is not a pure gaussian, as it is assumed in the Monte Carlo. On the other hand, we cannot guarantee that the properties of the absorber materials, reported in table 2.2, are perfectly well parametrized in the simulation. As a consequence, M_ψ^{MC} is 31 MeV deviated from its nominal value and σ_ψ^{MC} is 14 MeV lower than the one fitted to the real data. As the experimental resolution does not allow the determination of the ψ' mass and width, they are fixed using both resonances values obtained in the Monte-Carlo, together with M_ψ and σ_ψ fitted, according to:

$$M'_\psi = M_{\psi'}^{MC} - M_{J/\psi}^{MC} + M_{J/\psi}^{fitted} \tag{4.14}$$

and

$$\sigma_{\psi'} = \sigma_{J/\psi}^{fitted} \times \frac{\sigma_{\psi'}^{MC}}{\sigma_{J/\psi}^{MC}} \; . \tag{4.15}$$

- 2[nd] step – In this intermediate step we extract the open charm contribution. The fit mass range stands between 1.7 - 2.2 GeV/c^2. The free parameter is $D\bar{D}/DY$, where the Drell-Yan and the J/ψ normalizations have been fixed to the values obtained in the previous step. The background R_{bkg} factor is fixed to 1., due to its strongly negative correlation with the $D\bar{D}$ signal. In fact, every small deviation of this factor from what is expected (1 in Pb–Pb interactions) gives, as a consequence, non-reliable values for the $D\bar{D}$ contribution, or even the elimination of this process from the mass spectrum. A systematic error on the final results due to fact that the R_{bkg} is fixed will be determined.

- 3rd and final step – The dimuon invariant mass spectrum is fitted for M > 2.9 GeV/c^2, since at this stage, the $D\bar{D}$ contribution is already known. The free parameters are the J/ψ, ψ' and Drell-Yan normalizations, and $M_{J/\psi}$ and $\sigma_{J/\psi}$. The R_{bkg} factor is fixed to one. The final fit mass range will also be object of a systematical error study.

These three step fits are performed using the maximum log-likelihood method. Figure 4.12 displays the final fit of the dimuon mass spectrum, already shown in its stripped version in figure 4.9. The meaning of the parameters is the following: $P_1 \equiv J/\psi$, $P_2 \equiv \psi'$ and $P_3 \equiv$ Drell-Yan normalizations in the 2.9 - 7.0 GeV/c^2 mass range, $P_4 \equiv M_{J/\psi}$ and $P_5 \equiv \sigma_{J/\psi}$. The printed parameter errors are the square root of the diagonal elements of the error matrix and correspond to one standard deviation from the mean. One should notice the very good χ^2.

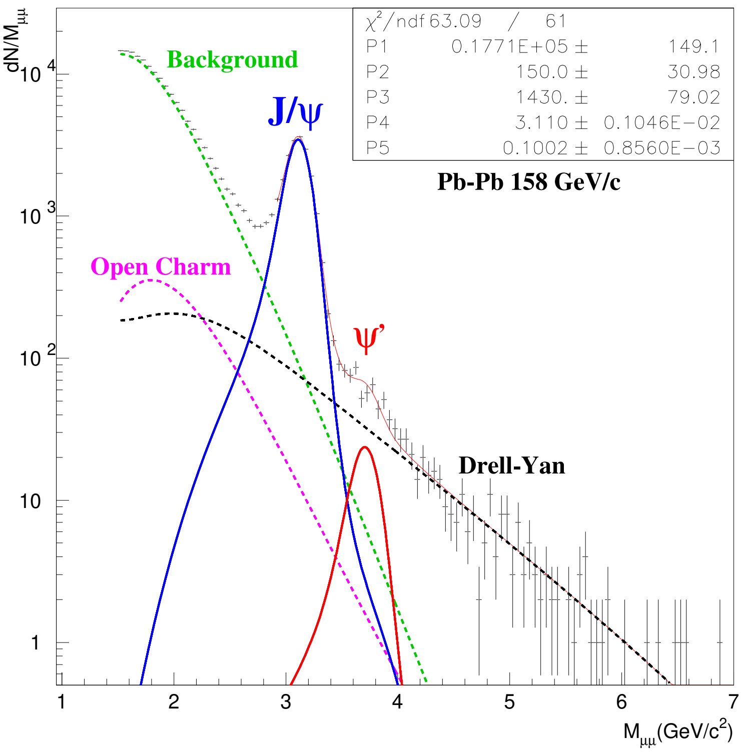

Figure 4.12: *The fitted dimuon invariant mass spectrum. See text for the meaning of parameters.*

Bibliography

[1] A. Romana, DIMUJET User's Guide (ver 2.00/02), 1997

[2] A. Romana, DIMUREC User's Guide (ver 2.00/03), 1997

[3] G.R. Lynch, O.I. Dahl, Nucl. Instrum. Meth. in Phys. Res. B58 (1991) 6

[4] C. Lourenço, J/ψ, ψ' and dimuon production in p–A and S–U collisions at 200 GeV/nucleon, PhD Thesis, Universidade Técnica de Lisboa, IST, January 1995

[5] R. Shahoyan, J/ψ and ψ' production in 450 GeV p–A interactions and its dependence on rapidity and X_F, PhD Thesis, Universidade Técnica de Lisboa, IST, April 2001

[6] T. Sjöstrand, Comp. Phys. Comm. 82 (1994) 74

[7] M. Gluck, E. Reya and A. Vogt, Z. Phys. C67 (1995) 433

[8] M. Arneodo et al. (EM Collaboration), Nucl. Phys. B333 (1990) 1; P. Amaudruz et al. (NM Collaboration), Phys. Lett. B295 (1992) 159

[9] A.C. Benvenuti et al. (BCDMS Collaboration) Phys. Rev. Lett. 66 (1991) 2712

[10] L.W. Whitlow et al., Nucl. Phys. B(Proc. Suppl.) 16 (1990) 215; Univ. Rochester report UR-1119 (1989); SLAC report 357 (1990)

[11] A.V Kotwal (E665 Collaboration), Fermilab-Conf-94/345

[12] A. Baldit et al. (NA51 Collaboration), Phys. Lett. B 332 (1994) 244

[13] A.D. Martin, R.G. Roberts and W.J. Stirling, Phys. Rev. D51 (1995) 4756

[14] M. Gluck, E. Reya and A. Vogt, Euro. Phys. J. C5 (1998) 463

[15] G. Borges, NA50 Internal Note 01/05

[16] L. Ramello (NA50 Collaboration), Quark Matter 2002, in Nucl. Phys. A715 (2003) 243c

[17] Particle Data Group, K. Hagiwara et al., Phys. Rev. D66 (2002)

[18] MINUIT - Function Minimization and Error Analysis, Reference Manual, version 96.03, Computing and Networks Division – CERN

שגיאות מי יבין מנסתרות נקני [1]

תהלים יט' יג'

Chapter 5

The J/ψ suppression in Pb–Pb collisions

The purpose of this chapter is to study the J/ψ behaviour with the collisions centrality, the main goal of the NA50 experiment. A special attention will be devoted to the Pb–Pb 2000 results, not only because they are the reference data sample, but also because their treatment and study is the main subject of this work. However, the Pb–Pb 1998 and 1996 data samples have been analysed under the same criteria used in 2000. A comparison among the results of all data taking periods will be performed.

5.1 The Pb–Pb 2000 data analysis

5.1.1 The collisions centrality

The main collision centrality estimator of the NA50 experiment is the neutral transverse energy, E_{T_0}, measured in the Electromagnetic Calorimeter, For notation simplicity we will quote E_T instead E_{T_0} hereafter. The J/ψ production is studied measuring its cross section in the different E_T intervals. During the Pb–Pb 2000 data taking 120000 J/ψ were collected, after the restricted data selection described in chapter 3. Such a high statistics sample has allowed the division of the E_T spectrum in 11 ranges, as shown in figure 5.1, in order to perform the analysis.

[1] *Who can understand his errors? cleanse thou me from secret faults.* Psalms 19:12

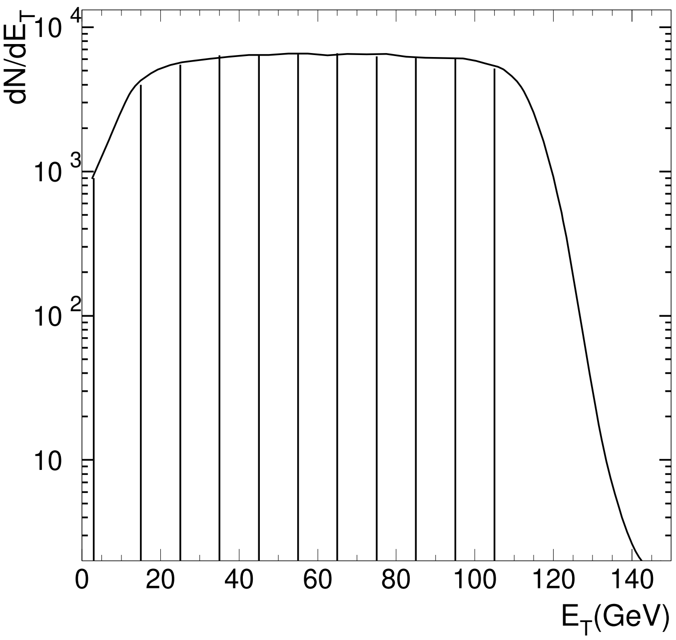

Figure 5.1: *The Pb–Pb E_T spectrum, concerning dimuon pairs of invariant mass ≥1.5 GeV/c^2, and its division in 11 regions.*

5.1.2 The cross section ratios

The J/ψ cross section is given by:

$$B_{\mu\mu}\sigma(J/\psi) = \frac{N_{J/\psi}}{\mathcal{L} \times A_{J/\psi}} \tag{5.1}$$

where $B_{\mu\mu}$ is the branching ratio of J/ψ into muons, $N_{J/\psi}$ is the number of measured J/ψ, $\mathcal{L}$ is the luminosity and $A_{J/\psi}$ is the J/ψ acceptance, quoted in table 4.1. $\mathcal{L}$ is given by the product of the number of target nuclei N_{tgt} per surface unit, by the number of incident ions N_{inc}, the lifetime LT, the efficiencies of the apparatus, ϵ, namely the reconstruction, target recognition and trigger efficiencies and corrections, Σ, for the different selection cuts described in section 3.4, as pile-up, parasitic and beam halo: $\mathcal{L} = N_{tgt} \times N_{inc} \times LT \times \epsilon \times \Sigma$.

We have seen in figure 1.23 that the number of Drell-Yan dimuons increases linearly with the number of nucleon-nucleon collisions. One may take advantage on this feature, which means that, as opposite to what happens with the J/ψ and ψ' resonances, the Drell-Yan process does not suffer from any nuclear medium effects. Therefore, in order to avoid the uncertainties associated with the luminosity calculations and taking into account that these uncertainties equally affect the Drell-Yan cross section measurement, we perform the ratio between the J/ψ and Drell-Yan normalizations, correcting each factor for the acceptance and obtaining in this way the ratio of the cross sections [2].

As referred in the previous chapter, the J/ψ and Drell-Yan normalizations are extracted in the dimuon mass region 2.9 – 7.0 GeV/c^2. Prior to obtain the total J/ψ cross section divided by a certain amount of the Drell-Yan continuum, we must extrapolate the normalizations and respective statistical errors to the suitable mass ranges and then perform the ratio. For the (J/ψ)/DY analysis the Drell-Yan mass range between 2.9 – 4.5 GeV/c^2 is usually chosen. This mass interval is somewhat arbitrary because, although the muons from the J/ψ decay and Drell-Yan have similar features, namely acceptances and momentum, the Drell-Yan normalization, as well as its statistical error, is determined mostly in the region where this process is the only contribution to the mass spectrum, i.e., at masses above ∼4.3 GeV/c^2. As the shape of the Drell-Yan cross section is completely defined in the Monte Carlo simulations, we have only to apply a renormalization factor to pass from the measured 2.9 – 7.0 GeV/c^2 mass range to the suitable one.

5.1.3 The statistical error evaluation

The extracted normalizations from the fit to the opposite sign mass spectra are affected by a statistical error, which evaluation takes into account both parameter correlations and non-linearities. In the same way, the statistical error on the (J/ψ)/DY ratio must account for the covariance between these two variables. The variance of the estimator $F \equiv$ (J/ψ)/DY ratio is given by:

$$\sigma_F^2 = \sum_{i=1}^{n}\sum_{j=1}^{n} \frac{\delta F}{\delta par_i}\frac{\delta F}{\delta par_j}\sigma_i \sigma_j C_{ij} \tag{5.2}$$

where n is the number of fitted parameters $par_{i(j)}$ (i.e., $N_{J/\psi}$ and N_{DY}), σ_i is the uncertainty on $par_{i(j)}$ and C_{ij} is the correlation coefficient between the parameters i and j.

Table 5.1 reports the error matrix of the fit shown in figure 4.12, calculated by the MINUIT package [3]. The diagonal elements are the square of the respective parameter error.

	$N_{J/\psi}$	$N_{\psi'}$	N_{DY}	$M_{J/\psi}$	$\sigma_{J/\psi}$
$N_{J/\psi}$	0.223E+05	0.824E+03	-0.409E+04	-0.922E-02	0.250E-01
$N_{\psi'}$	0.824E+03	0.972E+03	-0.146E+04	-0.140E-02	0.356E-02
N_{DY}	-0.409E+04	-0.146E+04	0.640E+04	0.642E-02	-0.226E-01
$M_{J/\psi}$	-0.922E-02	-0.140E-02	0.642E-02	0.109E-05	-0.303E-06
$\sigma_{J/\psi}$	0.250E-01	0.356E-02	-0.226E-01	-0.303E-06	0.728E-06

Table 5.1: *Error matrix corresponding to the fit shown in figure 4.12.*

[2]The NA50 Collaboration also performs the so-called minimum bias analysis, in which the J/ψ is normalized by those events defined by an incident Pb which interacts in target of the experiment [1, 2].

Table 5.2 shows the correlation matrix of the same fit. The correlation coefficient between different parameters is given by the non-diagonal elements.

	Global	$N_{J/\psi}$	$N_{\psi'}$	N_{DY}	$M_{J/\psi}$	$\sigma_{J/\psi}$
$N_{J/\psi}$	0.35468	1.000	0.177	-0.343	-0.059	0.197
$N_{\psi'}$	0.58803	0.177	1.000	-0.584	-0.043	0.134
N_{DY}	0.66917	-0.343	-0.584	1.000	0.077	-0.331
$M_{J/\psi}$	0.34358	-0.059	-0.043	0.077	1.000	-0.341
$\sigma_{J/\psi}$	0.46929	0.197	0.134	-0.331	-0.341	1.000

Table 5.2: *Correlation matrix corresponding to the fit shown in figure 4.12.*

The major contribution to the statistical error of the $J/\psi/DY_{2.9-4.5}$ ratio comes from Drell-Yan and depends almost on its statistics above the ψ' mass range. In fact, while the relative error on the J/ψ normalization stands within 1%, the relative error on the Drell-Yan one is $\sim$ 8% in peripheral E_T intervals and 6% for E_T regions above 40 GeV. The relative error on the $J/\psi/DY_{2.9-4.5}$ ratio becomes $\sim$ 9% at low E_T and 7% at mid and high centrality.

5.1.4 The measurement of the (J/ψ)/DY ratio as a function of E_T

While the ratio uncertainties coming from the absolute normalizations and efficiencies are negligible, when compared with the statistical errors, since they cancel out in the ratio, other sources of systematic errors in the (J/ψ)/DY ratio measurement must be investigated. An exhaustive study of the (J/ψ)/DY results has been done, either to check the stability of their measurement, or to identify causes leading to systematic errors. The most significant uncertainty comes from Drell-Yan, whose cross section calculations depend strongly on the parton density functions. The technical procedure to achieve J/ψ and Drell-Yan normalizations was object, itself, of several checks and tunings, before final criteria are reached.

5.1.4.1 Systematic effects on fit techniques

The following systematic effects on the fit procedure to extract the J/ψ and Drell-Yan normalizations have been investigated:

- The final fit mass range
- Drell-Yan fitted versus counted

- The influence of the intermediate mass region — IMR
- The stability of the M_ψ and σ_ψ parameters with E_T

In the fit procedure a special care is given to Drell-Yan. The J/ψ dominates the dimuon signal mass spectra and it will be shown that its normalization is almost insensitive to systematic effects, such as fit starting points or IMR contributions. But, the Drell-Yan normalization, due to its relative small statistics, can change significantly, depending strongly on the different technical procedures to fit the mass spectra. Fortunately, the Drell-Yan is the only contribution after the ψ' mass range. Therefore, one can establish a general criterium to guide the options that must be taken: the high mass Drell-Yan must be fitted as well as possible. Such a procedure ensures a non-biased fitted Drell-Yan contribution preventing the introduction of spurious effects in the J/ψ over Drell-Yan ratio pattern.

• The choice of the final fit mass range

In principle, one should fit the mass spectrum starting at 1.7 GeV/c^2, or even at 1.5 GeV/c^2, since the inclusion of the IMR takes into account the J/ψ smearing tail. The left plot of figure 5.2 shows the J/ψ distributions as a function of E_T, extracted from the final fit mass ranges: 1.7—7.0 and 2.9—7.0 GeV/c^2. On the right plot their ratio is displayed. One verifies that the J/ψ sensitivity to the inclusion of the IMR in the fit is

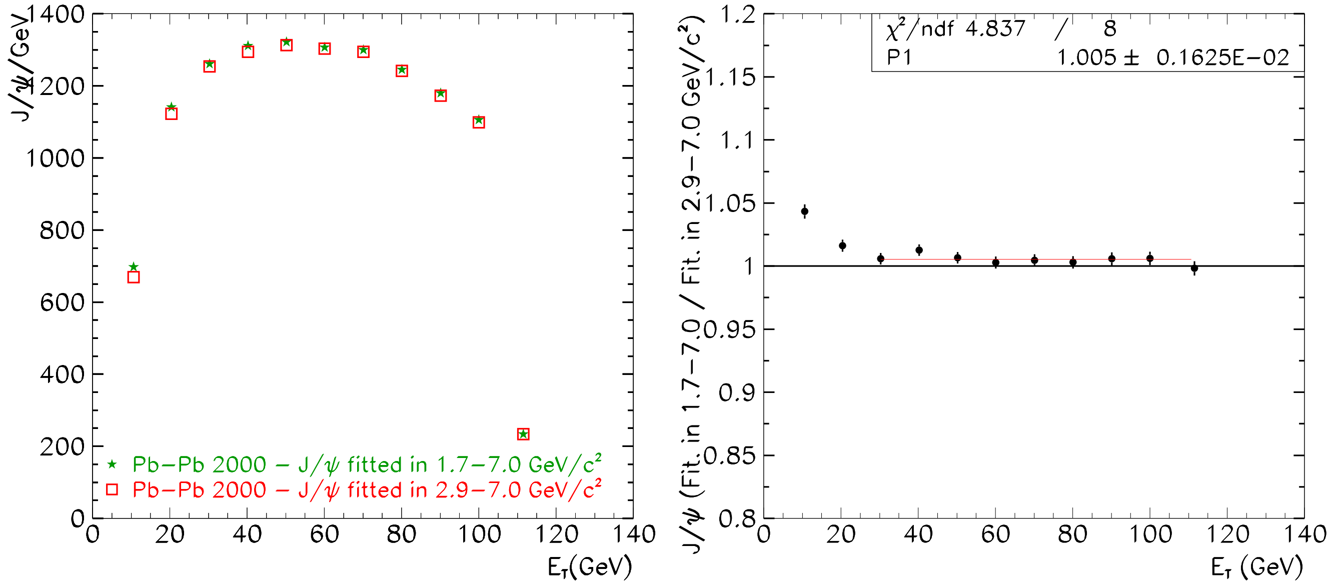

Figure 5.2: *The J/ψ normalizations for the 11 E_T regions, extracted from the fits to 1.7 - 7.0 and 2.9 - 7.0 GeV/c^2 mass ranges (left). Ratios between the two normalizations (right).*

$\sim$ 0.5%. The 4.5% and 1.7% differences, seen in the peripheral E_T regions, should not be taken into account, since the respective fits starting at 1.7 GeV/c^2 have poor quality, when compared to the ones starting at 2.9 GeV/c^2 (see figure 5.3). The reason has to do with the fact that, at very low E_T, a P$\times$Dtarget cut of 2% is not sufficient to clean the off-target produced events. These dimuons are mainly J/ψ produced in the absorber, which are reconstructed with masses in the 2.4–2.8 range. For E_T > 25 GeV the dimuon spectra become much cleaner, allowing a very good quality fit for both mass ranges and thus a very small J/ψ sensitivity, as can be seen in figure 5.4.

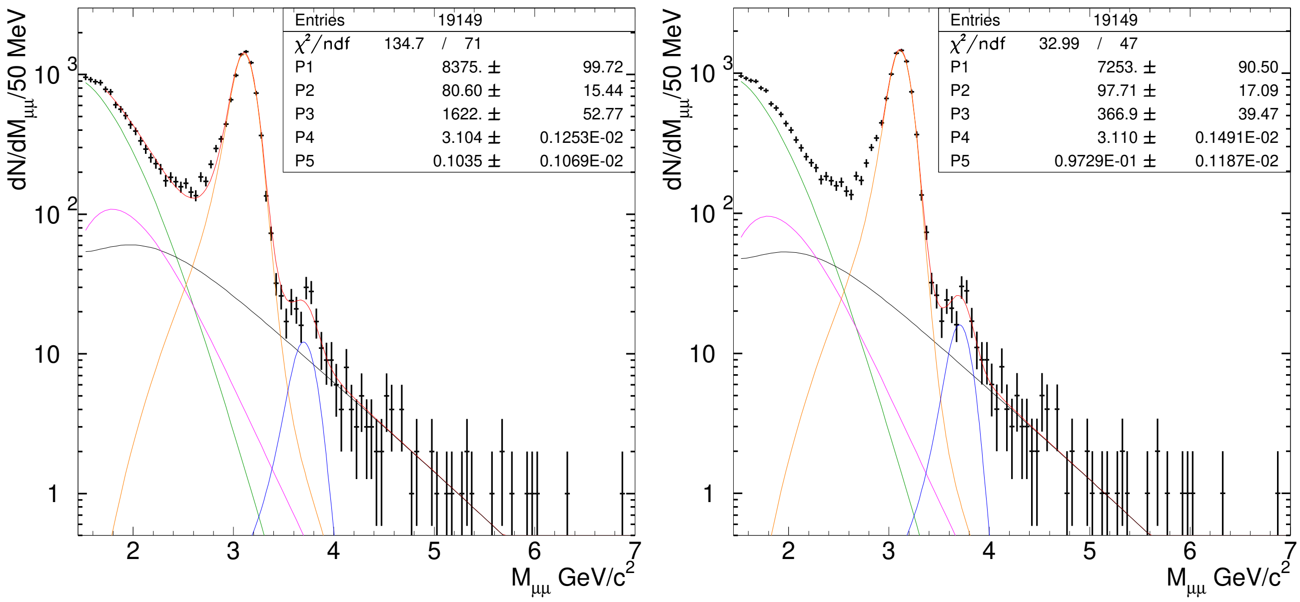

Figure 5.3: *Fits to 1.7—7.0 (left) and 2.9—7.0 GeV/c^2 (right) mass ranges for the most peripheral E_T region.*

Figure 5.5 shows the Drell-Yan high mass data ($M_{\mu\mu}$ > 4.2 GeV/c^2) and the respective fitted results on the left plot. Globally, high mass Drell-Yan from the fit starting at 1.7 GeV/c^2 is systematically above the fitted results from 2.9—7.0 range. On the right plot, the ratios between the fitted results show an E_T dependent discrepancy.

Figure 5.6 shows the ratios between the high mass Drell-Yan fitted results and data, when the fits start at 1.7 or 2.9 GeV/c^2. High mass Drell-Yan is worse fitted if the fit starts at 1.7 GeV/c^2 and an E_T dependence is visible through a linear fit with two free parameters. On the contrary, only a statistical effect is present if the fit starts at 2.9 GeV/c^2. For this reason, the final fit is performed in the 2.9—7.0 GeV/c^2 mass range.

From the J/ψ measurement point of view, and taking into account the very small difference in the J/ψ normalizations when fitted in the different mass ranges, it is sufficient to start the fit at 2.9 GeV/c^2 (2 σ_ψ away from the fitted M_ψ value).

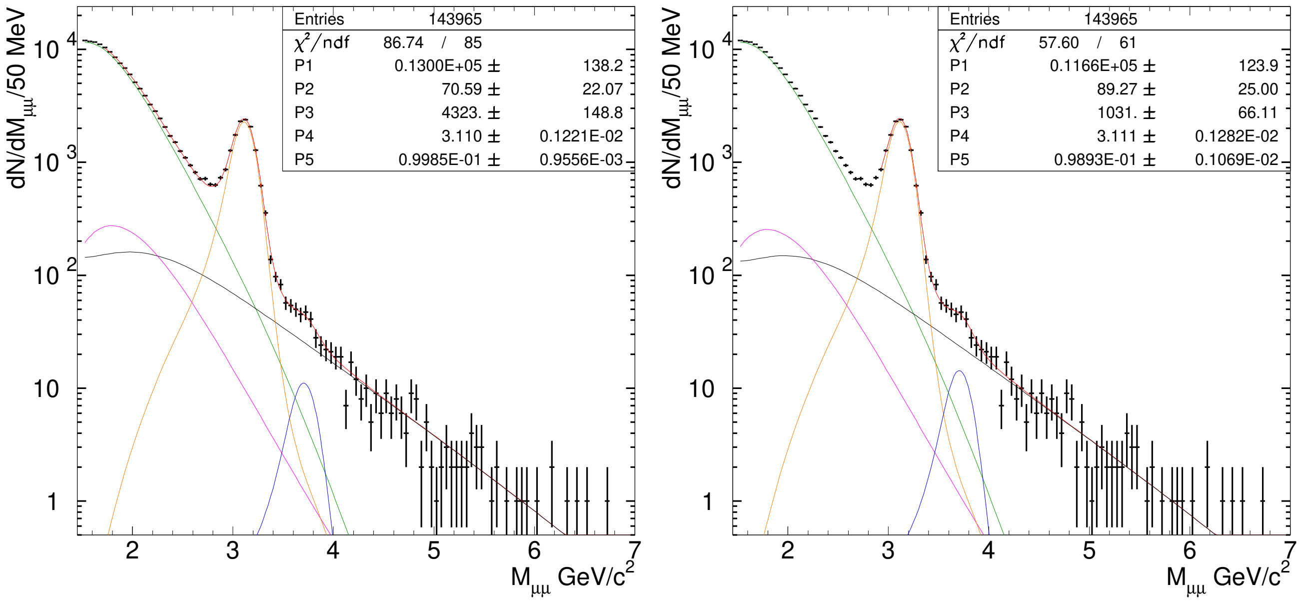

Figure 5.4: *Fits to 1.7 - 7.0 (left) and 2.9 - 7.0 GeV/c^2 (right) mass ranges for the 65$\leq E_T <$75 GeV interval.*

In conclusion, the mean systematic error in the (J/ψ)/DY normalization ratio, associated to the choice of the 2.9-7.0 GeV/c^2 mass range, comes exclusively from the uncertainty in the J/ψ normalization and is estimated to be +0.5%.

- **Drell-Yan fitted versus counted**

Noticing the differences between the high mass Drell-Yan data and respective fitted results when the fits start at much lower mass values (1.7 or 2.9 GeV/c^2), it could be argued that, due to the fact that the high mass Drell-Yan is the only contribution to the mass spectrum, it should be fixed and then extrapolated backward in mass, since its shape is determined by Monte Carlo. Through this way, one could, in principle, ensure that the Drell-Yan normalization would be free from systematic effects imposed by other dilepton sources. However, the left plot of figure 5.5 shows that the pattern of the Drell-Yan fitted results, as a function of E_T, is much smoother than the data one (counted events). Since the Drell-Yan evolution with E_T must be smooth, as no nuclear in-medium effects affect these dilepton pairs, one should take advantage of the fitted results. On the other hand, the same figure shows that, in fact, the Drell-Yan normalization is not totally a consequence of its high mass range. By fixing it, the results on the (J/ψ)/DY ratio become too much dependent on the fluctuations imposed by the relative small high mass

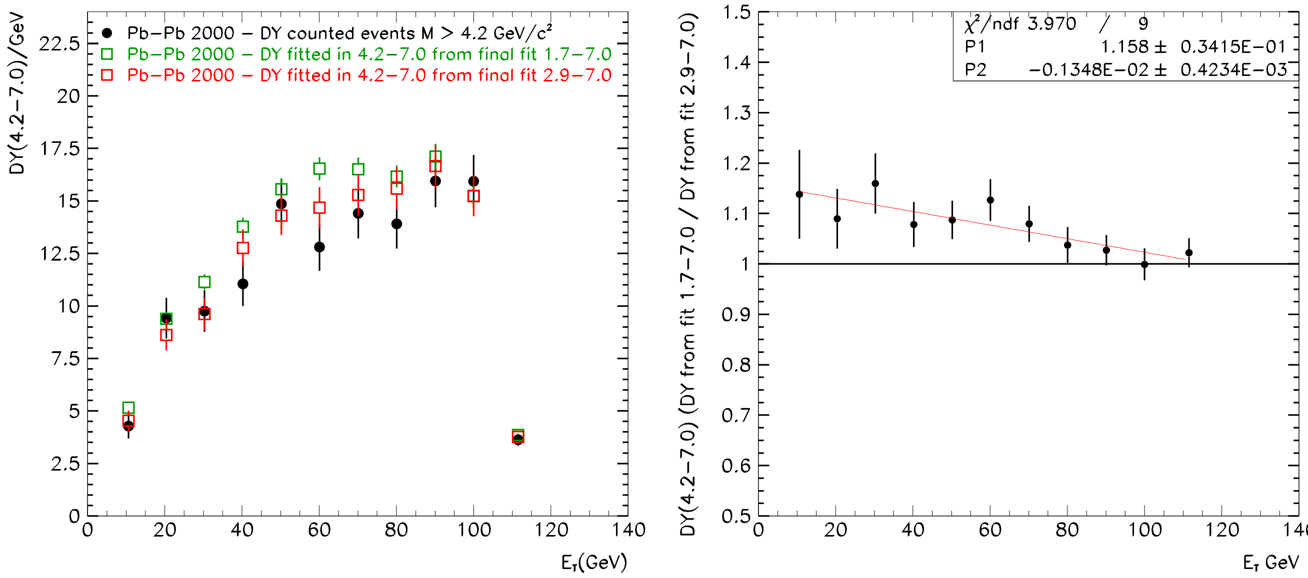

Figure 5.5: *The Drell-Yan events with $M_{\mu\mu}$ > 4.2 GeV/c^2 and the respective renormalized fitted results from mass spectrum fits starting at 1.7 and 2.9 GeV/c^2 (left). The ratio between the fitted results (right).*

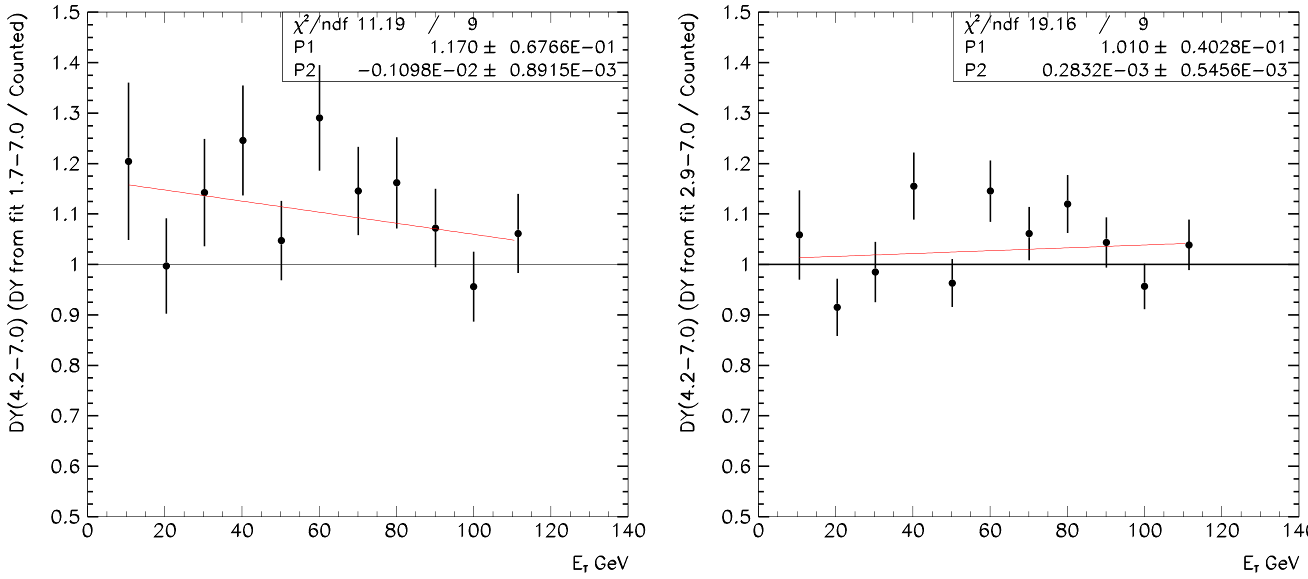

Figure 5.6: *The ratios between the high mass Drell-Yan, fitted in two large mass domains, 1.7—7.0 GeV/c^2 (left) and 2.9—7.0 GeV/c^2 (right) and extrapolated to 4.2—7.0 GeV/c^2, and the direct high mass Drell-Yan fitted in the same region.*

Drell-Yan statistics. Nevertheless, in order to determine a possible systematic error on the (J/ψ)/DY results, such a procedure has been developed. Figure 5.7 shows the ratios between the (J/ψ)/DY results obtained with the standard procedure (3$^{\text{rd}}$ step, with the fit starting at 2.9 GeV/c^2, in conformity with section 4.2.2) and fixing the Drell-Yan normalization at 2.9 - 7.0 GeV/c^2, extrapolated from the fit at 4.2-7.0 GeV/c^2. Again, only a statistical effect is observed; the trend is the same to the one seen on the right plot of figure 5.6, proving that the J/ψ normalization is not sensitive to such change in the Drell-Yan one. Thus, there is no place for a systematic error in (J/ψ)/DY results.

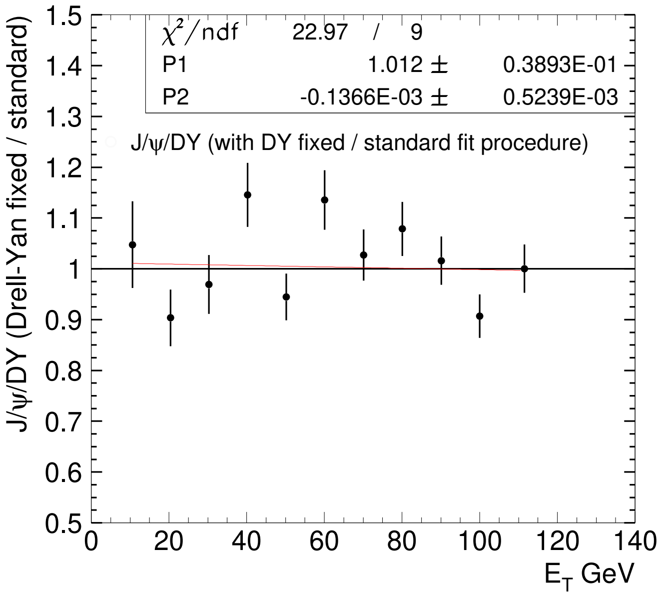

Figure 5.7: *Ratios between the (J/ψ)/DY results: the one in which the 2.9 - 7.0 GeV/c^2 Drell-Yan normalization is obtained from the extrapolation of the 4.2-7.0 GeV/c^2 direct fit and the one extracted from the standard fit technique procedure.*

• The influence of the IMR

In order to determine the open charm contribution and to fix it in the final step, the standard analysis uses the mass range between 1.7—2.2 GeV/c^2 and the R_{bkg} factor fixed to 1. Another source of uncertainty comes from the theory — the fitted $D\bar{D}$ normalization depends on Monte Carlo choices, namely on the physical parameters that determine their cross section, as the charm quark mass, m_c, the imposed width of the transverse momentum of the incoming partons, σ_{k_T}, and the parton density functions. Therefore, one should investigate in what extent the $D\bar{D}$ shape, the fit mass range in the IMR, as well as the procedure of fixing the R_{bkg} factor, affects the (J/ψ)/DY final results.

In what respects the D and $\bar{D}$ mesons, three factors can affect their measured cross section: the generation parameters, the R_{bkg} value and Drell-Yan normalization. In fact, the Drell-Yan yield in the 1.7 - 2.2 mass range can change by ∼11%, depending on the used PDF. Such a difference imposes a change on the $D\bar{D}$ normalization, provided the J/ψ and the R_{bkg} parameters are fixed, since these four physical processes are the known sources of the IMR. Concerning two Drell-Yan generations, tables 5.3 and 5.4 report the fitted parameters in the 2^{nd} step, namely the R_{bkg} factor and the $D\bar{D}/DY$ ratio when the R_{bkg} factor is fitted or fixed.

E_T GeV	R_{bkg}	$D\bar{D}/DY$ (R_{bkg} fitted)	$D\bar{D}/DY(R_{bkg}=1)$
3-15	1.13 ± 0.05	0.80 ± 0.32	1.60 ± 0.13
15-25	0.94 ± 0.04	2.12 ± 0.47	1.43 ± 0.13
25-35	1.01 ± 0.03	1.45 ± 0.55	1.68 ± 0.15
35-45	1.04 ± 0.02	0.78 ± 0.45	1.65 ± 0.15
45-55	1.04 ± 0.02	0.21 ± 0.56	1.38 ± 0.15
55-65	1.02 ± 0.02	0.78 ± 0.77	1.50 ± 0.16
65-75	1.02 ± 0.02	0.61 ± 0.70	1.52 ± 0.17
75-85	1.00 ± 0.02	2.20 ± 0.83	2.06 ± 0.17
85-95	1.00 ± 0.02	1.68 ± 0.72	1.45 ± 0.17
95-105	1.00 ± 0.02	2.13 ± 0.86	2.13 ± 0.19
105-150	1.02 ± 0.02	0.32 ± 0.78	1.29 ± 0.18

Table 5.3: *The R_{bkg} factor fitted in the IMR: 1.7 - 2.2 GeV/c^2, as well as the $D\bar{D}/DY$ ratio when the R_{bkg} factor is fitted or fixed (Drell-Yan generated with GRV LO 94 PDFs).*

E_T GeV	R_{bkg}	$D\bar{D}/DY$ (R_{bkg} fitted)	$D\bar{D}/DY(R_{bkg}=1)$
3-15	1.13 ± 0.05	1.04 ± 0.34	1.91 ± 0.14
15-25	0.94 ± 0.04	2.52 ± 0.52	1.72 ± 0.15
25-35	1.01 ± 0.02	1.79 ± 0.50	1.99 ± 0.17
35-45	1.04 ± 0.02	1.02 ± 0.57	1.97 ± 0.16
45-55	1.04 ± 0.02	0.38 ± 0.69	1.65 ± 0.17
55-65	1.02 ± 0.02	1.03 ± 0.70	1.79 ± 0.18
65-75	1.02 ± 0.02	0.83 ± 0.78	1.82 ± 0.19
75-85	1.00 ± 0.02	2.61 ± 0.79	2.43 ± 0.20
85-95	1.00 ± 0.02	2.03 ± 0.79	1.74 ± 0.19
95-105	1.00 ± 0.02	2.53 ± 0.99	2.50 ± 0.22
105-150	1.02 ± 0.02	0.52 ± 0.94	1.56 ± 0.20

Table 5.4: *The R_{bkg} factor fitted in the IMR: 1.7 - 2.2 GeV/c^2, as well as the $D\bar{D}/DY$ ratio when the R_{bkg} factor is fitted or fixed (Drell-Yan generated with CTEQ 4L PDFs).*

A strong anti-correlation ($> -95\%$) between the two parameters is verified. Indeed, if fitted, the R_{bkg} factor is less than 2 standard deviations apart from the expected value, 1, but the $D\bar{D}/DY$ parameter becomes very uncertain and this behaviour remains whatever the IMR is chosen. On the contrary, the R_{bkg} factor is not sensitive to the different Drell-Yan or $D\bar{D}$ generations studied. This happens because the combinatorial background dominates the IMR by factors that vary from 3, in the peripheral collisions, to 20 in the most central ones. Precisely for this reason, fixing the R_{bkg} factor has the consequence of changing the $D\bar{D}$ contribution parameter by a huge amount. Nevertheless, such a procedure does not change the absolute number of events in the final fit mass range (2.9 - 7.0 GeV/c^2), because there is only a transfer of events from one dilepton source to the other. Therefore, the (J/ψ)/DY results remain unchanged.

In order to test the stability of the $D\bar{D}$ contribution to the dimuon mass spectrum, as well as its influence on (J/ψ)/DY results, D and $\bar{D}$ mesons have been generated using different charm quark masses, intrinsic k_T width and parton density functions. However, in the NA50 phase space domain, the $D\bar{D}$ differential cross sections sensitivity to the uncertainties on these physical assumptions is negligible, as shown in figures 4.3, 4.4 and 4.5. Consequently, $J/\psi/DY$ ratio is not sensitive to the $D\bar{D}$ cross section shape.

Two other different IMR were chosen to extract the $D\bar{D}/DY$ parameter, namely 1.5 - 2.2 and 1.7 - 2.6 GeV/c^2, but no influence on the (J/ψ)/DY result is verified, as shown in figure 5.8.

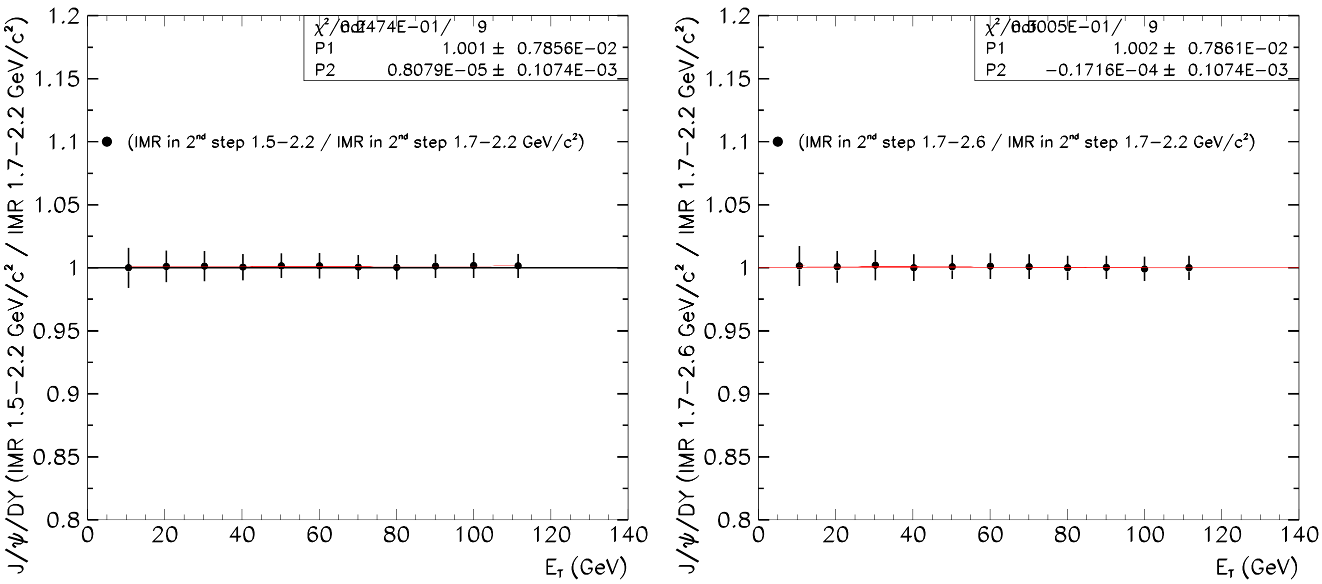

Figure 5.8: *Ratios of (J/ψ)/DY results obtained with different IMR in the second step of the fit procedure, in order to extract the $D\bar{D}/DY$ parameter.*

In conclusion, the systematic uncertainty on the (J/ψ)/DY results due to the several constraints that affect the IMR is compatible with zero.

• **The stability of the M_ψ and σ_ψ parameters with E_T**

Figure 5.9 shows the fitted M_ψ and σ_ψ parameters for the 11 centrality classes. No system-

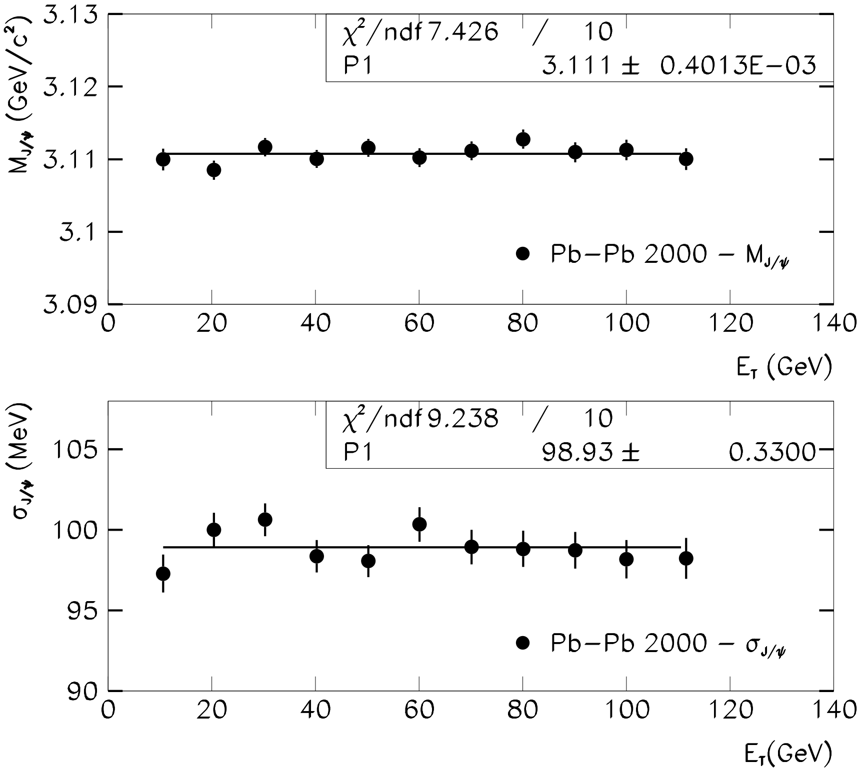

Figure 5.9: *The M_ψ and σ_ψ fitted parameters for the 11 E_T regions.*

atic behaviour of these parameters with the transverse energy is seen. The fluctuations in the J/ψ mass are only statistical. The mean fitted value of the J/ψ mass is found to be systematically 0.45% higher (14 MeV) than the Particle Data Group value [4], due to not sufficient energy loss correction for each event (see section 4.1). The σ_ψ fluctuates around 99 MeV. Since the experimental J/ψ mass and dispersion should not depend on E_T, in principle they could be fixed with a mean value extracted from all regions. However, if these parameters become fixed, mainly σ_ψ, the J/ψ normalization is almost not affected (less than 1%), but the Drell-Yan changes in the opposite direction of the J/ψ one and consequently the (J/ψ)/DY ratio becomes biased. This effect is more pronounced as the σ_ψ fitted value in a individual region lays away from the imposed mean value. That is, a 2 MeV difference between the σ_ψ fitted and the mean value implies ∼5% change in the Drell-Yan normalization. Therefore, for a better evaluation of the normalizations it is suitable to let free M_ψ and σ_ψ.

5.1.4.2 The (J/ψ)/DY dependence on parton density functions in the Drell-Yan calculations

The Drell-Yan cross section, K factor and isospin correction (from pp to A–B) depend on the structure functions. As already shown, the Drell-Yan normalization is mainly determined in the region where it is the only contribution to the mass spectrum ($M_{\mu\mu} \gtrsim 4.3$ GeV/c^2). All PDFs, either Leading Order (LO) or Next to Leading Order (NLO), fitted to this data give the same number of Drell-Yan events, although they do not superimpose themselves. As statistics in this mass range are relatively low, there is no sensitivity to verify which PDF fits better the data. Once the high mass is adjusted, the different Drell-Yan shapes cross each other at ∼4.2–4.3 GeV/c^2 [3] and then become more and more apart, towards the J/ψ mass domain. This feature does not mean that the different Drell-Yan shapes would actually cross at that point. Indeed, they could even cross each other under the J/ψ peak, but although Drell-Yan statistics in this mass domain are typically a factor of 6 higher, they do not contribute significantly to its normalization. While the number of J/ψ is weakly affected, having the maximum variation of 0.7%, a 14% difference between Drell-Yan cross sections in the 2.9-4.5 GeV/c^2 mass range is observed, when this process is calculated using LO or NLO structure functions (CTEQ4L [5] and MRS 43 [6]). On the other hand, Drell-Yan generated with NLO PDFs MRS 43 and GRV HO, both using $\overline{MS}$ renormalization scheme, give the same result. Figure 5.10 shows several Drell-Yan shapes fitted to the same data, i.e., in the same E_T region.

It is known that the LO evaluation cross section underestimates the measured total cross section by a factor of 1.8 or more (see section 1.8). Concerning this issue, it is shown in [7] that the theoretical K factor:

$$K_{th}^{(1)} = \frac{\sigma_{NLO}}{\sigma_{LO}} = \frac{\sigma_1(\alpha_s^n) + \sigma_1(\alpha_s^{n+1})}{\sigma_1(\alpha_s^n)} \tag{5.3}$$

is nearly independent on the mass when the denominator and the Born term of the numerator are calculated with LO PDFs and the NLO correction to the Born part in the numerator is calculated with NLO PDFs and a two-loop calculation in α_s. This suggests not evaluating Drell-Yan cross sections at the Born level, using NLO structure functions. Besides, the LO and NLO PDFs are both tuned to fit the same data from deep inelastic scattering (DIS). If NLO PDFs would be used together with a LO evaluation of the $F_2(x)$ structure function, the result would no longer agree with the data [8].

In conclusion, in order to ensure consistency, since Drell-Yan is calculated at the Born level, the use of LO PDFs should follow. In the present study, the set of GRV LO 94 [7] PDFs has been used, although it has been verified that the more recent GRV LO 98 [10] PDFs provide the same Drell-Yan shape, over the whole dimuon mass range considered, $M_{\mu\mu} > 1.5$ GeV/c^2. Several other ones have been tested in order to establish an uncertainty on the (J/ψ)/DY result. In this case, the uncertainty on the (J/ψ)/DY ratio has the same magnitude, whatever the Drell-Yan mass range is chosen to normalize

[3] The mass range where Drell-Yan is the only signal is smaller and smaller as E_T increases because combinatorial background and $D\bar{D}$ contributions increase with the collisions centrality.

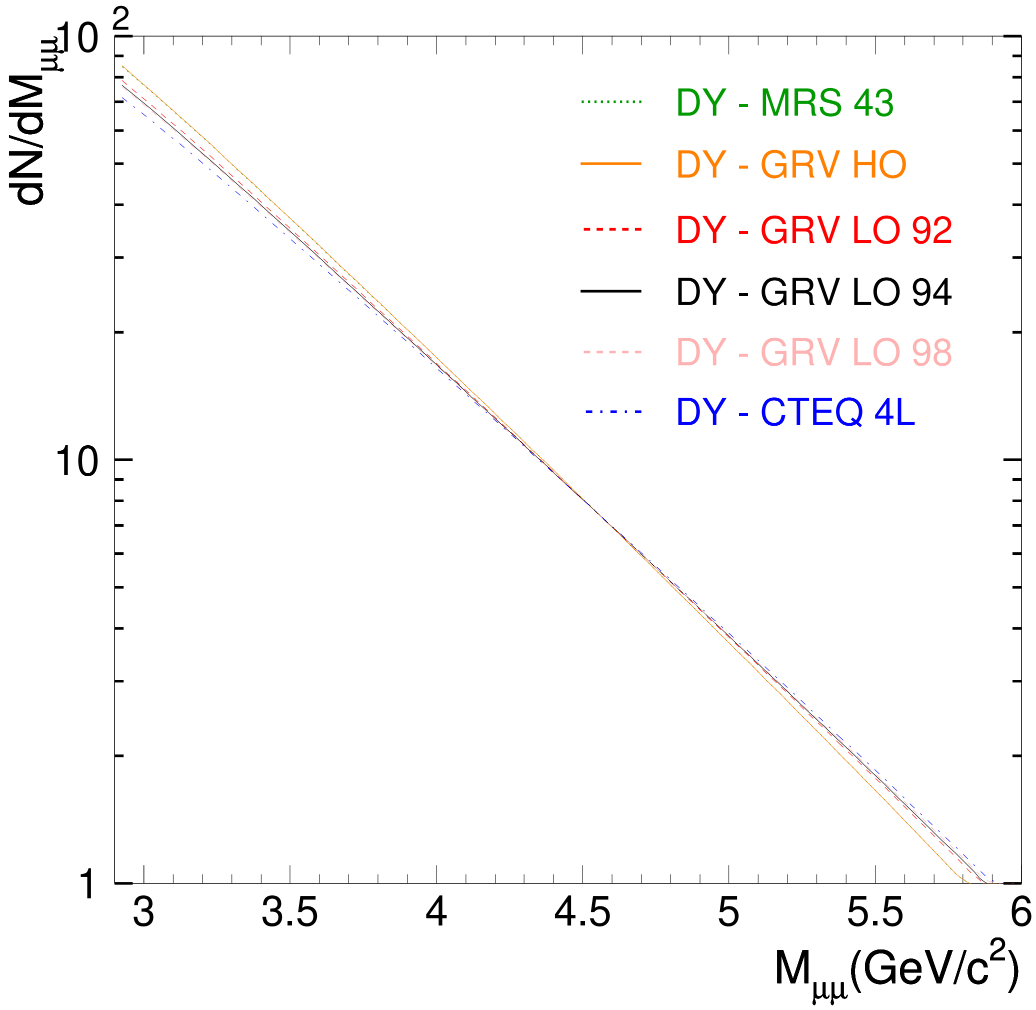

Figure 5.10: *The Drell-Yan obtained with several PDFs normalized to the same data.*

the J/ψ, because, although all LO PDFs give almost the same 4.2—7.0 normalization ($< 1\%$), the acceptances in this mass range become significant different (4%). However, one should keep the 2.9-4.5 GeV/c^2 domain, since both dilepton processes have the same features, namely acceptance and momentum. The uncertainty in J/$\psi/DY_{2.9-4.5}$ ratio due to the different PDFs, calculated at the same order (LO), is estimated to be +3.5%.

5.1.5 Overall systematic uncertainty on $(J/\psi)/DY$ measurement

For completeness, the set of uncertainties on $(J/\psi)/DY$ measurement should include the one related to the spectrometer acceptances evaluation. Such systematic error is estimated to be $\pm 1.36\%$ and comes exclusively from the uncertainty on the J/ψ acceptance. The systematic error on the Drell-Yan one is included in the uncertainty due to the use of different PDFs, since shapes and respective acceptances are correlated.

Table 5.5 summarizes the relative systematic errors on the $J/\psi/DY_{2.9-4.5}$ ratio. The overall systematic error stands in the interval $[-1.36\%, +3.79\%]$.

Systematic effect	$\Delta(J/\psi/DY_{2.9-4.5})$
IMR constraints	compatible with 0.
DY fitted vs counted	compatible with 0.
Final fit mass range	$+0.5\%$
PDF (GRVLO94/CTEQ4L)	$+3.5\%$
$Acc(DY_{2.9-4.5})/Acc(J/\psi)$	$\pm 1.36\%$

Table 5.5: *The relative systematic errors in the $J/\psi/DY_{2.9-4.5}$ ratio.*

5.1.6 The Pb–Pb 2000 results

The $J/\psi/DY_{2.9-4.5}$ values for the 11 E_T regions are reported in table 5.6. For each E_T range result, a relative systematic error varying from -1.36% to $+3.79\%$ should be considered.

The $(J/\psi)/DY$ ratio as a function of the transverse energy, corrected for the acceptance values quoted in table 4.1, is shown in figure 5.11. A steady decrease of the ratio as the collisions centrality increases is observed, without saturation, showing that J/ψ is strongly suppressed in Pb–Pb interactions. A factor of 2 between peripheral and central collisions is seen. The statistical fluctuations come from Drell-Yan, as can be observed on the right plot of figure 5.12. The J/ψ fitted normalizations are shown on the left plot. These J/ψ and Drell-Yan E_T distributions are not corrected for target identification inefficiency, as well as for trigger and reconstruction efficiencies, which cancel out in the ratios; however, as referred in section 3.4.2, the NOCIMD target algorithm is fully efficient for $E_T > 15$ GeV. A preliminary result of this Pb–Pb 2000 data analysis has been presented in [11] and this refined one in [12, 13].

E_T GeV	$< E_T >$ GeV	$J/\psi/DY_{2.9-4.5}$
3-15	10.6	26.60 $\pm$ 2.97
15-25	20.4	23.48 $\pm$ 2.08
25-35	30.3	23.52 $\pm$ 2.00
35-45	40.2	18.29 $\pm$ 1.35
45-55	50.2	16.55 $\pm$ 1.14
55-65	60.1	16.01 $\pm$ 1.14
65-75	70.1	15.26 $\pm$ 1.05
75-85	80.1	14.36 $\pm$ 0.98
85-95	90.1	12.69 $\pm$ 0.84
95-105	100.0	13.00 $\pm$ 0.89
105-150	111.5	11.18 $\pm$ 0.76

Table 5.6: *The $J/\psi/DY_{2.9-4.5}$ values for the 11 E_T regions. Errors are only statistical. A band that accounts for the systematic uncertainties [-1.36%, $+3.79\%$] should be considered.*

5.2 The Pb–Pb 1998 results

The main goal of the Pb–Pb 1998 data taking was to clarify and to overcome the re-interactions problem that the Pb–Pb 1996 multi-target, composed by 7 sub-targets, has raised. The re-interactions of beam fragments from a first interaction occurring downstream in the target may not be detected and rejected, leading to measured E_T and E_{ZDC} values typical of a much more central (single) collision [2]. So, for the Pb–Pb 1998 run, a single sub-target with 7% of λ_I^{Pb} was used. The statistics are smaller by a factor of 4 with respect to the previous data taking, so the number of J/ψ after data selection is significantly smaller than the one obtained in Pb–Pb 1996 or in Pb–Pb 2000. However, this data taking has a major advantage relatively to the Pb–Pb 1996 one, which is the NOCIMD target identification algorithm, that allows analyses extended to low centralities. After Pb–Pb 1998 data reconstruction and selection (see table 3.4), the number of J/ψ is $\sim$50000. In order to perform the standard analysis as a function of the transverse energy, the statistical data sample has been divided in 7 E_T regions. The fit procedure has followed the criteria used for the Pb–Pb 2000 analysis.

We have noticed a global J/ψ mass shift of +16 MeV with respect to the Pb–Pb 2000 and 1996 ones due to a wrong interaction vertex assignment during the events reconstruction. This is not a problem for the J/ψ cross section measurement, since its mass is a free parameter in the fit; however this systematic error on the interaction vertex has affected in the same way all dilepton sources of the mass spectrum. For this reason, the Drell-Yan mass range has been adjusted by +16 MeV, for comparison purposes with the other data samples. The $J/\psi/DY_{2.9-4.5}$ values for the 7 E_T regions are reported in

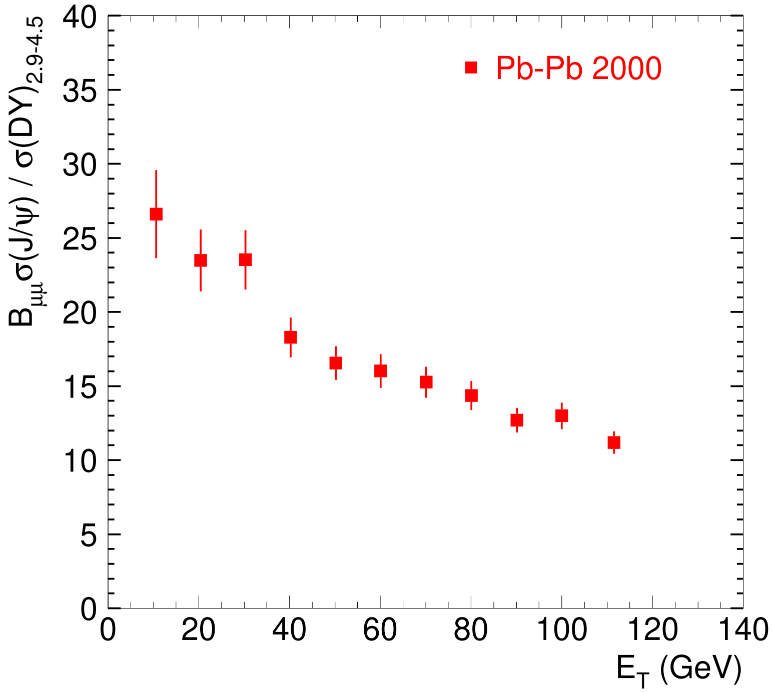

Figure 5.11: *The $J/\psi/DY_{2.9-4.5}$ as a function of E_T. Errors are only statistical. See in the text the systematic value to be considered.*

table 5.7.

E_T GeV	$< E_T >$ GeV	$J/DY_{2.9-4.5}$
3-20	15.7	25.76 ± 4.17
20-35	30.8	19.03 ± 1.89
35-50	46.7	15.04 ± 1.30
50-65	62.7	13.79 ± 1.11
65-80	78.8	13.33 ± 1.09
80-95	94.9	11.31 ± 0.92
95-120	109.9	11.19 ± 1.30

Table 5.7: *The $J/\psi/DY$ values for the Pb–Pb 1998 data. Errors are only statistical. See text for systematic errors.*

As expected, the statistical error on the $(J/\psi)/DY$ ratio is much higher in the Pb–Pb 1998 data sample. The relative error is around 10%. In what respects the systematic errors, they are very similar to the ones found in the 2000 data results. The fit technique is the same, as well as the setup [4]. An exception is the fit mass region — the difference of

[4] The differences between Setup 12 (Pb–Pb 1998) and Setup 19 (Pb–Pb 2000) are the single target thickness, which is 3 mm and 4 mm, respectively, and the target region, which in 2000 was placed in

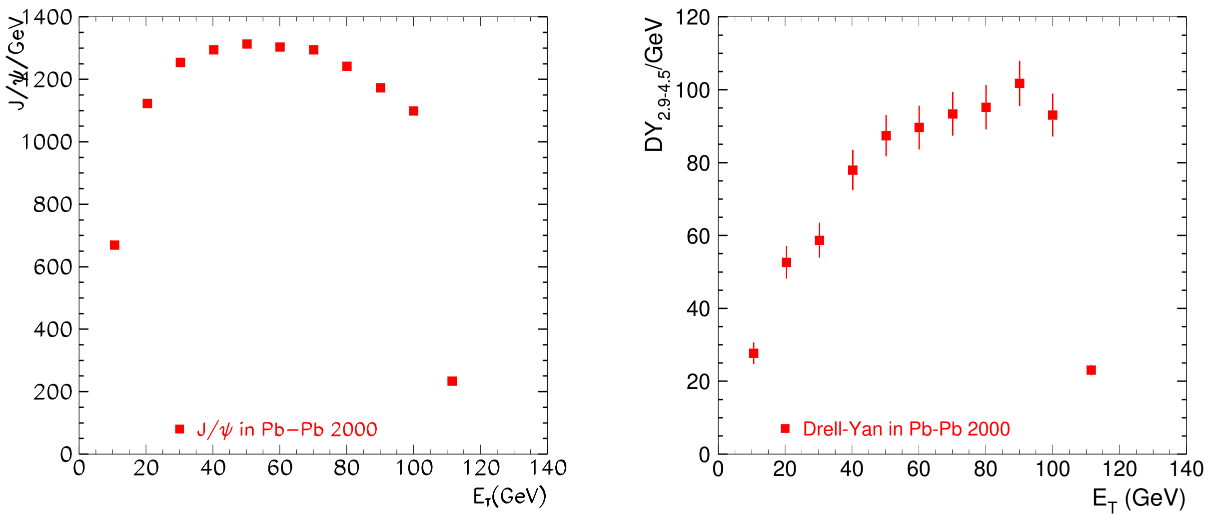

Figure 5.12: *The J/ψ and Drell-Yan (2.9-4.5 GeV/c^2) distributions with E_T, for the 11 E_T regions, (not corrected for inefficiencies).*

J/ψ normalizations is also only 0.4%, but for all E_T regions, including the most peripheral one. The reason for this uniform behaviour is the higher value of the P$\times$Dtarget cut (6%), which is sufficient to eliminate the background, mostly composed by J/ψ produced in the absorber. The systematic uncertainty in Drell-Yan due to the use of different PDFs is independent on the setup. The J/ψ and Drell-Yan acceptances are smaller for the Setup 12, since the P$\times$Dtarget cut is higher. They are 11.39 ± 0.01(stat) and 12.66 ± 0.01(stat), respectively. The ratio between these acceptances is 1.111, less than 1% different with respect to the year 2000 acceptances ratio, thus perfectly compatible within errors. In fact, it has been checked that the relative difference between J/ψ and Drell-Yan acceptances is independent on the P$\times$Dtarget cut, providing that mass and momentum ranges are similar, which is the case of J/ψ and Drell-Yan in the 2.9-4.5 mass range. For this reason we keep the same systematic acceptance errors. Thus, the overall systematic error to be applied to the Pb–Pb 1998 results stands between -1.36% and $+3.78\%$.

Figure 5.13 shows the J/$\psi/DY_{2.9-4.5}$ ratio as a function of E_T for the Pb–Pb 1998 data sample. The J/ψ/DY dependence with the transverse energy is the same as the one seen in the 2000 results, i.e., the J/ψ strong suppression, relatively to Drell-Yan, as the collisions centrality increase.

Figure 5.14 shows the behaviour of J/ψ and Drell-Yan as functions of E_T, concerning the Pb–Pb 1998 data. No significant fluctuations are observed.

Figure 5.15 shows the comparison between Pb–Pb 2000 and 1998 results. Good compatibility is verified.

vacuum.

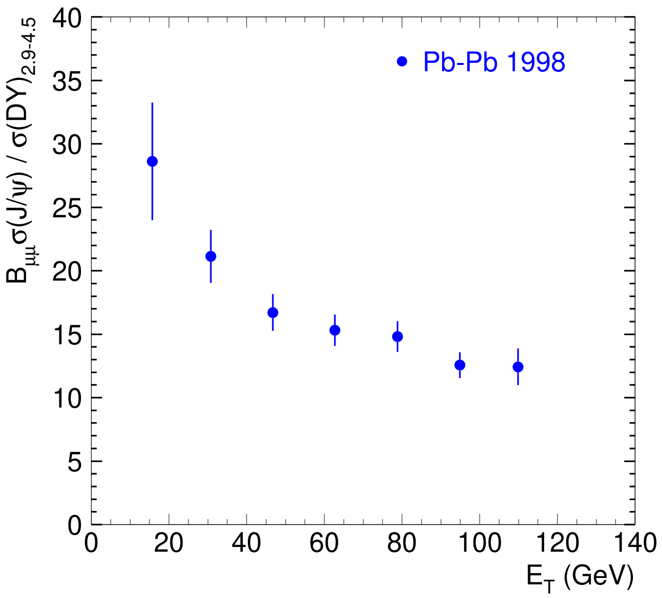

Figure 5.13: *The Pb–Pb 1998 results on $(J/\psi)/DY$ as a function of E_T. The errors are only statistical. See text for systematic errors.*

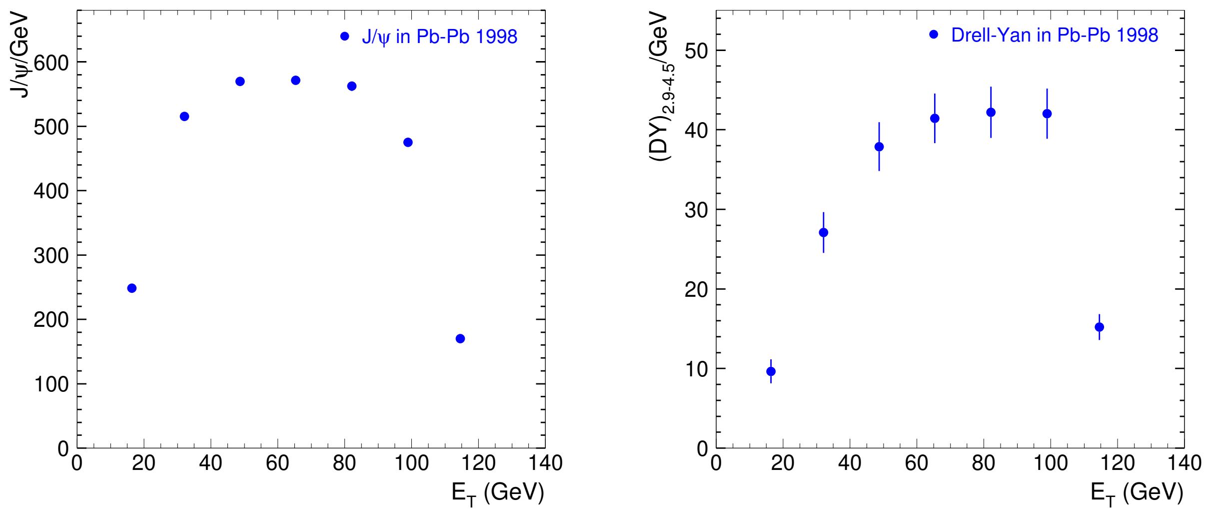

Figure 5.14: *The J/ψ and Drell-Yan normalizations as functions of E_T, for the Pb–Pb 1998 data sample, (not corrected for inefficiencies).*

5.3 The Pb–Pb 1996 results

Section 3.6 describes the advantages and drawbacks of the Pb–Pb 1996 run. Taking into account their particular features, the data have been analysed under the same criteria as for Pb–Pb 2000 (and 1998).

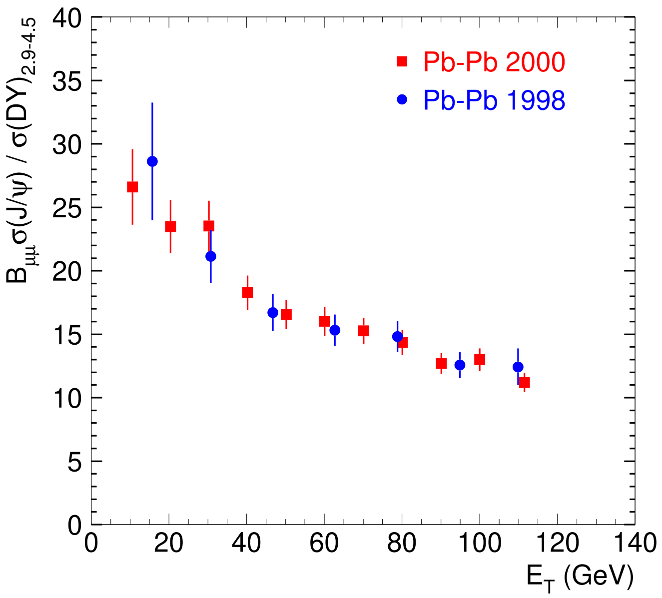

Figure 5.15: *The comparison between Pb–Pb 2000 and 1998 results, concerning* $J/\psi/DY_{2.9-4.5}$ *as a function of* E_T*. Statistical errors only. See text for systematic errors.*

In order to overcome the inefficiency of the target identification algorithm, one has to include the flag NOCIBI = 8, which signals an interaction in the multi-target system, but not signalling the fired sub-target. While the number of events with NOCIBI = 8 is negligible for E_T>40-50 GeV, 90% of the low centrality events have no precise sub-target identification. Although the $E_T - E_{ZDC}$ band ensures that we are selecting in-target interactions, two main consequences arise: for the transverse energy and J/ψ mass calculations purposes it is assumed that the hit sub-target is the middle positioned one, the 4$^{\text{th}}$. This feature results in a wrong assignment of the event centrality and in a poor mass resolution. Regarding the latter, an enlargement of the J/ψ width with respect to mid and high centrality events, is verified. However, this is not a problem because, provided the J/ψ width is a free parameter of the fit, the extracted J/ψ cross section is not affected. Also, one expects this smearing effect in the continuum to be very small. Nevertheless, the typical E_T measurement deviation may be of the order of 10%.

Pb–Pb 1996 data have been analysed with the 11 Pb–Pb 2000 E_T regions. Fig 5.16 shows the (J/ψ)/DY as a function of E_T. The (J/ψ)/DY yield in the most central collisions is artificially high, due to the re-interaction problem, already referred. So, the last two E_T regions should be skipped out. The fluctuation seen in region 7 is beyond the statistical errors, suggesting the existence of systematic errors not under control.

Figure 5.17 shows the comparison among (J/ψ)/DY results from the three data samples analysed. Although the results are consistent within statistical errors, one should be cautious about the Pb–Pb 1996 results. As referred, the target identification algorithm inefficiency has imposed the inclusion of events flagged with NOCIBI = 8 (interaction in a not recognized sub-target), in order to have sufficient statistics to perform the analysis at

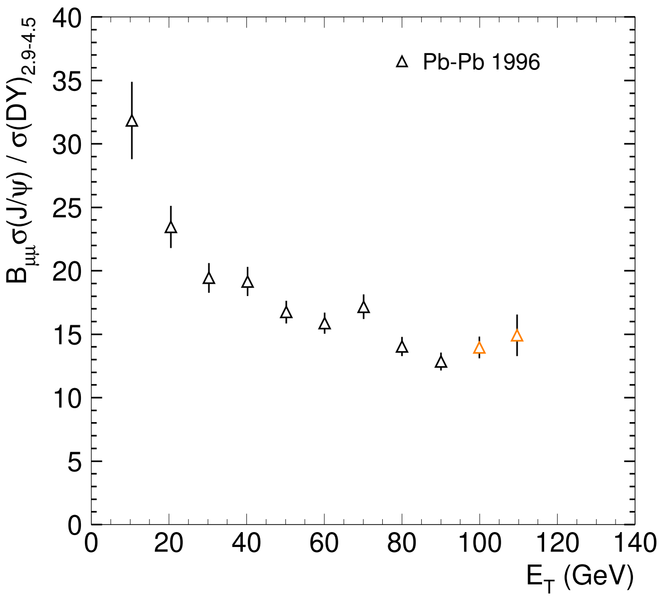

Figure 5.16: *The Pb–Pb 1996 results of (J/ψ)/DY as a function of E_T. The errors are only statistical. The last two points are affected by the re-interaction problem.*

low centrality. Although the enlargement of the J/ψ width does not affect the J/ψ cross section, one cannot guarantee that, for the peripheral collisions, the transverse energy is correctly calculated, or that the results are free from Pb-air interactions contamination. The last E_T regions of the 1996 data have been skipped out, since the re-interactions, shifting (J/ψ)/DY values towards high centralities, give artificial results.

5.4 An overall measurement of the J/ψ suppression

Pb–Pb 1998 data has been analysed using the 2000 data E_T regions, in order to get an overall measurement of the J/ψ suppression as a function of E_T, relatively to Drell-Yan. Due to the reasons pointed out in the previous section, the Pb–Pb 1996 results are not included in the average.

Figure 5.18 shows the Pb–Pb 1998 data analysed in 7 and 11 E_T regions. Although the 1998 sample limited statistics, as compared to the 2000 one, has lead the division of the E_T spectrum in only 7 regions, the results with 11 regions do not show any visible systematic effect due to lower populations in each range. Furthermore, no significant statistical fluctuations are observed.

Since the two data samples are consistent with each other and the systematic errors are under control, namely in what regards the target identification algorithm, an average can be performed. The advantage of such procedure is the more accurate measurement

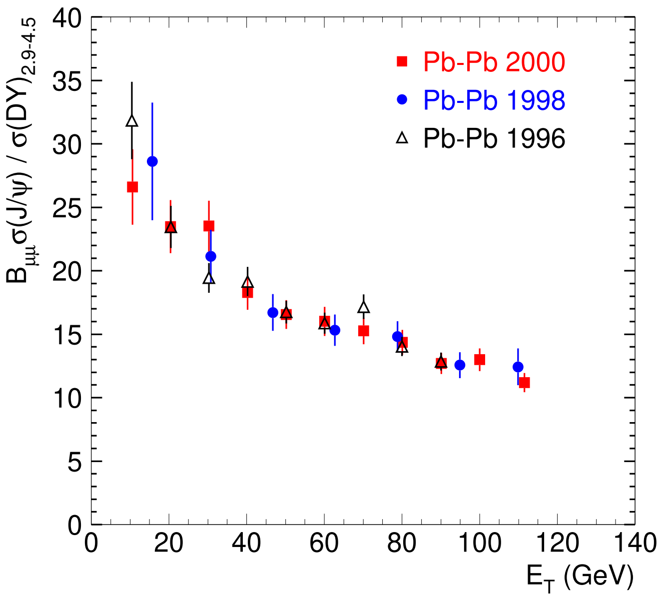

Figure 5.17: *The Pb–Pb results on $(J/\psi)/DY$ as a function of E_T, concerning the three analysed data periods. Errors are only statistical.*

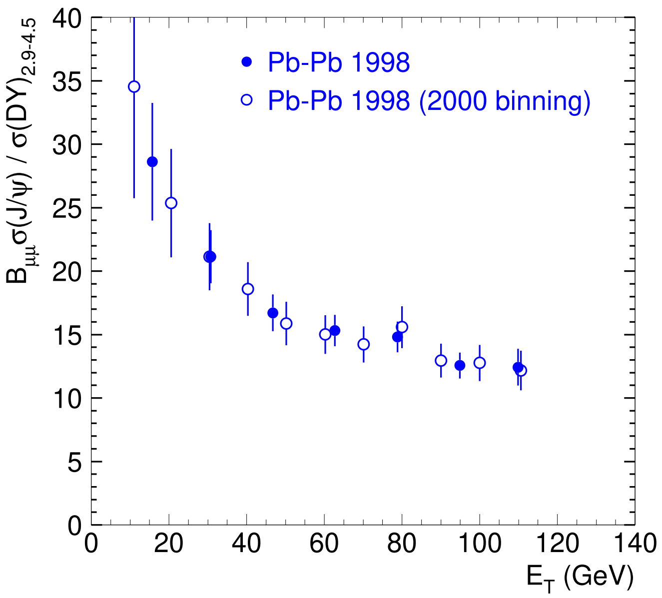

Figure 5.18: *The $(J/\psi)/DY$ as a function of E_T for Pb–Pb 1998 data, with 7 and 11 regions.*

of the J/ψ suppression. Table 5.8 reports the (J/ψ)/DY results for the two data sets analysed in the same E_T regions, as well as the averaged results.

As expected, the mean values are closer to the Pb–Pb 2000 results. As the statistical samples are very different in magnitude, the results follow mainly the 2000 ones,

E_T GeV	$< E_T >$ GeV	Pb–Pb 2000	Pb–Pb 1998	Average
3-15	10.6	26.60 ± 2.97	34.55 ± 8.80	27.41 ± 2.81
15-25	20.4	23.48 ± 2.08	25.37 ± 4.27	23.84 ± 1.87
25-35	30.3	23.52 ± 2.00	21.14 ± 2.64	22.65 ± 1.59
35-45	40.2	18.29 ± 1.35	18.60 ± 2.12	18.37 ± 1.14
45-55	50.2	16.55 ± 1.14	15.88 ± 1.72	16.34 ± 0.95
55-65	60.1	16.01 ± 1.14	15.01 ± 1.53	15.65 ± 0.92
65-75	70.1	15.26 ± 1.05	14.22 ± 1.42	14.90 ± 0.84
75-85	80.1	14.36 ± 0.98	15.58 ± 1.64	14.69 ± 0.84
85-95	90.1	12.69 ± 0.84	12.95 ± 1.33	12.77 ± 0.71
95-105	100.0	13.00 ± 0.89	12.77 ± 1.42	12.93 ± 0.76
105-150	111.5	11.18 ± 0.76	12.16 ± 1.56	11.37 ± 0.68

Table 5.8: *The $J/\psi/DY_{2.9-4.5}$ values for Pb–Pb 2000, Pb–Pb 1998 and average. Errors are only statistical.*

namely their statistical errors and Drell-Yan fluctuations. Nevertheless, the relative error decreases to 6%. Figure 5.19 shows the overall measurement of the J/ψ suppression as a function of E_T , relatively to Drell-Yan. The systematic errors lay on the interval $[-1.36\%, +3.79\%]$.

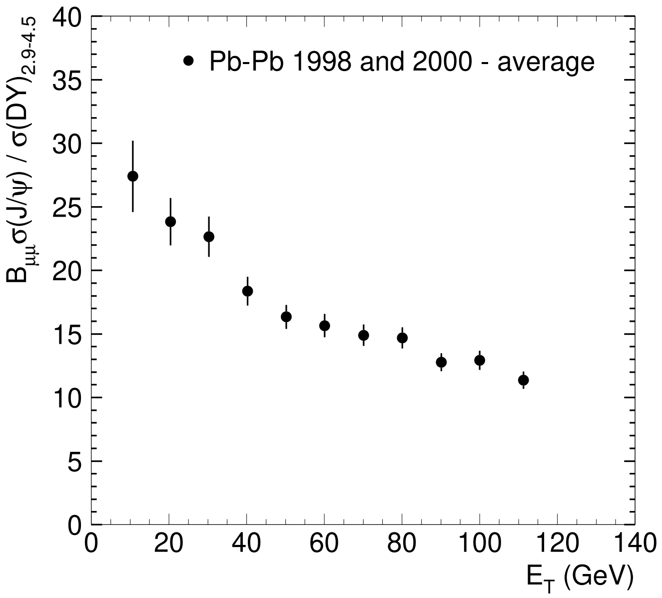

Figure 5.19: *The averaged results of Pb–Pb 1998 and 2000 data, concerning $(J/\psi)/DY$ as a function of E_T. Errors are only statistical. The systematic errors stand between -1.36% and $+3.79\%$.*

5.5 (J/ψ)/DY as a function of the energy density

In the framework of the Bjorken model, the energy density reached in a nucleus-nucleus collision is proportional to the number of participating nucleons per unit transverse area [14]. Equation 1.10 can be expressed as:

$$\epsilon_0(\tau_0) = \epsilon(E_T(y^* = 0)) = \frac{|\frac{dE_T}{dy}|_{y^*=0}}{c\tau_0 s} \ , \tag{5.4}$$

where $E_T \equiv E_T^{tot}$ should be the total transverse energy measured by the NA50 electromagnetic calorimeter and s is the transverse area of overlap between the nuclei. However, the calorimeter measures the neutral transverse energy in a pseudorapidity interval $\Delta\eta$ and not at y*=0. Therefore, one should proceed to the conversion between the two kinematic conditions [15]:

$$\left|\frac{dE_T}{dy}\right|_{y^*=0} = \frac{\Delta E_T}{\Delta\eta} C(\Delta\eta \ \rightarrow \ y^* = 0) \ . \tag{5.5}$$

The total electromagnetic transverse energy $E_T \equiv E_T^{tot}$ is defined as $3E_T^0$, assuming that the measured energy comes mostly from pions. The measured $E_T^0(\Delta\eta)$ is divided in N($E_T^0(\Delta\eta)^i$ regions:

$$E_T^0(\Delta\eta) = \sum_{i=1}^{N} E_T^0(\Delta\eta)^i \tag{5.6}$$

and for each $E_T^0(\Delta\eta)^i$ range of mean energy $< E_T^0(\Delta\eta) >^i$ the following relation is valid:

$$\left|\frac{dE_T}{dy}\right|^i_{y^*=0} = \frac{3 < E_T^0(\Delta\eta) >^i}{\Delta\eta} \frac{\left|\frac{dE_T}{d\eta}\right|_{y^*=0}}{\frac{1}{\Delta\eta}\int_\eta^{\eta+\Delta\eta} \frac{dE_T^{tot}}{d\eta} d\eta} \ . \tag{5.7}$$

The second factor on the right hand side has been calculated using the measured pseudorapidity distributions of charge particles shown in figure 5.20 [16, 17]. As the phase space in rapidity becomes more and more narrow with the increasing centrality, the value C($\Delta\eta \rightarrow y^* = 0$) varies between 1.43 ± 0.02 and 1.61 ± 0.01.

At the SPS energies several experiments [17, 18, 19] have observed a scaling law

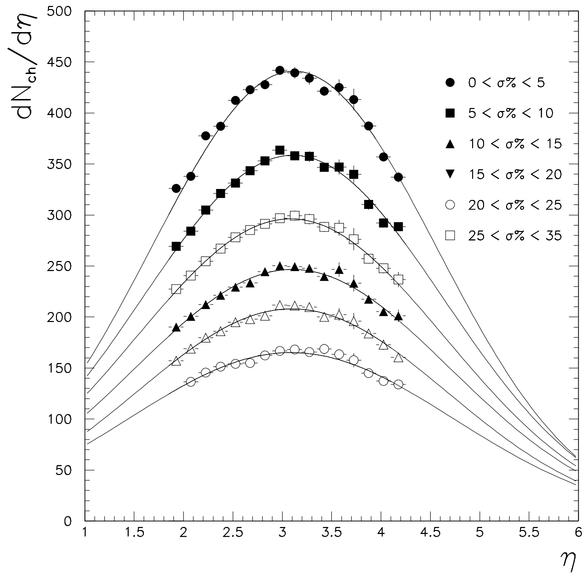

Figure 5.20: *Pseudorapidity distributions of charged particles in Pb–Pb collisions at 158 GeV/nucleon, obtained with E_T as the centrality estimator [16, 17].*

between the number of participating nucleons [5], N_{part} ,in a nucleus-nucleus collision and particle production, as well as $dE_T/d\eta|_{max}$ [20]. This behaviour is expected in scenarios dominated by soft processes, in which the produced particles undergo a strong rescattering in the final state and the memory of the exact history of multiple collisions is lost. Then, it may be assumed that each participant nucleon contributes with the same amount of energy to particle production and the scaling with N_{part} is approximately linear:

$$< E_T > \simeq q < N_{part} > \quad . \tag{5.8}$$

Thus, eq. 5.4 becomes:

$$\epsilon_0^i = 3 \frac{q < N_{part}/s >^i C(\Delta\eta \rightarrow y^* = 0)}{c\tau_0 \Delta\eta} \quad . \tag{5.9}$$

N_{part}/s is calculated in the framework of the Glauber model [21] of the nucleus-nucleus collisions. Such a model considers an A–B interaction as a superposition of

[5] Also called *wounded*. A nucleon is designed as wounded if it has interacted inelastically one, or more times, with one, or more nucleons, and fragmentation of such wounded nucleon eventually produces the observed secondary hadrons.

independent interactions between the beam and target nucleons. The model also assumes that the nucleon-nucleon cross section remains unchanged as the two nuclei cross each other. This is an approximation because a nucleon, after a collision, may become excited and subsequently interact with other nucleon with a different cross section. The physical inputs are the density distribution of the nucleons inside the nucleus, ρ, and the non-diffractive nucleon-nucleon inelastic cross-section, σ_{in}, of about 30 mb. The Pb nuclear density is parametrized by a two-parameters Fermi function [22], also known as the Woods-Saxon distribution:

$$\rho(r) = \frac{\rho_0}{1 + \exp\frac{(r-r_0)}{c}} , \tag{5.10}$$

where r_0 is the half-density radius of 6.624 fm and c is a diffuseness parameter of 0.546 fm, as measured in electron-nucleus scattering experiments; ρ_0 is the average nuclear density, taken as 0.17 fm^{-3}.

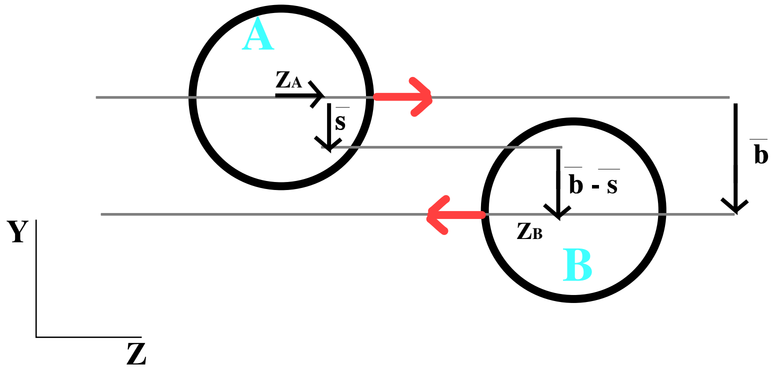

Figure 5.21: *The longitudinal view of an A–B collision with impact parameter $\vec{b}$.*

In a A–B collision with impact parameter $\vec{b}$ (see figure 5.21 for a pictorial view), the density of participating nucleons per surface unit, perpendicular to the beam direction z, is given by [23, 15]:

$$n_{part}^{AB}(\vec{b}) = AT_A(\vec{s})[1 - (1 - T_B(\vec{s} - \vec{b})\sigma_{in})^B] + BT_B(\vec{s} - \vec{b})[1 - (1 - T_A(\vec{s})\sigma_{in})^A] , \tag{5.11}$$

where $T_A(\vec{s}) = \int_{-\infty}^{+\infty} \rho_A(z, \vec{s})dz$ is the nuclear profile function. A plot of n_{part} as a function of the coordinate x ($y = b/2$) in the transverse plane, for several values of $\vec{b}$, is shown in figure 5.22. The distributions are bell-shaped with maxima located at the middle point between the colliding nuclei centers.

For a given $\vec{b}$, the probability of having a hard nucleus-nucleus collision at the point

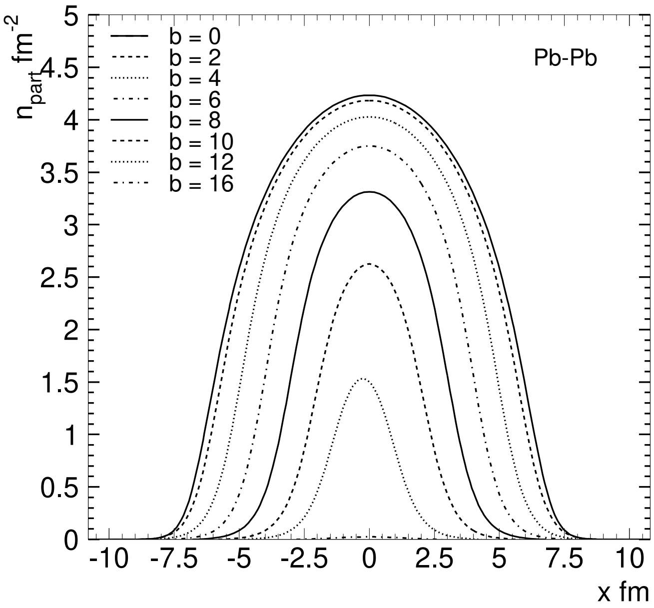

Figure 5.22: *The density of participants as a function of x ($|x| < (2R_{Pb}^{max} - b)/2$) for several impact parameters values.*

$\vec{s}$ is:

$$P(\vec{s},\vec{b})d^2\vec{s} = \frac{T_A(\vec{s})T_B(\vec{s}-\vec{b})d^2\vec{s}}{\int T_A(\vec{s})T_B(\vec{s}-\vec{b})d^2\vec{s}} \ , \tag{5.12}$$

where $T_A(\vec{s})T_B(\vec{s}-\vec{b})d^2\vec{s}$ is the number collisions at point $\vec{s}$. Thus, the mean value of the number of participating nucleons per surface unit, at a given $\vec{b}$, becomes:

$$< \frac{N_{part}}{s}(\vec{b}) >= \int n_{part}^{AB}(\vec{b})P(\vec{s},\vec{b})d^2\vec{s} \ . \tag{5.13}$$

Once this mean value is calculated, one needs to determine the correlation factor, q, between the number of participating nucleons and the transverse energy. The E_T spectrum of a hard process, such as Drell-Yan or charmonium production, is determined by the number of collisions, rather than by the number of participating nucleons [24]:

$$\frac{dN}{dE_T}^{th}\Big|_{DY} \propto \int 2\pi b[1 - P_0(b)]N_{coll}(b)P_{AB}(E_T|b)db \ , \tag{5.14}$$

where $[1 - P_0(b)]$ is the probability of having at least one inelastic collision at impact parameter b. $P_{AB}(E_T|b)$ is the conditional probability that a given E_T is measured in a collision with impact parameter b [24]. This probability is taken as a gaussian distribution around the mean value $< E_T >= q < N_{part}(b) >$:

$$P_{AB}(E_T|b) = \frac{1}{\sqrt{2\pi}\sigma_{E_T}(b)} \exp -\frac{1}{2}\frac{(E_T - q < N_{part}(b) >)^2}{\sigma^2_{E_T}(b)} \ , \tag{5.15}$$

with

$$\sigma^2_{E_T}(b) = wq < E_T(b) >= wq^2 < N_{part}(b) > \ . \tag{5.16}$$

q and ω are, therefore, adjusted to reproduce the experimental E_T distribution. Figure 5.23 shows a fit to the high mass Drell-Yan ($M_{\mu\mu} > 4.2$ GeV/c^2) E_T spectrum of Pb–Pb 2000 collisions, where $P_1 \equiv q$, $P_2 \equiv w$ and P_3 stands for the normalization. The parameter q depends on the characteristics of the detector, in particular on the rapidity and transverse momentum range in which the produced secondary hadrons are measured, while the parameter ω accounts for the detector resolution. The fit is performed for $E_T >$

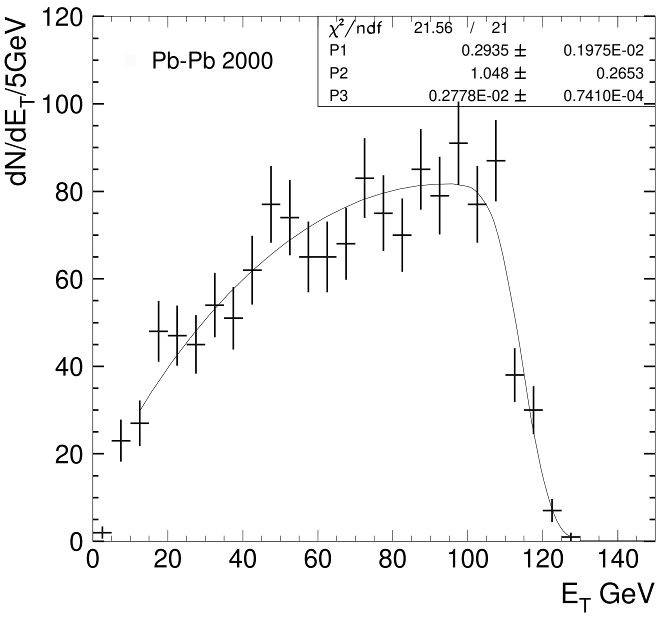

Figure 5.23: *Fit of high mass Drell-Yan ($M > 4.2$ GeV/c^2) E_T spectrum with eq. 5.14.*

15 GeV, since in this E_T range the efficiency for the target identification algorithm is 1. Figure 5.24 shows the E_T–b correlation as given by equation 5.15, after the extraction of q and ω parameters. In a similar way, taking into account the experimental resolution, the number of participating nucleons for a given E_T is smeared, as shown in figure 5.25.

The average values of N_{part}/s and their widths (r.m.s.), as well as the energy densities reached for each E_T region, are reported in table 5.9. For completeness, the average values of the impact parameters b are also quoted. Notice that the energy densities calculated are in agreement with the reached values expected for the SPS Pb–Pb collisions

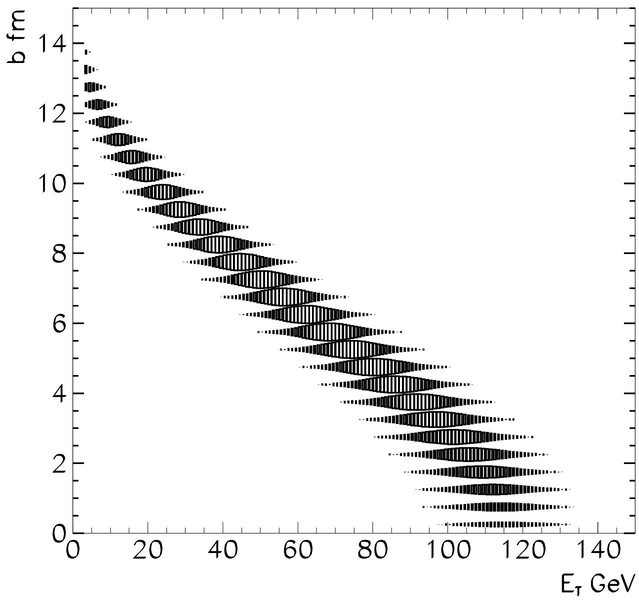

Figure 5.24: *The correlation between the transverse energy, as measured by the NA50 electromagnetic calorimeter, and the impact parameter b calculated for Pb–Pb collisions at 158 GeV/c, regarding Drell-Yan events with mass above 4.2 GeV/c^2.*

at nucleon-nucleon center of mass energy of 17.3 GeV [25].

E_T GeV	$< E_T >$ GeV	b	r.m.s.	$< N_{part}/s >$ fm^{-2}	r.m.s.	ϵ GeV/fm^3	r.m.s.
3-15	10.6	11.63	0.73	1.08	0.32	1.15	0.34
15-25	20.4	10.12	0.49	1.75	0.19	1.86	0.20
25-35	30.3	9.04	0.46	2.14	0.14	2.27	0.15
35-45	40.2	8.10	0.45	2.42	0.12	2.60	0.13
45-55	50.2	7.23	0.46	2.63	0.10	2.87	0.11
55-65	60.1	6.39	0.47	2.80	0.08	3.06	0.09
65-75	70.1	5.57	0.50	2.94	0.07	3.27	0.08
75-85	80.1	4.73	0.54	3.05	0.06	3.46	0.07
85-95	90.1	3.84	0.61	3.14	0.05	3.66	0.06
95-105	100.0	2.86	0.73	3.21	0.04	3.83	0.05
105-150	111.5	1.77	0.76	3.25	0.03	3.89	0.04

Table 5.9: *Average impact parameters, participating nucleons per surface unit and energy densities reached for each E_T range.*

Once the energy density is calculated, the weighted average between the (J/ψ)/DY 1998 and 2000 analyses as a function of ϵ follows. This can be seen in figure 5.26. As the energy density is proportional to the transverse energy, the J/ψ suppression pattern

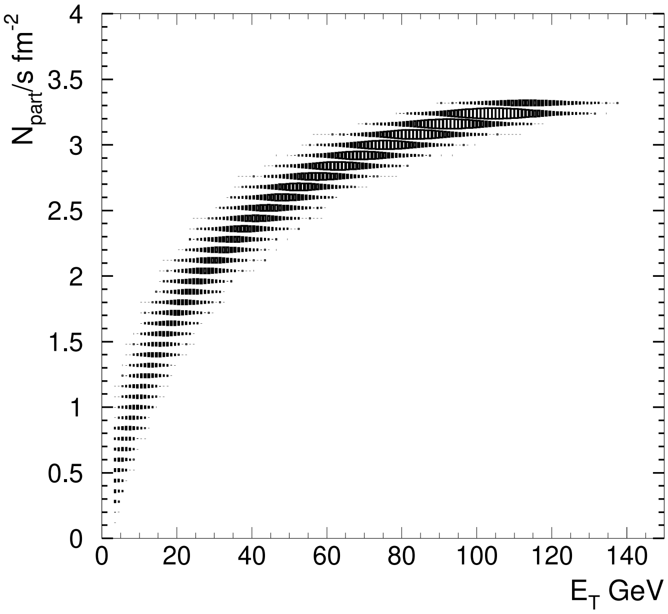

Figure 5.25: *The correlation between the transverse energy and the number of participating nucleons per surface unit, calculated by Glauber theory.*

becomes similar for both centrality variables. However, due to the non-linearity between the number of participating nucleons per surface unit and the transverse energy (see figure 5.25) the (J/ψ)/DY ratio becomes more and more contracted with the increasing energy density.

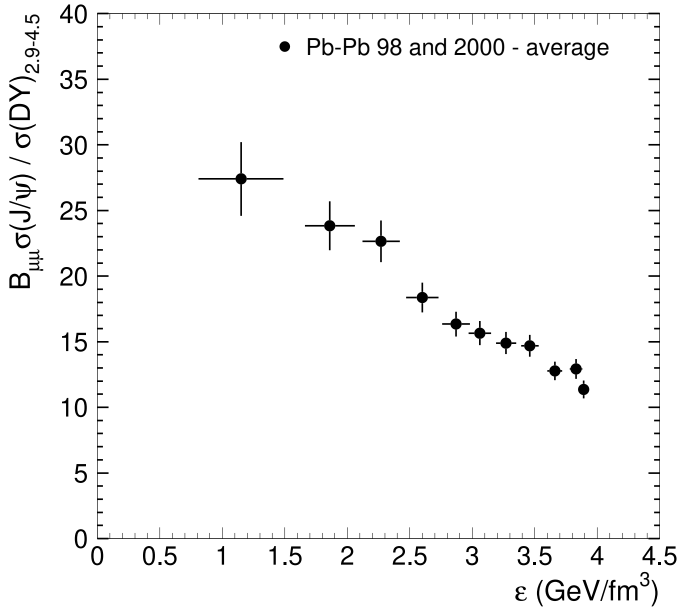

Figure 5.26: *The (J/ψ)/DY as a function of the energy density.*

Bibliography

[1] M.C. Abreu et al. (NA50 Coll.), Phys. Lett. B450 (1999) 456

[2] M.C. Abreu et al. (NA50 Coll.), Phys. Lett. B477 (2000) 28

[3] MINUIT - Function Minimization and Error Analysis, Reference Manual, version 96.03, Computing and Networks Division – CERN

[4] Particle Data Group, K. Hagiwara et al., Phys. Rev. D66 (2002)

[5] H.L. Lai et al. (CTEQ Coll.), Phys. Rev. D55 (1997) 1280

[6] A.D. Martin, R.G. Roberts and W.J. Stirling, Phys. Rev. D51 (1995) 4756

[7] R. Vogt, hep-ph/0207359

[8] R. Vogt, private communication

[9] M. Gluck, E. Reya and A. Vogt, Z. Phys. C67 (1995) 433

[10] M. Gluck, E. Reya and A. Vogt, Eur. Phys. J. C 5 (1998) 461

[11] L. Ramello (NA50 Coll.), Quark Matter 2002, Nucl. Phys. A715 (2003) 243c

[12] H. Santos (NA50 Coll.), Quark Matter 2004, in J. Phys. G: Nucl.Part. Phys. 30 (2004) S1175

[13] B. Alessandro et al. (NA50 Coll.), "A new measurement of J/ψ suppression in Pb–Pb collisions at 158 GeV per nucleon", article submitted to Eur. Phys. J. C

[14] J.D. Bjorken, Phys. Rev. D27 (1983) 140

[15] B. Chaurand, NA50 Internal Note

[16] M.C. Abreu et al. (NA50 Coll.), Phys. Lett. B530 (2002) 33

[17] M.C. Abreu et al. (NA50 Coll.), Phys. Lett. B530 (2002) 43

[18] M.M. Aggarwal et al. (WA98 Coll.) Eur. Phys. J. C 18 (2001) 651

[19] F. Antinori et al. (WA97 and NA57 Coll.) Eur. Phys. J. C 18 (2000) 57

[20] M.M. Aggarwal et al. (WA98 Coll.), Quark Matter 1996, in Nuc. Phys. A619 (1996) 200c

[21] R.J. Glauber, Lectures in Theoretical Physics, Ed. by W.E. Brittin and L.G. Dunham (Interscience, NY, 1959) Vol. 1, 315

[22] H.De Vries et al., Atomic Data and Nuclear Data Tables 36 (1987) 495

[23] J.P. Blaizot and J.Y. Ollitrault, Phys. Rev. Lett. 77 (1996) 1703

[24] D. Kharzeev, C. Lourenço, M. Nardi and H. Satz, Z. Phys. C 74 (1997) 307

[25] H. Satz, Rep. Prog. Phys. 63 (2000) 1511

Chapter 6

The ψ' suppression in Pb–Pb collisions

The study of the ψ' production in Pb–Pb collisions implies special care of the data treatment, namely careful identification of systematic sources, since this resonance is a weak signal, not only due to its small dimuon cross-section, much lower than the J/ψ one, but also due to its large suppression with the increasing collisions centrality. Another challenge is the extraction of the ψ' signal itself from the several overlapping dimuon sources of about the same or even bigger cross section values (see figure 6.1).

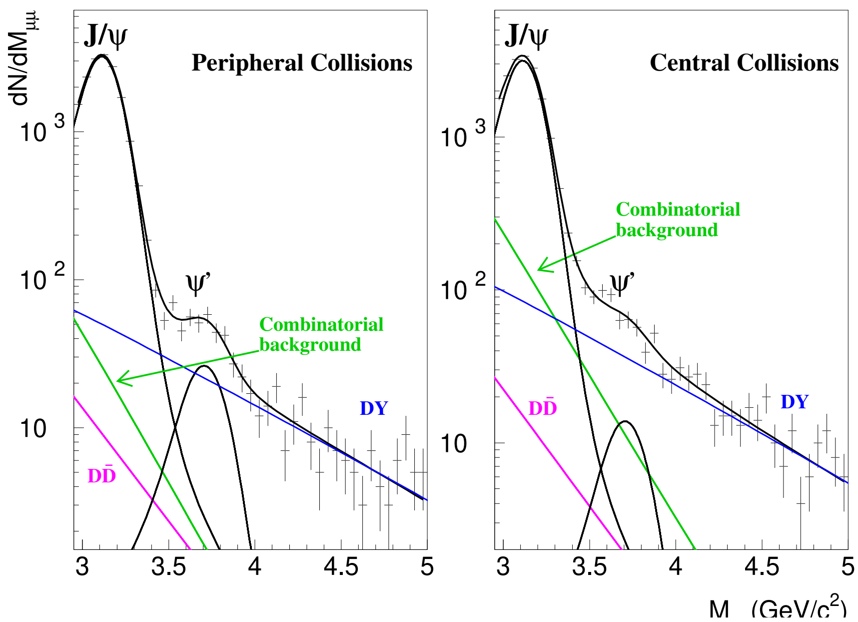

Figure 6.1: *The large ψ' suppression with increasing centrality.*

The ψ' standard analysis makes use of the transverse energy as the centrality estimator, as the J/ψ analysis does. The data sample is the same used for the J/ψ production study, since the data selection, either concerning track reconstruction or detector variables, should not depend on mass. However, it is interesting to note the importance of some cuts in the cleaning of ψ' sample, namely the ones ensuring in-target interactions. Figure 6.2 shows a dimuon invariant mass spectrum produced at low centrality values, composed by off-target events. A large spread of the J/ψ shape is seen, since dimuons are reconstructed with an interaction vertex spread over a large range around the target. A significant number of these events below the ψ' peak are J/ψ produced in interactions upstream from the target, and if they would improperly be considered as valid events for the analysis, the ψ' cross section would be seriously distorted.

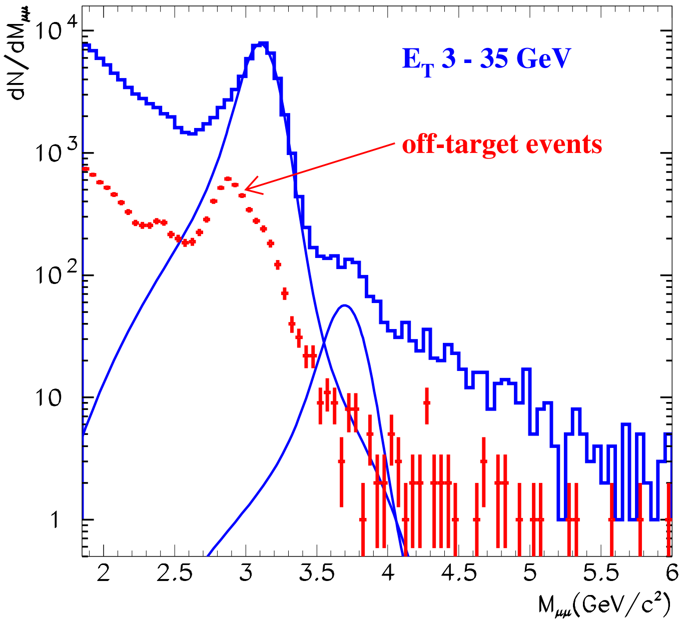

Figure 6.2: *J/ψ produced off-target pollutes the ψ' mass region.*

After the data selection, 905 ψ' events are suitable for analysis. This amount allows the division of the E_T spectrum in 7 intervals, since this number is enough to define a pattern as a function of centrality and, at the same time, keeps the statistical errors within reasonable values. The fit procedure to extract the ψ' signal follows the same steps described in section 4.2.2. The Drell-Yan mass range chosen to normalize the ψ' is 4.2-7.0 GeV/c^2. This normalization is extracted from the final fit mass range $2.9 \leq M_{\mu\mu} \leq 7.0$ and not from a direct fit to the high mass region. One should remind that the relative statistical error on the Drell-Yan yield is independent on the mass range chosen to normalize the resonances, although the main contribution to the statistical error comes from the high mass range. In fact, the relative error on the Drell-Yan yield in the 4.2–7.0 region, extracted from a 2.9–7.0 fit (where the Drell-Yan yield is factor of 6 higher), is only 20% smaller than the one obtained fitting directly the high mass range.

6.1 The systematic uncertainties

The ψ', while a much weaker signal, is very sensitive to every different procedure adopted to fit the dimuon invariant mass spectrum, as opposed to the J/ψ case. In each E_T range, the ψ', J/ψ and Drell-Yan yields are extracted simultaneously and the fit procedure is the same used for J/ψ analysis, since this technique has been tuned in order to describe correctly the whole dimuon invariant mass spectrum beyond 1.5 GeV/c^2. Thus, similar systematic studies concerning final fit mass regions and IMR have been performed in order to verify their influence on the ψ' measurement. Once more, the general criterium to guide the options is to ensure that the high mass Drell-Yan is well described, i.e., avoiding underestimation or overestimation of the data (counted events). Indeed, the main systematic uncertainty on the ψ' normalization comes from Drell-Yan, both regarding its normalization and chosen PDF.

6.1.1 The systematic error on the fit method

Regarding final fit of opposite sign dimuon mass spectrum, if the fit starts at 1.7 GeV/c^2 the ψ' normalizations decrease roughly by 20%. We have seen in the previous chapter that, when starting the fit at 1.7 GeV/c^2, the high mass Drell-Yan is not fitted properly; consequently, it biases the ψ' by the same amount and with the same trend as a function of E_T, but in the opposite direction, since these physical components of the fit are negatively correlated ($-50\% \sim -60\%$). This happens because, once the combinatorial background and open charm contributions are fixed, the dimuon sources that may change in the ψ' mass range, are the ψ' itself, the Drell-Yan and the J/ψ. However, being a strong signal, the J/ψ sensitivity to the fit mass region is less than 0.5% of events (over the whole mass range); therefore, in this game, whatever is lost or gained by Drell-Yan is transferred to or from ψ'. Figure 6.3 shows the ψ' and high mass Drell-Yan normalizations as a function of E_T, extracted from fits to the two different dimuon mass ranges. One notices the Drell-Yan smooth behaviour with the increasing centrality and the much better agreement between fit results from the 2.9–7.0 range and the counted events, for $M_{\mu\mu}$ >4.2 GeV/c^2.

In conclusion, the 20% discrepancy due to the different fit mass ranges is not considered as a systematic uncertainty, but a bias. Two more fit mass ranges were performed to check the ψ' normalization sensitivity: 2.95–7.0 and 3.0–7.0 GeV/c^2. Figure 6.4 shows the ψ' distributions against E_T compared with the values obtained with the standard fit mass region, 2.9–7.0 GeV/c^2. No sensitivity is observed. Indeed, good stability on the

ψ' fit results is verified.

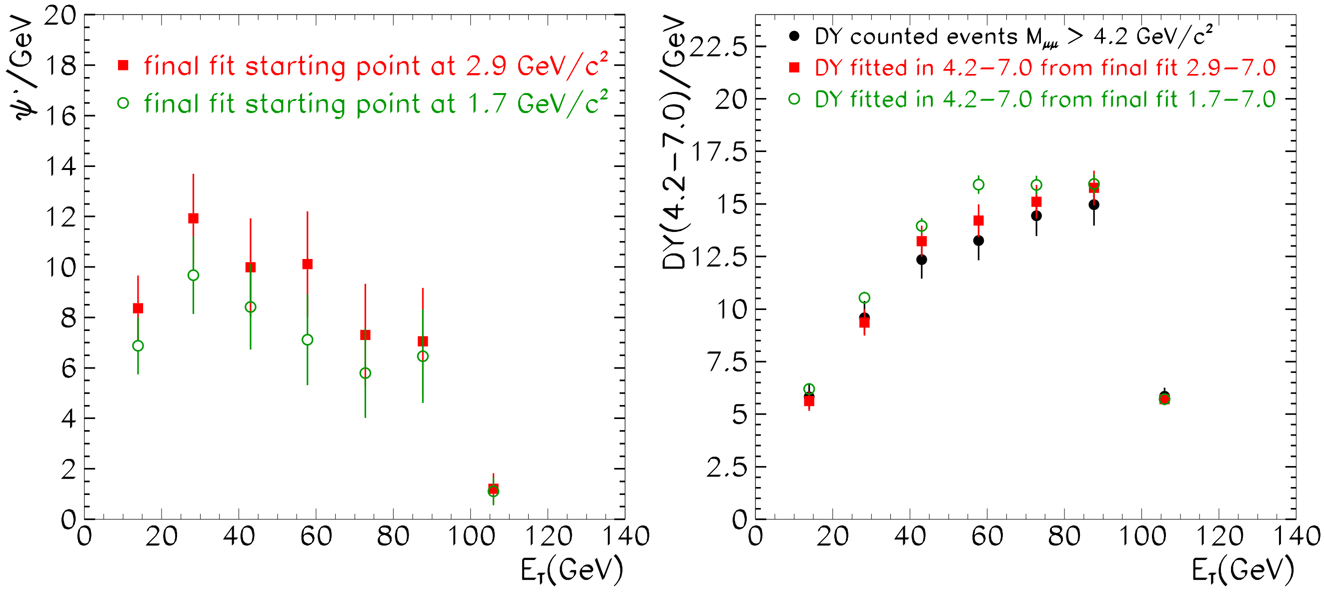

Figure 6.3: *Comparisons between ψ' (left) and high mass Drell-Yan (right) normalizations for the 7 E_T regions, extracted from the fits to 1.7 - 7.0 and 2.9 - 7.0 GeV/c^2 mass ranges.*

The influence of the intermediate mass region on the ψ' normalizations has been also verified. As shown in the previous chapter, constrains associated with the IMR, namely different $D\bar{D}$ simulations, R_{bkg} factor evaluation and fit mass ranges in the second step, have no consequences in the final step fitted J/ψ and Drell-Yan normalizations. However, the ψ' yield is slightly affected, by 1.5% at most, as shown in figure 6.5.

6.1.2 The influence of PDFs on the ψ' normalization

The ψ' measured cross section is dependent on the uncertainty related to the parton density functions chosen to generate Drell-Yan in the Monte Carlo simulations, as opposite to the J/ψ case. Consequently, the values of ψ'/DY and ψ'/(J/ψ) ratios as a function of centrality are also dependent, leading to slight different behaviours as the transverse energy increases. Figure 6.6 shows the ratios between ψ'/DY results, as well as ψ'/(J/ψ) as functions of E_T, when Drell-Yan is generated with GRV LO 94 or CTEQ 4L. A linear fit with two free parameters is performed in order to evaluate the systematic uncertainties: for the ψ'/DY ratio, they vary from -2.8% to $+3.7\%$ and for ψ'/(J/ψ) the variation stands between $+2\%$ and $+8.6\%$.

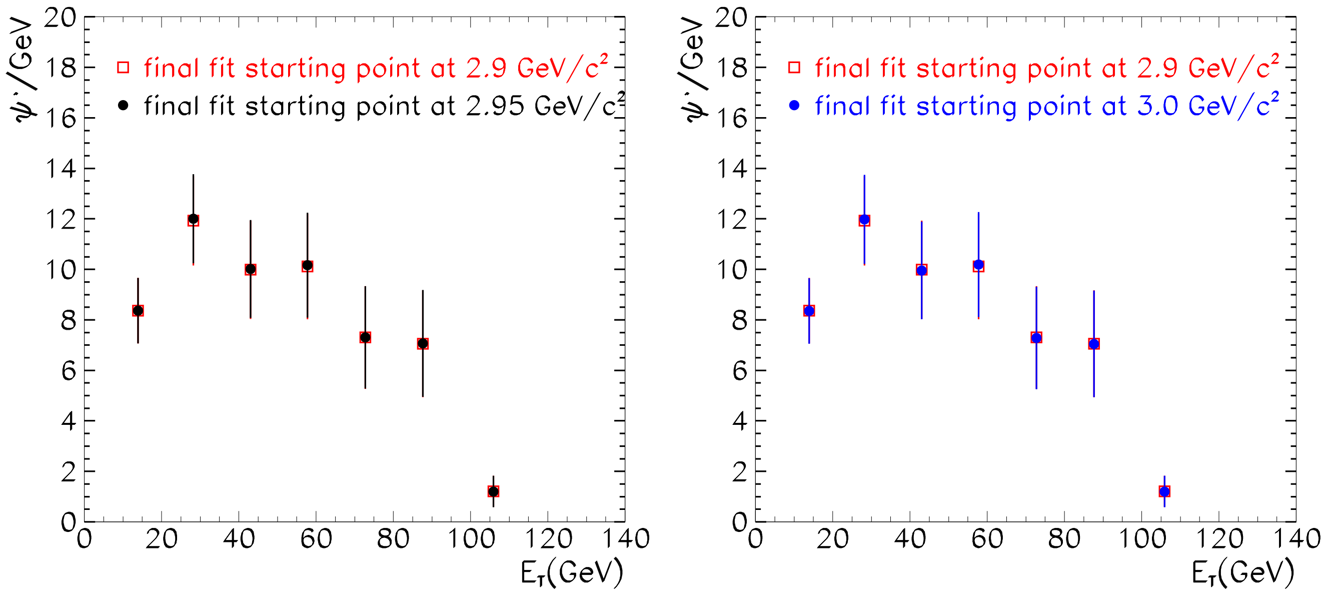

Figure 6.4: *Comparisons between ψ' normalizations for the 7 E_T regions, extracted from the fits to 2.9 - 7.0 and 2.95 - 7.0 GeV/c^2 mass ranges (left) and 2.9 - 7.0 and 3.0 - 7.0 GeV/c^2 mass ranges (right).*

6.1.3 The P×Dtarget cut on ψ' studies

The influence of the P×Dtarget cut level on the ψ' measured cross section has been checked. Figure 6.7 shows the dimuon vertex distribution (see section 3.2.3) for the ψ' and J/ψ mass ranges, i.e., $< M^{J/\psi,\psi'} > \pm 3\sigma^{J/\psi,\psi'}$, concerning several P×Dtarget cut levels, namely 0%, 2%, 5% and 10%. As expected, the higher the cut level the narrower the vertex distributions, since we are dealing with a geometrical variable limiting the maximum transverse distance for a reconstructed track with respect to the target (recall section 3.3.1). Qualitatively, a large spread of the 0% P×Dtarget cut distributions is observed, somewhat natural since no geometrical cut is applied. No visible asymmetries for both mass ranges are seen. This does not mean that the loss of statistics is the same for the two samples. In fact, the background contamination of each dimuon source, as well as its consequences, may be very different. An example is given by figure 6.2 – while the number of J/ψ produced off-target may bias slightly its normalization if not removed properly, the implications of such a background may be very significant in the ψ' sample. For this reason, the number of events removed by a 2% P×Dtarget cut, with respect to each dimuon sample, is higher for ψ' than for J/ψ. Considering a clean sample (i.e., a sample free from off-target events), as the P×Dtarget cut is performed

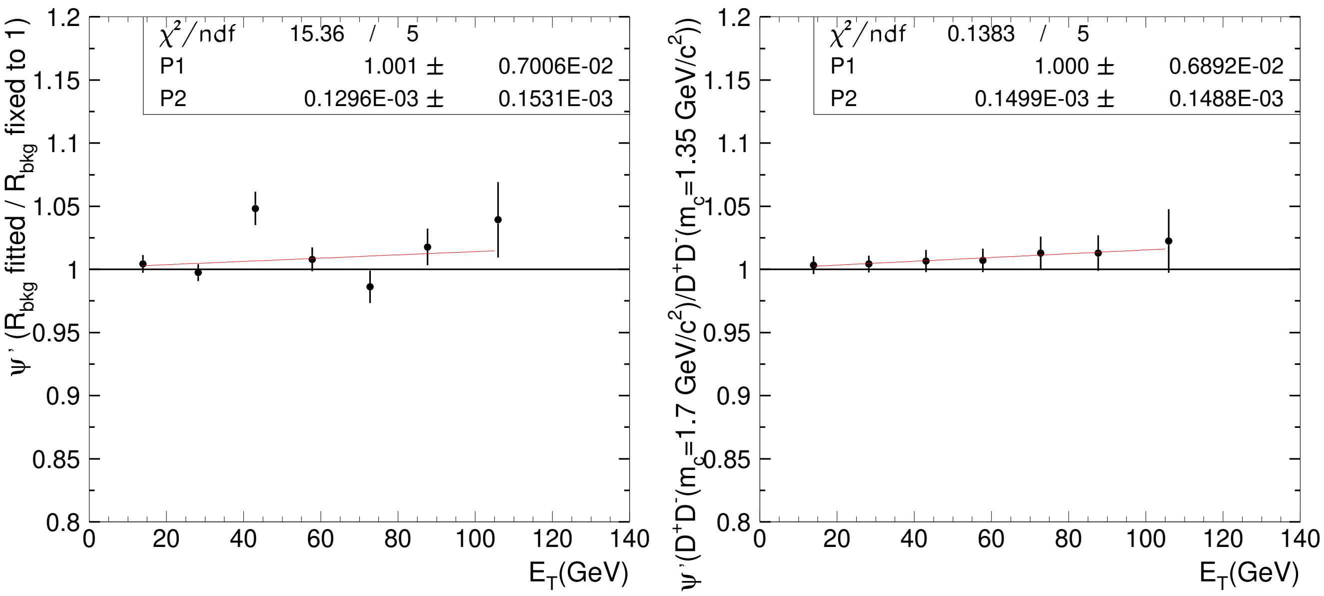

Figure 6.5: *Ratios between ψ' normalizations, obtained when the R_{bkg} factor is fitted instead of being fixed to 1 (left) and when $D\bar{D}$ is simulated using the c–quark mass of 1.7 instead of 1.35 GeV/c^2 (right).*

at muon level, the dimuon statistics loss between two cut values should be twice this relative difference. This is because the probability that both muons in the same event be rejected by this geometrical cut is small. If the number is overcome, it means that we are still removing garbage muons. However, this statement is valid providing that the χ^2 probability distribution is flat, which is nearly the case for J/ψ mass and momentum ranges, after combinatorial background subtraction (recall figure 3.4). In fact, this is not completely true for other mass ranges, namely for the ψ' mass range, as shown in figure 6.8. Once the garbage muons are removed, a higher P×Dtarget cut implies the loss of good events only. This feature can be verified in table 6.1 which reports the statistics loss for both resonances, after application of each P×Dtarget cut level. Data shown are selected after all cuts, but the P×Dtarget one.

After a 2% P×Dtarget cut, the statistics loss tends to be slightly higher than expected, even for signal samples (i.e., after combinatorial background subtraction). This is a consequence of the not totally flat χ^2 prob(P×Dtarget) distributions. However, this does not necessarily mean that spurious events are being kept. The off-target events concentrate in the spike and have been removed with a 2% cut. Higher and higher cut levels would not improve the fit distributions and would be very penalizing in statistics. Furthermore, comparisons among results obtained with the four different cut levels quoted have been performed, confirming that no systematic behaviour of $\psi'/(\mathrm{J}/\psi)$ as a function of centrality is present. An example is given in figure 6.9, which shows the $\psi'/(\mathrm{J}/\psi)$ ratio obtained with a 10% P×Dtarget cut divided by the same ratio obtained with a 2% cut,

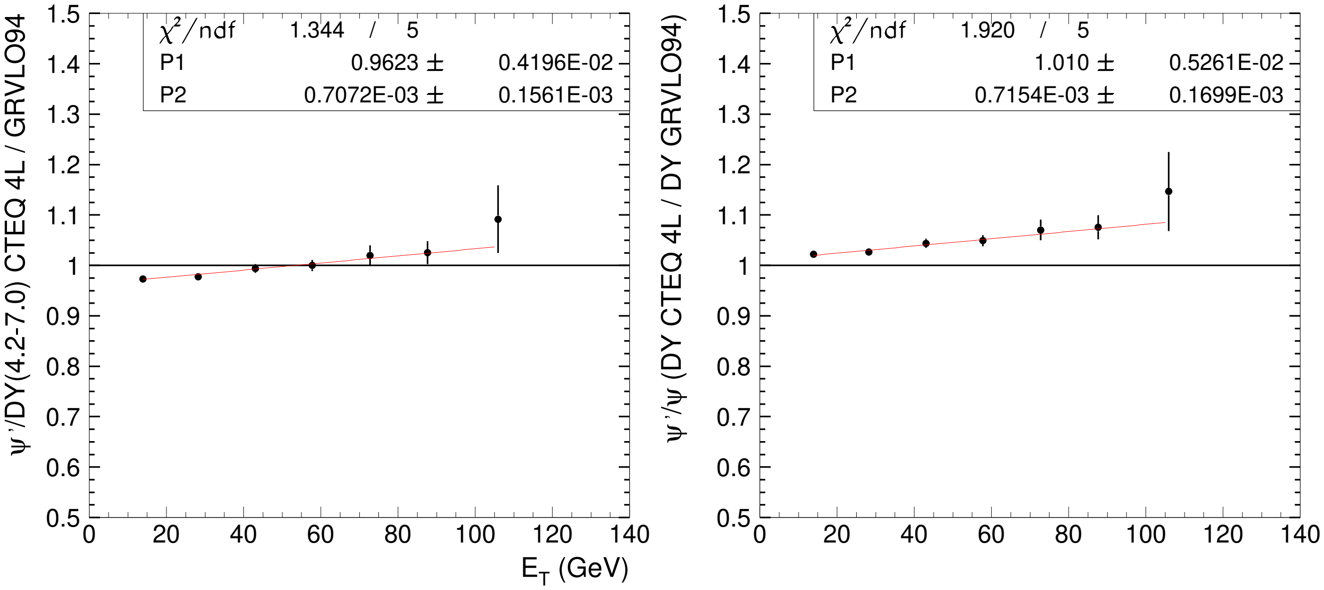

Figure 6.6: *Ratios between ψ'/DY results (left), as well as $\psi'/(J/\psi)$ (right), when Drell-Yan is generated with GRV LO 94 and CTEQ 4L, and two parameters fits.*

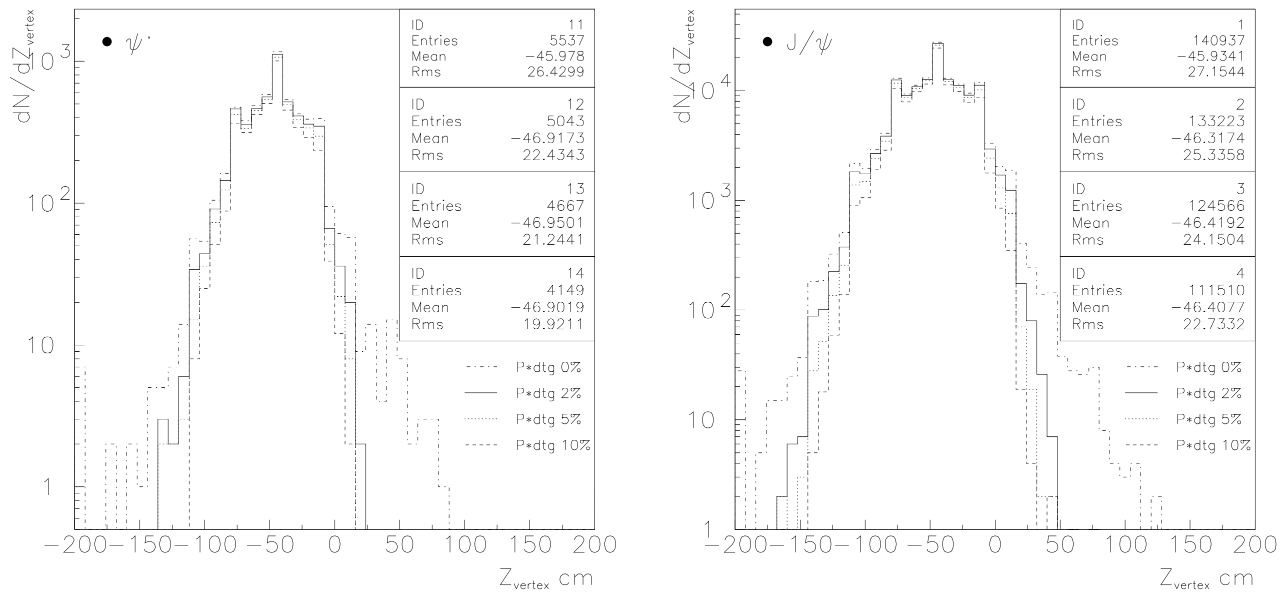

Figure 6.7: *Effect of $P{\times}D$target cut for ψ' (left) and J/ψ (right) vertex distributions.*

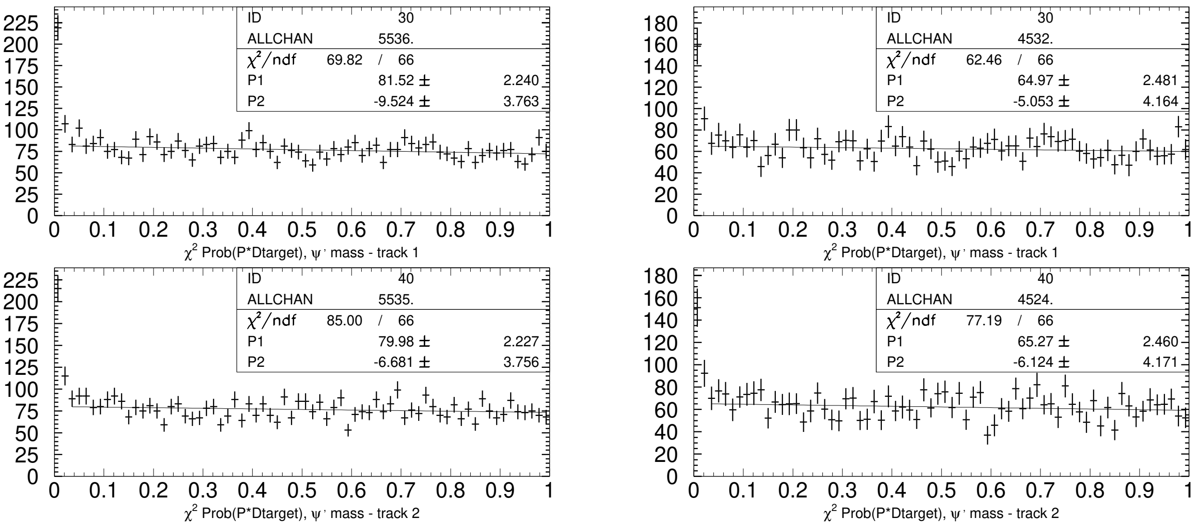

Figure 6.8: *χ^2 prob(P×Dtarget) for ψ' mass range, before (left) and after (right) combinatorial background subtraction.*

P×Dtarget cut	events in ψ' range	statistics loss (opposite signs)	events in J/ψ range	statistics loss (opposite signs)
0%	5537	—	140937	—
2%	5043	(-8.92 ± 0.53)%	133223	(-5.47 ± 0.08)%
5%	4667	(-7.46 ± 0.52)%	124566	(-6.50 ± 0.09)%
10%	4149	(-11.10 ± 0.64)%	111510	(-10.48 ± 0.12)%

Table 6.1: *The ψ' and J/ψ statistics losses imposed by increasing P×Dtarget cut levels. The invariant mass ranges considered are $3.4 \leq M_{\mu\mu} < 4.0$ and $2.8 \leq M_{\mu\mu} < 3.4$, respectively.*

fitted by a straight line with two free parameters, in which the slope value is compatible with zero.

6.1.4 Overall systematic uncertainty on ψ'/DY and ψ'/(J/ψ) measurements

In conclusion, the systematic errors associated with the ψ' yield are bigger than the ones associated with the J/ψ. An uncertainty between -3.3% and $+4.5\%$ should be considered on the ψ'/DY results and, at most, $+9\%$ on the ψ'/(J/ψ) ratios. These amounts have resulted from the quadratic sum of all uncertainties estimated, namely the error on the fit method, spectrometer acceptances and the uncertainties associated with chosen PDFs and c-quark mass, that, although directed related to Drell-Yan and open charm yields,

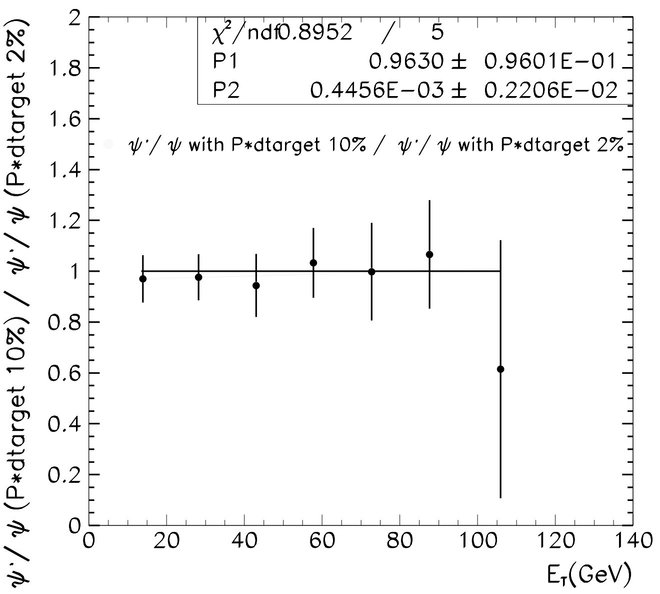

Figure 6.9: *Ratios between $\psi'/(J/\psi)$ results obtained with 10% and 2% P×Dtarget cut levels for the 7 E_T ranges. The linear fit confirms the absence of a bias in E_T.*

influence the ψ' fitted normalization.

6.2 ψ' results for Pb–Pb 2000 data

Table 6.2 reports the ψ'/DY results for the 2000 data. The relative statistical error stands between 20% and 33%, the most central being 56%. The relative error on the Drell-Yan normalization varies from 8% for peripheral collisions to 5% for the central ones (these values are smaller than the ones evaluated in the J/ψ/DY analysis, since the number of E_T ranges now is 7 instead of 11). On the other hand, the relative error on the ψ' yield is 16% at low E_T increasing smoothly up to 30% with centrality, excluding the most central result, which is affected by an error of 50%. As referred in section 5.1.3, the ratios between normalizations take the covariance between the two variables into account. The systematic errors come mainly from the uncertainty on the ψ' normalization due to different parton density functions used to generate Drell-Yan in the Monte Carlo simulations. They are E_T dependent, as shown in the previous section, and small when compared with the statistical errors.

Figure 6.10 shows the ψ' production as a function of the transverse energy, relatively to Drell-Yan, concerning the Pb–Pb 2000 data. A strong ψ' suppression as the interactions centrality increases is observed. Comparing results between central and peripheral collisions, a suppression factor of ~70%, relatively to Drell-Yan yields, is found. The errors bars are only statistical. One should take into account the relative systematic errors, reported in table 6.2.

E_T GeV	$< E_T >$ GeV	$B_{\mu\mu}\psi'/DY_{4.2-7.0}$
3-20	13.9	1.812 ± 0.379 (stat) $^{+0.032}_{-0.060}$ (syst)
20-35	28.2	1.551 ± 0.302 $^{+0.028}_{-0.039}$
35-50	43.0	0.919 ± 0.213 $^{+0.018}_{-0.018}$
50-65	57.8	0.867 ± 0.211 $^{+0.019}_{-0.015}$
65-80	72.7	0.589 ± 0.183 $^{+0.015}_{-0.010}$
80-95	87.6	0.545 ± 0.182 $^{+0.018}_{-0.010}$
95-150	105.9	0.257 ± 0.139 $^{+0.012}_{-0.005}$

Table 6.2: *$B_{\mu\mu}\psi'/DY_{4.2-7.0}$ values for Pb–Pb 2000 data. The errors are statistical plus systematic.*

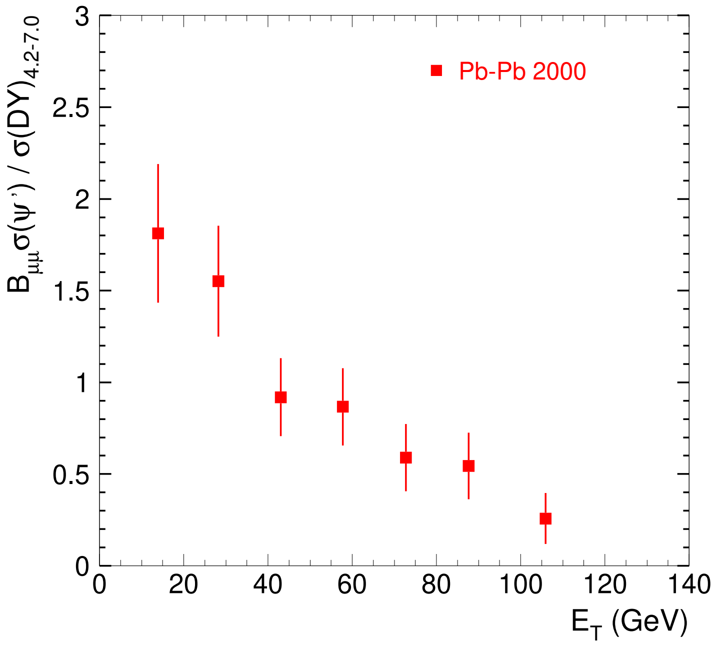

Figure 6.10: *The ψ'/DY as a function of the transverse energy. The errors are only statistical. See table 6.2 for the systematic errors.*

If a strong suppression of ψ' relatively to Drell-Yan is expected, as the vector meson is a weak bound state and suffers from nuclear medium effects [2], interesting is to evaluate the relative behaviour of the two resonances in the hot and dense medium provided by Pb–Pb collisions. The values of ψ' and J/ψ cross sections ratio, both corrected for their branching ratios into lepton pairs [1], are reported in table 6.3. The statistical errors come mainly from the ψ', since the J/ψ statistical uncertainty is less than 1%. They vary from

[1]For simplicity, hereafter referred as $\psi'/(\mathrm{J}/\psi)$ in the text.

15% to 40%, the most central one being 73%. The estimated systematic errors are also quoted.

Figure 6.11 shows the $\psi'/(\mathrm{J}/\psi)$ ratio as a function of the transverse energy. A

E_T GeV	$< E_T >$ GeV	$B'_{\mu\mu}\psi'/B_{\mu\mu}J/\psi\ \times 10^3$
3-20	13.9	$(8.98 \pm 1.38\ ^{+0.27}_{-0.20})$
20-35	28.2	$(8.25 \pm 1.74\ ^{+0.31}_{-0.19})$
35-50	43.0	$(6.54 \pm 1.80\ ^{+0.31}_{-0.15})$
50-65	57.8	$(6.51 \pm 1.90\ ^{+0.37}_{-0.15})$
65-80	72.7	$(4.79 \pm 1.89\ ^{+0.32}_{-0.11})$
80-95	87.6	$(5.02 \pm 2.14\ ^{+0.39}_{-0.11})$
95-150	105.9	$(2.66 \pm 1.95\ ^{+0.24}_{-0.06})$

Table 6.3: *$B'_{\mu\mu}\psi'/B_{\mu\mu}J/\psi$ values for Pb–Pb 2000 data, concerning the 7 centrality regions. The errors are statistical plus systematic.*

steady decrease against centrality occurs, showing that ψ' is more suppressed than the J/ψ in Pb–Pb collisions. A factor of 2.5 between peripheral and central interactions is observed.

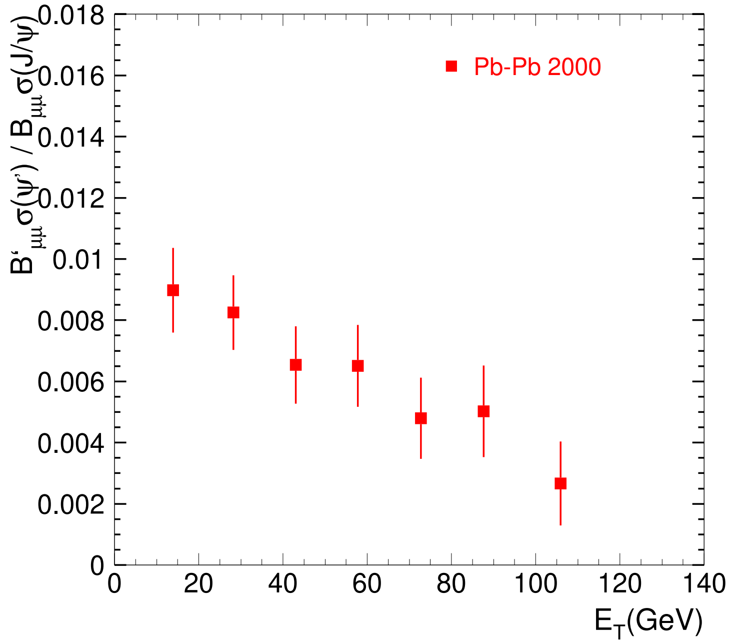

Figure 6.11: *$B'_{\mu\mu}\psi'/B_{\mu\mu}J/\psi$ as a function of the transverse energy. The errors are only statistical. See table 6.3 for the systematic errors.*

6.3 The ψ' analysis for Pb–Pb 1998 data

Another analysis on ψ' production has been performed using the Pb–Pb 1998 data. The considerations about fit methods and data selection, deeply studied using the 2000 data sample, remain valid for these data. Due to the fact that the lead target was placed in air, similar P×Dtarget and vertex determination studies have been performed, in order to prevent a ψ' sample contaminated by off-target events. In this case, data have been divided in two large E_T ranges, below and above 50 GeV. The aim is to discard Pb-air interactions that would be tagged as Pb–Pb peripheral collisions. Figure 6.12 shows Z_{vertex} distributions concerning E_T<50 GeV and E_T>50 GeV, both for ψ' mass range ($< M^{\psi'} > \pm 3\sigma^{\psi'}$). No visible discrepancies between low and high E_T distributions are seen. A similar behaviour, concerning the J/ψ mass range (also $< M^{J/\psi} > \pm 3\sigma^{J/\psi}$), is observed in figure 6.13.

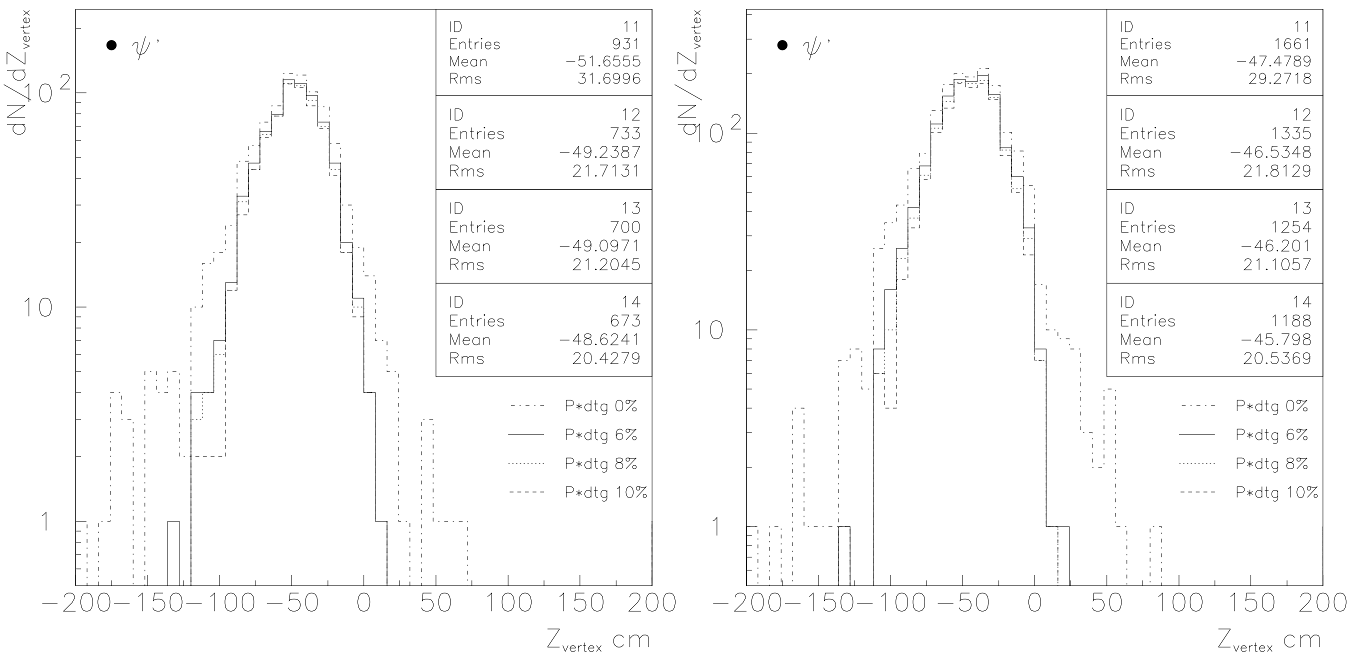

Figure 6.12: *Z_{vertex} distributions concerning Pb–Pb 1998 data for E_T<50 GeV (left) and E_T>50 GeV (right) in the ψ' mass range.*

The χ^2 prob(P×Dtarget) distributions concerning same mass and transverse energy ranges are shown in figures 6.14 and 6.15. Again, no visible differences between low and high centrality distributions are seen, as well as between both resonance mass ranges. A cut of 6% should be performed in order to remove the off-target produced muons. This value is higher than the one applied for 2000 data (P×Dtarget > 2%), since the target region is not in vacuum. After this cut level, both ψ' and J/ψ samples have approximately

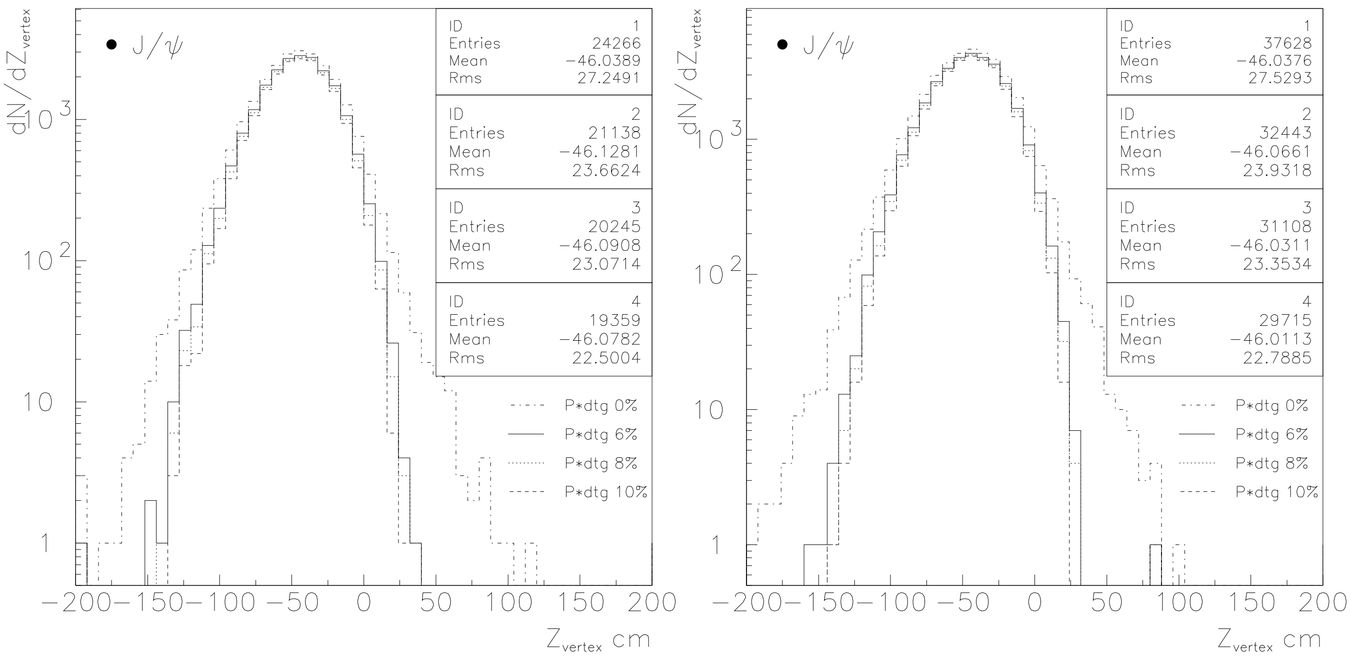

Figure 6.13: *Z_{vertex} distributions concerning Pb–Pb 1998 data for E_T<50 GeV (left) and E_T>50 GeV (right) in the J/ψ mass range.*

the same trend on the statistics loss imposed by the increasing P×Dtarget cut levels, either for E_T<50 GeV or E_T>50 GeV. However, when comparing 6% with no cut at all, one verifies that the statistics loss is much higher for ψ' than for J/ψ, confirming that the garbage muons are more significant in the ψ' sample. Most of these muons are off-target J/ψ produced upstream from the target, reconstructed with masses in the ψ' range.

P×Dtarget cut	events in ψ' range	statistics loss (opposite signs)	events in J/ψ range	statistics loss (opposite signs)
0%	931	—	24266	—
6%	733	(-21.27 ± 1.82)%	21138	(-12.89 ± 0.30)%
8%	700	(-4.50 ± 1.07)%	20245	(-4.22 ± 0.19)%
10%	673	(-3.86 ± 1.02)%	19359	(-4.38 ± 0.20)%

Table 6.4: *The ψ' and J/ψ statistics loss imposed by increasing P×Dtarget cut levels concerning events with E_T<50 GeV.*

These studies confirm the good performance of the NOCIMD target identification algorithm, working in worse conditions, as was the case of the target placed in air.

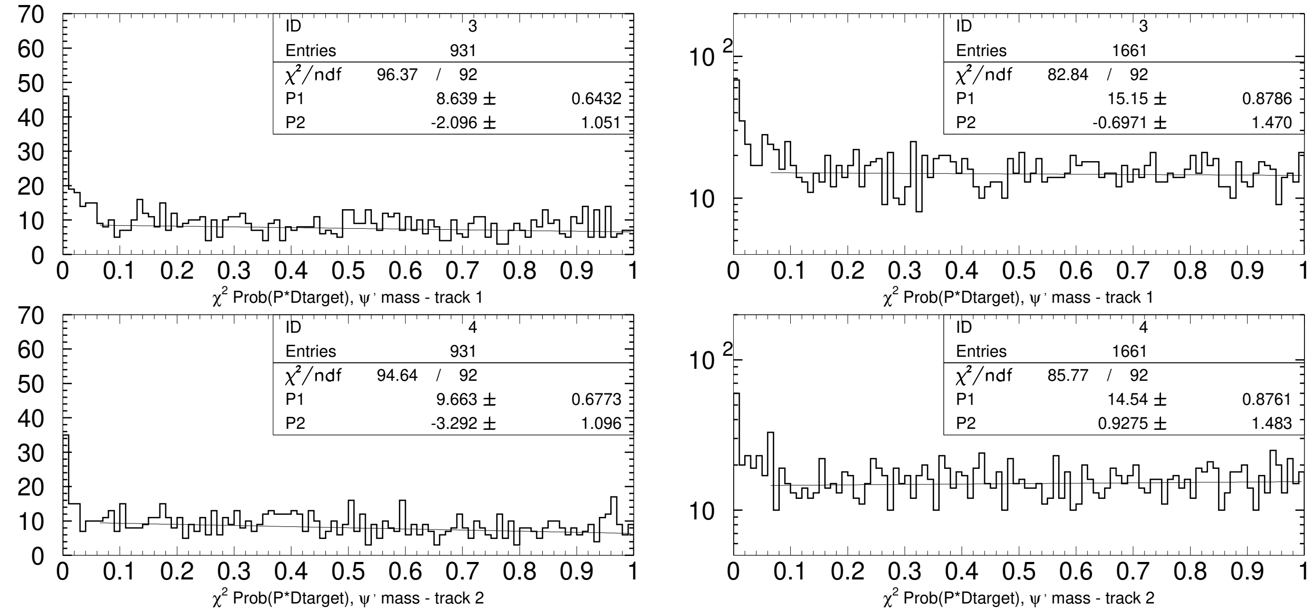

Figure 6.14: *χ^2 prob(P×Dtarget) distributions concerning Pb–Pb 1998 data for E_T<50 GeV (left) and E_T>50 GeV (right) in the ψ' mass range.*

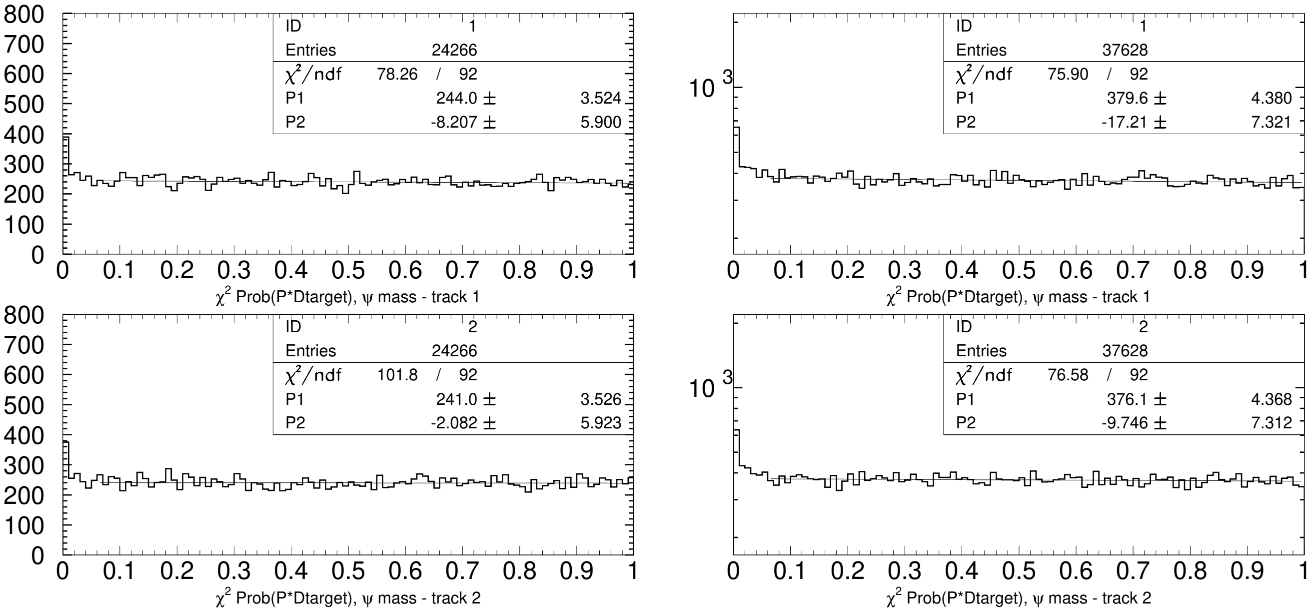

Figure 6.15: *χ^2 prob(P×Dtarget) distributions concerning Pb–Pb 1998 data for E_T<50 GeV (left) and E_T>50 GeV (right) in the J/ψ mass range.*

P×Dtarget cut	events in ψ' range	statistics loss (opposite signs)	events in J/ψ range	statistics loss (opposite signs)
0%	1661	—	37628	—
6%	1335	(-19.63 ± 1.32)%	32443	(-13.78 ± 0.24)%
8%	1254	(-6.07 ± 0.91)%	31108	(-4.11 ± 0.15)%
10%	1188	(-5.26 ± 0.88)%	29715	(-4.48 ± 0.16)%

Table 6.5: *The ψ' and J/ψ statistics loss imposed by increasing P×Dtarget cut levels concerning events with E_T>50 GeV.*

6.3.1 ψ' results for Pb–Pb 1998 data

Table 6.6 reports both ψ'/DY and ψ'/(J/ψ) values, concerning the Pb–Pb 1998 data analysis. Only statistical errors are shown. Ensuring a ψ' sample free from dimuons produced off-target and considering that the remaining sources of uncertainty are independent on both data periods, one should take as systematic errors the ones evaluated through the 2000 data sample. The main systematic error comes from the uncertainty on the ψ' normalization, resulting from different Drell-Yan cross sections evaluated in the ψ' mass range, either generated with GRV LO 94 or with CTEQ 4L (recall figure 6.6). Thus, in what respects the ψ'/DY ratio, an uncertainty varying from -3.3% at peripheral collisions to $+4.5\%$ at most central ones, should be considered. Concerning the ψ'/(J/ψ) ratio, its relative systematic error increases slightly against E_T, up to +9%. In view of the large statistical errors of the Pb–Pb 1998 data sample, these systematic errors become almost negligible.

E_T GeV	$< E_T >$ GeV	$B_{\mu\mu}\psi'/DY_{4.2-7.0}$	$B'_{\mu\mu}\psi'/B_{\mu\mu}J/\psi \times 10^3$
2-22	15.7	2.058 ± 0.783 (stat)	9.30 ± 2.53
22-38	30.8	1.350 ± 0.398	8.26 ± 1.90
38-54	46.7	0.949 ± 0.307	7.35 ± 1.96
54-70	62.7	0.614 ± 0.255	5.18 ± 1.89
70-87	78.8	0.785 ± 0.275	6.86 ± 2.07
87-104	94.9	0.271 ± 0.226	2.80 ± 2.20
104-130	109.9	0.741 ± 0.387	7.71 ± 3.47

Table 6.6: *$B_{\mu\mu}\psi'/DY_{4.2-7.0}$ and $B'_{\mu\mu}\psi'/B_{\mu\mu}J/\psi$ values for Pb–Pb 1998 data. The errors are only statistical. The systematic errors are explained in the text.*

Figure 6.16 shows the ψ' production relatively to Drell-Yan, as a function of the transverse energy, concerning the Pb–Pb 1998 data. Despite of the relative small statistics, the ψ'/DY results confirm the pattern observed in the 2000 data sample. The ψ' yield decreases steadily as the collisions centrality increase but, due to lack of statistics of this data sample, the ratio seems to saturate at high centrality.

Figure 6.17 shows the ψ'/(J/ψ) ratio as a function of E_T. Also this ratio seems to

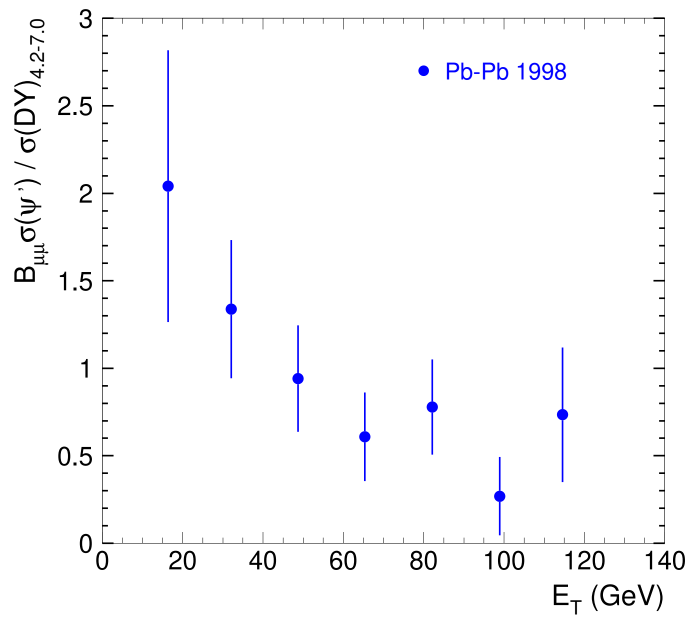

Figure 6.16: *$B_{\mu\mu}\psi'/DY$ as a function of the transverse energy. The errors are only statistical. See text for systematic error details.*

saturate at high centrality.

Figure 6.18 shows the comparison between the results of the two data takings

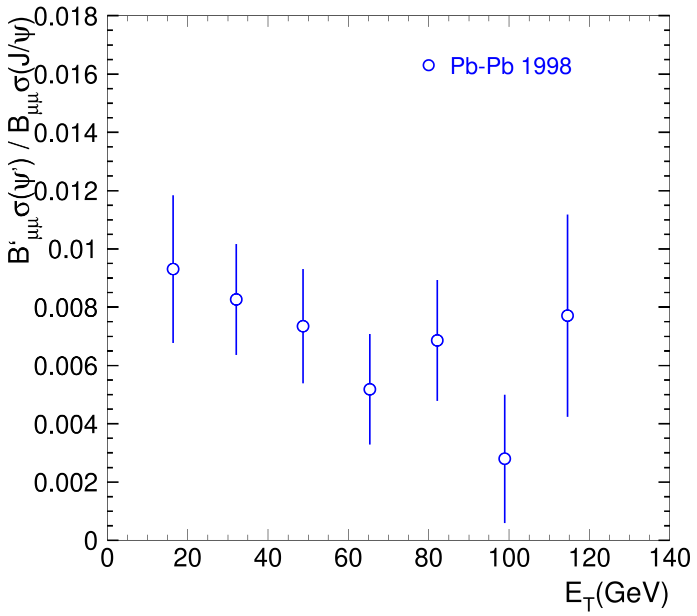

Figure 6.17: *$B'_{\mu\mu}\psi'/B_{\mu\mu}J/\psi$ as a function of the transverse energy. The errors are only statistical. See text for systematic error details.*

concerning ψ'/DY and ψ'/(J/ψ). Both results are perfectly compatible. The preliminary results on ψ' suppression from Pb–Pb 2000 and 1998 data have been presented for the first time at [1].

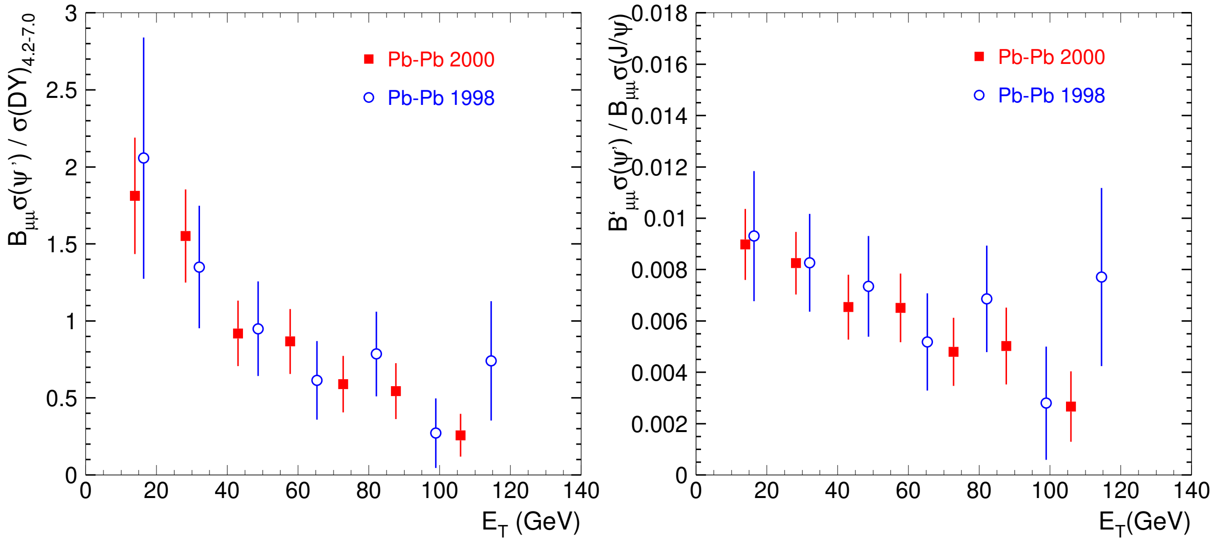

Figure 6.18: *Comparisons between Pb–Pb 1998 and 2000 results: $B_{\mu\mu}\psi'/DY$ (left) and $\psi'/(J/\psi)$ (right) as functions of E_T.*

6.4 An overall measurement of the ψ' suppression

As for J/ψ analysis, Pb–Pb 1998 data has been analysed using the same E_T regions as in 2000, in order to obtain overall measurements of the ψ' suppression, relatively to Drell-Yan, as well as to J/ψ, as functions of the transverse energy. Whatever the E_T division is used, the Pb–Pb 1998 results have the same trend, as shown in figure 6.19.

Since the two date samples are consistent with each other and the systematic errors are under control, namely in what respects the target identification algorithm, one can perform the average. The advantage of such procedure is a more accurate measurement of the ψ' suppression. Table 6.7 reports the ψ'/DY results for the two data sets analysed in the same E_T regions, as well as the averaged results. The latter are displayed in figure 6.20. The statistical errors are roughly 10%–25% smaller than the 2000 ones. In what concerns the relative systematic errors they are the ones evaluated for 2000 and 1998 data samples, i.e., they stand between -3.3% at peripheral collisions and $+4.5\%$ at central ones.

In a similar way, the relative behaviour of the two charmonium states as a function

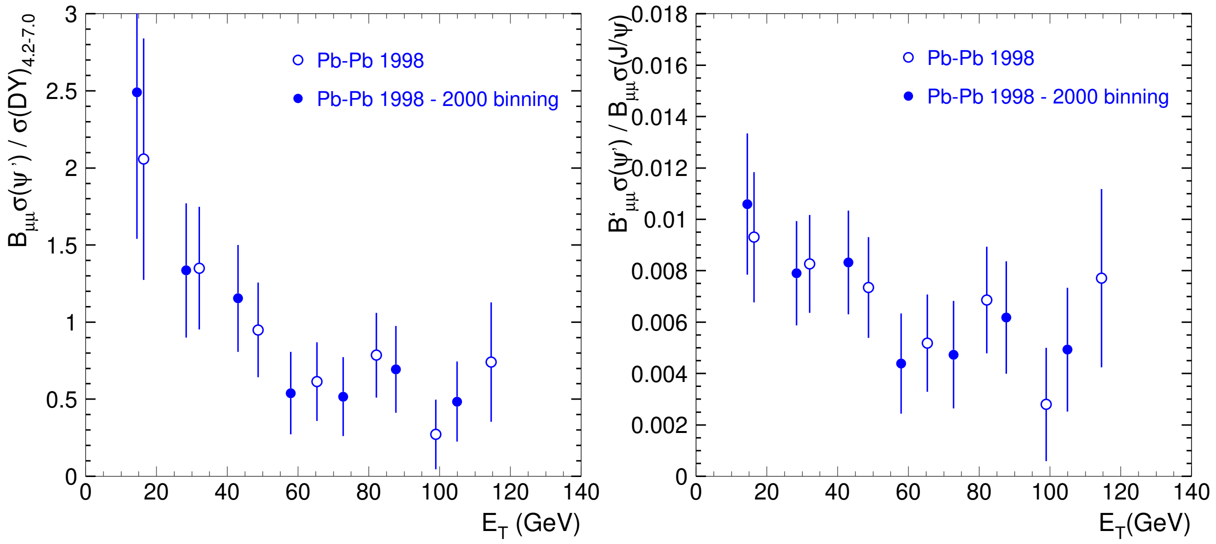

Figure 6.19: *$B_{\mu\mu}\psi'/DY$ (left) and $\psi'/(J/\psi)$ (right) for Pb–PB 1998 data analysed with different E_T ranges.*

E_T GeV	$< E_T >$ GeV	Pb–Pb 1998	Pb–Pb 2000	Average
3-20	13.9	2.490 ± 0.950	1.812 ± 0.379	1.905 ± 0.352
20-35	28.2	1.336 ± 0.436	1.551 ± 0.302	1.481 ± 0.248
35-50	43.0	1.154 ± 0.347	0.919 ± 0.213	0.983 ± 0.181
50-65	57.8	0.539 ± 0.267	0.867 ± 0.211	0.741 ± 0.166
65-80	72.7	0.517 ± 0.256	0.589 ± 0.183	0.564 ± 0.149
80-95	87.6	0.694 ± 0.281	0.545 ± 0.182	0.589 ± 0.153
95-150	105.9	0.484 ± 0.260	0.257 ± 0.139	0.307 ± 0.122

Table 6.7: *$B_{\mu\mu}\psi'/DY_{4.2-7.0}$ values for Pb–Pb 1998, Pb–Pb 2000 and average. The errors are only statistical. See text for systematic errors.*

of the transverse energy in Pb–Pb collisions is obtained through the average between Pb–Pb 2000 and Pb–Pb 1998 results. This is shown in figure 6.21 and reported in table 6.8. The ratio of $\psi'/(J/\psi)$ decreases with centrality by a factor of 2.5 between peripheral and central collisions. The statistical errors are, at least, 15% lower than the 2000 ones. Again, being the nature of systematic errors the same for the two data samples, the average values also have a maximal systematic uncertainty of +9%.

Table 6.8 reports the $\psi'/(J/\psi)$ results for the two data sets analysed with the same E_T regions, as well as the averaged results.

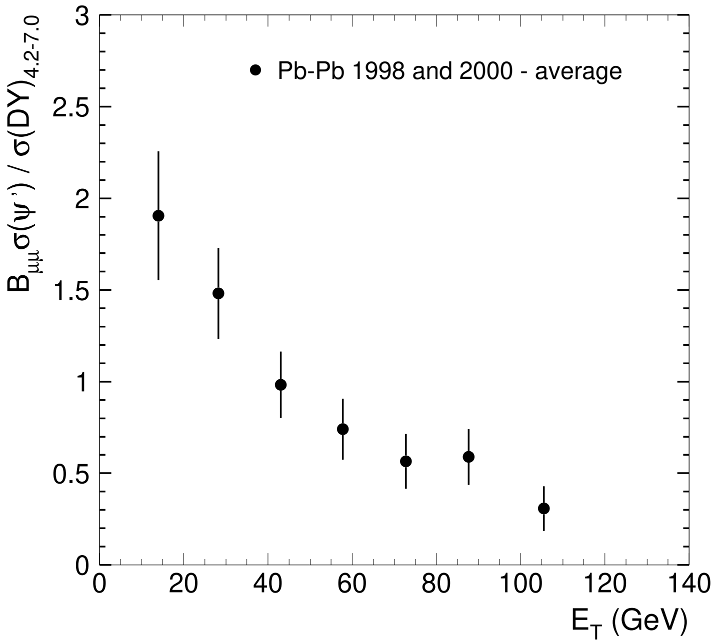

Figure 6.20: *$B_{\mu\mu}\psi'/DY$ as a function of the transverse energy. The errors are only statistical. See text for systematic errors.*

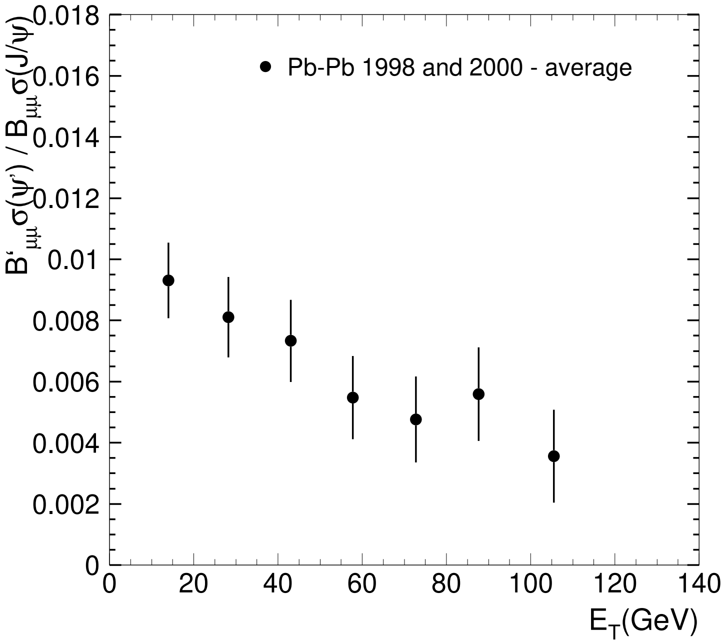

Figure 6.21: *$B'_{\mu\mu}\psi'/B_{\mu\mu}J/\psi$ as a function of the transverse energy. The errors are only statistical. See text for systematic errors.*

E_T GeV	$< E_T >$ GeV	Pb–Pb 1998 $\times 10^3$	Pb–Pb 2000 $\times 10^3$	Average $\times 10^3$
3-20	13.9	10.59 $\pm$ 2.75	8.98 $\pm$ 1.38	9.30 $\pm$ 1.24
20-35	28.2	7.90 $\pm$ 2.03	8.25 $\pm$ 1.74	8.10 $\pm$ 1.32
35-50	43.0	8.32 $\pm$ 2.02	6.54 $\pm$ 1.80	7.33 $\pm$ 1.34
50-65	57.8	4.39 $\pm$ 1.95	6.51 $\pm$ 1.90	5.48 $\pm$ 1.36
65-80	72.7	4.73 $\pm$ 2.10	4.79 $\pm$ 1.89	4.76 $\pm$ 1.40
80-95	87.6	6.18 $\pm$ 2.19	5.02 $\pm$ 2.14	5.59 $\pm$ 1.53
95-150	105.9	4.93 $\pm$ 2.41	2.66 $\pm$ 1.95	3.56 $\pm$ 1.52

Table 6.8: *$B'_{\mu\mu}\psi'/B_{\mu\mu}J/\psi$ values for Pb–Pb 1998, Pb–Pb 2000 and average. The errors are only statistical. See text for systematic errors.*

As expected, the averages are closer to the Pb–Pb 2000 results, since the statistics of this data sample is 2.5 times bigger than the Pb–Pb 1998 one. However, the advantage resides on the accuracy, since the relative error of the averages are significantly lower than the 2000 ones.

Bibliography

[1] H. Santos (NA50 Coll.), Quark Matter 2004, in J. Phys. G: Nucl.Part. Phys. 30 (2004) S1175

[2] S. Digal, P. Petreczky and H. Satz, Phys. Lett. B514 (2001) 57

Chapter 7

Charmonia suppression Pb–Pb versus p–A and S–U collisions

7.1 J/ψ suppression as a function of centrality

One question raised since the first observation of J/ψ suppression in Pb–Pb collisions is: to what extent is the J/ψ/DY ratio, concerning peripheral interactions, compatible with the results obtained in lighter systems, namely p–A and S–U?

In the framework of NA50 a coherent comparison can be done, since these data were taken with the same spectrometer, so systematic effects related to trigger and reconstruction efficiencies are the same for all data sets. Besides, the transverse energy released in S–U collisions has been measured with the same electromagnetic calorimeter. Data taken before 2000 could not answer definitely that question. Pb–Pb 1995 data, due to the lack of statistics, has only one low E_T point; on the other hand, in Pb–Pb 1996 and 1998 (the latter before using the NOCIMD selection), peripheral collisions suffered from target identification algorithm inefficiency and eventual Pb-air contamination. For this reason, a last and best quality data sample has been taken with the target region placed in vacuum. Such improved experimental conditions have allowed the study of charmonia production without restrictions over the whole E_T phase space. In parallel, NA50 has taken high statistics p–A data. The combination of these analyses with a S–U data reanalysis [1] has resulted in a new measurement of the J/ψ suppression in these lighter systems [1, 2, 3].

Figure 7.1 shows the comparison between Pb–Pb 2000 and 1998 J/ψ/DY results and the updated absorption curve which fits NA50 p–A and NA38 S–U data (see section 1.7.2), which have been rescaled in energy and rapidity, in order to met the same kinematical domain of the Pb–Pb collision system. Both data results and curve have been presented in [4, 1] using Drell-Yan evaluated with MRS 43 [5]. Thus, a $\sim$10% difference between these J/ψ/DY normalizations and the old ones is present, in conformity with the study presented in section 5.1.4.2. In these lighter systems the physical phenomenon involved in J/ψ suppression is assumed to be the normal absorption of the pre-equilibrium $c\bar{c}$ pair or J/ψ in nuclear matter. The measured absorption cross section is σ_{abs}=4.2±0.4 mb.

Indeed, Pb–Pb peripheral collisions are in perfect agreement with p–A and S–U

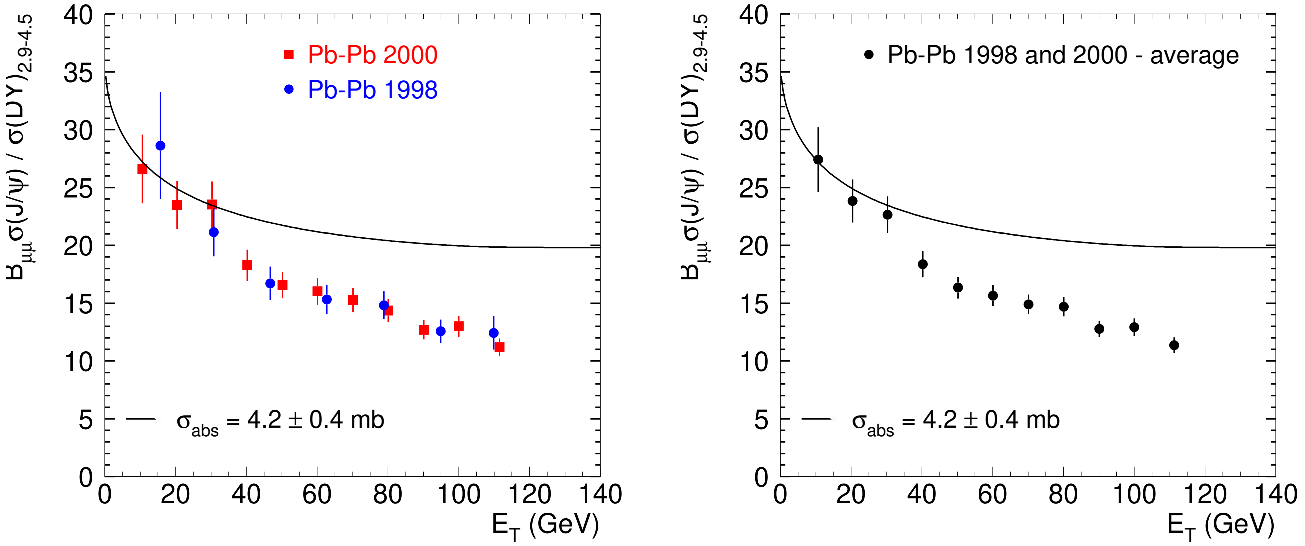

Figure 7.1: *Comparison between Pb–Pb 2000 and 1998 results and the absorption curve that fits the NA50 p–A and NA38 S–U data, rescaled to 158 GeV/nucleon, the Pb–Pb energy. The same comparison with the Pb–Pb data weighted average is shown on the right panel.*

results. A clear departure of the $B_{\mu\mu}\sigma(J/\psi)/\sigma(DY)$ ratio from this normal absorption curve is observed at mid-centrality, $E_T\sim$ 30 GeV. Furthermore, no visible saturation of the ratio at high E_T is observed, as opposed to the absorption curve trend.

In order to compare the J/ψ suppression among different systems, we use $L(b)$, the average path length crossed by the $c\bar{c}$ pair inside the nucleus [6], estimated within the Glauber model framework. At a given impact parameter b, $< L >$ is calculated as $< \rho(r)L > /\rho_0$, where $\rho(r)$ is the nuclear density, given by equation 5.10 and normalized for each nucleus in order to give A nucleons upon integration; ρ_0 is the average nuclear density, taken as 0.17 fm^{-3}. $< \rho(r)L >$ is calculated as:

$$< \rho(r)L >= \frac{\int d^2b\ d^2s\ T_A(\vec{s})T_B(\vec{b}-\vec{s})\frac{(A-1)T_A(\vec{s})+(B-1)T_B(\vec{b}-\vec{s})}{2}}{\int d^2b\ d^2s\ T_A(\vec{s})T_B(\vec{b}-\vec{s})}\ , \qquad (7.1)$$

where $T_{A(B)}(\vec{s}) = \int dz\rho_{A(B)}(z,\vec{s})$ is the nuclear profile function. For a given position of the calculated $c\bar{c}$ pair creation point, the integrals are along the potential path of the $c\bar{c}$ system through the colliding nuclei. The average takes into account all possible positions, for a given value of b, of the $c\bar{c}$ pair creation point, weighted by the probability to create it at that point. Taking into account the experimental resolution, events contained in a given E_T range have an L distribution centered in $< L >$ and standard deviation ΔL. Figure 7.2 shows this correlation.

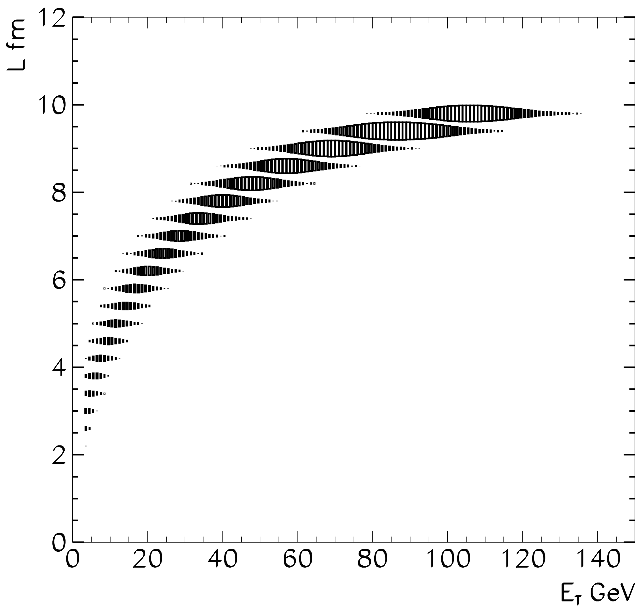

Figure 7.2: *The correlation between the transverse energy and the mean free path crossed by the $c\bar{c}$ pair inside the Pb nucleus.*

Taking into account the relative amount of protons and neutrons in each colliding nucleus, isospin corrections are needed when the Drell-Yan cross section is compared among different systems. So, the measured Drell-Yan cross sections have been normalized to proton–proton collisions as:

$$\sigma_{DY} = AB \cdot \frac{\sigma_{AB}^{DATA}}{\sigma_{AB}^{GRVLO94}} \cdot \sigma_{pp}^{GRVLO94} \ , \tag{7.2}$$

where $\sigma_{AB}^{GRVLO94}$ is the linear combination of the elementary cross sections (see equation 1.20), using GRVLO94 PDFs. Regarding Pb–Pb collisions, the predictions of PYTHIA for Drell-Yan events within the 2.9–4.5 mass interval and at the NA50 rapidity domain ($2.92 \leq y_{lab} < 3.92$) are: σ_{pp}=0.021 nb, σ_{pn}=0.028 nb, σ_{np}=0.018 nb and σ_{nn}=0.017 nb. Therefore the Drell-Yan cross section for Pb–Pb has been multiplied by 1.032. One should notice that, since J/ψ production at low x_F is dominated by gluon fusion, rather than by quark–antiquark annihilation, the isospin corrections are negligible and not considered.

Figure 7.3 shows the Pb–Pb analysis together with the results obtained in S–U and p–A interactions. The line is the common fit to p–A and S–U J/ψ/DY results. The J/ψ anomalous suppression emerges from this reference line at L=7∼8 fm. The contracted behaviour of the J/ψ/DY ratio at large values of L is due to the geometrical limit of this variable as the collisions become increasingly central. This is clearly observed in the E_T–L correlation.

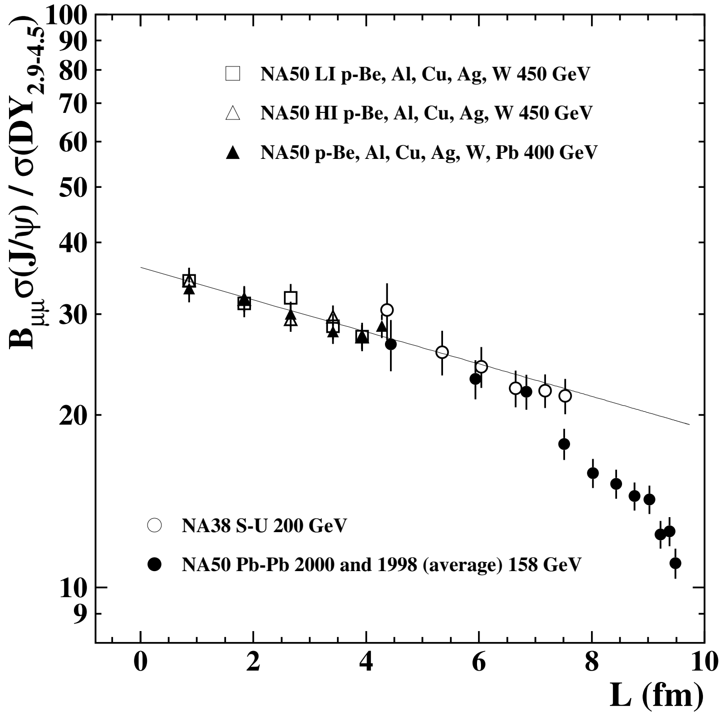

Figure 7.3: *The J/ψ/DY ratio as a function of L for several collision systems. The measured data have been rescaled to 158 GeV/nucleon and corrected for proton–proton isospin.*

The J/ψ suppression as a function of the energy density has been studied in section 5.5. Using this variable as the centrality estimator, figure 7.4 shows, both for S–U and Pb–Pb collisions, the J/ψ/DY ratio normalized to the normal nuclear absorption pattern:

$$R_{J/\psi} = \frac{\sigma(J/\psi)/\sigma(DY)_{measured}}{\sigma(J/\psi)/\sigma(DY)_{nuc.absorption}} \ . \tag{7.3}$$

One observes the departure from the normal behaviour at energy densities around 2.3 GeV/fm^3. This value is in qualitative agreement with the one found in p_T analysis, briefly described in section 1.7.3 and shown in figure 1.21 (right panel). A note of caution should be introduced as those energy density values, although calculated within the same framework, are slightly different from the ones presented here. They have not taken into account the centrality dependence of the $dE_T/d\eta$ distributions (recall figure 5.20), so a mean $C(\Delta\eta \to y^* = 0)$ factor has been applied to the several E_T ranges. Consequently, both sets of energy density calculations become a slightly different, mainly at low impact parameters. On the other hand, the $R_{J/\psi}$ suppression factor in Pb–Pb collisions stands around 0.6 at large energy densities. These measured results lay 10 standard deviations apart from the expected values.

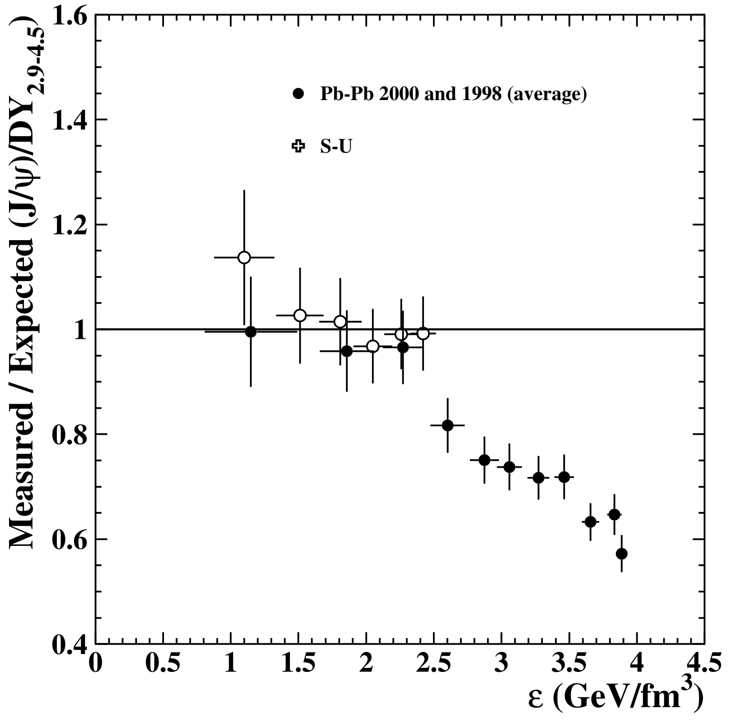

Figure 7.4: *Measured J/ψ/DY yields normalized to the yields expected (normal nuclear absorption), as a function of ϵ. The horizontal error bars represent the r.m.s. values quoted in table 7.1.*

Another pertinent centrality variable is the number of participants in the collision, N_{part}, as calculated in Glauber theory by integrating equation 5.11 over d^2s. This variable suffers, as well, from detectors smearing effects, displayed in figure 7.5. The J/ψ/DY ratio as a function of the number of participants in the collision is shown in figure 7.6. Again the same picture arises, i.e., the J/ψ/DY ratio leaves the normal trend at mid-centrality, $N_{part} \simeq$100 in this case. Due do the linearity between N_{part} and E_T, the J/ψ/DY ratio as a function of this centrality estimator exhibits the same behaviour as the one observed using E_T, i.e., a departure of the absorption curve at mid-centrality, followed by a continuous and smooth decrease as the collisions centrality increase.

Table 7.1 lists the Glauber calculations of L and N_{part}, concerning the 11 centrality intervals of the transverse energy measurement.

Since all these centrality variables, E_T, L, ϵ and N_{part}, calculated under the Glauber model of nucleus–nucleus collisions, are functions of the impact parameter b, they become

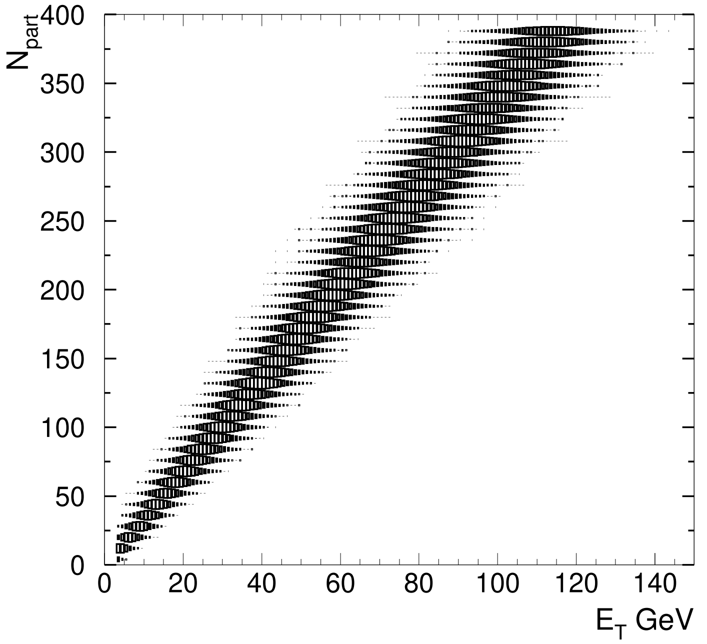

Figure 7.5: *The correlation between the transverse energy and the number of participating nucleons.*

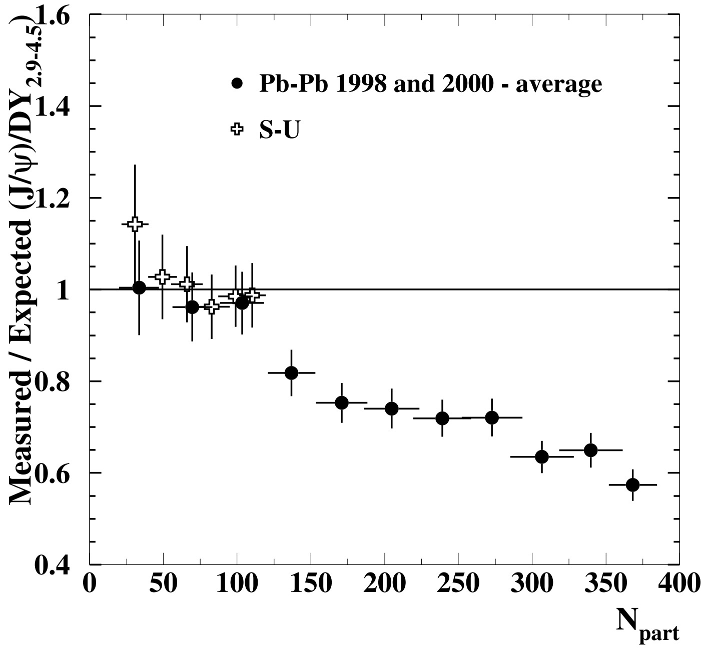

Figure 7.6: *Measured $J/\psi/DY$ yields normalized to the yields expected, as a function of N_{part}. The horizontal error bars represent the r.m.s. values quoted in table 7.1.*

E_T GeV	$< E_T >$ GeV	$< L >$ fm	r.m.s.	N_{part}	r.m.s.
3-15	10.6	4.64	0.74	27.1	13.5
15-25	20.4	6.18	0.45	67.9	13.5
25-35	30.3	7.10	0.36	102.2	15.0
35-45	40.2	7.79	0.30	136.1	16.2
45-55	50.2	8.30	0.25	170.3	17.5
55-65	60.1	8.70	0.23	204.3	18.7
65-75	70.1	9.02	0.19	238.7	19.7
75-85	80.1	9.29	0.18	272.5	20.6
85-95	90.1	9.44	0.13	306.4	21.6
95-105	100.0	9.64	0.20	339.6	21.5
105-150	111.5	9.79	0.07	367.9	16.5

Table 7.1: *Mean free path crossed by the $c\bar{c}$ pair inside the Pb nucleus and the number of participating nucleons for each centrality interval.*

strictly correlated. Therefore, whatever the chosen centrality estimator, the abnormal picture follows: somewhere at mid-centrality (E_T~30 GeV, L ~7 fm, ϵ ~2.3 GeV/fm^3 or N_{part} ~100) the J/ψ/DY ratio departs from the reference line, interpreted as being the normal absorption of J/ψ in nuclear matter. Which phenomenon is responsible for such anomalous behaviour is not definitely known. Next chapter is devoted to this exciting discussion.

7.2 ψ' suppression as a function of centrality

When compared to the J/ψ suppression pattern, a completely different behaviour of the ψ' as a function of centrality is found. Figure 7.7 (left panel) shows the ψ'/DY ratio for several systems: p–A (A $\equiv$ Be, Al, Cu, Ag, W and Pb) obtained at 400 GeV/c incident momentum, S–U at 200 AGeV/c, both rescaled to 158 GeV/c, and Pb–Pb at 158 AGeV/c. An incompatible behaviour of the ratio $B_{\mu\mu}\sigma(\psi')/\sigma(DY)$ as a function of L, between p–A and A–B interactions, is observed. Using an exponential parametrization, $\exp(- < \rho L > \sigma_{abs})$, we measure an absorption cross-section of 7.3 $\pm$ 1.6 mb for ψ' in p–A collisions [1], while in ion induced reactions the value obtained is much larger, 19.0 $\pm$ 2.3 mb. Moreover, ψ' suppression is, as a function of centrality, the same in S–U and Pb–Pb interactions. All data have been corrected for isospin. Concerning Pb–Pb collisions, the Drell-Yan cross section has been multiplied by 0.99, taking into account the cross section calculations by PYTHIA in the 4.2–7.0 GeV/c^2 and 2.92$\leq y_{lab} <$3.92

[1] This result is only an approximation, but it is compatible with the one obtained through full Glauber calculations, which fit an absorption cross-section of 7.7 $\pm$ 0.7 mb in p–A collisions.

ranges: σ_{pp}=2.6 pb, σ_{pn}=4.0 pb, σ_{np}=2.3 pb and σ_{nn}=2.0 pb.

The right plot in figure 7.7 exhibits the relative suppression between the two charmonium states as a function of the product of the projectile and target atomic mass numbers. The ratio $B'_{\mu\mu}\sigma(\psi')/B_{\mu\mu}\sigma(\psi)$ is parametrized by the power law $\mathrm{A}^{\Delta\alpha}$, where α accounts for all nuclear effects suffered by the resonances. The measured non-zero value of this parameter, $\Delta\alpha$=-0.047$\pm$0.008, means that the ψ' is more absorbed than the J/ψ, already in p–A collisions [3, 1]. Furthermore, a ψ' strong suppression with respect to J/ψ is measured for the heavier systems, S–U and Pb–Pb, the latter standing $\sim$12 standard deviations away from the extrapolated p–A result.

In order to compare the $\psi'/(\mathrm{J}/\psi)$ yields in A–B collisions with the ones obtained in p–A, as a function of the product A$\times$B, one should measure them in the full E_T domain. Either in S–U or in Pb–Pb, only the E_T ranges free from inefficiencies of target recognition algorithms can be used to measure the integrated $\psi'/(\mathrm{J}/\psi)$ yield. The E_T range available in Pb–Pb is almost the total, i.e., 3–150 GeV, while for S–U is 13–88 GeV [7]. The corrections applied to the measured $\psi'/(\mathrm{J}/\psi)$ ratio in the limited E_T ranges make use of the approximate linear ψ' suppression relatively to J/ψ as functions of the transverse energy, observed in both S–U and Pb–Pb collision systems. In what concerns the latter, in order to evaluate the contribution of the $\psi'/(\mathrm{J}/\psi)$ yield from the 0–3 E_T region not considered, a linear fit has been performed to the available $\psi'/(\mathrm{J}/\psi)$ ratio (recall figure 6.11) and extrapolated to the unexplored E_T domain. The correction factor is, then, given by the ratio between the averages of the integrals, that is:

$$Cor = \frac{\frac{1}{b-a}\int_a^b f(Et)dEt}{\frac{1}{b'-a'}\int_{a'}^{b'} f(Et')dEt'} = \frac{\frac{1}{150-0}\int_0^{150}\frac{\psi'}{J/\psi}(Et)dEt}{\frac{1}{150-3}\int_3^{150}\frac{\psi'}{J/\psi}(Et')dEt'} \; . \tag{7.4}$$

The $\psi'/(\mathrm{J}/\psi)$ yield measured in Pb–Pb collisions, concerning the 3–150 E_T domain, is (5.64$\pm$0.51)$\times 10^{-3}$. After this correction, estimated to be 2%, the true result becomes (5.75$\pm$0.52)$\times 10^{-3}$.

7.3 J/ψ and ψ' productions – measured over expected

A comparison between ψ' and J/ψ suppressions as functions of L, normalized to the suppressions expected, is performed. Figure 7.8 shows, for several interacting systems, the ratio of the measured charmonium yields and the corresponding expected values. The latter are computed as resulting only from normal absorption in nuclear matter, by means of a full Glauber calculation giving $\sigma_{abs}^{J/\psi} = 4.2 \pm 0.4$ mb, as extracted from a simultaneous fit to p–A and S–U interactions, in the case of J/ψ , and $\sigma_{abs}^{\psi'} = 7.7 \pm 0.7$ mb, as deduced only from p–A collisions, since its absorption cross section value is not compatible with the one obtained in S–U reactions. The L value corresponding to the departure from the

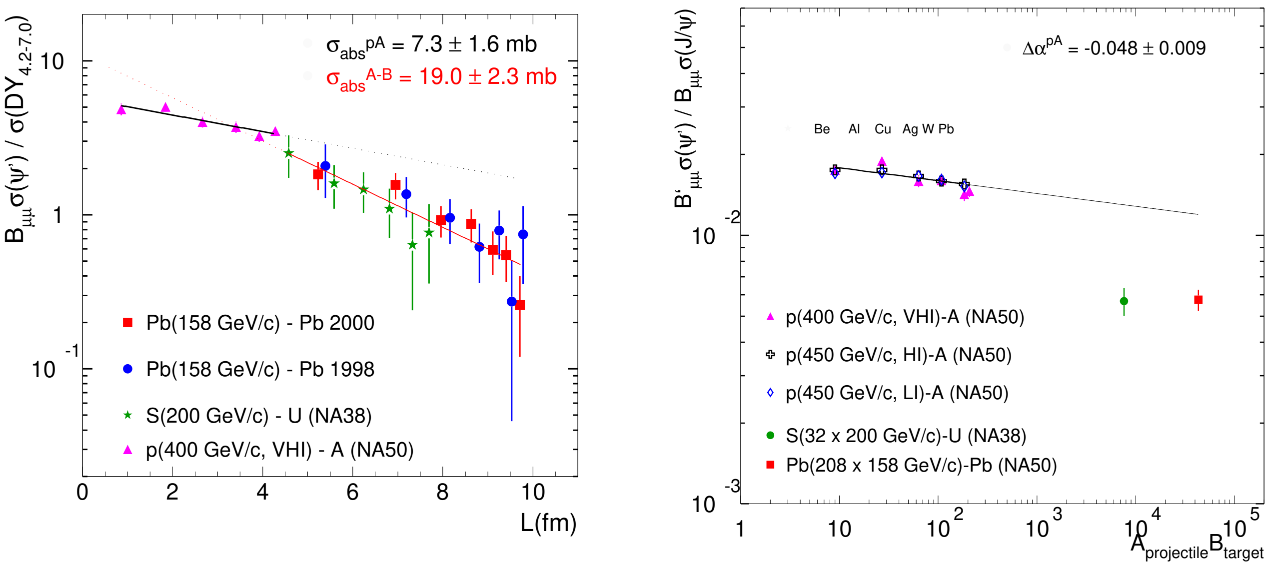

Figure 7.7: *$B_{\mu\mu}\sigma(\psi')/DY$ as a function of L (left). $B'_{\mu\mu}\sigma(\psi')/B_{\mu\mu}\sigma(\psi)$ as a function of A–B (right). Data measured at different energies have been rescaled to 158 GeV/nucleon. On the left plot, all data are corrected for proton–proton isospin.*

normal absorption is lower for ψ' than for J/ψ: 4 fm and 7 fm, respectively. This result is in agreement with the predictions from lattice QCD studies. Indeed, in this framework, as the ψ' mass is much closer to the $D\bar{D}$ threshold, only a 50 MeV excitation is needed to break it up, while 640 MeV are needed to excite a J/ψ above the $D\bar{D}$ threshold [8].

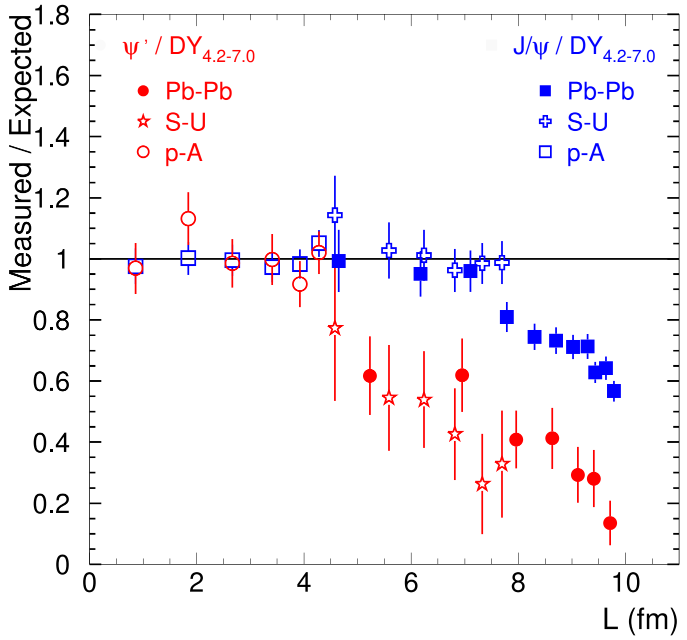

Figure 7.8: *Measured J/ψ and ψ' yields normalized to the yields expected, as a function of L, assuming that the only source of suppression is the ordinary absorption in the nuclear medium.*

Bibliography

[1] G. Borges (NA50 Coll.), Quark Matter 2004, in J. Phys. G: Nucl. Part. Phys. 30 (2004) S1351, PhD Thesis in preparation

[2] B. Alessandro et al. (NA50 Coll.), Phys. Lett. B553 (2003) 167

[3] B. Alessandro et al. (NA50 Coll.), Eur. Phys. J. C 33 (2004) 31

[4] H. Santos (NA50 Coll.), Quark Matter 2004, in J. Phys. G: Nucl. Part. Phys. 30 (2004) S1175

[5] A.D. Martin, R.G. Roberts and W.J. Stirling, Phys. Rev. D51 (1995) 4756

[6] C. Gerschel and J. Hüfner, Z. Phys. C 56 (1992) 171

[7] M.C. Abreu et al. (NA38 Coll.), Phys. Lett. B449 (1999) 128

[8] S. Digal, P. Petreczky and H. Satz, Phys. Lett. B514 (2001) 57

You say you got a real solution
well, you know,
we'd all love to see the plan.
You ask me for a contribution,
well, you know,
we're doing what we can.

John Lennon and Paul McCartney

Chapter 8

Comparisons with theoretical models

In this chapter, the J/ψ and ψ' suppressions are compared to the available theoretical models. Such approaches, either assuming purely hadronic scenarios or quark-gluon plasma, are constrained by the NA50 data. For this reason, some conventional hadronic models (see [1] and references therein), as well as models assuming QGP [2, 3], that in the past were compared to published Pb–Pb 1996 and 1998 results, cannot be compared, in a straightforward way, with these new results. In fact, they should be re-evaluated against the new data, as well as the new measured J/ψ absorption cross section.

A brief description of the models is given before comparisons with the data. The aim is only to give an introduction to the subject. The authors themselves give detailed descriptions and fundaments.

8.1 Charmonia production by statistical coalescence models

While the standard picture assumes that charmed mesons are predominantly produced in the early hard scattering processes, these models have a completely different approach [4, 5]. They assume that c and $\bar{c}$ quarks are produced at the very early stages of the collisions, during the pre-equilibrium partonic phase and the creation of $c\bar{c}$ pairs, as well as their possible annihilation, is neglected. Then, the number of c and $\bar{c}$ quarks remains approximately unchanged during the subsequent evolution (either in a deconfined medium or in a hadron gas). Finally, they are distributed over open charm mesons and charmonia at the hadronization stage in accordance with the laws of statistical mechanics.

These models were fitted to the Pb–Pb 1996 and 1998 data [1, 6, 7, 8]. Their applicability is restricted to the following number of participants in a collision: 100< N_{part} <350. Figure 8.1 shows the comparison of one of these models [8] with data. The model has two free parameters: $\sigma_{c\bar{c}}^{NN}$, the effective cross section of charm production by a nucleon pair, and η, the fraction of J/ψ entering the kinematic acceptance of the NA50 spectrometer. The agreement is quite good in the restricted domain of applicability, 27<E_T<100 GeV. However, the extrapolation to peripheral collisions gives a sharp increase of the theoretical function with decreasing E_T (or N_{part}). The qualitative explanation is the following — the smaller is the volume of the system the larger is the probability that c and $\bar{c}$ meet each other at hadronization stage to form a hidden charm meson. This assumption is not supported by the data and it would be even less if compared with Pb–Pb 2000 or Pb–Pb 1998 peripheral points. On the other hand, the upper limit of applicability has to do with the fact that the model does not account for hypothetical E_T fluctuations, beyond E_T> 100 GeV and present in the data, as proposed by [3]. In this E_T range the number of participants does not essentially change as E_T grows, so the relation $< E_T > \simeq q < N_{part} >$ (see section 5.5), being an ingredient of the model, can not be used anymore. Besides, assuming E_T fluctuations, the data points for E_T> 100 GeV are not necessarily related directly to the J/ψ suppression pattern but rather to an increase of the volume in which the energy density exceeds ϵ_c, resulting, thus, in an amplification of the J/ψ suppression [3].

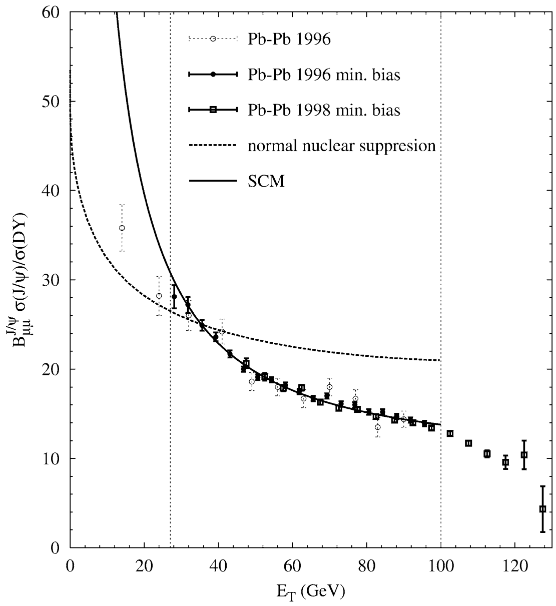

Figure 8.1: *Comparison between $B_{\mu\mu}J/\psi/DY$ old NA50 data and a statistical coalescence model [8]. The absorption cross section is σ_{abs}=6.4 mb, fitted to NA38 p–A and S–U data. The data stands for Pb–Pb 1996 and 1998 published analyses [6, 1]. Two vertical lines show the applicability domain of the model under consideration.*

Two of these authors argue that the statistic coalescence model also accounts for the observed ψ' suppression relatively to J/ψ [8]. In their point of view, the data beyond

$N_{part} \sim 100$ are compatible with a constant relative behaviour of the two resonances (see figure 8.2). This is in contradiction with a two–parameter fit performed using any set of data presented, particularly the averaged result between Pb–Pb 2000 and 1998. Excluding the first point, the slope is (-5.48±2.22)×10^{-3}, clearly not compatible with zero. Even considering only the last five points, the slope becomes (-4.92±2.93)×10^{-3}.

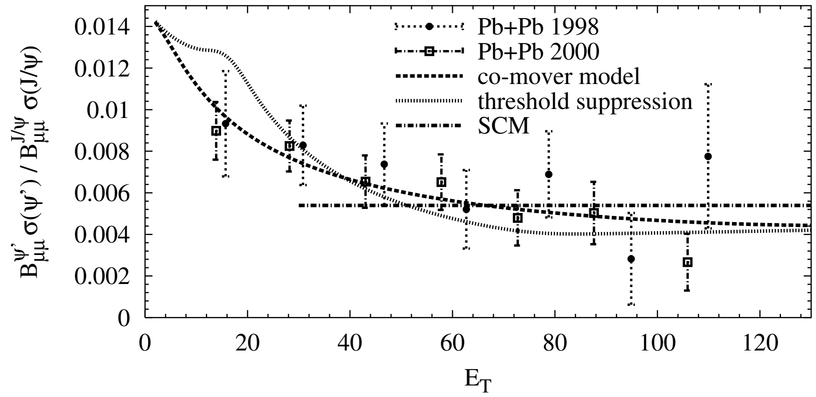

Figure 8.2: *Comparison between $B'_{\mu\mu}\psi'/B_{\mu\mu}J/\psi$ ratio and statistical coalescence model [8].*

8.2 J/ψ suppression by comovers

After formation, charmonium states are surrounded by a dense system of hadrons (mainly pions), the *comovers*. These secondaries, formed after $\tau_0 \sim$ 1–2 fm, may scatter with the pre-resonance $c\bar{c}$ pair or the J/ψ itself, since the typical formation time of a J/ψ from a colour octet state is less than τ_0. A spectator hadron moving with a velocity similar to the J/ψ enhances the probability to form open charm at the expense of charmonium production [9]. While a small effect is expected in p–A interactions, comover scattering should become more important as $\sqrt{s}$ and the collision system increase. So, unless the J/ψ–comovers interaction cross section is negligible, an important contribution to the J/ψ suppression is expected, namely at RHIC and LHC.

The comovers model is strongly constrained by the existing data, namely the experimental σ_{abs} fitted to NA50 p–A and NA38 S–U J/ψ/DY results. Two free parameters account for the J/ψ suppression: the comovers interaction cross section σ_{co}, which controls the centrality dependence of the ratio, and the absolute normalization. For a $\sigma_{abs} = 4.5$ mb, a $\sigma_{co} = 0.65$ mb is extracted from the preliminary Pb–Pb 2000 data analysis [10, 11]. Then, this value also describes the J/ψ suppression in S–U interactions, indicating that there is room for comovers in this collision system. The comparison is shown in figure 8.3. One should keep in mind that, any comparison between theoretical models and a large band of points, where three among five analyses concern the same data, become easily compatible. Figure 8.4 shows the comparison between the same model, rescaled by -7% [1], and the present analysis. The agreement is good, although maybe a σ_{co}=0.65 mb underestimates peripheral collisions. A new fit to these results would probably give a higher σ_{co}.

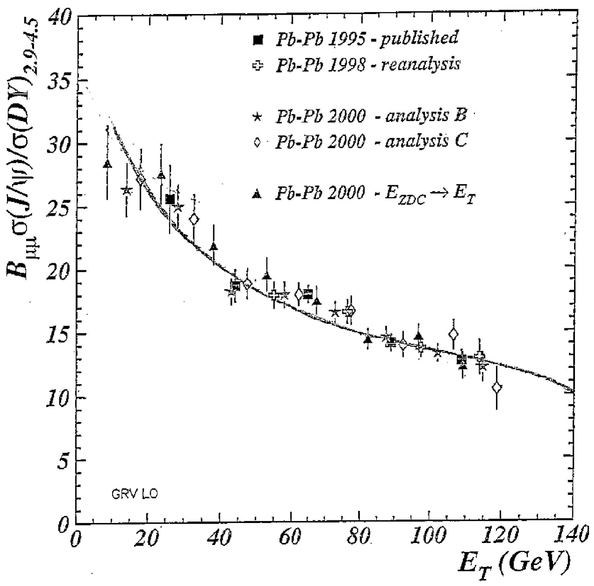

Figure 8.3: *Comparison between preliminary Pb–Pb 2000 results presented at QM2002 [10] and J/ψ dissociation by comovers model [11].*

Some authors argue that the J/ψ dissociation by comovers is very unlikely due to its small size and large binding energy of ~640 MeV. The J/ψ break up requires interactions with sufficiently hard gluons, but the gluon density within secondaries is too soft for hadronic matter at meaningful temperatures [12].

A different approach to J/ψ suppression by comovers is given in reference [13]. In this case, the dissociation of J/ψ by the lowest-lying pseudoscalar and vector mesons in the hadronic medium, assuming to be a hadron gas at temperature T, is considered. The fireball temperatures found at low centrality collisions lie in the range 160–180 MeV, in fair agreement with the results from particle abundances in heavy ion collisions at freeze-out [14] (see also figure 1.8), from lattice QCD calculations [16] and with the limiting temperature of a hadron gas, as estimated from the experimental hadron level density. The

[1] This rescale is to account for the difference between this J/ψ/DY normalization and the preliminary one of QM2002 [10], in which a different J/ψ (and ψ') parametrization from equation 4.2 has been used. The J/ψ suppression pattern remains unchanged.

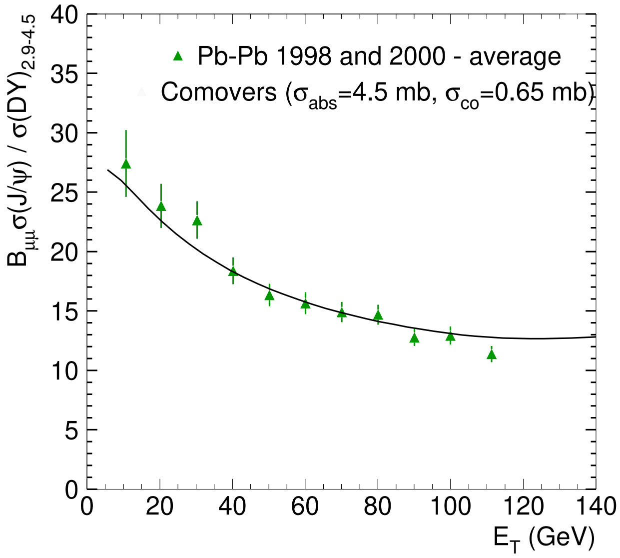

Figure 8.4: *Comparison between the averaged Pb–Pb 2000 and 1998 results and J/ψ dissociation by comovers model [11] tuned to preliminary Pb–Pb 2000 results.*

extrapolation to higher centralities is performed assuming that the increase of the average nucleon number per unit of overlapping area, for decreasing impact parameter, leads to the rise of temperature and energy density. Taking into account the nucleus-nucleus collision geometry, the J/ψ suppression is given in terms of the normal absorption in nuclear matter and the dissociation by comovers. Figure 8.5 shows the comparison between the suppression curves and data. The combination of the two mechanisms increases more and more against centrality with the rising temperature. However, clearly they are not sufficient to account for the experimental J/ψ suppression, suggesting that the remain is caused by quark-gluon plasma formation. The curve with initial temperature T=180 MeV fits the low centrality data and follows close to the data at large centrality. But in this case, the temperature rises up to 200 MeV at the transverse length $l \simeq$11 fm of the fireball, which is likely a too high value for a hadron gas. On the right panel, the comparison is performed using also the energy-temperature dependence, but concerning the Hagedorn gas. The temperature increase is small since the available energy density has to be shared among the large number of degrees of freedom in the vicinity of the Hagedorn temperature. Curve (b) takes into account nuclear geometrical effects.

A note of caution is in order. This model has been tested using the still preliminary NA50 analyses, presented at QM2004 [15]. Such results presented a $\sim$8% discrepancy between peripheral Pb–Pb and S–U collisions, which is no longer present, as can be seen, e.g., in figures 7.4 and 7.6. The model is also constrained by the assumption that J/ψ suffers from the same dissociation effects in both p–A and S–U collision systems, that is, the normal absorption in nuclear matter. In fact, the J/ψ absorption obtained in S–U interactions is σ_{abs}=7.0$\pm$3.0 mb suggesting that another suppression mechanism is present in this colliding system. However, if one assumes realistic limits for the hadron

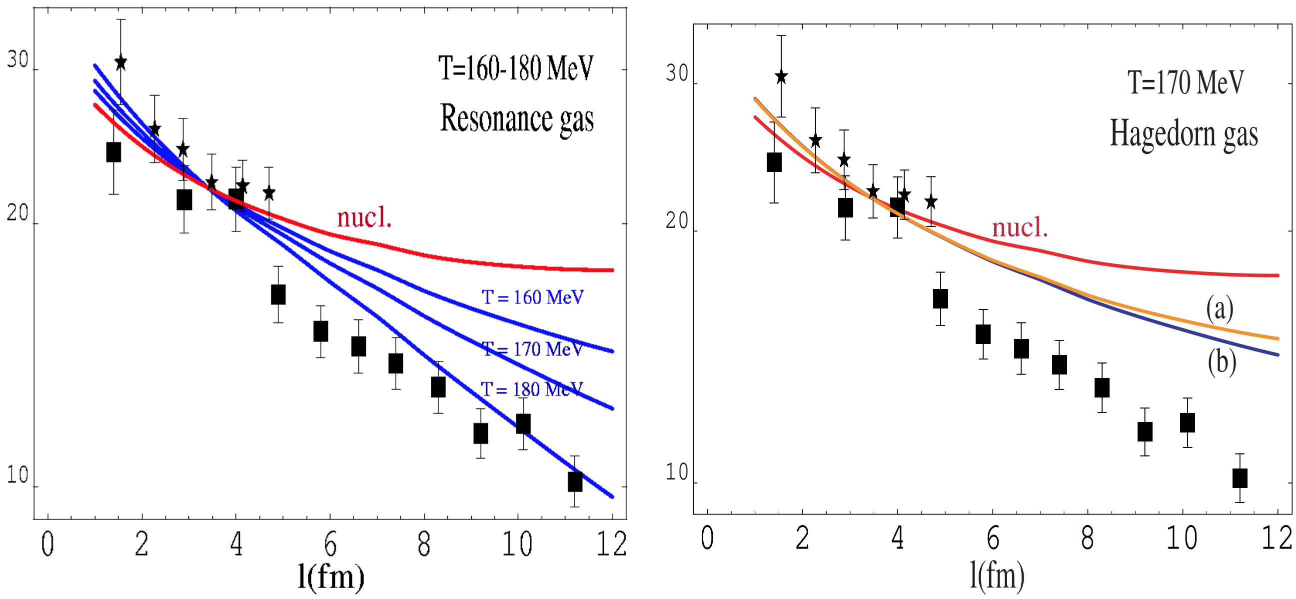

Figure 8.5: *Comparison between the suppression curves and J/ψ/DY from NA38 S–U (stars) and NA50 Pb–Pb (squares) preliminary results (see text for explanations). Left panel: the absorption by comoving particles for T=160–180 MeV, assuming a resonance gas and geometrical effects. The temperatures indicated refer to l = 3.4 fm. Right panel: the same as left one, but using the energy–temperature dependence of a Hagedorn gas. The upper curves stand for the nuclear absorption component. (from [13]).*

gas temperature, as is the case of T=170 MeV, no curve can fit the data, even at high centrality.

8.3 Charmonia suppression plus regeneration model

In this model charmonia production is investigated within a kinetic theory framework simultaneously accounting for dissociation and regeneration processes in both quark-gluon plasma and hadron gas phases of the reaction. It is assumed that charmonium states are produced in the primary hard scattering processes. The model implements in-medium properties of open and hidden charm states, inferred from finite-T lattice QCD calculations, namely the continuous decrease of the open charm threshold across the phase transition, together with T-independent charmonium masses and J/ψ resonance state survival above T_c [18]. Its core is a kinetic rate equation for the time evolution of charmonium states, τ_Ψ, in a system (fireball) of volume V_{FB}, assuming open charm states thermal equilibrium: $\frac{dN_\Psi}{d\tau} = -N_\Psi L(\tau) + G(\tau) = -\frac{1}{\tau_\Psi}[N_\Psi(\tau) - N_\Psi^{eq}(\tau)]$, which applies as long as a well-defined Ψ state exists ($\Psi \equiv$ J/ψ, ψ' and χ). L and G are loss and gain terms; $N_\Psi(\tau) = n_\Psi(T)V_{FB}(\tau)$, where $n_\Psi(T)$ is the resonance density [19]. This rate equation is integrated over the fireball evolution of the collision for Ψ states, for specific initial conditions, namely experimental yields from pp to A–B collisions and (pre-equilibrium) nuclear absorption. The initial charmonium numbers, N_Ψ, are assumed to follow hard production, subject to (pre-equilibrium) nuclear absorption. Figure 8.6 compares the model to the preliminary Pb–Pb 2000 data analysis [10], assuming a model input absorption cross section of $\sigma_{abs} = 4.5$ mb [2]. The model agrees with data quite well, although the comparison is again rough due to the several analyses band effect. Nevertheless, the agreement is confirmed in figure 8.7. All curves are rescaled by the already referred -7% value. Since the primordial J/ψ number is well above the equilibrium level, J/ψ regeneration (the gain term) is very moderate and, therefore, J/ψ suppression is the main effect at SPS energies. On the contrary, at RHIC energies the regeneration effect is dominant.

Typical values of the fireball thermalization time, τ_0, are 1/3 fm/c at RHIC ($\sqrt{s}$=200 GeV) and 1 fm/c at SPS ($\sqrt{s}$=17.3 GeV). The curve, identified as 'variable τ_0', is related to the limited description of the fireball. In particular, thermalization is expected to be delayed (and/or incomplete) at large impact parameters due to less energetic conditions.

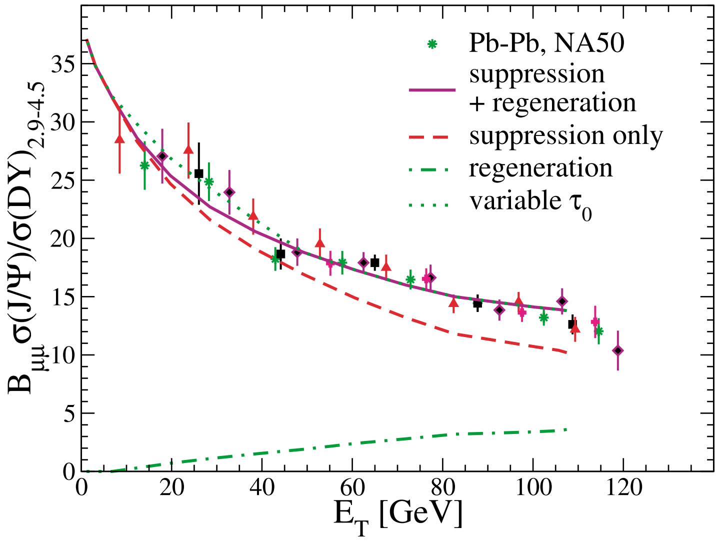

Figure 8.6: *Comparison between Pb–Pb 2000 results presented at QM2002 [10] and suppression plus regeneration model [18]*

In–medium effects are also needed to reproduce the relative behaviour of the charmonium states [20]. Figure 8.8 shows the comparison between suppression plus regeneration model and the ψ'/J/ψ ratio. With vacuum D-meson masses (m$_D$) the calculation underestimates ψ' suppression. The evaluation including in-medium effects improves the

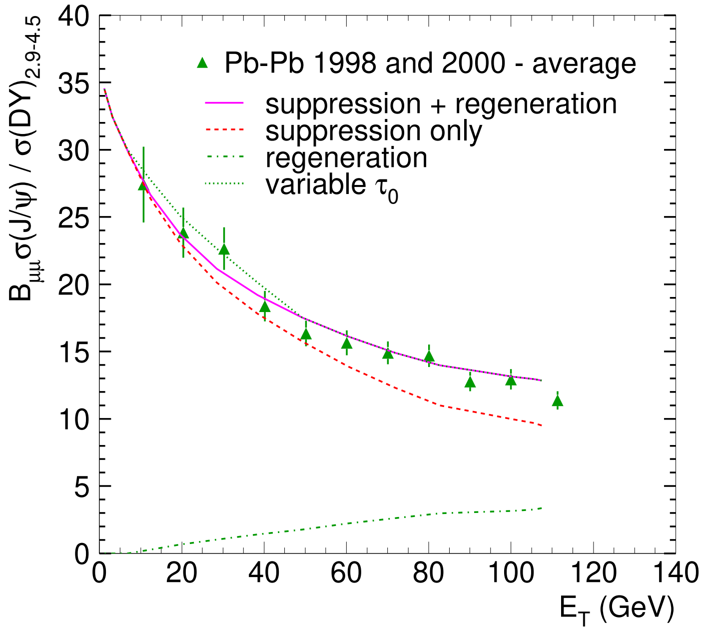

Figure 8.7: *Comparison between Pb–Pb 2000 results and suppression plus regeneration model.*

agreement, interpreted as being a direct consequence of the reduction of the $D\bar{D}$ threshold (m^*_D) in the hadron gas, opening the $\psi' \longrightarrow D\bar{D}$ decay channel. In order to reproduce the most recent NA50 data, an absorption cross section value of $\sigma^{\psi'}_{abs}$=7.9±0.6 mb, larger than the J/ψ one of 4.4 mb, has been used as input for the calculations, instead of a common value for J/ψ and ψ' absorption cross sections in nuclear matter, as being σ_{abs}=4.4 mb, improving, thus, the initial conditions.

The model takes into account some thermal off-equilibrium corrections, namely the thermal relaxation time, τ_c^{therm}, which reduces N_Ψ^{eq} in the early phases, and another one, related with the effective volume over which the charm quantum number is conserved. Although it seems that these corrections do not affect significantly the result, a definite conclusion would be useful.

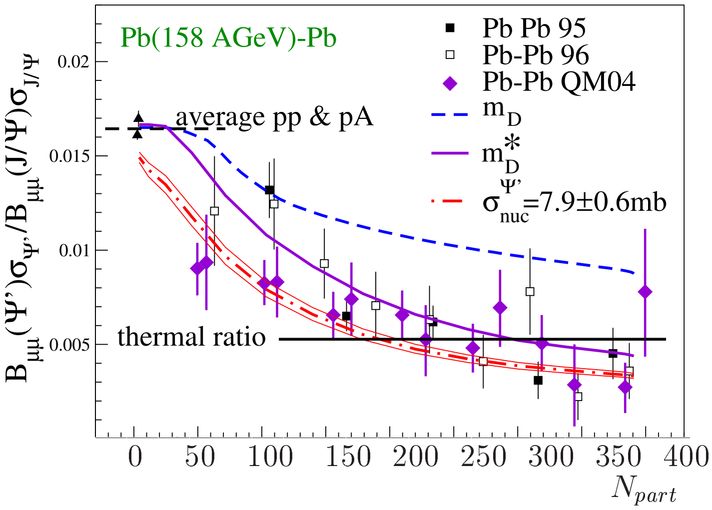

Figure 8.8: *$B'_{\mu\mu}\psi'/B_{\mu\mu}J/\psi$ ratio in Pb–Pb collisions at $\sqrt{s}$=17.3 GeV; solid (dashed) line: with (without) in-medium effects using a uniform nuclear absorption cross section of σ_{abs}=4.4 mb; dashed-dotted line: as solid line but with an updated value for the ψ' cross section, $\sigma_{abs}^{\psi'}$=7.9±0.6 mb [20].*

8.4 J/ψ suppression by parton percolation

Parton percolation is a geometric, pre-equilibrium form of deconfinement [2, 3]. Further interactions can thermalize this interconnected partonic system, turning it into a quark-gluon plasma, so that parton percolation constitutes an essential pre-requisite for QGP formation [24]. Some basic features are:

- In a nucleus-nucleus collision partons interact in the transverse nuclear plane. While at low densities individual partons from incident nuclei can be resolved, at higher densities, partons form a dense interacting cluster where independent partons are no longer meaningful.
- Considering a distribution of partons of transverse size πr^2 (*discs*) over the transverse plane πR_A^2, with $r \ll R_A$, the percolation threshold, u_c, is related to the critical density of partons by the expression: $u_c = \frac{N_c}{\pi R_A^2}\pi r^2 = n_c \pi r^2$. Since the partons overlap, only the fraction $1 - exp(-u_c) \simeq 2/3$ of the nuclear area is covered by partons.

[2] An elucidative description of the model is found in [21].

[3] Different approaches to J/ψ break up and percolation in nuclear collisions are given in terms of strings [22, 23].

- If the parton condensate formed through percolation contains partons hard enough to resolve the produced charmonium states, these partons can break-up charmonia, so that the onset of J/ψ suppression could coincide with that of parton percolation.

In order to apply the percolation model to a given A–B collision system, at a center of mass energy $\sqrt{s}$ per nucleon-nucleon collision, the fundamental needed parameters are: the nucleon density in the transverse plane, $n_s A$, and the parton density functions, $dN_q(s,Q^2)/dy$, determined in deep inelastic experiments, where x is the nucleon momentum fraction carried by the parton and Q the momentum resolution scale. At c.m.s. mid-rapidity (y_{cm}=0), $x = k_T/\sqrt{s}$, where k_T is the transverse momentum of the parton. In nuclear collisions, k_T defines the transverse size of the partons, setting the resolution scale to $k_T \simeq Q$. Joining these ingredients in the expression:

$$n_s A\Big(\frac{dN_q(s,Q^2)}{dy}\Big)_{x=Q_c/\sqrt{s}} = \frac{u_c}{(\pi/Q_c^2)} \tag{8.1}$$

one determines for what value of A, at given $\sqrt{s}$, percolation sets in, and it specifies the value $Q = Q(A, \sqrt{s})$ at the onset point. For Pb–Pb collisions at $\sqrt{s}$=17.3 GeV, $Q_c \simeq$0.7 GeV. This value is not sufficient to resolve the J/ψ, since the density of partons is too low, 0.9 or 1.0 GeV being necessary. On the contrary, the resolution scales for χ_c and ψ' states are smaller then the one at percolation point, being 0.6 GeV and 0.5 GeV, respectively. Thus, the first onset of J/ψ suppression at Pb–Pb collisions should occur at $N_{part} \simeq 125$, corresponding to J/ψ eliminated by the feed down absence from χ_c and ψ'. The combination of these thresholds and the nuclear collision profile determines the distribution of the charmonium production in the transverse plane, predicting which J/ψ are formed in the cluster and which are not. A survival pattern is, thus, determined as a function of centrality. Figure 8.10 compares the percolation model with preliminary Pb–Pb 2000 results [10] and the final ones, both normalized to the normal nuclear absorption. Uncertainties related to theoretical and experimental sources lead to smearing of the theoretical survival pattern. The agreement is quite good at low and mid–centrality. At high E_T the model predicts a smaller J/ψ survival probability than the one shown by data.

It would be interesting to apply the model to the $\psi'/(\mathrm{J}/\psi)$ behaviour as a function of centrality, in Pb–Pb collisions. In fact, the model assumes that the ψ' formed inside the percolating cluster disappears at its onset resolution scale; however, this too strong assumption seems not to be confirmed by the experimental results.

* * *

Recent lattice QCD calculations indicate that in a hot and dense medium of quarks and gluons, ψ' and χ states are dissociated at or below T_c, while J/ψ survives up to 1.5–1.9 T_c [25, 26]. So, a question can be raised: how to accommodate this theoretical prediction with the experimental results on charmonia production?

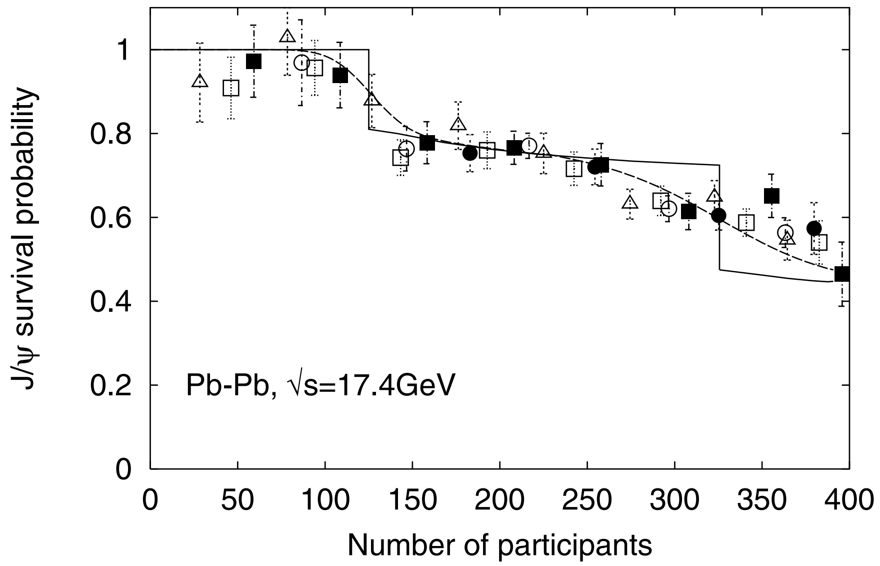

Figure 8.9: *J/ψ survival pattern in Pb–Pb collisions. Points are preliminary Pb–Pb 2000 results normalized to the normal nuclear suppression, the dashed curve is parton percolation suppression pattern and the solid line is the percolation onset (from [24]).*

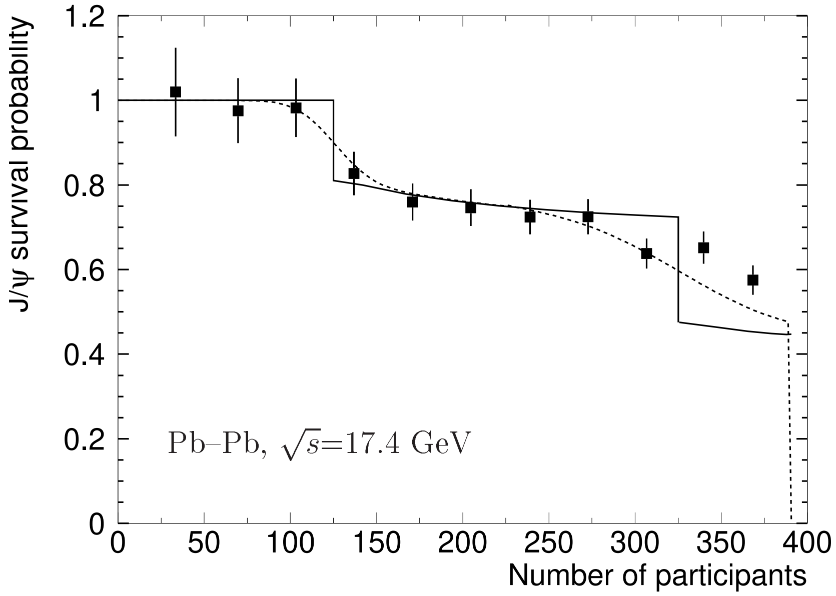

Figure 8.10: *J/ψ survival pattern in Pb–Pb collisions. Points are the Pb–Pb 2000 final results normalized to the normal nuclear suppression, the dashed curve is parton percolation suppression pattern and the solid line is the percolation onset.*

Bibliography

[1] M.C. Abreu et al. (NA50 Coll.), Phys. Lett. B477 (2000) 28

[2] M. Nardi and H. Satz, Phys. Lett. B442 (1998) 14

[3] J.P. Blaizot, P.M. Dinh and J.Y. Ollitrault, Phys. Rev. Lett. 85 (2000) 4012

[4] M.I. Gorenstein, A.P. Kostyuk, H. Stöcker and W. Greiner, Phys. Lett. B509 (2001) 277

[5] P. Braun-Munzinger, K. Redlich and J. Stachel, nuc-th/0304013

[6] M.C. Abreu et al. (NA50 Coll.), Phys. Lett. B450 (1999) 456

[7] A. Andronic, P. Braun-Munzinger, K. Redlich and J. Stachel, nuc-th/0304036

[8] A. Kostyuk and H. Stöcker, GSI 2004-1 (2004) 86

[9] R. Vogt, Phys. Rep. 310 (1999) 197

[10] L. Ramello (NA50 Coll.), Quark Matter 2002, in Nucl. Phys. A715 (2003) 243c

[11] A. Capella and D. Sousa, Eur. Phys. J. C 30 (2003) 117

[12] D. Kharzeev and H. Satz, Phys. Lett. B 334 (1994) 155

[13] L. Maiani, F. Piccinini, A.D. Polosa and V. Riquer, hep-ph/0408150

[14] J. Stachel, Phys. Lett. B465 (1999) 15

[15] H. Santos (NA50 Coll.), Quark Matter 2004, in J. Phys. G: Nucl. Part. Phys. 30 (2004) S1175

[16] F. Karsch, E. Laermann and A. Peikert, Nucl. Phys. B605 (2001) 579

[17] R. Hagedorn, Nuovo Cimento, Suppl. 3, (1965) 147

[18] Loïc Grandchamp, R. Rapp and G.E. Brown, Phys. Rev. Lett. 92 (2004) 212301

[19] Loïc Grandchamp, R. Rapp and G.E. Brown, J. Phys. G: Nucl. Part. Phys. 30 (2004) S305

[20] Loïc Grandchamp, R. Rapp and G.E. Brown, J. Phys. G: Nucl.Part. Phys. 30 (2004) S1355

[21] H. Satz, Quark Matter 1999, in Nucl. Phys. A661 (1999) 104c

[22] N. Armesto, M.A. Braun, E.G. Ferreiro and C. Pajares, Phys. Rev. Lett. 77 (1996) 3736

[23] J. Dias de Deus, R. Ugoccioni and A. Rodrigues, hep-ph/9907352

[24] S. Digal, S. Fortunato and H. Satz, Eur. Phys. J. C 32 (2004) 547

[25] M. Asakawa and T. Hatsuda, Phys. Rev. Lett. 92 (2004) 012001

[26] F. Karsch, Quark Matter 2004, in J. Phys. G: Nuc. Part. Phys. 30 (2004) S693

Chapter 9

Conclusions

Several thoretical models describe charmonia suppression in Pb–Pb collisions, either assuming thermalized quark-gluon plasma, or non-thermalized deconfined partonic medium or even pure hadronic scenarios. It is remarkable that so different approaches, give so good descriptions of the data. But, this also means that we may be still far way from a definite conclusion about the physical state created at the SPS, although the QGP scenario seems to be favoured in the detriment of the hadronic one. In particular, values of the required parameters to fit the data must be confirmed by other experiments, from both SPS and RHIC.

Regarding the NA50 experimental conclusions, they are summarized as follows:

- Concerning Pb–Pb collisions at center of mass energy $\sqrt{s}$=17.3 GeV, J/ψ is strongly suppressed with respect to Drell-Yan, as the collisons centrality increase;
- Results from Pb–Pb peripheral collisions are in perfect agreement with the ones observed in lighter systems, namely p–A and S–U;
- A departure from this behaviour occurs at mid-centrality, $E_T \simeq 30$ GeV (or $L \sim 7$ fm, $\epsilon \sim 2.3$ GeV/fm^3 or $N_{part} \sim 100$), followed by a continuous decrease of the J/ψ/DY ratios as centrality increases;
- As J/ψ, ψ' is strongly suppressed relatively to Drell-Yan as a function of E_T. A factor of 7 between peripheral and central collisions is verified;
- A steady decrease of the ratio between the two charmonium states, as a function of E_T, is observed, showing that ψ' is more suppressed than J/ψ in Pb-Pb collisions. Comparing results among central and peripheral interactions, a suppression factor of 40% is found;
- The ψ' suppression pattern is the same, regarding S–U and Pb–Pb collisions, and not compatible with the one exhibited at proton induced reactions;

- A comparison between ψ' and J/ψ suppressions, normalized to the suppression expected, shows that the ψ' anomalous suppression sets in earlier than for J/ψ.

Almost 20 years after the first predictions of H. Satz and T. Matsui, charmonium production remains as one of the most significant topics of the heavy ions program. NA50 data have been taken and evaluated. The results of J/ψ and ψ' production are presented within the possible accuracy. But, theoretical work is moving on. Indeed, this story is far from the end...